Antra Gaile

MEASUREMENT OF THE HIGGS BOSON PAIR PRODUCTION IN THE WWZZ DECAY CHANNEL AND DEVELOPMENT OF MTD CONTROL AND SAFETY SYSTEMS IN THE CMS EXPERIMENT

Doctoral Thesis

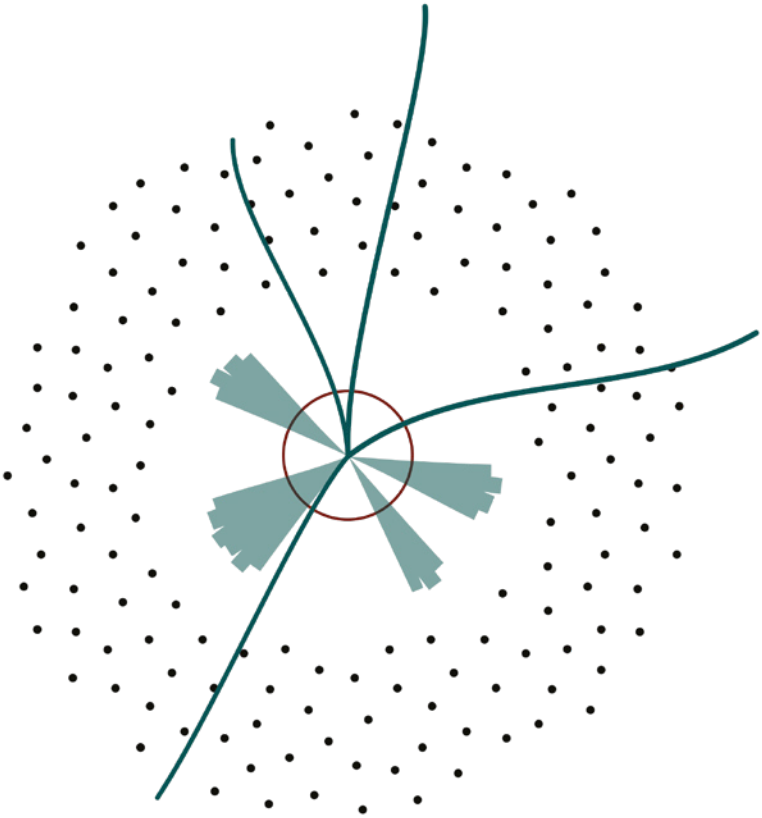

RTU Press
Riga 2026

RIGA TECHNICAL UNIVERSITY

Faculty of Natural Sciences and Technology
Institute of Particle Physics and Accelerator Technologies

ANTRA GAILE
Doctoral Student of **Riga Technical University's** and **University of Latvia's** Study Programme "Particle Physics and Accelerator Technologies"

MEASUREMENT OF THE HIGGS BOSON PAIR PRODUCTION IN THE WWZZ DECAY CHANNEL AND DEVELOPMENT OF MTD CONTROL AND SAFETY SYSTEMS IN THE CMS EXPERIMENT

Doctoral Thesis

Scientific supervisors:
Associate Professor Dr. phys.
TONI ŠĆULAC
Dr. phys.
FRANK GLEGE
Associate Professor Dr. phys.
KĀRLIS DREIMANIS

Riga 2026

ANOTĀCIJA

Higsa bozona sektora turpmāka izpēte ir nozīmīga augstas enerģijas fizikas kopienai, un tā ir noteikta kā viens no galvenajiem Lielā hadronu paātrinātāja fizikas programmas mērķiem. Pirms vairāk nekā 10 gadiem tika pierādīta Higsa bozona pastāvēšana, un aptuveni 10 gadu laikā varētu paziņot par Higsa bozonu pāru (*HH*) eksistenci. *HH* meklējumi ne tikai pārbauda vienu no pēdējiem neapstiprinātajiem elementārdaļiņu standartmodeļa (SM) parametriem, bet arī sniedz ieskatu mehānismos, kas norisinājušies agrīnajā Visumā. Šajā darbā ir izklāstīta pasaulē pirmās $HH \to WW^*ZZ^* \to 4l$ analīzes izstrāde un īstenošana. Tika analizēts 200 fb^{-1} liels datu kopums, kas ievākts ar Kompaktā mionu solenoīda (*CMS*) detektoru piecu gadu laikā. Šie rezultāti ļāva noteikt novēroto (paredzamo) 95 % ticamības pakāpes augšējo robežu, kas ir 142,3 (176,8) reizes lielāka par SM vērtību *HH* rašanās šķērsgriezumam. Apkopoti pierādījumi, kā mērķēta $HH \to WW^*ZZ^*$ kanāla analīzes iekļaušana uzlabotu kombinēto jutību *HH* novērošanai turpmākajos pētījumos. Papildus tam ir aprakstīts darbs pie detektora kontroles jeb vadības sistēmas izveides vienam no jaunajiem *CMS* eksperimenta apakšdetektoriem, *MTD* (minimāli jonizējošo daļiņu laika noteikšanas detektors), kas tiek izgatavots nākamajai eksperimenta fāzei. *MTD* mērķis ir nodrošināt precīzu laika informāciju par lādētajām daļiņām, kas to šķērso, tādējādi garantējot *CMS* detektora nevainojamu darbību. Šajā darbā prezentētās metodes un tehniskie risinājumi veicina vienu no *CMS* galvenajiem mērķiem – nodrošināt, ka *CMS* eksperiments arī turpmākajos gados ir viens no vadošajiem Higsa bozona fizikas precizitātes mērījumu veicējiem.

ABSTRACT

The continued exploration of the Higgs sector is central for the high energy physics community, it has also been set as one of the main missions for the Large Hadron Collider (LHC) physics program. More than ten years ago the discovery of Higgs boson production was claimed, and in around ten years the discovery of Higgs boson pair (HH) production could be declared. Measuring HH production not only tests one of the last unverified parameters of the Standard Model of particle physics (SM) but also provides a window into the mechanism that is believed to have shaped the early Universe. This Thesis presents the design and implementation of a world-first $HH \to WW^*ZZ^* \to 4l$ analysis. A dataset of 200 fb^{-1} collected with the Compact Muon Solenoid (CMS) detector across five data-taking years has been analysed. These results have allowed to set an observed (expected) 95 % confidence limit (CL) upper limit of 142.3 (176.8) times the SM value of the HH cross section. Findings showcase a proof-of-concept study of how an explicit inclusion of the $HH \to WW^*ZZ^*$ decay channel could improve the combined sensitivity for the HH production in future studies. Additionally, work has been presented on the detector control system (DCS) of a test-stand for one of the new CMS subdetectors, the Minimum ionising particle Timing Detector (MTD), built for the next era of the experiment. The goal of the MTD is to provide precision timing information for charged particles traversing it, thus ensuring flawless operation of the CMS detector. The methods and technical developments presented in this Thesis contribute to the long-term endeavour of ensuring that the CMS experiment remains at the forefront of precision Higgs physics in the years to come.

ANNOTATION

La poursuite de l'exploration du secteur du Higgs est au cœur des préoccupations de la communauté de la physique des hautes énergies et a également été définie comme l'un des principaux objectifs du programme de physique du Grand collisionneur de hadrons (LHC). Il y a plus de dix ans, la découverte du bosons de Higgs a été annoncée, et dans les prochaines années, l'observation de la production de paires de bosons de Higgs (HH) pourrait être établie. La mesure de la production HH permet non seulement de tester l'un des derniers paramètres encore non vérifiés du Modèle standard de la physique des particules (SM), mais aussi d'ouvrir une fenêtre sur les mécanismes qui auraient façonné l'Univers primordial. Cette Thèse présente la conception et la mise en œuvre d'une analyse $HH \to WW^*ZZ^* \to 4l$ unique au monde. Un ensemble de données correspondant à une luminosité intégrée de 200 fb^{-1}, collecté avec le détecteur *Compact Muon Solenoid* (CMS) sur une période de cinq ans, a été analysé. Ces résultats ont permis d'établir une limite supérieure observée (attendue) à 95 % de niveau de confiance de 142,3 (176,8) fois la valeur prédite par le SM pour la section efficace de production HH. Les résultats présentent également une démonstration de faisabilité montrant comment l'inclusion explicite de la désintégration $HH \to WW^*ZZ^*$ pourrait améliorer la sensibilité combinée à la production de HH dans de futures études. En plus, des travaux relatifs au système de contrôle du détecteur d'un banc d'essai pour l'un des nouveaux sous-détecteurs de CMS, le MTD, développé pour la prochaine phase du détecteur, sont présentés. L'objectif du MTD est de fournir des informations temporelles précises pour les particules chargées, garantissant ainsi le fonctionnement optimal du détecteur CMS dans des conditions de forte luminosité. Les méthodes et développements techniques présentés dans ce travail contribuent à l'effort à long terme visant à garantir que l'expérience CMS demeure à la pointe des mesures de précision du boson de Higgs dans les années à venir.

Contents

Acronyms

ALICE – A Large Ion Collider Experiment 44, 64

AOD – analysis object data 76

ATLAS – A Toroidal LHC ApparatuS 11, 17, 19, 22, 24, 32–38, 44, 48, 51, 64, 150

AUC – area under curve 120, 121, 126, 127

BDT – boosted decision tree 71, 101, 111–130, 132, 133, 140, 142, 147, 148, 151, 152

BEH – Brout–Englert–Higgs 12, 17, 20–22, 24, 39, 45

BNL – Brookhaven National Laboratory 40

BR – branching ratio 24, 26, 32, 33, 89, 90, 92, 93, 127, 129, 144

BSM – Beyond-the-Standard-Model 12, 17, 24, 27, 30, 31, 34, 36, 39, 129, 130, 152

BTL – barrel timing layer 66, 67, 78, 81, 86

CDF – Collider Detector at Fermilab 40

CERN – European Organization for Nuclear Research 39–42, 61, 67, 77, 79, 81, 85, 150

CHS – charged hadron subtraction 73

CKM – Cabbibo–Kabayashi–Maskawa 20

CL – confidence level 19, 33–36, 137, 139, 143, 145, 146, 148–150

CMS – Compact Muon Solenoid 11–15, 17, 19, 22, 24, 32–40, 44, 46–54, 56–58, 60, 62–64, 67–70, 73, 74, 76–80, 82, 83, 85, 86, 88, 89, 94, 95, 97, 98, 104, 107, 113, 135, 137, 141, 143, 145, 146, 149, 150

CMSSW – CMS software 51, 76

CP – charge-partity 20, 27

CPPF – concentration preprocessing and fan-out 60

CPU – central processing unit 61, 62

CR – control region 130–132, 138, 140–143, 146, 147

CSC – cathode strip chamber 57–59, 70

CTF – combinatorial track finder 69

CU – control unit 79

DAQ – Data Acquisition 65, 87

DCS – detector control system 12–14, 49, 63, 78–80, 82–88, 150, 151

DELPHI – DEtector with Lepton, Photon and Hadron Identification 79

DIM – distributed information management 85

DIP – data interchange protocol 85

DM – detector module 66

DNN – deep neural network 108, 116, 151, 152

DSS – detector safety system 12, 13, 63, 81, 88, 150

DT – drift tube 57, 58, 70

DU – device unit 79, 80

DY – Drell-Yan 33, 92, 103, 106, 147

EB – electromagnetic barrel calorimeter 54

ECAL – electromagnetic calorimeter 54, 55, 57, 66, 68, 71, 72, 95, 99, 105, 106

EE – electromagnetic endcaps calorimeter 54

EFT – effective field theory 27

ESPPU – European Strategy for Particle Physics update 37

ETL – endcap timing layer 66, 67, 78

EW – electroweak 19–21, 26, 31

EWSB – electroweak symmetry breaking 11, 17, 19, 21, 39

FPGA – field-programmable gate array 59, 61

FSM – Finite State Machine 79, 80, 85, 87, 88

FSR – final-state radiation 75

GEM – gas electron multipliers 57–59, 65, 70

ggF – gluon-gluon fusion 24, 25, 28–32, 34–36

GPU – graphical processing unit 62

GSF – Gaussian sum filters 71

HB – hadronic barrel calorimeter 56, 57

HCAL – hadronic calorimeter 56, 68, 105, 106

HE – hadronic endcap calorimeter 56

HEFT – Higgs Effective Field Theory 27, 28, 34–36

HF – hadronic forward calorimeter 56, 57

HGCAL – High Granularity Calorimeters 64, 67

HH – Higgs boson pair 11–14, 17, 24, 26–39, 44, 88–90, 93–95, 97, 101, 104, 111, 113, 117, 118, 122, 124, 127–129, 133, 136, 138, 140–144, 146, 148–152

HL-LHC – High-Luminosity LHC 11–13, 45, 47, 59, 64, 78, 141, 146, 148–150

HLT – high-level trigger 51, 59, 61, 62, 65, 76, 101, 102, 104

HO – hadronic outer calorimeter 56, 57

HPD – hybrid photodiode transducer 57

ID – identifier 71, 98, 102–105, 107–109, 126, 127, 134, 135, 140, 151

IP – impact parameter 52, 53, 105, 106

ISR – initial-state radiation 75

JCOP – Joint Controls Project 78–80, 83

JEC – jet energy correction 109, 110

JER – jet energy resolution 109, 135, 136

JES – jet energy scale 135, 136

JHU – Johns Hopkins University 97

KEK – High Energy Accelerator Research Organization 40

KF – Kalman filtering 69, 70

L1 – Level-1 59–61, 64, 65, 76, 98, 99, 136

LEP – Large Electron–Positron Collider 42, 44, 79

LGAD – low gain avalanche diode 67

LHC – Large Hadron Collider 11–13, 24, 28, 32, 34, 39–49, 52, 53, 55, 57, 59, 66, 67, 75, 77, 78, 80, 88, 95, 150

LHCb – LHC beauty 44, 64

LO – leading order 24, 25, 30, 75, 95, 97

LS – long shutdown 45–47, 52, 53, 56, 57, 61, 64, 78, 151

MC – Monte Carlo 51, 74–77, 89, 91, 92, 95–100, 103, 104, 106–110, 114, 121, 124–126, 128, 130, 132–136, 140–142, 145, 147, 148

MET – missing transverse energy 56, 57, 67–70, 74, 77, 90, 107, 110, 117, 126

MIP – minimum ionising particle 11, 55, 57, 64

ML – machine learning 61, 65, 89, 113

MTD – MIP Timing Detector . . . 11–14, 64–67, 77, 78, 81, 83–88, 150, 151

MTRS – massive temperature readout system . . . 83–86

MVA – multivariate algorithm . . . 72, 104, 106, 126, 127

NbTi – Niobium-Titanium . . . 42, 51

NLO – next-to-leading order . . . 24, 25, 30, 31, 75, 95, 130

NNLL – next-to-next-to-leading logarithmic . . . 31

NNLO – next-to-next-to-leading order . . . 30, 31

OPC – open platform communications . . . 80

OSOF – opposite sign (electric charge) opposite flavour . . . 91, 111

OSSF – opposite sign (electric charge) same flavour . . . 90, 91, 98, 111, 146

PDF – parton distribution function . . . 30, 31, 75, 76, 97, 134

PF – particle flow . . . 69–72, 76, 77, 105, 110

Pixel – pixel detector . . . 52–54, 69, 95

PLC – programmable logical controller . . . 63, 79, 80, 83, 85, 86

pp – proton–proton . . . 12, 13, 32, 40, 42–44, 46, 59, 67, 75, 94, 134, 150

PS – Proton Synchrotron . . . 42, 46

PSB – Proton Synchrotron Booster . . . 42

PU – pileup . . . 44, 47, 52, 64–66, 72, 73, 76, 94, 97, 98, 106, 108, 109, 134, 140

PUPPI – pileup per particle identification . . . 73, 110

PV – primary vertex . . . 69, 71, 73, 97, 106

QCD – quantum chromodynamics . . . 20, 30, 31, 33, 90, 92, 108, 134

QFT – quantum field theory . . . 17, 20

RF – radio frequency . . . 46

RHIC – Relativistic Heavy Ion Collider . . . 40

ROC – receiver operating characteristic . . . 120, 121

RPC – resistive plate chamber . . . 57–59, 65, 70

SCADA – supervisory controls and data acquisition . . . 78

SE – ECAL preshower detector . . . 54, 55

SF – scale factor . . . 97, 98, 107, 109, 127, 134, 136

SHAP – SHapley Additive exPlanation . . . 118, 119, 126

SiPM – silicon photomultiplier . . . 57, 66, 67, 82

SM – Standard Model of particle physics 11–14, 17–20, 22–24, 26–28, 30, 31, 33–36, 39, 129, 137, 143, 146, 148–150

SMI – State Manager Interface . . . 79

sPHENIX – super Pioneering High Energy Nuclear Interaction eXperiment . . . 40

SPS – Super Proton Synchrotron . . . 42, 46

SR – signal region . . . 101, 110, 114, 121, 124, 125, 128–130, 132–135, 138, 140–148

STAR – Solenoidal Tracker at RHIC . . . 40

SV – secondary vertex . . . 52, 69, 73, 106

TC – thermoelectric cooler . . . 66, 67, 81–83, 86

TEC – tracker outer endcaps . . . 53

tHH – HH associated production with a top quark . . . 30

TIB – tracker inner barrel . . . 53

TID – tracker inner disks . . . 53

TIF – tracker integration facility . . . 81, 83–86

TnP – “Tag and Probe” . . . 98

TOB – tracker outer barrel . . . 53

ttH – Higgs boson associated production with a $t\bar{t}$ pair . . . 24–26, 104, 126, 127

ttHH – HH associated production with a $t\bar{t}$ pair . . . 29, 30

UL – ultra legacy . . . 95

USA – United States of America . . . 40

UV – ultra violet . . . 36

VBF – vector boson fusion . . . 24, 25, 28, 29, 32, 34–36, 152

VFP – feedback voltage bias . . . 95

VH – Higgs-strahlung . . . 24–26

VHH – HH-strahlung . . . 29, 30, 35

WLCG – World-wide LHC Computing Grid . . . 77

WP – working point . . . 71, 98, 104–109, 113

YETS – year-end technical stop . . . 45, 46, 52

1. INTRODUCTION

Particle physics studies the sub-atomic world of fundamental particles and their interactions. It questions what the Universe is made of and tries to answer the unanswered questions of Nature. Currently, the Standard Model of particle physics (SM) is the most complete theoretical framework that describes elementary particles and their interactions. It has been extensively tested across decades by various experiments in laboratories around the globe and has provided astonishing agreement between the theory and experiment.

The discovery of the Higgs boson in 2012 by the ATLAS (A Toroidal LHC ApparatuS) and CMS (Compact Muon Solenoid) collaborations using data from two Large Hadron Collider (LHC) flagship experiments completed the particle content of the SM [1], [2]. Moreover, this observation confirmed the existence of the field responsible for the electroweak symmetry breaking (EWSB) and the generation of particle masses. Since the discovery, a great effort has been made studying the properties of the Higgs boson, including its couplings to other particles and to itself. This allows to probe the fundamental structure of the Higgs potential and search for possible deviations from the SM.

Single-Higgs production processes are well measured and understood; moreover, they are consistent with the SM predictions. The Higgs boson pair (HH) production, on the other hand, is yet in the search phase due to its rarity. The HH production provides experimental sensitivity to the Higgs self-coupling, thus shedding light on the shape of the Higgs potential, the stability of the vacuum, and whether the Higgs field alone can explain EWSB or additional fields are needed. As the Higgs self-coupling strength is fixed by the SM, any deviations would be indications of new physics.

The measurement of the HH production is equally as challenging as it is exciting. It has roughly three orders of magnitude smaller production cross section at LHC energies than the single-Higgs production. Thus, extracting a possible HH signal signature from the abundant background processes requires advanced event triggering, physics object reconstruction, event selection, and categorisation techniques that have to exploit the full capabilities of the CMS detector. Moreover, robust and reliable analysis methods need to be developed in preparation for the future data-taking periods.

In the near future, the LHC will undergo a major upgrade to increase the number of particle collisions, thus entering into its Phase-II, the High-Luminosity LHC (HL-LHC) [3]. The increase in collisions and the collected data will allow for more detailed studies of the fundamental particles and rare phenomena, such as the HH production. To fully exploit the physics potential of the HL-LHC, the CMS detector is undergoing major upgrades to sustain higher data rates. A completely new subdetector is being built – the MIP Timing Detector (MTD) [4], where MIP stands for the minimum ionising particles. It will provide CMS with crucial timing information, allowing to unravel the complex aftermath of particle collisions.

This Thesis is dedicated to the study of HH production in its $HH \to WW^*ZZ^* \to 4l$

decay channel using proton–proton (pp) collision data collected with the CMS detector. This channel has never been explicitly targeted, and thus this analysis is unique not only to the LHC, but in general to the whole particle physics community. Here, one Higgs boson decays into a pair of W bosons and the other into a pair of Z bosons, resulting in four leptons in the final state. For both vector boson species, one of them is off-shell in terms of its mass, thus denoted with a star. To tackle this channel, the Thesis focusses on the development of the full event selection and categorisation, background estimation, and signal extraction. It builds the foundation for the future $HH \to WW^{*}ZZ^{*}$ analysis and contributes to the ongoing Compact Muon Solenoid (CMS) effort to measure the Higgs boson self-coupling. Beyond this physics analysis, a crucial part of this work involves contributions to the detector control system (DCS) and detector safety system (DSS) for one of MTD's test-stands. The flawless operation of the MTD in the Phase-II era will be crucial for an improved measurement of the HH production. For simplicity, throughout this Thesis natural units of $\varepsilon_0 = \hbar = c = 1$ are used, unless explicitly stated.

To tackle this exploration, the Thesis has been structured into eight chapters:

Chapter 1 provides a brief introduction and its sections outline the aim, tasks and significance of this work.

Chapter 2 introduces the theoretical framework and motivation for HH production studies. It reviews the SM, the role of the Brout–Englert–Higgs (BEH) mechanism, Higgs boson and its properties, and possible Beyond-the-Standard-Model (BSM) extensions. Moreover, it introduces the HH production mechanism and the current experimental searches.

Chapter 3 describes the experimental environment, including the LHC accelerator complex and the CMS detector. Both current and future setups are discussed.

Chapter 4 outlines physics object reconstruction and identification at the CMS detector. It characterises also the event simulation.

Chapter 5 reports the necessary steps for building a DCS at the LHC experiments. Its sections detail the MTD test-stand, its DCS design choices and architecture, as well as indicates its limitations and possible evolution.

Chapter 6 explains the analysis of HH production in the chosen final state, including the motivation to pursue this channel, the analysed datasets, object and event selection, background estimation, and statistical interpretation.

Chapter 7 summarises the analysis results and outlines prospects for future measurements in the HL-LHC era.

Chapter 8 encapsulates the final conclusions and remarks of this Thesis.

1.1. Aim of the Doctoral Thesis

The aim of this Thesis is to study the production of HH in pp collisions at the LHC, using data collected with the CMS detector over a span of five years. It includes designing the analysis framework, performing data analysis and setting an upper limit on the production cross section, via the $HH \to WW^*ZZ^* \to 4l$ decay channel. Additionally, the Thesis develops the DCS and DSS for a MTD test-stand that is to become the DCS prototype.

1.2. Tasks of the Doctoral Thesis

1. Review the theoretical motivation for researching HH production, the novelty of using the $HH \to WW^*ZZ^*$ multilepton decay channel.

2. Describe the experimental environment of the LHC and CMS, emphasizing the subsystems and physics object reconstruction relevant to the $HH \to WW^*ZZ^*$ multilepton study.

3. Design and validate the event selection, categorisation, and signal extraction for the $HH \to WW^*ZZ^* \to 4l$ analysis, perform the data analysis and measure the upper limit of the HH cross section.

4. Review the necessary requirements for the MTD test-stand's DCS and contribute to its development.

1.3. Thesis Statements to be Defended

1. The analysis of HH production provides experimental sensitivity to the structure of the Higgs potential and enables to set constraints on the self-coupling parameter within the current experimental reach.

2. The results obtained from the $HH \to WW^*ZZ^* \to 4l$ channel analysis are compatible with the SM predictions within the current statistical and systematic uncertainties.

3. The developed analysis framework is scaleable and readily extendable to larger data sets, providing a solid foundation for future HH production studies at the HL-LHC.

4. A DCS for the MTD test-stand is designed, implemented, and commissioned. The system meets the operational requirements and serves as a functional prototype for the final MTD DCS.

1.4. Scientific Novelty

1. This Thesis presents the first ever measurement of the HH production cross section in the $HH \to WW^*ZZ^* \to 4l$ decay channel using the CMS data.
2. The created design, implementation and optimisation of the analysis strategy for the $HH \to WW^*ZZ^* \to 4l$ channel has allowed to reach sensitivity of the HH production cross section below 200 times the SM value.
3. This Thesis provides insight in the novel DCS for the MTD test-stand.

1.5. Practical Significance

1. This Thesis represents the first feasibility and sensitivity study of the $HH \to WW^*ZZ^*$ four lepton decay channel at CMS, establishing the methodological framework required for future analyses, and possible combinations.
2. The developed tools and methods for event categorisation, object identification, and calibration and methods for background suppression, signal extraction, systematic uncertainty treatment are directly applicable to broader searches for multiboson, multilepton and exotic signatures.
3. This Thesis encapsulates the needed steps for building a DCS that ensures safe and effective detector operation. The built DCS has been vital for a successful development, assembly and commissioning of the MTD.

1.6. Approbation of PhD Thesis in Scopus and Web of Science Indexed Articles

During the doctoral study period, the author of the Thesis co-authored 262 publications as a member of the CMS collaboration. Of these, 46 are publications of the CMS Higgs Physics Analysis Group where the author is an active member. Statistics retrieved on 26.01.2026 from https://inspirehep.net/authors/2643592 (Scopus ID of the author: 57214117093, ORCID: https://orcid.org/0000-0003-1350-3523).

Additionally, these six documents can be highlighted, two of which are internal to the CMS collaboration. They are internally reviewed and approved by experts, conveners, and the whole CMS collaboration because they contain valuable, technical information, critical for knowledge transfer and the eventual inclusion in further CMS publications.

[1] *CMS internal note (parts in Chapter 4 in the Thesis)*
A. Gaile, N. Strautnieks, A. Petkovic, A. Sculac, T. Sculac, E. Pajuste, K. Dreima-

nis. "Low-p_T electron selection efficiency studies". Technical report, CERN, Geneva, 2022, CMS AN-21/165. This note resulted in: CMS Collaboration. "Low-$\mathrm{p_T}$ electron Electron ID scale factors from CMS in proton-proton collisions at $\sqrt{s} = 13$ TeV using J/ψ events". CMS Detector Performance Summary, CERN, Geneva, 2023, CMS-DP-2023-081.

[2] *Open access paper (parts in Chapter 3 in the Thesis)*
CMS MIP Timing Detector group, including **A. Gaile**. "Optimization of LYSO crystals and SiPM parameters for the CMS MIP timing detector", JINST 19, 12, P12020, 2024,
DOI:10.1088/1748-0221/19/12/P12020.

[3] *CMS internal note (Chapter 6 in the Thesis)*
A. Gaile A. Sculac, R. Jiang, C. Charlot, T. Sculac, K. Dreimanis. "Search for non-resonant Higgs boson pair production in WWZZ decay mode with full Run 2 and early Run 3 dataset". Technical report, CERN, Geneva, 2024, CMS AN-24/245.

[4] *Proceedings in the conference LHCP2025 (parts in Chapter 2 in the Thesis)*
A. Gaile "Non-resonant HH and Higgs self-coupling measurements by CMS". At the Thirteenth Annual Large Hadron Collider Physics conference, Taiwan, 2025, DOI:10.22323/1.499.0105.

[5] *Open access paper (parts in Chapters 3 and 5 in the Thesis)*
CMS BTL group, including **A. Gaile**. "The CMS barrel timing layer: test beam confirmation of module timing performance", Nuclear Instruments and Methods Section A, 1081, 170823, 2026, DOI:10.1016/j.nima.2025.170823.

1.7. Dissemination in International Scientific Conferences

[1] A. Gaile "Non-resonant HH and higgs-self couplings measurements by CMS". Presentation at the The Thirteenth Annual Large Hadron Collider Physics (LHCP2025) conference, May 2025,
URL: https://indico.cern.ch/event/1419878/contributions/6442906/.

[2] A. Gaile "Study of Non-Resonant HH Production in WWZZ Decay Mode at CMS Experiment". Presentation at the 4th CERN Baltic Conference, October 2024, URL: https://indico.cern.ch/event/1416853/contributions/6178181/.

[3] A. Gaile "Detector control and safety system for MIP Timing Detector". Poster at the 3rd CERN Baltic Conference, October 2023,
URL: https://indico.cern.ch/event/1288731/contributions/5600676/.

[4] A. Gaile “Run 3 electrons, new studies/ recipes – J/ψ studies”. Presentation at the HZZ Workshop, June 2023,
URL: https://indico.cern.ch/event/1233959/contributions/5310341/.

[5] A. Gaile “Development of the MTD Control and Safety Systems at CMS”. Presentation at the 2nd CERN Baltic Conference, October 2022,
URL: https://indico.cern.ch/event/1147717/contributions/5069252/.

[6] A. Gaile, N. Strautnieks, J. Proskurins “Improving low-p_T electron reconstruction for Higgs physics at CMS”. Presentation at the 1st CERN Baltic Conference, June 2021, URL:
https://indico.cern.ch/event/970609/contributions/4415897/.

1.8. Use of Artificial Intelligence Tools in the Doctoral Thesis

The summary of the Thesis was prepared using the `Tildes Birojs 2022` machine translation tool. The tool was used from desktop software, therefore, only the standard machine translation model is available, without enhancements offered by artificial intelligence or large language models. The summary was translated from English into Latvian and used as the first translation layer for all chapters.

2. MOTIVATION FOR HIGGS BOSON PAIR PRODUCTION STUDIES

On the 4th of July, 2012, the ATLAS and CMS collaborations jointly announced the discovery of a scalar boson with a mass of about 125 GeV. This boson, compatible with the Higgs boson predicted by the BEH mechanism [5], [6], is an integral part of the SM [1], [2], as it explains EWSB. The mass of the Higgs boson is a free parameter within the SM, and fixing its value provides a significant insight in the nature of our Universe. Since the discovery of the Higgs boson and the first attempt at measuring its mass, a great effort has been made studying the properties of the Higgs boson. Up to now, each measurement within the uncertainties remains consistent with the SM prediction. In many cases, we have been able to advance past the discovery to precision measurements, e.g., by measuring the Higgs boson coupling strength to vector bosons. However, some properties remain more elusive and we are still in the search phase. In such cases, we have been able to set only the upper or lower limit on the value. An example of such a case is Higgs boson self-interaction or self-coupling.

The study of the Higgs boson self-coupling sheds light on the shape of the Higgs potential and the EWSB. The Higgs self-coupling strength is fixed by the SM, as will be introduced in Section 2.1, therefore, any deviations could be indicative of several BSM physics scenarios with various theories suggesting sizeable modifications of this value. The most direct method for experimentally probing the Higgs self-coupling is the study of HH production. However, this production mode is very rare, with a predicted cross section three orders of magnitude lower than that of single-Higgs boson production, making any experimental search challenging.

In this chapter, theoretical and experimental motivation is provided for pursuing a HH production measurement. Section 2.1 gives a quick glimpse into the SM and its symmetries, while Section 2.2 expands on the BEH mechanism and on the Higgs potential, as well as its role in the EWSB. What is known about the Higgs boson and its impact on the HH searches is expanded in Section 2.3. Section 2.4 introduces the SM shortcomings and how HH production can unmask potential new physics. Section 2.5 summarises main production mechanisms for the HH production and in Section 2.6 follows a short description of HH decay channels, finally, highlighting the experimental motivation for studying the HH production.

2.1. The Standard Model of Particle Physics and its Symmetries

The SM remains the best theoretical framework describing the sub-atomical world of fundamental particles and their interactions. It is a quantum field theory (QFT) based on gauge symmetries and it can precisely predict the properties of the particles contained within it. Moreover, it describes three of the four fundamental forces. The framework is able to explain the weak, strong, and electromagnetic interactions of particles. However, it fails to describe gravity. So far, all attempts to formulate a consistent quantum field version of gravity have been unsuccessful. However, gravitational effects at the particle scale are many orders of magnitude weaker than the other fundamental interactions, and far below current experimental sensitivities. Thus, the absence of gravity from the SM does not hinder its success at collider energies.

Fundamental or elementary particles are point-like constituents of matter and, by definition, have no substructure. They can be grouped into the building blocks of matter – fermions – and force carriers – bosons – as can be seen in a schematic representation in Fig. 2.1. For simplicity, it does not show the corresponding antimatter particles, but highlights possible particle and force interactions.

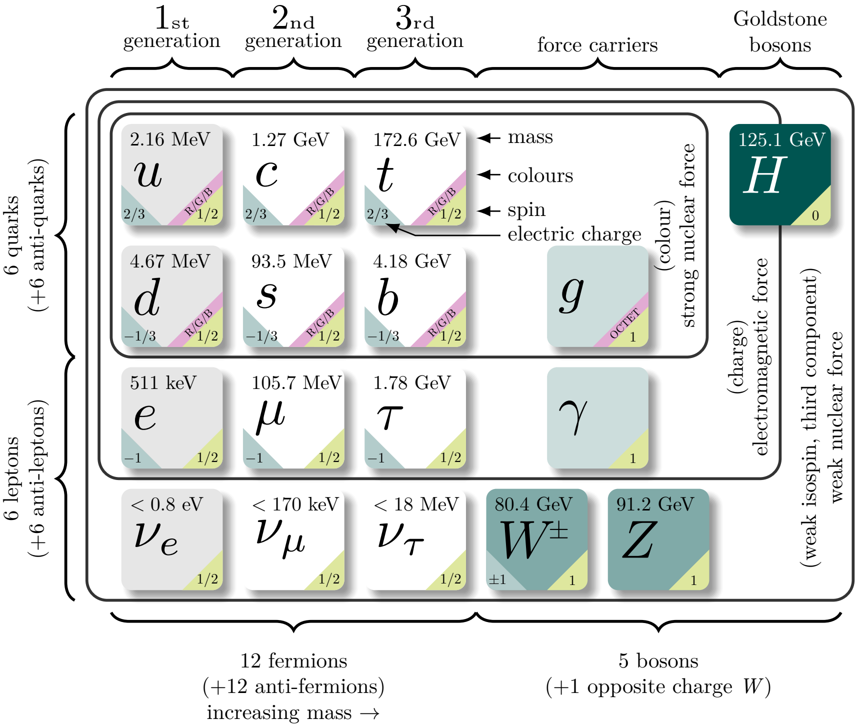

Figure 2.1. The fundamental particles of the SM, adapted from [7], indicate the mass, colour, spin and charge numbers as well as classification within generations and noting possible interactions.

The fundamental forces are mediated by bosons. Bosons are intermediate interaction particles with integer spin. Each spin-1 boson is associated with a different force. Photons, γ, mediate electromagnetic interaction. The electromagnetic force is the interaction between particles that have an electric charge. As photons are massless, the electromagnetic force has infinite range, and as photons do not carry an electric charge, they do not interact with themselves. Gluons, g, mediate the strong interaction, which acts between particles that carry the colour charge – quarks and gluons. It is the strongest of the fundamental forces. There are three colour charges of quarks – red, green, and blue. Gluons carry a liner colour-anticolour combination, thus they can interact with themselves, leading to interesting phenomena like the "colour confinement". It limits strong force's range although gluons are massless. The three weak bosons, W^+, W^- and Z, mediate the weak interaction. All three are massive particles, and can interact with themselves. The W bosons carry an electric charge, while the Z bosons are electrically neutral. The weak interaction is responsible for processes that change the flavour (type) of particles. It is important to note that the weak interaction couples only to the left-handed fermions and the right-handed antifermions. This chirality describes how the field transforms under the Lorentz group, and for massless particles it also describes the direction of the spin relative to the momentum.

The framework that is the SM started with a unified description of the weak and electromagnetic interactions combined into a single electroweak (EW) interaction. However, this symmetry was spontaneously broken, distinguishing the two forces and creating other consequences, as will be expanded upon in Section 2.2. The Higgs boson, the only spin-0 elementary particle, is responsible for the EWSB. Its mass is around $m_H \approx 125$ GeV, as measured by ATLAS and CMS collaborations [1], [2]. The uniqueness of the Higgs boson gives it a central importance for the SM, as will be shown in further sections.

Elementary fermions have spin $s = 1/2$ and are further classified into leptons and quarks. There are three generations of elementary fermions, however, theory-wise, there is no reason why there should be exactly three "copies" of each particle. At the same time, the detection of neutrino oscillations gives experimental proof that at least three distinct neutrino mass states exist (thus, three generations of leptons) [8], and from the precision measurements of the Z boson width, it is known that there are exactly three light neutrinos coupling to it [9]. Each next generation is more massive than the previous, with their masses spanning orders of magnitude. Only the first generation fermions are stable, others are unstable and through various processes decay to stable particles.

Leptons do not feel the strong force, but participate in the weak interaction given the correct chirality; the charged leptons also interact via the electromagnetic force. Electrons are stable, while muons have a lifetime of around $2 \cdot 10^{-6}$ s and taus have a lifetime of around $3 \cdot 10^{-13}$ s [10]. Neutrinos were predicted to be massless, but due to the observation of neutrino oscillations it was proved that they have extremely low mass [8]. Currently, only upper limits with confidence level (CL) of 90 % of possible masses are set: $m_{\nu_e} < 0.8$ eV, $m_{\nu_\mu} < 0.19$ MeV, $m_{\nu_\tau} < 18.2$ MeV (measurement for tau neutrino mass is reached for a CL of 95 %) [10]. Again, the SM cannot explain the neutrino masses, as well as the EWSB, and the Higgs sector alone cannot incorporate them.

The other type of fermions are quarks. Quarks can have one of six flavours: u (up),

d (down), c (charm), s (strange), t (top/truth), and b (bottom/beauty). Throughout this Thesis, when referencing quarks either their short or long name will be used interchangeably. Quarks can interact via electromagnetic, weak, and strong forces. As coloured states can not exist freely, quarks are detectable only as colour neutral bound states – hadrons. This is a direct consequence of the "colour confinement". Hadrons made from a quark and an antiquark are called mesons while three quark systems are referred to as baryons. As quark flavour is not conserved in the weak interaction, the weak and mass eigenstates of quarks do not coincide and are therefore subject to mixing. Mixing is characterised by the Cabbibo–Kabayashi–Maskawa (CKM) matrix [11], and it enables flavour-changing decays, and gives a natural source of the combined charge-partity (CP) violation.

As the SM is a QFT, each particle can be interpreted as an excitation of a corresponding field permeating the space-time. It combines the symmetry group for strong interactions (in other words, quantum chromodynamics (QCD)) $SU(3)_C$, where the subscript denotes the colour charge, with the EW interaction symmetry group term $SU(2)_L \times U(1)_Y$, where the subscript L denotes the left-handedness and Y the weak hypercharge. The weak hypercharge is denoted as $Y = 2(Q - I_3)$ with Q being the electric charge, and I_3 the third component of isospin. Combined, these form the gauge group upon which the SM is based, shown in Eq. (2.1). Everything from the particle content to their charges and interactions is determined by symmetry groups.

$$SU(3)_C \times SU(2)_L \times U(1)_Y \tag{2.1}$$

To reiterate, the $SU(3)_C$ gauge bosons, the force carriers, are eight gluons, and $\gamma, W^{\pm}, Z$ are four gauge bosons for $SU(2)_L \times U(1)_Y$. The number of force carriers corresponds to the number of generators in the symmetry group. To make the SM mathematically consistent, renormalisation needs to be introduced. Renormalisation removes the infinities that arise in loop diagram calculations in QFT by absorbing them into redefinitions of masses, couplings and fields. Thus, only finite observable quantities are left. As only gauge-invariant operators with dimension less than four are renormalisable, it fixes the structure of the SM Lagrangian. The SM Lagrangian can be written as Eq. (2.2):

$$\mathcal{L}_{SM} = -\frac{1}{4}F_{\mu\nu}F^{\mu\nu} + i\bar{\psi}\gamma^{\mu}D_{\mu}\psi + y_{ij}\bar{\psi}_i\psi_j + h.c., \tag{2.2}$$

where $F_{\mu\nu}F^{\mu\nu}$ is the kinetic energy of the vector bosons and $F_{\mu\nu}$ is the field strength tensor for the gauge field; $i\bar{\psi}\gamma_{\mu}D^{\mu}\psi$ fermion coupling to the corresponding gauge bosons as ψ are the fermion fields and γ_{μ} Dirac's matrices and D^{μ} gauge covariant derivative; $y_{ij}\bar{\psi}_i\psi_j + h.c.$ Yukawa couplings with "h.c." as the Hermitian Conjugate.

There are no explicit mass terms for bosons in the SM Lagrangian, as they would break the gauge invariance. Thus, fundamentally everything should be massless, however, we know that matter has mass. To solve this, the BEH mechanism is proposed to break the $SU(2)_L \times U(1)_Y$ symmetry, allowing weak gauge bosons to gain mass.

2.2. The Electroweak Symmetry Breaking and the BEH Mechanism

Within the EW symmetry, there are four massless gauge fields – W_μ^1, W_μ^2, W_μ^3, for the $SU(2)_L$ and B_μ for the $U(1)_Y$ part – and two coupling constants – g for the $SU(2)_L$ and g' for the $U(1)_Y$ part. An external mechanism is needed to break this symmetry. The BEH mechanism was proposed in 1964 independently by Robert Brout and François Englert [5], Peter Higgs [6] and Gerald S. Guralnik, Carl R. Hagen and Thomas W. B. Kibble [12], as well as Alexander Migdal and Alexander Polyakov [13]. These groups proposed a complex spin-0 scalar quantum field, the Higgs field, (see Eq. (2.3)) that acquires a non-zero vacuum expectation value after spontaneous symmetry breaking. This mechanism enables the spontaneous breaking of electroweak symmetry, separating the electromagnetic and weak interactions and giving mass to the weak gauge bosons.

$$\phi = \begin{pmatrix} \phi^+ \\ \phi^0 \end{pmatrix} = \frac{1}{\sqrt{2}} \begin{pmatrix} \phi^1 + i\phi^2 \\ \phi^3 + i\phi^4 \end{pmatrix} \tag{2.3}$$

Higgs field's Lagrangian can be written as Eq. (2.4). It has a kinematic and potential term. The kinematic term has a covariant derivative $D_\mu = \partial_\mu + igT \cdot W_\mu^a + \frac{ig'}{2} Y B_\mu$ where T are Pauli matrices, and a spans from 1 to 3. In turn, the Higgs potential, $V(\phi)$, is given as Eq. (2.5), where both μ_c and λ_c are constants.

$$\mathcal{L}_H = |D_\mu \phi|^2 - V(\phi) \tag{2.4}$$

$$V(\phi) = -\mu_c^2 \phi^2 + \lambda_c \phi^4 = -\mu_c^2 (\phi^\dagger \phi) + \lambda_c (\phi^\dagger \phi)^2 \tag{2.5}$$

The ground state had been arbitrarily chosen, e.g. $\phi^1 = \phi^2 = \phi^4 = 0$ and $\phi_3 = v$, with v as another constant – the vacuum expectation value. Thus, the choice breaks the symmetry spontaneously. If the quadratic term was positive, the potential would have a minimum at zero, but in the case of a negative term, it would be a maximum, thus forcing the field to a new minimum, given as Eq. (2.6).

$$\phi^\dagger \phi = \frac{-\mu^2}{2\lambda_c} = \frac{v^2}{2} \tag{2.6}$$

Perturbing the potential around the minimum would yield Eq. (2.7). Visually an example is given in Fig. 2.2, where we can see the non-zero minimum and the arbitrary choice of direction for the claimed minimum. At this stage of the symmetry breaking, the Goldstone theorem [15] has to be respected. It states that upon a spontaneous breaking of a global symmetry, one massless scalar particle must exist for each broken generator of symmetry. Thus, in the case of EWSB three of the four initial generators need to be broken. The unbroken one is the one that becomes the gauge boson of the electromagnetic

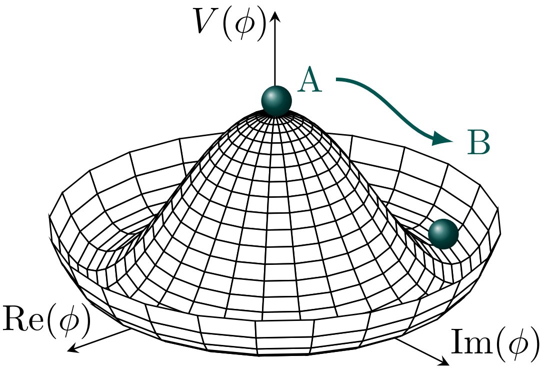

Figure 2.2. An illustration of the spontaneous symmetry breaking via the BEH mechanism, displaying the Higgs potential and how a stable minimum, B, is reached from an unstable maximum, A, adapted from [14].

interaction, while the three broken ones come from the Higgs doublet. If originally the Higgs doublet had four real components, after the symmetry breaking, only one remains as a physical scalar particle, while the other three, through the BEH mechanism, become components of the W^+, W^- and Z bosons.

$$\phi(x) = \frac{1}{\sqrt{2}} \begin{pmatrix} 0 \\ v + H(x) \end{pmatrix} \tag{2.7}$$

When expanding the Higgs Lagrangian around the chosen point and collecting the quadratic terms in the gauge boson fields, mass terms for gauge bosons can be identified. This leads to $m_H = \sqrt{2\mu_c^2} = \sqrt{2\lambda_c v^2}$, $m_W = \frac{gv}{2}$ and $m_Z = \frac{\sqrt{g'^2 + g^2 v}}{2}$, and similar terms for the interactions of W and Z bosons to the Higgs have entered the Lagrangian. In the case of fermions, their masses are acquired by their interaction with the Higgs field via the Yukawa coupling, leading to $m_f = \frac{h_f v}{\sqrt{2}}$ where h_f is the Higgs-fermion interaction. It is noteworthy that Higgs boson couplings to bosons are proportional to the square of the boson mass while in the case of fermions the couplings are linearly proportional to fermion masses. This leads to stronger interactions both in Higgs boson production and its decay to bosons and third-generation fermions. More on this in Section 2.3.

Fig. 2.3 shows the measured Higgs boson couplings to other particles, indicating its remarkable agreement with the SM prediction. These measurements are performed by the ATLAS and CMS collaborations. The couplings are measured by evaluating the cross section for various Higgs boson production and decay modes. In Fig. 2.3a the (square root of) coupling modifier is shown as a function of (vector boson) fermion mass, while the Fig. 2.3b shows the comparison between the coupling chosen by Nature, g_i, versus the one predicted by the SM, g_i^{SM}. This is done using the Kappa framework [18] with

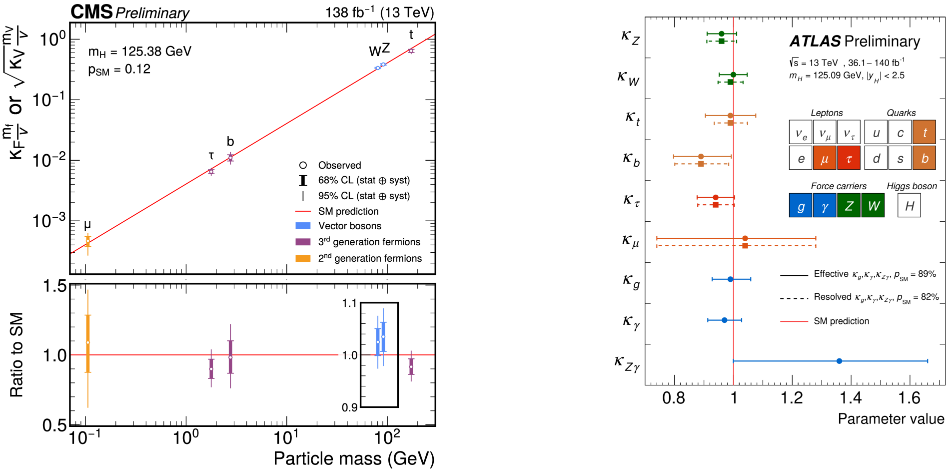

(a) As a function of fermion or boson mass

(b) Parameter value from the fit

Figure 2.3. The measured coupling modifiers of the Higgs boson to fermions and gauge bosons [16], [17].

coupling modifiers defined as ratio $\kappa_i = \dfrac{g_i}{g_i^{SM}}$.

$$
\begin{aligned}
V(H) =& -\mu_c^2\frac{1}{2}(v+H)^2 + \lambda\left(\frac{1}{2}(v+H)^2\right)^2 \\
=& -\frac{\mu_c^2}{2}(v^2+2vH+H^2) + \frac{\lambda}{4}\left(v^4+4v^3H+6v^2H^2+4vH^3+H^4\right) \\
=& ... + (\lambda v)\,H^3 + \left(\frac{\lambda}{4}\right)H^4 \\
=& ... + \lambda_{HHH}H^3 + \lambda_{HHHH}H^4
\end{aligned}
\tag{2.8}
$$

The Higgs potential can be written explicitly noting the Higgs cubic and quadratic couplings. This is done by perturbing the the potential about the minimum and arriving to Eq. (2.8), where λ_{HHH} is the tri-linear and λ_{HHHH} quadri-linear coupling constants of Higgs boson self-coupling, and their dependancy is shown in Eq. (2.9).

$$
\lambda_c = \frac{m_H^2}{2v^2} = \frac{\lambda_{HHH}}{v} = 4\lambda_{HHHH} \tag{2.9}
$$

To understand more of Higgs potential we must study interactions that involve vertices with three or four Higgs bosons, e.g. Higgs pair or Higgs triplet production. In this work, the trilinear Higgs self-coupling gets the centre attention, thus, the term "Higgs self-coupling" refers specifically to it, unless stated otherwise. For simplicity, from here onwards $\lambda = \lambda_{HHH}$. The SM predicts the Higgs self-coupling to hold the value given in Eq. (2.10). The Kappa framework is again widely used for comparing the ratio $\kappa_\lambda = \dfrac{\lambda}{\lambda_{SM}}$

of the Higgs self-coupling chosen by Nature and the value predicted by the SM. Any deviation from unity could indicate some BSM influence.

$$\lambda_{SM} = \frac{m_H^2}{2v^2} = 0.129 \tag{2.10}$$

Therefore measurements of the HH production cross section can be used to set constrains on κ_λ. However, these measurements prove to be challenging due to the rarity of HH events. Still, by gathering more and more data and by improving analysis techniques, including more final states, the sensitivity has increased drastically, moving us from setting limits on the HH production slowly towards the regime of discovering it. More on this is expanded in Section 2.5 and Section 2.6.

2.3. The Higgs Boson

The Higgs boson is a direct consequence of the BEH mechanism. It is the physical, scalar particle associated to the Higgs field. Ever since its discovery, the Higgs boson has been put to several tests and measurements. Slightly more than ten years later, we have produced a number of measurements of its mass and width, production cross sections, decay branching ratio (BR), spin-parity and various couplings, including its self-coupling.

There have been several Higgs boson mass measurements done by the CMS collaboration, as well as the ATLAS collaboration, testing several decay channels, both individually and as combinations. In [19], the mass of $m_H = 125.38 \pm 0.14$ GeV is quoted, with precision around 0.2 %. Regarding the Higgs boson's quantum numbers, by performing an angular study, it has been shown that the spin, J, and parity, P, agrees with the SM hypothesis: $J_P = 0^+$ [20].

At a high energy hadron collider, such as the LHC, Higgs bosons can be produced through several different production mechanisms. The dominant production mode is the gluon-gluon fusion (ggF), followed by the vector boson fusion (VBF), the Higgs-strahlung (VH) and the Higgs boson associated production with a tt pair (ttH). Figure 2.4 shows some of the leading order (LO) processes for the Higgs boson production that all have been studied by the CMS collaboration, they are represented in a diagrammatical formulation with Feynman diagrams [21]. In these diagrams, fields are represented by lines, and places where they meet, vertices, represent the interaction terms in the Lagrangian. Solid lines represent fermions, spring-like lines depict gluons. Wavy lines are vector bosons and dashed lines are scalar bosons. They are usually read from left to right, where the left side represents the initial state and the right side represents the final state.

The figure also shows various Higgs boson interactions, labelled with the coupling modifiers κ. As can be seen, the LO single-Higgs boson production is not sensitive to the Higgs boson self-coupling, however, if we take into account the next-to-leading order

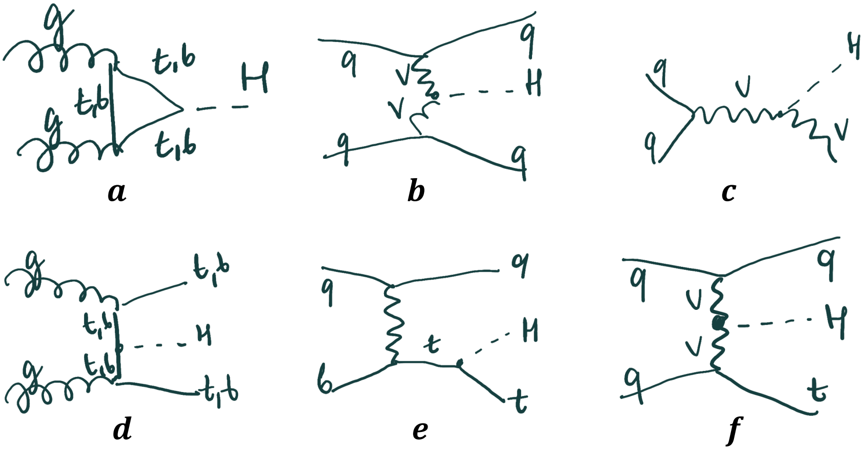

Figure 2.4. Feynman diagrams of the leading order Higgs boson production in ggF (a) and VBF (b), associated production with a W or Z (V) boson (VH) (c), associated production with a top or bottom quark pair (ttH or bbH) (d) and associated production with a single top quark (tH) (e,f).

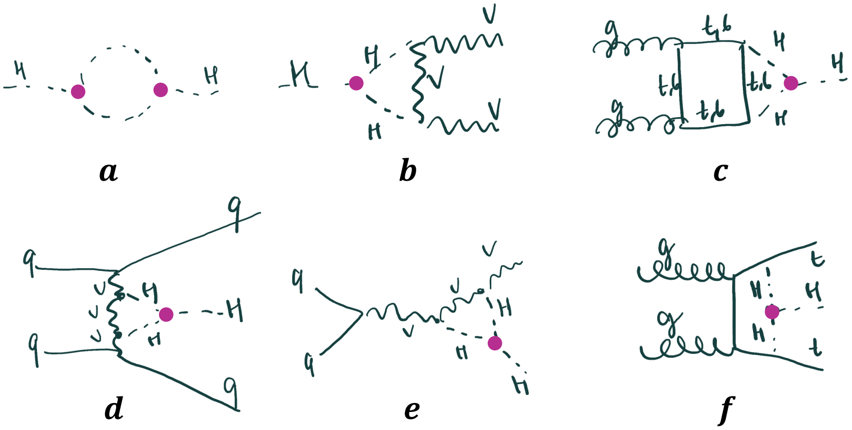

Figure 2.5. Feynman diagrams of the next-to-leading order diagrams sensitive to Higgs self-coupling, (a) Higgs boson self-energy or boson propagator, (b) decay width to bosons, single-H boson production in (c) ggF, (d) VBF, (e) VH and (f) ttH. For convenience Higgs self-coupling λ marked with a pink dot.

(NLO) order EW corrections, several processes sensitive to κ_λ appear. This is summarised in Fig. 2.5. Here, the most sensitive would be the VH and ttH production modes; however, their rates are relatively low compared to the sensitivity from the HH studies. At the same time, when combining single-Higgs and HH measurements, it is possible to create more general statements about κ_λ and other Higgs boson couplings, as they can be measured simultaneously [22].

The Higgs boson is unstable and it rapidly decays into a pair of bosons or a pair of fermions. It can decay to particles lighter than itself, so practically all decays to the SM particles are allowed, with an exception of the decay to top quarks. The Higgs boson can decay to massless particles via virtual loops. Higgs boson's lifetime is expected to be $\tau_H \approx 1.6 \cdot 10^{-22}\ s$ and its natural width is $\Gamma = 4.14 \pm 0.02$ MeV [10].

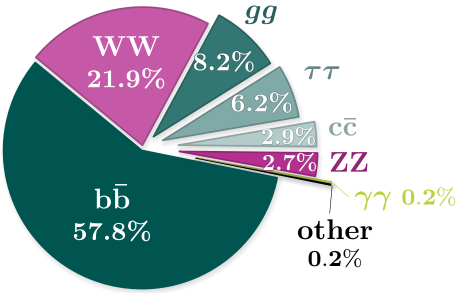

Figure 2.6. Higgs boson decay channels, adapted from [23], values calculated for $m_H = 125.3$ GeV [24].

As mentioned before, the Higgs boson couples to vector bosons with an amplitude proportional to the square of boson's mass, and to fermions with an amplitude proportional to fermion's mass. Therefore, the coupling is stronger to heavier particles, such as the third generation of quarks and fermions. Figure 2.6 shows Higgs boson BR for a Higgs boson with mass 125.3 GeV. A BR is calculated as the ratio of the partial width over the total width, characterising the probability for a certain decay to occur. Clearly, the most dominant is the Higgs decay into a pair of b quarks. As a more detailed example, the second most probabilistic decay is into a pair of W bosons. The ratio is given as

$$\mathcal{BR}(H \to W^+W^-) = (2.186 \cdot 10^{-1})^{+0.98\ \%}_{-0.98\ \%}(\text{theory})^{+0.99\ \%}_{-0.96\ \%}(m_q\ \text{unc.})^{+0.64\ \%}_{-0.61\ \%}(\alpha_s\ \text{unc.})$$

and for a rarer decay into a pair of Z bosons:

$$\mathcal{BR}(H \to ZZ) = (2.692 \cdot 10^{-2})^{+0.98\ \%}_{-0.98\ \%}(\text{theory})^{+0.99\ \%}_{-0.96\ \%}(m_q\ \text{unc.})^{+0.63\ \%}_{-0.62\ \%}(\alpha_s\ \text{unc.})$$

There are many other decay channels, and even though their BR is smaller, they could provide very clean signatures, for example the $H \to \gamma\gamma$ decay channel. The uncertainties listed for these calculations are from missing higher-order corrections (marked as "theory"), quark masses, m_q, and the strong coupling constant, α_s. More on this is expended in Ref. [24].

2.4. Beyond the Standard Model

Although the SM is an internally consistent theory it does not describe all of the Nature and several questions remain. Both broad and almost philosophical questions of matter and antimatter asymmetry, the nature of dark matter and dark energy, as well as more specific aspects, such as the lack of explanation for neutrino masses. As an example, matter and antimatter is expected to be produced and annihilated in pairs; however, our Universe is primarily composed of matter. There is no mechanism within the SM that could account for such a imbalance, while several BSM models enchance CP violation to a degree that allows for a matter dominated Universe.

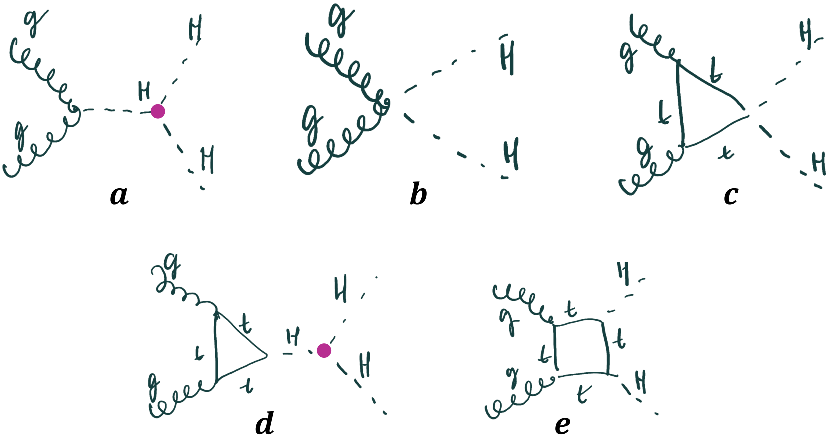

Figure 2.7. Feynman diagrams of the HEFT coefficients (a) c_g coupling between a pair of gluons and a Higgs boson, (b) c_{2g} coupling between a pair of gluons and a HH, (c) c_2 coupling between a HH and a top quark pair, (d) Higgs boson self-coupling that can potentially be modified, (e) top Yukawa coupling that could be modified. For convenience Higgs self-coupling, λ, marked with a pink dot.

A multitude of SM extensions provide additional fields and particles. To test for new physics in the Higgs sector, various SM extension models can be probed using a Higgs Effective Field Theory (HEFT) approach which considers only the effective couplings between particles. It builds on the effective field theory (EFT), which is a framework for describing physical phenomena at a given energy scale without requiring detailed knowledge of the underlying high-energy theories. It uses systematic expansion of the energy of the process and the scale of the new physics, and by integrating out the heavy degrees of freedom obtains an effective Lagrangian that involves only the light fields.

HEFT is a powerful tool as it is designed to consider only those interactions and effects relevant in a specified scale. HEFT uses a set of five couplings, two already present in the SM – the Higgs self-coupling and the Higgs coupling to the top quark. Additionally, three anomalous couplings are used: c_2 which describes the Higgs boson interaction with top pairs, c_g which describes Higgs interaction with gluons, and c_{2g} which describes two Higgs contact interaction with gluons. For completeness, the corresponding Feynman diagrams are shown in Fig. 2.7.

2.5. Higgs Pair Production Mechanisms

Similarly as in the single-Higgs case, HHs can be produced through several different production mechanisms. HH production Feynman diagrams for processes probed at the LHC are shown in Fig. 2.8. The dominant production mode is through ggF and it has two contributing processes. In both processes two gluons fuse, this mostly happens through a virtual top quark loop, more rarely through any other virtual quark loop. In one of the subprocesses, two Higgs bosons are produced from the loop ("box" diagram, see Fig. 2.8 b), while in the other, one a virtual Higgs boson is produced and then it quickly decays to two Higgs bosons ("triangle" diagram, see Fig. 2.8 a).

Both diagrams interact destructively, leading to a small cross section. Moreover, it can be seen from the diagrams that only the "triangle" is sensitive to Higgs self-coupling, λ, while the other provides a handle to measure the Higgs boson interaction to top (or bottom) quark, k_t or k_b. This has to be taken into account when studying Higgs self-coupling. In addition, kinematic differences are expected between these two contributions. The invariant mass distribution of HHs is shown in Fig. 2.9 for each of the contributions and their combination, indicating the differences. The "triangle" contribution behaves like an off-shell resonant process and is dominant at low m_{HH} up to $2m_H$, and produces Higgs bosons nearly back-to-back with small transverse momentum, p_T, thus creating a relatively soft spectrum. The "box" contribution acts more like a continuum process and is dominant at high m_{HH}, and produces Higgs bosons with larger recoil and smaller opening angle. Overall, when talking about the HH production within the SM context, it is referred to as "non-resonant", as the HH is produced directly, without an intermediate particle going on-shell.

The second most dominant HH production mechanism is VBF which has three underlying subprocesses. In all of them, a quark of each incoming proton radiates a virtual vector boson ($W^{\pm}$ or Z), which then fuse (see Fig. 2.8 c, d) or exchange another virtual

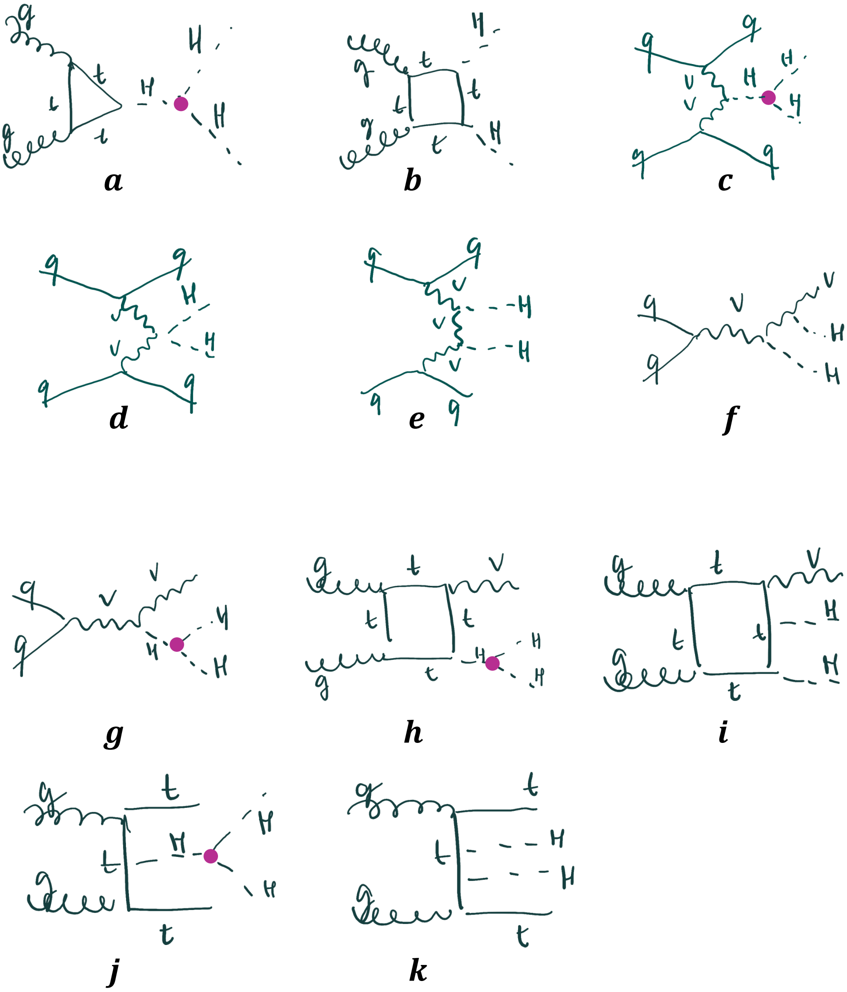

Figure 2.8. Feynman diagrams of some of the major HH production modes: (a) ggF via the triangle loop, (b) ggF via the box loop, (c) VBF sensitive to the Higgs self-coupling λ, (d) VBF with the HHVV vertex, (e) VBF with the VVH vertex, (f) VHH, (g) VHH, sensitive to λ, (h) VHH, with a box diagram, sensitive to λ, (i) VHH, with a box diagram, (j) ttHH, sensitive to λ, (k) ttHH, for convenience Higgs self-coupling, λ, is marked with a pink dot.

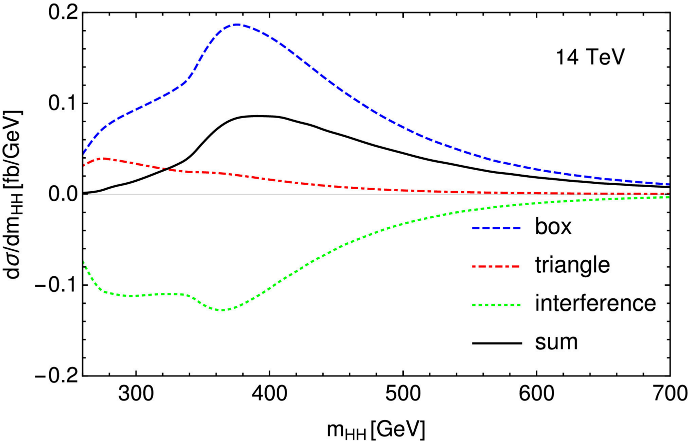

Figure 2.9. HH invariant mass distribution at LO for the different contributions to the ggF mechanism and their interference, example at 14 TeV [25].

vector boson (see Fig. 2.8 e). In one of the subprocesses (c), one virtual Higgs boson is produced that later decays to two Higgs bosons, this production mode is sensitive to Higgs self-coupling. Another subprocess (d) produces two Higgs bosons via a four point interaction, this production mode is sensitive to the measurement of Higgs boson coupling to two vector bosons k_{2V}. In the third subprocess (e), a virtual vector boson is exchanged between the creation of Higgs bosons, making it sensitive to the Higgs boson and vector boson coupling modifier measurement k_V.

Other sub-dominant HH production processes are HH associated production with a *tt* pair (ttHH), HH-strahlung (VHH) and HH associated production with a top quark (tHH). Although the cross section for these production modes is very small, they provide interesting handles for BSM searches. Also, for these production processes there are several subprocesses, their Feynman diagrams can be seen in Fig. 2.8 f-k.

LO calculations for ggF HH production channel have been performed as early as in the 1980s, the NLO and next-to-next-to-leading order (NNLO) calculations joined in 2010s, but the next-to-next-to-next-to-leading order (N^3LO) calculations have arrived only in 2020s providing various improvements both in the calculations and the reduction of the calculation uncertainties. The uncertainties on the ggF cross section calculation come from multiple sources – parton distribution function (PDF), the running of the strong coupling constant, α_s, the dependence on top quark mass, m_t, whilst various QCD corrections are accounted by the scale uncertainty.

Fig. 2.10 shows the total cross sections at the NLO level in QCD for the HH production in *pp* colliders, in Fig. 2.10a as a function of the centre-of-mass energy and in Fig. 2.10b as a function of k_λ, the ratio of the Higgs boson self-coupling coupling versus the self-coupling coupling predicted by the SM. The thickness of the lines corresponds to the scale and PDF uncertainties. For all production modes, the HH production cross section increases with

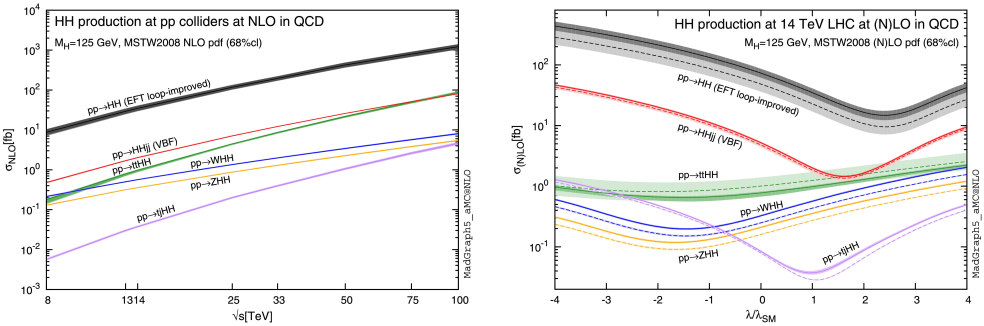

(a) As a function of centre-of-mass energy

(b) As a function of the self-coupling coupling λ, normalised with the SM value

Figure 2.10. Total cross sections at the NLO in QCD for the six largest HH production channels at proton-proton colliders [26].

the centre-of-mass energy, as well as when k_λ deviates far from the SM value. However, it is worth noting that around $\kappa_\lambda \approx 2.3$, due to the strongest interference between the "box" and the "tringle" contributions, the HH cross section is the lowest. Beyond this minimum, the κ_λ rises approximately quadratically with its modulus. This deviation can be a strong handle when looking for BSM which would alter the HH production rate. Not shown in the figures, but the HH production cross section is dependant from the Higgs boson mass. As an example, at $\sqrt{s} = 13$ TeV with $m_H = 125.09$ GeV the $\sigma_{HH} \approx 30.74$ fb while for $m_H = 125.38$ GeV the $\sigma_{HH} \approx 30.83$ fb which is less than a 0.3 % change in the cross section for a 0.2 % change in the Higgs boson mass.

From the figures, it is clearly visible that the ggF via a top loop is the dominant production mechanism for the HH production with the sub-leading production modes being with cross sections of one order of magnitude smaller. At the same time, ggF HH production cross section is three orders of magnitude smaller than the single-Higgs boson production cross section in ggF H production. The calculated cross sections of the HH production are summarised in Table 2.1. These calculations are made for the Higgs boson mass of $m_H = 125$ GeV, at the NNLO accuracy in the finite top quark mass approximation and the central scale, μ_0. The central scale is equal to the renormalisation scale, μ_R, and the factorisation scale, μ_F, as $\mu_0 = \mu_R = \mu_F = M_{HH}/2$. The scale uncertainty is obtained by probing six relative variations of μ_R and μ_F and the PDF uncertainty is estimated with the Born-improved approximation on `PDF4LHC21_40` set [25].

At the same time, single-Higgs boson production at $\sqrt{s} = 13$ TeV is estimated as

$$\sigma_H^{ggF} = 44.14^{+7.6\ \%}_{-8.1\ \%}(\text{scale}) \pm 3.1\ \%(\alpha_s\text{+PDF})\ \text{pb},$$

where these calculations were performed with the `dFG` program at NNLO+NNLL (next-to-next-to-leading logarithmic) QCD and NLO EW accuracies and the PDF uncertainty evaluated on `PDF4LHC15_nnlo_30` set [24]. Thus, $\sigma_H/\sigma_{HH} \approx 1500$! To give a rough

Table 2.1

Cross sections of HH for ggF and VBF production modes, at two centre-of-mass energies at pp collisions

Production mode	$\sqrt{s}$, GeV	σ_{HH}, fb	α_s+PDF uncertainty	m_t+scale uncertainty
ggF	13	30.77	± 2.3 %	-23 %+6 %
ggF	13.6	34.13	± 2.3 %	-23 %+6 %
VBF	13	1.687	±2.7 %	-0.04 %+0.05 %
VBF	13.6	1.874	± 2.7 %	-0.03 %+0.05 %

estimate, there is about one Higgs boson event every 1 to 1.5 billion pp collisions at the LHC, thus one HH is produced around once every trillion collisions.

2.6. HH Decay Channels and Current Experimental Searches

There are many possible final states for Higgs boson decays, with HH decays doubling that number. The BRs for some of the most common decays are shown in Fig. 2.11. By nature, there is no one "golden channel" with a large BR and high signal to background ratio, like it is the case with the four-lepton decay channel of the single-Higgs boson production. Each search channel deals with a trade-off of choosing between a large number of signal events and the purity of the final state. Often in the case of a high BR, we have to deal with complex backgrounds, while in the cases of clear and easily recognisable signature, we usually suffer from a very low BR.

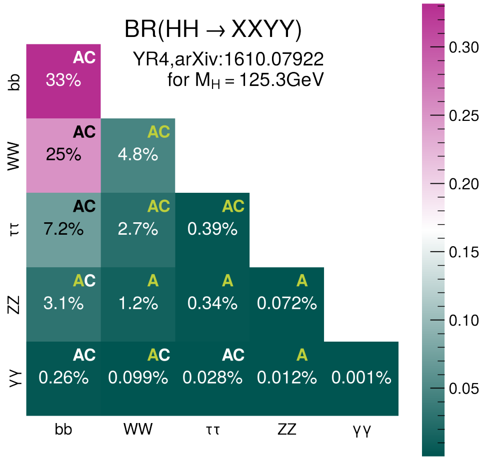

Figure 2.11. BRs for the most popular HH search channels. The columns indicate the final state of one of the Higgs bosons and the rows indicate the final state of the other. Channels marked with "A" correspond those analysed by the ATLAS collaboration, while "C" marks the ones analysed by the CMS collaboration. Green letter indicates inclusion in multilepton analysis.

Each channel has its benefits and drawbacks. For example, in the case of (at least) one of the Higgs bosons decaying to a pair of b quarks, we are significantly increasing the channel's BR; however, as this is a fully hadronic final state we have to deal with large background rates, predominantly coming from $t\bar{t}$ and QCD multi-jet production. Also, we need to effectively identify jets originating from b quarks, and which b quarks have originated from a Higgs boson.

On the other hand, channels with one of the Higgs bosons decaying to a pair of photons suffer from a low BR, while having the advantage of a very clean photon pair signature. Other great handles are channels with (at least) one of the Higgs bosons decaying to a pair of taus. This allows for an intermediate BR and various techniques in detecting them in the detector. Taus can provide a good handle for the QCD multi-jet background rejection, while introducing Drell-Yan (DY) as background in leptonically decaying τ cases. Overall, all channels with leptons, such as muons and electrons, in the final decay products can be used as a good handle against the QCD multi-jet background. Such cases can come from channels with (at least) one Higgs boson decaying to a pair of vector bosons, which in turn can decay leptonically, semi leptonically or hadronically. Often here we have to deal with a rich decay menu consisting of jets, charged leptons, and neutrinos.

The study of the HH production is very challenging due to the small production cross section and the abundance of decay modes. Overall, the low production cross section demands a high selection efficiency in each of the search channels and finally a combination of all studied channels. As more and more data are collected, the end goal would be to explore the HH production in each decay channel (including, but not limited to the scope of Fig. 2.11) to achieve the highest possible sensitivity. While the sensitivity for the measurement is still too low, each analysis can set an upper limit on the HH production cross section, or more often the signal strength, μ or μ_{HH}, defined as Eq. (2.11), where σ is the measured HH production cross section and $\sigma_{\text{SM (theory)}}$ is the cross section value predicted by the SM (theory). In addition, several searches can provide restrictions on various Higgs couplings, e.g., k_λ or k_{2V}, or new physics scenarios.

$$\mu = \mu_{HH} = \frac{\sigma}{\sigma_{\text{SM}}} = \frac{\sigma}{\sigma_{\text{theory}}} \tag{2.11}$$

Historically, three channels have dominated the HH sensitivity in searches conducted by both ATLAS and CMS collaborations: $HH \to b\bar{b}b\bar{b}$, $HH \to b\bar{b}\tau^+\tau^-$ and $HH \to b\bar{b}\gamma\gamma$. Regarding the latest results from the CMS and ATLAS collaborations, using datasets of 120 fb^{-1} to 140 fb^{-1} at centre-of-mass energy, $\sqrt{s}$, 13 TeV, all analyses have supported the background-only model and have used the CL method [27] to derive upper limits on the HH production cross section. The CMS collaboration has put a 95 % CL observed (expected) upper limit of 3.9 (7.8) times the SM predicted cross section for HH production when investigating the $b\bar{b}b\bar{b}$ channel [28], a 3.3 (5.2) upper limit when investigating $b\bar{b}\tau^+\tau^-$ channel [29] and a 7.7 (5.2) upper limit when investigating $b\bar{b}\gamma\gamma$ [30]. While the ATLAS collaboration has put a 95 % CL observed (expected) upper limit of 5.4 (8.1) times the SM predicted cross section for HH production when investigating the $b\bar{b}b\bar{b}$ channel [31], a 5.9 (3.3) upper limit when investigating $b\bar{b}\tau^+\tau^-$ channel [32] and a 4.0 (5.0) upper limit when investigating $b\bar{b}\gamma\gamma$ [33].

Some HH analysis gain the sensitivity by merging several HH decay modes. Here, the best example is the HH multilepton analysis where the events are selected and categorised based on the final states, more precisely the multiplicity of leptons and hadronically decaying tau leptons. Such an analysis has been performed by both collaborations. The analysis performed by the CMS collaboration explicitly targets only three decay channels: WW^*WW^*, $WW^*\tau^+\tau^-$ and $\tau^+\tau^-\tau^+\tau^-$ [34]. Later, categorising them into seven search categories where lepton multiplicity ranges from zero (targeting four τ_h) to four (targeting no τ_h). In the four-lepton category no requirement on the number of jets is posed, while the four lepton invariant mass must be above 140 GeV so to not overlap an existing $HH \to b\bar{b}ZZ^*$ search. Overall, this analysis has put a 95 % CL observed (expected) upper limit of 21 (19) times the SM predicted cross section on the HH production.

The analysis performed by the ATLAS collaboration includes events from more decay modes, including $b\bar{b}ZZ^*$, VV^*VV^* (with $V = W$ or Z), $VV^*\tau^+\tau^-$, $\tau^+\tau^-\tau^+\tau^-$, $\gamma\gamma VV^*$ and $\gamma\gamma\tau^+\tau^-$ [35]. These events are later categorised in one of nine search categories, where lepton multiplicity ranges from two to four and final states with hadronic τ decays are not covered as much as in the CMS analysis. In this search, the only category with four leptons explicitly targets decays where one Higgs boson decays via a b quark pair, and overall $b\bar{b}ZZ^*$ is preferred over, e.g. WW^*ZZ^*, as an inverted Z boson mass window is required for most search categories. Overall, this combination has put a 95 % CL observed (expected) upper limit of 17 (11) times the SM predicted cross section on the HH production. ATLAS's multilepton search puts a slightly tighter limit while combining more search categories, which CMS has covered in other analyses.

Recently, both the ATLAS and the CMS collaborations have independently published HH combination analysis [36], [37], that include analysis using LHC Run 2 dataset, thus has analysed around 140 fb^{-1} at $\sqrt{s} = 13$ TeV (more on the dataset is explained in Chapter 3). Moreover, a combination has been performed also using both collaboration data [38]. The combinations show the best sensitivity for HH production, as well as the most stringent interval for κ_λ and κ_{2V}. Additionally, combinations have explored their sensitivities for some BSM processes, by exploring several HEFT interpretations. When combining, any possible overlap between analysis channels is carefully removed, and, where applicable, measurement uncertainties are correlated and unified.

The combination performed by the ATLAS collaboration [36] includes $b\bar{b}b\bar{b}$, $b\bar{b}\tau^+\tau^-$, $b\bar{b}\gamma\gamma$, $b\bar{b}ll$ and multilepton (mentioned above) decay channels. The total combination covers more than a half of the HH decay channels, and explores both ggF and VBF production modes. Again, the CL method is used and the signal strength is defined as the ratio of the measured inclusive (ggF and VBF) production cross section to the SM

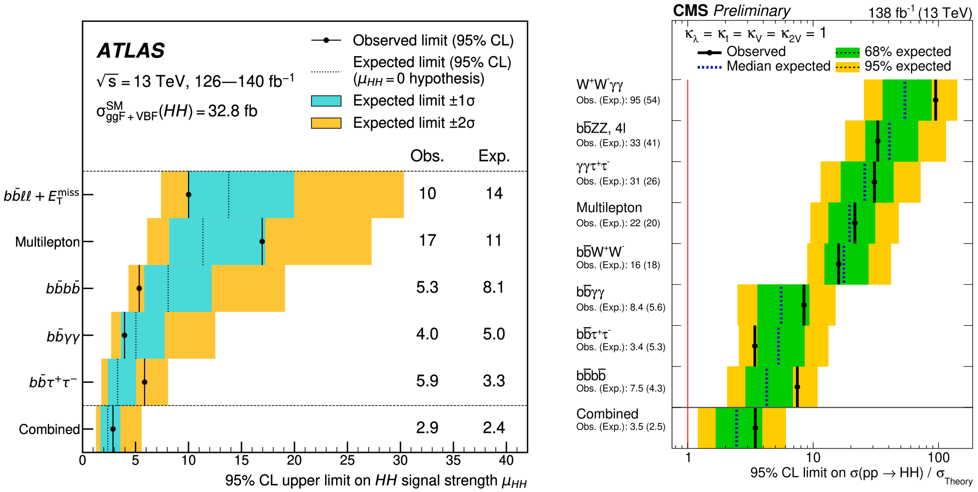

(a) By the ATLAS Collaboration [36]

(b) By the CMS Collaboration [37]

Figure 2.12. Observed and expected 95 % CL upper limits on the signal strength for inclusive HH production.

prediction. An observed 95 % CL upper limit of 2.9 is placed on the HH production signal strength, while 2.4 is expected. Observed and expected upper limits per analysis channel and in combination are shown in Fig. 2.12a.

The ATLAS HH combination explores also κ_λ in both ggF and VBF HH production processes. Assuming other Higgs boson couplings as predicted by the SM, a fit to data yields observed (expected) 95 % CL interval $-1.2 < \kappa_\lambda < 7.2$ ($-1.6 < \kappa_\lambda < 7.2$) which is compatible with the SM prediction of $\kappa_\lambda = 1.0$. $b\bar{b}\gamma\gamma$ channel is the most sensitive to κ_λ. Similarly, κ_{2V} is explored setting an observed (expected) 95 % CL interval of $0.6 < \kappa_{2V} < 1.5$ ($0.4 < \kappa_{2V} < 1.6$), compatible with the SM prediction. Here, the most sensitive is the $b\bar{b}b\bar{b}$ analysis. Additionally, several HEFT interpretations are given, constraining the effective ggHH interactions (c_{2g} coupling modifier).

The HH production combination done by the CMS collaboration [37] covers the same channels but targeted via different analyses: it combines $b\bar{b}\gamma\gamma$, $b\bar{b}\tau^+\tau^-$, $b\bar{b}b\bar{b}$, $b\bar{b}WW^*$, $WW\gamma\gamma$, $\tau^+\tau^-\gamma\gamma$ and multilepton (mentioned above) analysis. Most analysis target both ggF and VBF production mode and in the case of $b\bar{b}b\bar{b}$ analysis also VHH production mode is researched. Upper observed limit of 95 % CL is set on the inclusive HH production cross section as 3.5 times the SM while the expected limit is 2.5. The limit on the inclusive HH cross section per channel and their contribution can be seen in Fig. 2.12b.

The CMS HH combination explores also the upper limit on the HH cross section as a function of κ_λ and κ_{2V}, by doing this the HH production can be excluded at 95 % CL for observed $-1.39 < \kappa_\lambda < 7.02$, while the expected interval is $-1.02 < \kappa_\lambda < 7.19$. Similarly, κ_{2V} coupling modifier is restricted to an observed range $0.62 < \kappa_{2V} < 1.42$

and the expected $0.69 < \kappa_{2V} < 1.35$. Intervals for both coupling modifiers are in line with the SM predictions and we can experimentally exclude $\kappa_{2V} = 0$. Similarly as in the ATLAS HH combination, $b\bar{b}\gamma\gamma$ is the most sensitive to κ_λ and $b\bar{b}b\bar{b}$ is the most sensitive to κ_{2V}. Using HEFT, several BSM interpretations are given by setting an upper limit on the HH cross section within various benchmarks, as well as several ultra violet (UV) complete models.

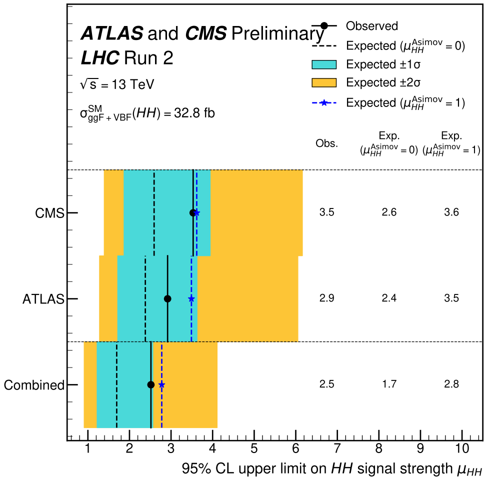

Figure 2.13. Expected and observed 95 % CL upper limits on the total HH signal strength, defined as the ratio of the measured cross section to the sum of the ggF and VBF HH SM production cross sections [38].

Moreover, both collaborations have combined their results, performing the most complete search of HH production [38]. It encapsulates all the searches previously mentioned, and, under the hypothesis of no HH production, sets an observed 95 % CL upper limit on the HH signal strength of 2.5, with an expected limit of 1.7, as shown in Fig. 2.13. The combined constraints on κ_λ and κ_{2V} are also set, reaching the observed $-0.71 < \kappa_\lambda < 6.1$ and $0.73 < \kappa_{2V} < 1.3$.

Regarding the very latest HH production results, both collaborations have published some preliminary results for data with $\sqrt{s} = 13.6$ TeV. Many more results are in the pipeline and will become public in very near future. From the CMS side, the $HH \to b\bar{b}b\bar{b}$ and $HH \to b\bar{b}\gamma\gamma$ have been explored with a dataset of around 60 fb^{-1} at $\sqrt{s} = 13.6$ TeV. The $b\bar{b}b\bar{b}$ analysis has set an observed (expected) upper limit at 95% CL of 4.4 (4.4) times the SM value [39], while the $b\bar{b}\gamma\gamma$ has set an observed (expected) upper limit at 95% CL of 7.4 (8.7) times the SM value [40]. From the ATLAS collaboration side, truly exciting results are presented for the $HH \to b\bar{b}\gamma\gamma$ analysis, as it combines over 300 fb^{-1} with both $\sqrt{s} = 13$ TeV and $\sqrt{s} = 13.6$ TeV. Among the increase in data, the analysis strategy has undergone several improvements, thus, this search has set an observed (expected) upper limit at 95% CL of 3.8 (3.8) times the SM value [41].

Motivated by the upper limits and the excluded ranges already set, both collaborations have explored options to improve steps in data-taking, tagging and processing. An example of improvement that the CMS collaboration has already implemented for Run 3 is a novel strategy for targeting $HH \to b\bar{b}b\bar{b}$ decay at the trigger level. This is done by exploiting the improved heavy flavour tagging and creating new trigger paths targeting energetic b-tagged jets. The trigger efficiency as a function of reconstructed HH mass is shown in Fig. 2.14a, a clear improvement can be seen. In 2023, these paths allowed to increase the trigger efficiency in the $HH \to b\bar{b}b\bar{b}$ analysis by 57 % with respect to Run 2 [42]. Similarly, new trigger paths were put in place for 2024 to target the $HH \to b\bar{b}WW^*$ decay channel as current triggers do not cover the phase-space well enough for low transverse momentum leptons [43]. In Fig. 2.14b, the trigger efficiency as a function of muon transverse momentum is shown, it can be seen that in the newly covered low transverse momentum region the efficiency is improved between 1.5 and 3 times. For more information on the CMS detector and future improvements, see Section 3.3 and its Subsection 3.3.9.

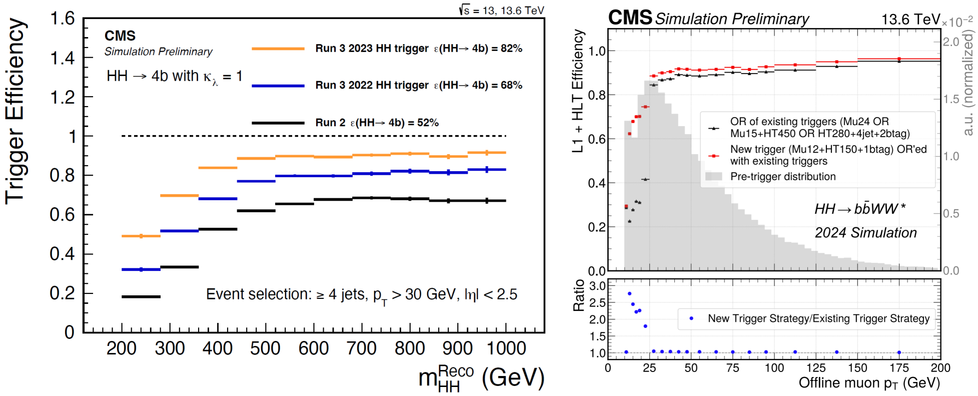

(a) Triggers targeting $HH \to b\bar{b}b\bar{b}$ [42]

(b) Triggers targeting $HH \to b\bar{b}WW^*$ [43]

Figure 2.14. Trigger improvements for Run 3 analysis performed by the CMS collaboration.

Moreover, both collaborations have done projections to different integrated luminosity values. The CMS collaboration has given projection predictions already within the HH combination, and again together with the ATLAS collaboration providing projections for the European Strategy for Particle Physics update (ESPPU) 2026 [44]. The projection follows the same recipe used in the previous projections, the signal and background yields are scaled up by a factor equal to the increase of the integrated luminosity. The level of systematic uncertainties are based on the best available knowledge and assumed reduced in most cases.

Several scenarios are evaluated: (S1) when the systematic uncertainties are assumed to be at the same level as of Run 2, (S2) when a reduction of systematic uncertainties are expected in most cases, and theoretical systematic uncertainties are halved, however, the identification and reconstruction efficiencies of b-tagged jets and hadronic taus remain as in the current analysis, (S3) which is an improvement of S2 as b-tagged jet and hadronic tau identification efficiency is improved by 5 %. No improvements on online or offline reconstruction of physics objects coming from the detector upgrades are assumed, however, these are expected. The results are scaled to 2 ab^{-1} and 3 ab^{-1}.

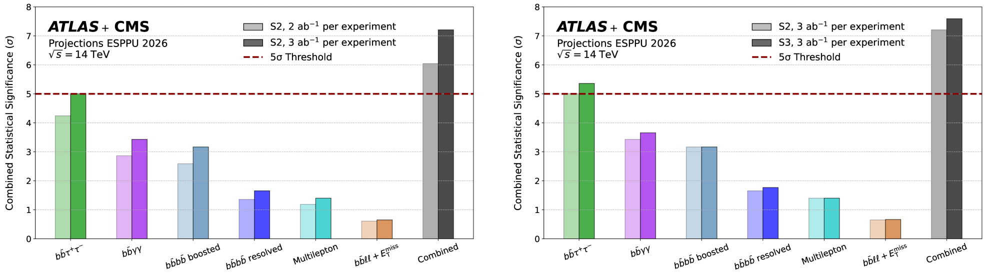

(a) Comparison for S2

(b) Comparison for 3 ab^{-1}

Figure 2.15. HH statistical significance per final state channel, combined between ATLAS and CMS collaborations, in a comparison between integrated luminosities for the S2 systematics scenario (left) and in a comparison between systematics scenarios at 3 ab^{-1} (right) [44].

In Fig. 2.15, a comparison for the HH statistical significance is shown. Here the results from both ATLAS and CMS collaborations are combined and shown for each channel and in combination. In Fig. 2.15a, a comparison between 2 ab^{-1} and 3 ab^{-1} integrated luminosity at S2 scenario is compared. It can be seen that under the conservative S2 only $b\bar{b}\tau^+\tau^-$ at 3 ab^{-1} could reach 5 σ (standard deviation) observation, which can be classified as discovery. However, a combination could provide discovery of HH already at 2 ab^{-1}. In Fig. 2.15b, a comparison between S2 and S3 at 3 ab^{-1} is shown. Here, the combination could exceed 7σ observation! Outside of the scope of the figures, it is worth noting that going from S2 to S3 brings around 5 % gain in precision while the increase in luminosity brings a gain of 20 % on the signal significance. Moreover, single-experiment observation is unlikely with 2 ab^{-1} while graspable with 3 ab^{-1}, especially if further analysis optimisation is done.

As previously shown, there is no golden channel for the analysis of HH production and to achieve good sensitivity, all possible final states need to be investigated and combined. Therefore, this Thesis and the accompanying CMS physics analysis summary presents a novel $HH \to WW^*ZZ^* \to 4l$ search, which will be combined to the initial analysis of the $HH \to WW^*ZZ^*$ leptonic and semileptonic decay search. Later, it could be integrated in the whole CMS HH multilepton analysis. More about the motivation and the design of the $HH \to WW^*ZZ^* \to 4l$ analysis can be found in Chapter 6. The decay channel of $HH \to WW^*ZZ^*$ is included in the ATLAS multilepton's analysis, however, not its final state of four leptons [35]. Regarding the CMS's multilepton search [34], it has a four-lepton search category, however, it is designed to target the $HH \rightarrow WW^{*}WW^{*}$ decay. Minor phase-space overlap is present and is dealt with in Chapter 6.

2.7. Summary

Within this chapter, the theoretical framework and motivation for the HH production studies were introduced. It reviewed the SM, highlighting the role of the BEH mechanism in the EWSB. It focused on understanding Higgs bosons, before introducing several BSM extensions to solve the unanswered questions. Finally, the HH production mechanism and decay channels was expanded on, illustrating motivation behind the current and future HH production studies. It laid the theoretical foundation of the $HH \rightarrow WW^{*}ZZ^{*} \rightarrow 4l$ decay channel explored in detail in this Thesis.

It showed how compelling the theoretical motivation for the HH production is. Yet, in several parts of the chapter, it was noted how challenging the experimental investigation is because of the small production cross section and complex possible final states. Addressing these challenges requires a specific experimental environment – a high-energy, high-luminosity collider and a multipurpose detector capable of precise particle reconstruction and identification. Luckily, such an environment exists, and the next chapter describes the unique setting in which this study is performed, introducing the European Organization for Nuclear Research (CERN) accelerator complex, the LHC, and the CMS detector.

3. EXPERIMENTAL ENVIRONMENT

Each physics theory must be complemented by experimental data that validate or reject it. Fundamental theories describing elementary particles and their interactions have extremely high requirements for the experimental environment to test them. Therefore, to push the boundaries and advance this field, scientists need to collaborate, working together for decades to construct the required experimental apparatus.

CERN (from the French *Conseil Européen pour la Recherche Nucléaire*) is a prime example of the necessary experimental environment, providing an accelerator complex, ground for experimental apparatus, and a fruitful community for growing science. CERN was founded in 1954 as a laboratory for peaceful scientific collaboration, providing an evolving accelerator complex and housing many experiments. It is located near Geneva, Switzerland, with experimental grounds extending on both sides of the French and Swiss boarder.

Beyond the CERN accelerator complex, there are several other experimental environments or hubs for high-energy physics. An example is Fermilab in the United States of America (USA), hosting the Tevatron [45], a proton-antiproton collider, which accelerated beams up to the centre-of-mass energy of nearly 1 TeV, and had two data-taking periods covering 1992-1996, and 2001-2011, respectively. Its two detectors Collider Detector at Fermilab (CDF) and DØ discovered the top quark [46], [47]. For heavy-ion physics, an important hub is Brookhaven National Laboratory (BNL) in the USA with its Relativistic Heavy Ion Collider (RHIC). RHIC could collide gold ions up to 100 GeV or spin polarised protons up to 250 GeV [48]. It had two operating detectors, Solenoidal Tracker at RHIC (STAR) and super Pioneering High Energy Nuclear Interaction eXperiment (sPHENIX), and the accelerator had been operational since 2000 and entered its 25th and final Run in 2025. Another example is the High Energy Accelerator Research Organization (KEK) in Japan which hosts the SuperKEKB electron-positron collider providing beams of electrons at 7 GeV and positrons at 4 GeV [49]. the first collisions took place in 2018, and it is still operational. The sole experiment, Belle-II, studies the properties of mesons containing b quarks.

All data analysed in this Thesis have been recorded at CERN, with the CMS detector, using LHC's pp collisions. The accelerator complex is described in Section 3.1, highlighting CERN's main collider in Section 3.2. Afterwards a short introduction of the experimental apparatus is given in Section 3.3, summarising its current subsystems and future changes.

3.1. CERN's Accelerator Complex

Currently, CERN's flagship accelerator is the LHC, which, at the time of writing of this Thesis, is the most powerful particle collider on Earth. However, the whole accelerator complex at CERN is powerful and versatile, and is not only used to fill the LHC, but also to provide protons or other ions to a multitude of experiments, as can be seen in Fig. 3.1.

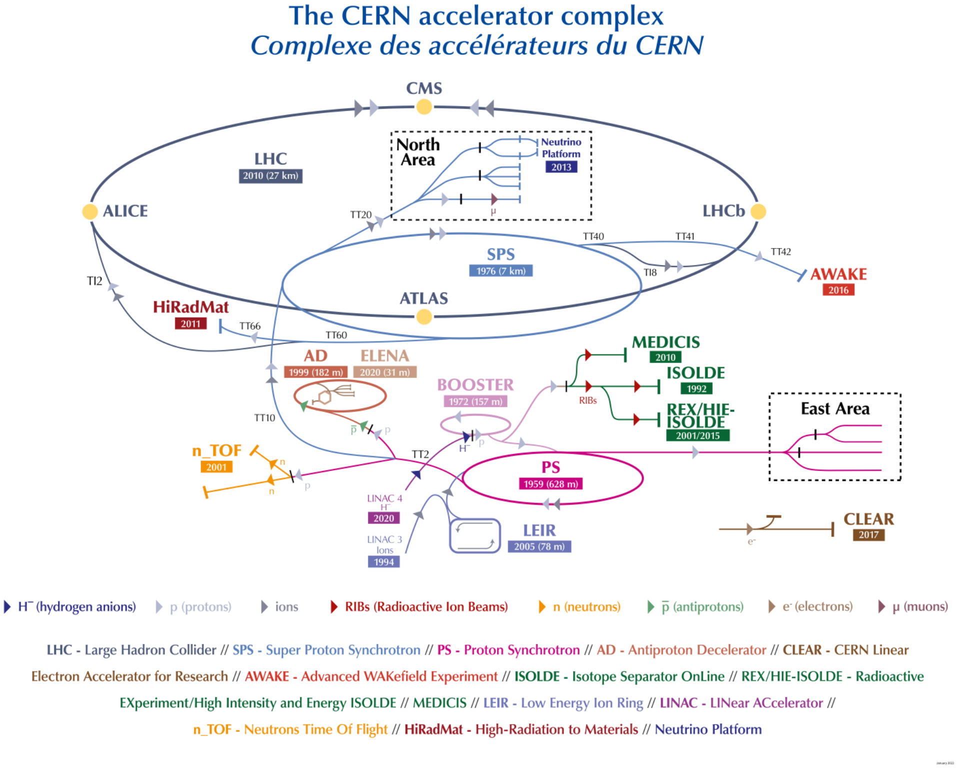

Figure 3.1. A schematic representation of CERN's accelerator complex [50].

As we are interested in collisions taking place in the LHC, let us follow the accelerator path protons have to take. Since 2020, the first acceleration step is done with LINAC 4 where negative hydrogen ions (H^-) are bunched together and accelerated to 160 MeV [51]. Even in the first step, the particles are accelerated in several stages sequentially going through a radio-frequency quadrupole, a drift tube, a coupled-cavity drift tube linear accelerator and finally a Pi-mode structure [51]. A dedicated ion source at the beginning of the machine produces hydrogen ions and feeds them for acceleration.

In 2020, LINAC 4 replaced LINAC 2, which for the previous 40 years was the first step towards proton beams. LINAC 2 accelerated protons, therefore, electrons were stripped from hydrogen atoms before entering the accelerator. The protons were then accelerated using radiofrequency cavities to 50 MeV [52]. The proton source was a simple bottle of hydrogen gas, the gas was passed through an electric field to strip off its electrons, leaving only protons ready to be accelerated.

The second acceleration step is performed by the Proton Synchrotron Booster (PSB) [53]. As it can accelerate protons, the H^- are stripped of their electrons during injection into the PSB. This is a rather compact structure with a circumference of 150 m and it accelerates protons to 2 GeV, also increasing the intensity of the beam.

The third acceleration step is done by the Proton Synchrotron (PS) which accelerates protons up to 26 GeV using conventional electromagnets distributed along its 620 m circumference [54]. From there the protons are sent to the Super Proton Synchrotron (SPS) which is the second largest machine in CERN's accelerator complex being $\approx 7\ km$ long [55]. The SPS accelerates protons to 450 GeV and sends the beam for injection into the LHC where it is split in two and accelerated up to 6.8 TeV using high-frequency cavities.

Filling of the LHC takes around four minutes per beam [56] as 12 cycles of the SPS are needed, in turn to fill up the SPS three to four PS cycles are needed. Including validation and readjusting, the injection step takes around 16 minutes. Afterwards, the ramping of the beam energy from 450 GeV to the desired collision energy of 7 TeV takes approximately 20 minutes.

3.2. The Large Hadron Collider

The LHC is the most powerful human made particle accelerator yet constructed [56]. It was built in the old Large Electron–Positron Collider (LEP) tunnel, which limited its dimensions but allowed for building cost reductions. It is approximately a circular underground tunnel at an average depth of 100 m and $\approx$ 27 km long. It consists of eight straight sections connected with eight arcs. The LHC is a particle-particle collider with two counter-rotating beams in two separate rings housed in a shared twin bore magnet. It can collide proton-proton (pp) beams, as well as proton-ion (mostly lead: p-Pb) or ion-ion (mostly lead-lead: Pb-Pb) beams, however, this work studies only the pp collisions.

In Fig. 3.2 a schematic layout of the accelerator is shown. The proton beam from SPS is split into two counter-rotating beams using fast kicker magnets and injected into the LHC via two transfer tunnels. Inside the LHC, the protons are accelerated using high-frequency accelerating cavity system situated in the fourth octant, and the beam dump is positioned in the sixth octant, both the third and the seventh octants are used for collimating the beams. Each straight section is 528 m long, and in four of them beams can be brought to cross.

The beams are bent by 1232 dipole magnets, each 15 m long, and are focused using 392 quadrupole magnets, each 5 m to 7 m long. Before entering detector caverns, the beams can be squeezed using designated magnets, and along the whole length of the machine several specially designed magnets are used for various corrections [56]. The windings of the superconducting magnets are made of Niobium-Titanium (NbTi) and are operated

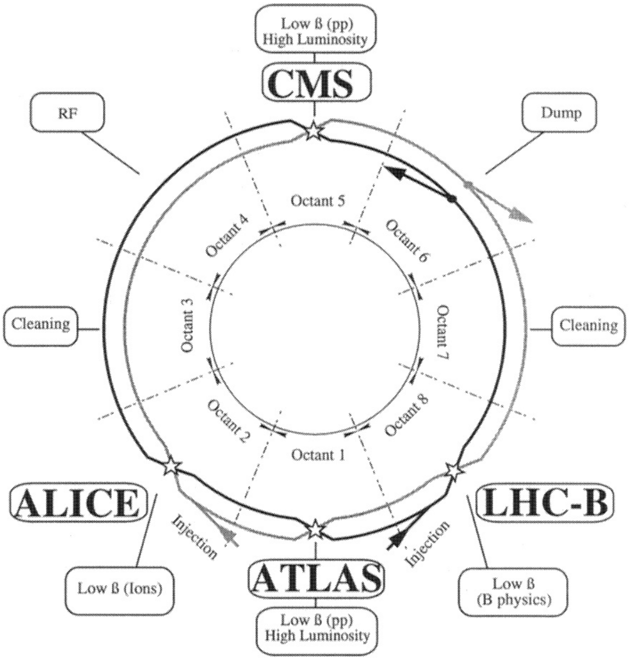

Figure 3.2. Schematic layout of the LHC, showing the interaction points, path of both beams, and function of each octant [57].

to create a magnetic field of more than 8 T. The superconductivity state is reached by cooling the magnets to 1.9 K using liquid helium.

The LHC was designed to create pp collisions of centre-of-mass, $\sqrt{s}$, energies up to 14 TeV. Due to two identical beams with energies E_{beam}, the centre-of-mass energy is calculated as Eq. (3.1).

$$\sqrt{s} = 2E_{beam} \tag{3.1}$$

The maximum reachable beam energy is limited by the peak dipole field in the storage ring. Even though its nominal field allows for energy of 7 TeV, the attainable field is influenced by fluctuations in the heat load and temperature margins. The higher the centre-of-mass energy, the more interesting collisions can take place. However, the quantity of collisions is just as important. The number of events generated per second, N_e, for a given process with cross section σ is given by Eq. (3.2), and it is directly proportional to the machine's instantaneous luminosity, L.

$$N_e = L \cdot \sigma \tag{3.2}$$

Instantaneous luminosity depends on the beam parameters as shown in Eq. (3.3):

$$L = \frac{N_b^2 \cdot n_b \cdot f_{rev} \cdot \gamma_r}{4\pi \cdot \varepsilon_n \cdot \beta^*} F, \tag{3.3}$$

where N_b – the number of particles per bunch, n_b – the number of bunches per beam, f_{rev} – the revolution frequency, $\gamma_r = 1/\sqrt{1 - v^2/c^2}$ – the relativistic factor which depends on particle's velocity v, ε_n – the normalized transverse beam emittance, β^* – the beam focusing at the collision point, and F the reduction factor due to the beams colliding at an angle. The nominal design expects $N_b \approx 1.15 \cdot 10^{11}$ protons per bunch and $n_b = 2808$ bunches per beam, with nominal spacing of 50 ns.

To describe the total number of collisions produced in a given time, the instantaneous luminosity is integrated, obtaining integrated luminosity, $\mathcal{L} = \int L dt$. Combining it with Eq. (3.2), it is easy to see that more events can be generated running the machine for longer periods of time or increasing the instantaneous luminosity. This is extremely important for processes with low cross section, e.g. HH production!

Additionally, multiple interactions can happen simultaneously at each bunch crossing. This effect is called the pileup (PU), and its average value is calculated with Eq. (3.4):

$$PU = \frac{L \cdot \sigma_{pp}^{inel}}{n_b \cdot f_{rev}}, \tag{3.4}$$

where σ_{pp}^{inel} – the inelastic pp cross section. The LHC was designed to have beam conditions with PU≈ 20, but as will be seen in the next section, the average PU has grown each year and exceeded all initial targets.

There are four large experiments situated at LHC's interaction points, as was marked in Fig. 3.2. The ATLAS (A Toroidal LHC ApparatuS) experiment is located in the interaction point 1 [58], the ALICE (A Large Ion Collider Experiment) is located in the interaction point 2 [59], the CMS (Compact Muon Solenoid) experiment is located in the interaction point 5 [60], and the LHCb (LHC beauty) experiment is located in the interaction point 8 [61]. Two of them – ATLAS and CMS – are high luminosity experiments with general purpose detectors designed to cover a large array of physics searches, while ALICE and LHCb are low luminosity experiments targeting specific physics cases, heavy ion physics and heavy flavour physics, respectively. There are also smaller, satellite experiments dedicated for distinct physics cases.

3.2.1. LHC Schedule

The concept of having a pp collider in the LEP tunnel was already discussed in 1984, and the LHC project was approved in December 1994, with its design proposal published prior. Construction began soon after in 1998 with several civil installations when LEP was still running, and after its official shut down in 2000, works in the tunnel and future experiment sites ramped up. Initially, it was expected that LHC will start its operation in 2005, however, several delays occurred both caused by budget constraints and engineering complexity. Fig. 3.3 shows an overview of the LHC operations, noting years,

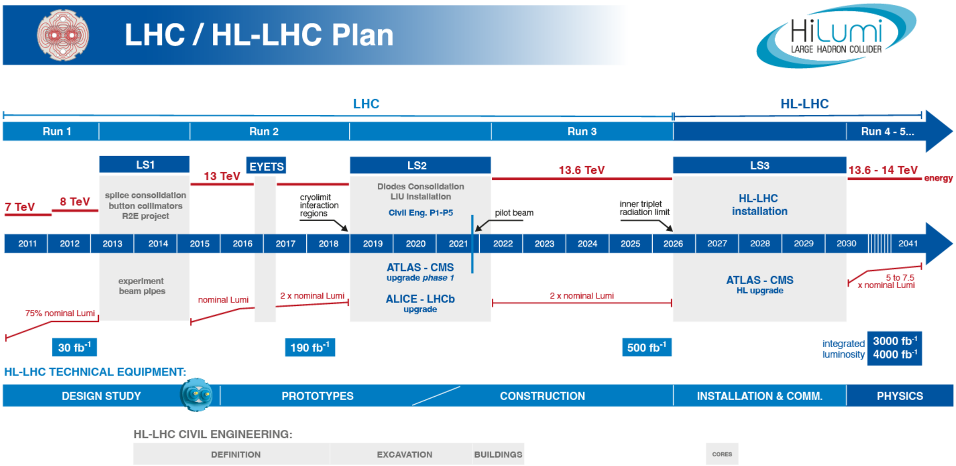

Figure 3.3. Schedule of the full LHC and HL-LHC operations [62].

centre-of-mass and integrated luminosity. Even excluding construction and commissioning, the first and last days of operation are expected to be more than 30 years apart. During these years, the machine has and will continue evolving. Two distinct phases can be highlighted: Phase-I and Phase-II. Where the Phase-II is the High Luminosity era, denoted with HL-LHC. Between the eras, major machine upgrades are expected. Each era consists of separate Runs spanning several years. Between Runs, long shutdowns (LSs) take place, where significant maintenance or accelerator and detector upgrades can happen. In between years, there are longer year-end technical stops (YETSs) accounted for planned maintenance. If needed, these stops can be extended, as was done between 2016 and 2017. Of course, also during the year several shorter, planned, and unplanned technical stops occur.

The very first proton beams circulated in the LHC in the end of 2008, however, due to an accident caused by a faulty electrical connexion between two magnets, a magnet quenched leading to a helium leak into the tunnel. The LHC was shut down for repairs and improvements. The first collisions were recorded in 2010, with a full-scale data-taking campaigns starting in 2011. The machine was running in a more conservative mode, with lower beam energies, larger spacing between bunches, Δt_b, and other parameters to ensure a safe start of operations. The first operational run, Run 1, covers 2010–2012, producing a revolutionising 6 fb^{-1} of collisions at $\sqrt{s} = 7$ TeV and 23.3 fb^{-1} of collisions at $\sqrt{s} = 8$ TeV [63]. Yet, even just a subset of this recorded luminosity was enough to claim the discovery of a new boson, compatible with the Higgs boson predicted by the BEH mechanism [1],[2].

After Run 1, the LHC entered its first LS which lasted two years. During this time, renovation and upgrades were carried out, not only at the LHC and its detectors, but also the PS and SPS to ensure flawless operation with an increase in the beam energy. The second operational run, Run 2, spanned between 2015 and 2018, producing 160 fb^{-1} of collisions at $\sqrt{s} = 13$ TeV [64]. Due to a lower transverse beam emittance and operational $\beta^* = 0.3$, the peak proton performance exceeded twice the design luminosity! 2015 was dedicated to establishing good beam conditions and preparing for intense luminosity production for the following years; magnet powering and training tests took place. In 2016, LHC produced data worth 40 fb^{-1} of integrated luminosity, the beams were brought for proton physics from mid-July to late October. Due to a vacuum leak in SPS, the number of bunches per train had to be limited. An extended YETS took place between the 2016 and 2017 operations. LHC performed a magnet replacement in the first and second octant as it had shown abnormal behaviour during the 2016 physics run. 2017 introduced multiple improvements in the beam operation and diagnostics and an issue with beam vacuum quality forced to adapt a new bunching schema that would allow to mitigate the influence of an unwanted electron cloud. Despite this challenge, a record integrated luminosity of 50 fb^{-1} was produced between the end of July and early November. 2018 was an overall successful operations year with no show-stoppers. The LHC generated 66 fb^{-1} of integrated luminosity between mid-April and the end of October.

The LS2 was expected to be 18 months long. However, it brought more challenges than originally foreseen, and thus the LS2 lasted three years. Many improvements were done with the Phase-II in mind. Several superconducting magnets were replaced, the beam dump was modified, new collimators were installed and cryogenic assemblies were refurbished. Also, the experiments took this opportunity to perform significant maintenance and work towards upgrades not only concerning Run 3 but also Phase-II.

Run 3 began in 2022 and will last until the middle of 2026. The LS2 allowed to record collisions at $\sqrt{s} = 13.6$ TeV, inching closer to the LHC design value. 2022 delivered 41 fb^{-1} between early July and the end of November. Air contamination in a radio frequency (RF) cavity halted data-taking for a month, however, the targeted integrated luminosity of 25 fb^{-1} was surpassed [65]. 2023 was equally challenging with a helium leak incident, however, LHC delivered 32 fb^{-1} between the end of March and mid of July [66]. On the contrary, 2024 was a great year for proton collisions, LHC had no significant show-stoppers and produced 122 fb^{-1} between the end of April and mid October in pp collisions. After the pp run, there was a lead-ion run as well. Similarly, also 2025 data-taking went smooth, altogether collecting more than 125 fb^{-1} in pp collisions from the beginning of May until the end of October. This year provided not only pp , but also light and heay ioon collisions!

To put LHC's operations into the context of experiments, during Run 2 (years 2016, 2017 and 2018) CMS collected 138 $\text{fb}^{-1} \pm 1.6$ % of golden-standard data, and in early Run 3 (year 2022 and 2023) CMS collected 62.6 $\text{fb}^{-1} \pm 1.4$ % of golden-standard data, or in combination around 200 fb^{-1}. Here, golden-standard means that all CMS subdetectors were flagged to be good for any kind of usage in physics analysis. The delivered luminosity versus time over the running periods can be seen in Fig. 3.4a while the PU evolution are shown in Fig. 3.4b.

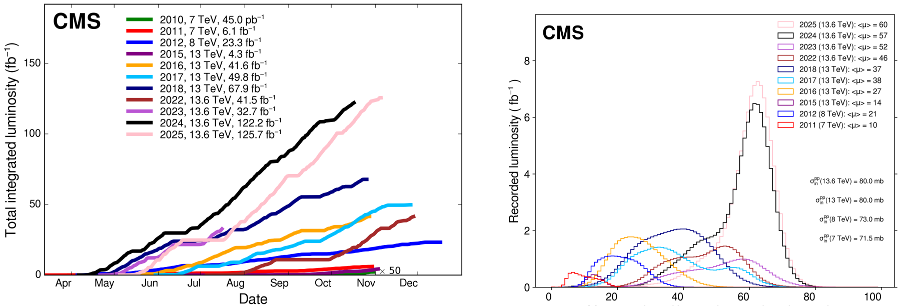

(a) delivered luminosity versus time (b) interactions per bunch crossing

Figure 3.4. Luminosity measurements by the CMS detector [67].

Past Run 3, running the accelerator without any significant luminosity increase would yield only marginal statistical gain. Therefore, to maintain the before scientific progress, the LHC must increase its luminosity. This will mark the transition from Phase-I to Phase-II. Extensive upgrades are foreseen for the LHC, the accelerator complex, as well as for the detectors [3]. The nominal collision energy might be increased reaching the design-nominal value of $\sqrt{s} = 14$ TeV.

The HL-LHC is designed to have an increased collision rate, thus the luminosity will increase by a factor of five with respect to the Phase-I LHC. To achieve this, several key technological challenges need to be solved, offering 11 T superconducting magnets, ultra-precise phase control superconducting cavities, new technologies for beam collimation, and long high-power superconducting links with zero energy dissipation. The preliminary design study expects to record around 250 fb^{-1} per year with a goal of 3000 fb^{-1} in about a decade. However, these targets have changed and evolved based on the up-to-date results from the LHC.

The upgrade will allow for Higgs boson property measurements with unprecedented precision and increased potential for the search of new physics. For statistics-limited measurements and searches, the increase in luminosity w.r.t. Phase-I will give a factor of 2.5 gain. Moreover, it will open a large new phase-space for rare processes. At the same time, it is worth noting that the improvement will not be only within the accumulated luminosity but also many new detector and trigger capabilities and opportunities as discussed in Section 3.3.9. Most of the installation and commissioning for the accelerator machine is foreseen during the LS3.

3.3. CMS Experiment

The CMS is located at LHC's interaction point 5, near Cessy (France) at an approximate depth of 100 m. It is a multi-purpose detector designed to explore physics at the TeV scale by studying proton-proton (and ion-ion) collisions [60].

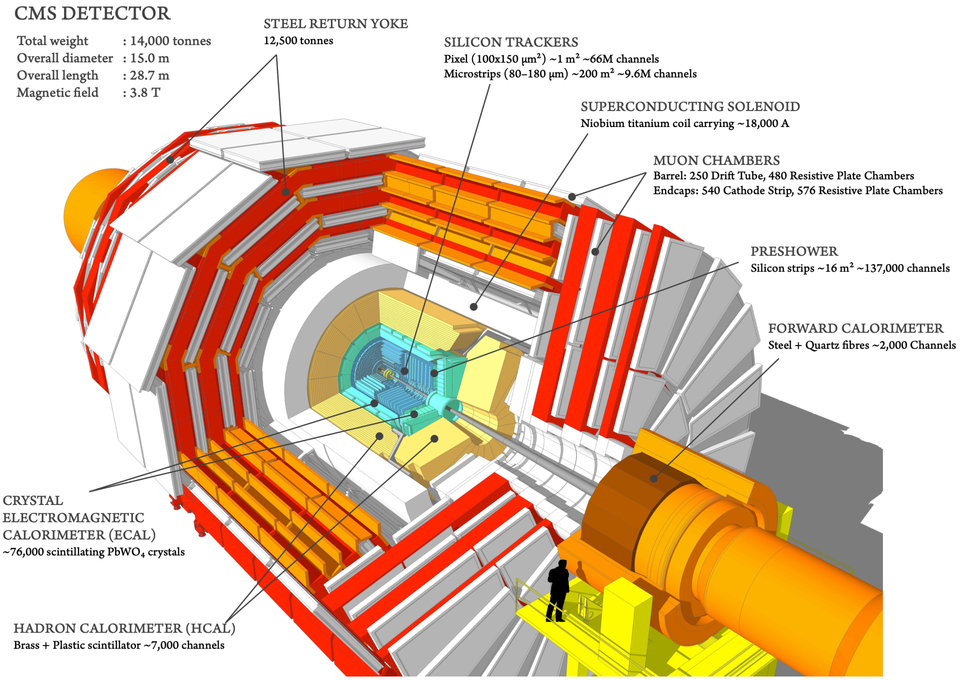

Figure 3.5. Cutaway diagram of CMS detector [68].

The detector's name highlights its main design features. It is *compact* due to its dense design – although the CMS detector is significantly smaller in volume compared to the ATLAS detector, it is almost twice as heavy. It has an extensive *muon* system comprising around 80 % of its total volume. And finally, at the heart of CMS sits a ≈4 T superconducting *solenoid* magnet. The detector has a cylindrical shape and azimuthal symmetry with a dimeter of 15 m and length along the beam axis of around 21 m, completely surrounding the interaction point. A cutaway diagram is shown in Fig. 3.5 illustrating the subdetectors, the beamline and a person for scale. In the diagram, the central part (barrel) and the two forward regions (endcaps) are clearly distinguishable.

As can be seen in the figure, the CMS is made of multiple concentric subdetectors with high-granularity and good time resolution, each specialised in detecting and measuring various particles and their properties, which together can reconstruct what has happened in the collision. The coordinate system used in the detector is described in Section 3.3.1, its heart, the superconducting solenoid, shown in figure in white, is described in Section 3.3.2.

Inside the superconducting magnet, closest to the beamline is the silicon tracker. In Fig. 3.5 denoted in cyan and further expanded on in Section 3.3.3. Tracker traces the paths and momenta of charged particles, as well as measures the position of the collision vertices. Between the tracker and the solenoid are the electromagnetic and hadronic calorimeters which measure the energy deposited by electrons, photons, and hadrons. Both calorimeters are shown in yellow in Fig. 3.5 and further expanded on in Section 3.3.4 and Section 3.3.5. Finally, outside the solenoid is the muon system which tracks muon path and measures their momenta. A quick introduction to CMS's trigger system and the data acquisition system is given in Section 3.3.7, while the fundamentals to CMS DCS are summarised in Section 3.3.8. Finally, Section 3.3.9 introduces the Phase-II upgrade.

3.3.1. The Coordinate System

A right-handed coordinate system is used in the CMS to characterise both its layout and the reconstructed particles. The x-axis points radially inward towards the centre of the LHC, the y-axis points vertically upwards and the z-axis points in the counter-clockwise beam direction as viewed from above. Due to the CMS's shape, spherical coordinates are commonly used. The azimuthal angle $\phi \in [-\pi, \pi]$ is measured from the x-axis in the xy plane, while the polar angle $\theta \in [0, \pi]$ is measured from the z-axis. A schematic illustration of the standard coordinate system at the CMS detector is shown in Fig. 3.6.

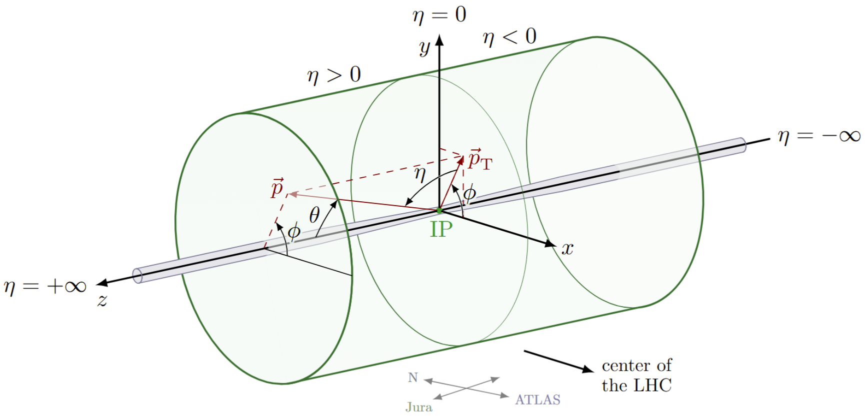

Figure 3.6. Schematic illustration of the standard coordinate system at the CMS detector, adapted from [23]. Illustrates the interaction point, x, y, z axis, the plane in which the transverse momentum, p_T, is measured, polar angle, θ, azimuthal angle, ϕ, as well as the pseudorapidity, η.

To combat the unknown initial momentum in the z-axis of the proton constituents, momentum and energy transverse to the beam direction, respectively, p_T and E_T, are used to characterise the final state particles as the initial momentum in the transverse plane is zero. The transverse momentum is calculated from momentum components in the xy plane as shown in Eq. (3.5). The imbalance of the energy measured in the transverse plane would be denoted as E_T^{miss}. For simplicity, further in the text E_T describes the missing energy, unless stated otherwise.

$$p_T = \sqrt{p_x^2 + p_y^2} \tag{3.5}$$

As accustomed at colliders, particle's angle from the transverse plane is conveniently described with pseudorapidity as defined in Eq. (3.6). A particle moving in the transverse plane would have $\eta = 0$ while a particle moving along a beamline would have $\eta = \infty$.

$$\eta = -\ln\left(\tan\left(\frac{\theta}{2}\right)\right) \tag{3.6}$$

Pseudorapidity is an approximation of rapidity, y, defined as Eq. (3.7). Both quantities match when particles are massless and is a good approximation when particle momentum is much larger than their mass.

$$y = \frac{1}{2}\ln\left(\frac{E + p_z}{E - p_z}\right) \tag{3.7}$$

Lastly, it is convenient to describe a Lorentz invariant quantity, the angular distance, ΔR, in terms of distances in $\eta - \phi$ with Eq. (3.8).

$$\Delta R = \sqrt{(\Delta\eta)^2 + (\Delta\phi)^2} \tag{3.8}$$

3.3.2. Superconducting Solenoid

At the heart of CMS sits a superconducting solenoid. It is 13 m long with an inner diameter of six m and a radial thickness of 312 mm, effectively it is a "thin coil" [69]. To keep the detector compact, a high-field magnet was needed, and a solenoidal field was favoured over a toroidal one due to its compact nature and to ensure that the muon tracks would lie in the transverse plane. This in turn would allow to use tracking information in the trigger as tracks would be pointing to the vertex. It was designed to reach 4 T and provide a bending power of 12 T·m; however, it is operated in a slightly more conservative setting and reaches a quasi-uniform 3.8 T magnetic field parallel to the z-axis. The solenoid is operated at 4.6 K cooled with liquid helium.

The magnetic flux is returned through an iron yoke that encapsulates both the barrel and the endcaps and serves also as a structural component. It has a high return field of around 2 T. The yoke not only reduces the stray field and acts as an absorber for the muon system, but also increases the homogeneity of the field within the solenoid.

The solenoid has a cold mass of 220 t, with four layers of windings made of reinforced

NbTi. One of the most impressive parameter of the solenoid is the ratio between the stored energy and the cold mass (11.6 kJ/kg) that causes a large mechanical deformation during energising. Compared with the ATLAS's barrel solenoid, the stored energy is of a similar order but the energy-over-mass ratio is almost six times larger for the CMS's solenoid. The high magnetic field value increases muon triggers robustness as the muon momentum and charge are primary determined by the curvature of the reconstructed track in the tracker. A stronger magnetic field results in greater track curvature, and, for the same detector resolution, allows improved track separation and more precise momentum determination. See Section 4.1 for more on the precision of muon reconstruction.

For particle detection as well as reconstruction, it is instrumental to know precisely the magnetic field within the whole detector, not only inside the solenoid but also within the yoke. The magnetic field measurements have been performed using standard equipment, as well as using cosmic muon reconstruction, as this can be done while underground and fully assembled. In Fig. 3.7, the simulated magnetic field value and field lines are shown. It was modelled using `TOSCA/OPERA-3D` finite element program, and showed excellent agreement with field measurement campaign conducted before lowering the magnet into the cavern [69]. The discrepancies of around 5 mT comprise less than one percent change. For comparison, to worsen the muon resolution by 10 %, the error in the magnetic field value needs to be greater than 2 %.

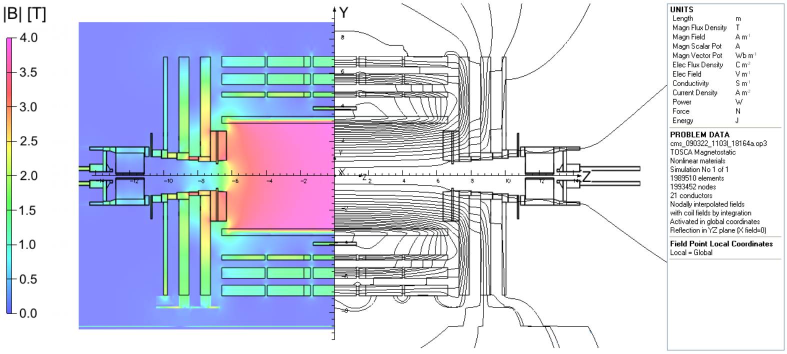

Figure 3.7. Value of the B field (left) and field lines (right) predicted on a longitudinal section of the CMS detector, for the underground model at a central magnetic flux density of 3.8 T; each fieldline represents a magnetic flux increment of 6 Wb [69].

The example shown in Fig. 3.7 represents the magnetic field of the magnet in the cavern, when operated at 3.8 T. It is a heavy computational task, but as the distribution of the magnetic field has to be known not only for the Monte Carlo (MC) simulations, but also the high-level trigger (HLT) and offline reconstruction in the CMS software (CMSSW), the mapping had to be optimised for computational efficiency. Therefore, a volume based geometry is used and 12-fold ϕ-symmetry of the yoke is employed. Nevertheless, if more precise values are needed, they are available.

3.3.3. Silicon Tracker

The silicon tracker is the closest subdetector to the beam line and the interaction point. It provides a precise and effective measurement of the trajectories of charged particles and reconstructs secondary vertices (SVs); it is fully silicon-based. The tracker had to have high granularity, fast response, and as little material budget as possible while being able to withstand the harsh radiation environment [70]. A low material budget was needed to reduce multiple scattering in the supporting detector material and reduce photon conversion. Moreover, to extract the dissipated heat and mitigate radiation damage, the detector is cooled. The CMS tracker is composed of a pixel detector (Pixel) as its innermost part and a silicon strip tracker outside of the Pixel.

During the data-taking of this Thesis, the Pixel has undergone a major upgrade called the CMS Phase-I upgrade during the YETS of the LHC between 2016 and 2017, as well as a serious maintenance in the LS2 between 2019 and 2021. For comparison, let us familiarise ourselves with the initial design of the Pixel, shown in Fig. 3.8. The initial Pixel had three cylindrical layers of hybrid Pixel modules at radii 44 mm, 73 mm and 102 mm, complemented by two discs of Pixel modules on each side at 345 mm and 465 mm providing three space points on each charged particle trajectory [72]. It was designed to be efficient in conditions with a maximum average PU of 25. The sensor pixel size was of $100 \times 150\,\mu\text{m}^2$ that yields a similar track resolution in all directions. The spatial resolution of a point is quoted around 10 µm in the transverse plane and around 15 µm to 20 µm in the longitudinal direction for the barrel layers. In general, the track resolution was estimated to be around 1.5 % in transverse momentum and the impact parameter (IP) resolution was 25 µm - 90 µm in the transverse plane and 45 µm - 150 µm longitudinally for non-isolated particles below $p_T < 10$ GeV [73]. The sensors were cooled to around

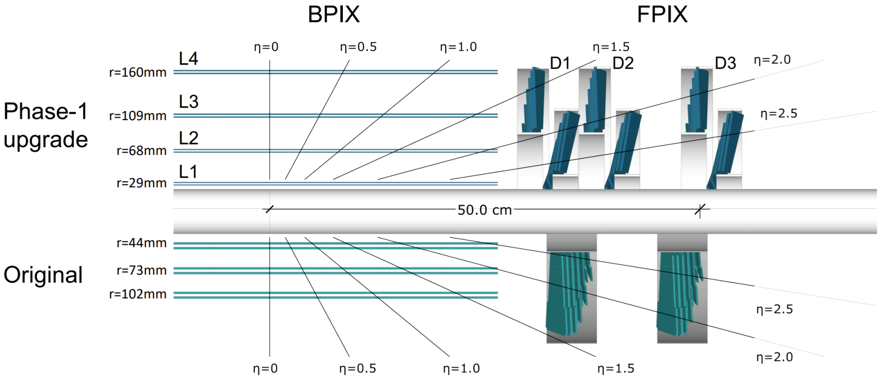

Figure 3.8. Layout of the CMS Phase-I Pixel compared to the original detector layout, in longitudinal view [71]. Its barrel (BPIX) and endcap or forward (FPIX) parts are highlighted.

$-10\,^\circ$C and even lower towards their end of life using liquid phase cooling with C_6F_{14}. It had full azimuthal coverage, while the track acceptance was limited to $|\eta| < 2.5$. As the accelerator complex was upgraded providing more radiation harsh environment for the detectors, yet more exciting conditions for physics, an upgrade of the Pixel was needed to ensure its robustness and reach the desired resolution.

The Phase-I upgrade brought exciting changes; the upgraded Pixel is more radiation hard, lighter, and provides more robust tracking [71]. Since during the LHC's LS1 a new, smaller in diameter beam pipe was installed, the first Pixel layer could be moved closer to the interaction point, optimising it to have four hit coverage. It had four barrel layers at radii 29 mm, 68 mm, 109 mm and 160 mm and three discs on each end at distances from the interaction point of 291 mm, 396 mm and 516 mm. The total silicon area increased from $1.1\,\mathrm{m}^2$ to $1.9\,\mathrm{m}^2$. A comparison between the original and upgraded Pixel can be seen in Fig. 3.8. The Phase-I Pixel covers regions both closer and further away from the interaction vertex. Moreover, the Pixel acceptance was increased to $|\eta| < 3.0$ and while the transverse momentum resolution remained around 1.5 %, the transverse IP resolution was improved to reach $20\,\mu\mathrm{m}$ - $75\,\mu\mathrm{m}$ [74]. CMS Phase-I Pixel is cooled down to $-20\,^\circ$C with two-phase CO_2, allowing the use of small-diameter and thin-walled pipes, thus reducing the material budget. This has allowed to have the same total material budget in the central region while significantly reducing it in the endcaps [71]. As the first Pixel layer is moved closer to the beam line in more radiation harsh environment, it was already expected that the innermost layer will be changed during the LHC's LS2, alongside other maintenance tasks that would allow to improve the quality of the collected data [75].

Outside of the Pixel, the strip detector is positioned. The silicon strip tracker is composed of the following subsystems – tracker inner barrel (TIB) and tracker inner disks (TID), tracker outer barrel (TOB) and tracker outer endcaps (TEC). Of them TIB and TID covers 20 cm $< r <$ 55 cm and 58 cm $< |z| <$ 124 cm, while TOB covers 55 cm $< r <$ 116 cm and TEC extends over 124 cm $< |z| <$ 282 cm. The silicon strip tracker has an active area of $198\,\mathrm{m}^2$, and it reaches to $|\eta| = 2.5$ [70].

Each subsystem is equipped with silicon micro-strip sensors with various dimensions, where the strips are positioned parallel to the beam axis in the barrel and radially on the discs. With each layer being further away from the interaction point, the granularity of the strips can be reduced, and their dimensions generally increase. As an example, in the closest layer of TIB the micro-strip sensors are $320\,\mu\mathrm{m}$ thick with a strip pitch of $80\,\mu\mathrm{m}$ while the first layer of TOB has micro-strips with a $500\,\mu\mathrm{m}$ thickness and a strip pitch of $183\,\mu\mathrm{m}$.

The TIB has four layers and TIDs each have three discs, both deliver up to four measurements on a trajectory with single point resolution of $23\,\mu\mathrm{m}$ and $35\,\mu\mathrm{m}$. The TOB surrounds the TIB and TID and consists of six barrel layers providing single point resolution of $35\,\mu\mathrm{m}$ to $53\,\mu\mathrm{m}$. Finally, each TEC is composed of nine discs. The position

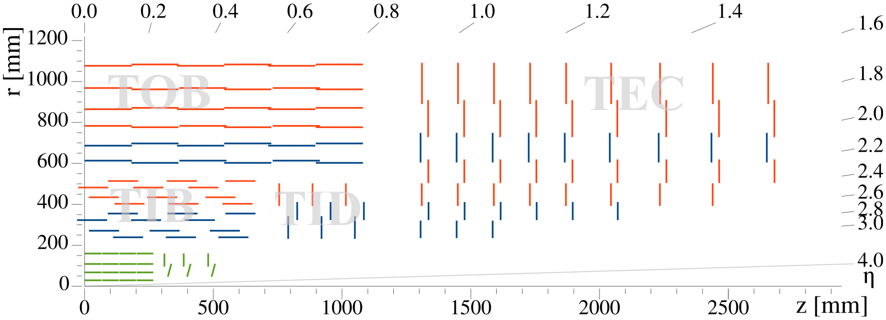

Figure 3.9. A sketch of one quarter of the Phase-I CMS tracking system in the r-z view. The Pixel is shown in green. Single-sided and double-sided strip modules are depicted as orange and blue segments, respectively [76].

of each subsystem and its layers can be compared in a quarter cross section sketch shown in Fig. 3.9 where in blue are denoted modules which are mounted back-to-back providing a second measurement in the same coordinate. For comparison, the Pixel is shown in green.

3.3.4. Electromagnetic Calorimeter

Outside the tracking system lies the electromagnetic calorimeter (ECAL) with the main goal of measuring the energy and time-of-arrival of photons and electrons. It is a hermetic and homogeneous scintillating calorimeter made of lead tungstate ($PbWO_4$) crystals. The use of high density crystals has allowed for a compact, radiation hard design with fine granularity. Moreover, the crystals serve both as a dense medium where electrons and photons turn into electromagnetic showers and as active scintillating material [77]. In short, incoming particles form electromagnetic showers and loose their energy. Due to the crystal characteristics, the showers are contained within the crystals.

In Fig. 3.10, a sketch of one quadrant of the ECAL's longitudinal section is shown, noting the electromagnetic barrel calorimeter (EB) and electromagnetic endcaps calorimeter (EE) as well as a ECAL preshower detector (SE), placed in front of the endcap crystals. The barrel part covers a pseudorapidity range $|\eta| < 1.479$, the crystals have a tapered shape and slightly vary with position in η, as can be seen in the figure. Moreover, they are mounted in a way to avoid cracks aligned with particle trajectories. The endcaps cover $1.479 < |\eta| < 3.0$ and are placed at a distance of $|z| = 3154$ mm. Although the detector can be seen as hermetic, the region where EB transitions into EE (around $\eta = 1.479$) is often considered as the gap region, as it has lower efficiency. Overall, there are 61200 crystals in the EB and 7324 crystals in each EE allowing for high resolution calorimetry.

Different solutions are used for the photodetectors in EEs and EB due to the expected level of radiation. In the barrel part, avalanche photodiodes are used while in the endcaps

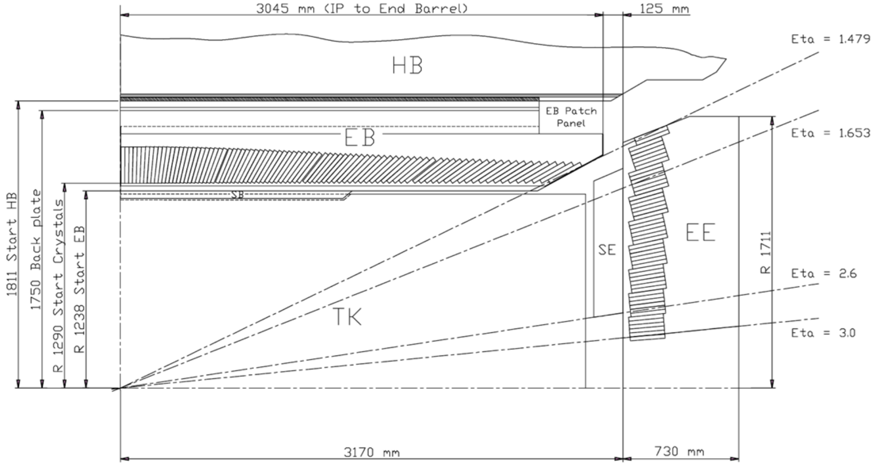

Figure 3.10. Longitudinal section of the ECAL (one quadrant) [77].

vacuum phototriodes are chosen. As the number of scintillation photons emitted by the crystal and their amplification are temperature dependent, ECAL has to be cooled keeping its crystals at a stable temperature within ± 0.05 ° C. At the same time, the nominal operating temperature is 18 ° C allowing for a water cooled solution. The maintenance of stable temperature increases the detector's lifetime.

As mentioned above, SEs are placed before the endcaps, their primary aim is to identify neutral pions and distinguish between electrons and minimum ionising particles (MIPs). They cover $1.653 < |\eta| < 2.6$ and are around 20 cm thick. A SE is a sampling calorimeter with two layers – a layer of lead that initiates showers and a layer of silicon strips to measure the deposited energy and the shower profile. Similarly to the silicon tracker, it is operated at $-10\,°$C.

The energy resolution provided by the ECAL was reported better than 1.8 %, 3.0 %, and 4.5 % of the energy deposited in $0 < |\eta| < 0.8$, $0.8 < |\eta| < 1.5$ and $1.5 < |\eta| < 2.5$, respectively [78]. The crystals darken over time because of the exposure to radiation, however, the change is constantly monitored using a laser system and automatically corrected for their response. In Run 2, the corrections were applied twice a week, while for Run 3 the corrections are applied with each new proton fill in the LHC. Initial measurements in 2011 were performed with a 440 nm laser, but it was upgraded to a 477 nm laser in 2012. Compared with the initial measurements in 2011, the relative response change to laser light was up to 10 % in the barrel, up to 50 % at $|\eta|<2.5$, and up to 90 % in the region closest to the beam pipe for Run 2 operations. For Run 3 these values are deteriorating, reaching 17 % in the barrel, up to 62 % at at $|\eta|<2.5$, and up to 96 % in the region closest to the beam pipe [79]. These measurements are performed every 40 minutes, to correct the recorded physics data.

3.3.5. Hadronic Calorimeter

The final detector partly in the solenoid is the hadronic calorimeter (HCAL) [80]. Its main objective is to measure hadronic jets and inexplicitly account for missing transverse energy (MET) – energy carried away with particles such as neutrinos that cannot be detected within the detector. As can be seen in Fig. 3.11, HCAL can be divided into four components of which two are the hadronic barrel calorimeter (HB) and the hadronic endcap calorimeter (HE) and two are more specific calorimeters: hadronic outer calorimeter (HO) and hadronic forward calorimeter (HF). Also this subdetector underwent an upgrade during the LS1 and maintenance during LS2, however, the changes with respect to Run 1 were not really geometric as the improvement considered signal readout technology, reducing the noise and anomalous signals [81].

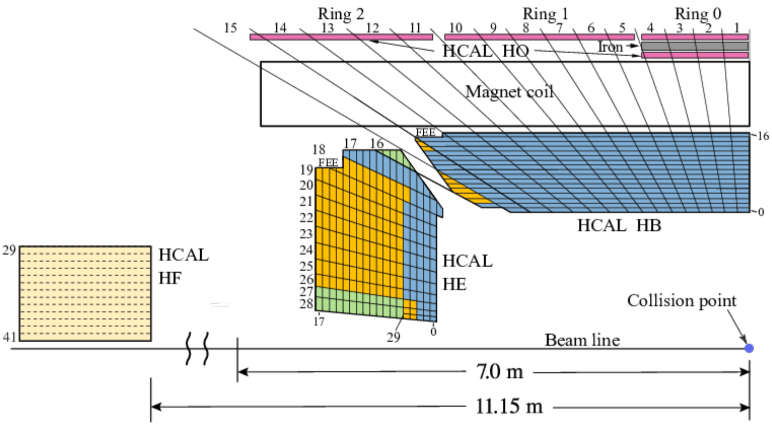

Figure 3.11. A schematic view of one quarter of the CMS HCAL showing the positions of its four major components: HB, HE, HO, and HF [82].

The HB is a sampling calorimeter that extends to $|\eta| = 1.39$, which means that two different materials are used to produce the hadron shower and to measure the deposited energy. It consists of 36 identical azimuthal wedges constructed of flat brass absorber plates parallel to the beam axis, and around these plates plastic scintillator tiles are grouped into 16 η regions, each corresponding to $\Delta\eta$ of 0.087. Several stainless steel plates are used for structural support. The scintillator response has been measured in test beams using pion and radioactive sources. The HEs also are sampling calorimeters made of brass absorbers and plastic scintillators. They are positioned at $|z| = 4007$ mm from the interaction point and cover $130 < |\eta| < 3.00$. Each HE has an 18-fold symmetry in ϕ and due to the harsher radiation region, its granularity is coarser than HB's. As can be seen in the schematic in Fig. 3.11, HE and HB overlap to prevent gaps. For both HE and HB a set of scintillators sharing the same η and ϕ in different layers are grouped together and referred to as a "tower", as can also be seen in Fig. 3.11. The tower arrangement closely follows and extends the granularity of the ECAL. For each tower the scintillation light is collected by wavelength shifting fibres and carried to photodetectors. After the upgrade silicon photomultipliers (SiPMs) replaced the previously chosen technology – hybrid photodiode transducer (HPD). HPDs were chosen because of their magnetic field tolerance, but provided unexpected electronic challenges.

Although hadrons deposit roughly one third of their energy in the ECAL, in low-η region there is not enough space in the HB to fully contain the decaying hadrons inside of the solenoid. Therefore, a HO calorimeter is placed outside the solenoid and is often referred to as the "tail catcher". It has five discs with one or two layers of scintillators and is using the magnet coil and return yoke as an absorber. It covers $|\eta| < 1.26$ and its segmentation matches closely that of the HB.

Finally, the HFs calorimeters are positioned on either side of the interaction point, covering $2.85 < |\eta| < 5.19$ at a distance of $|z| = 11150$ mm. Each module has steel wedges with embedded quartz fibres. The HF calorimeter is a Cherenkov sampling calorimeter as it uses the emission of Cherenkov light by the secondary charged particles traversing the quartz fibres. The light coming from HF is read out by multi-anode tubes. Due to the high-η coverage, the HF is crucial for identifying forward jets, accounting for MET and also measuring luminosity.

3.3.6. Muon Detectors

The CMS's middle name hints that the detection of muons is of central importance for the CMS's physics program, however, muons generated at LHC collisions are almost MIPs, they penetrate the detector without losing a significant amount of energy [83]. This is why a dedicated outer system is built to identify muons, and measure their charge and momentum. But even the muon system does not contain all muons and some escape the CMS detector altogether. Muons, especially energetic muons are great objects for triggering as they are characteristic for interesting events with energetic collisions. An example is the $H \to ZZ \to 4\mu$ channel already mentioned in Section 2.1.

The muon system has been designed with redundancy and robustness. It benefits from the solenoid's return field and prefers simple design with coarser yet suiting resolution. The muon system has been upgraded in both LS1 for Run 2 and in LS2 for Run 3, in both times the main improvements concerned off-detector electronics and solutions, while in LS2 a new subsystem was also added [84], [85]. In Run 2, the muon system consisted of three complementary subsystems: the drift tube (DT) system, the cathode strip chamber (CSC) system and the resistive plate chamber (RPC) system, however, for Run 3 the gas electron multipliers (GEM) system was added. A schematic representation of their position can be seen in Fig. 3.12. It is a view made for Run 3 as it shows GEM, however, other subsystem position has remained the same.

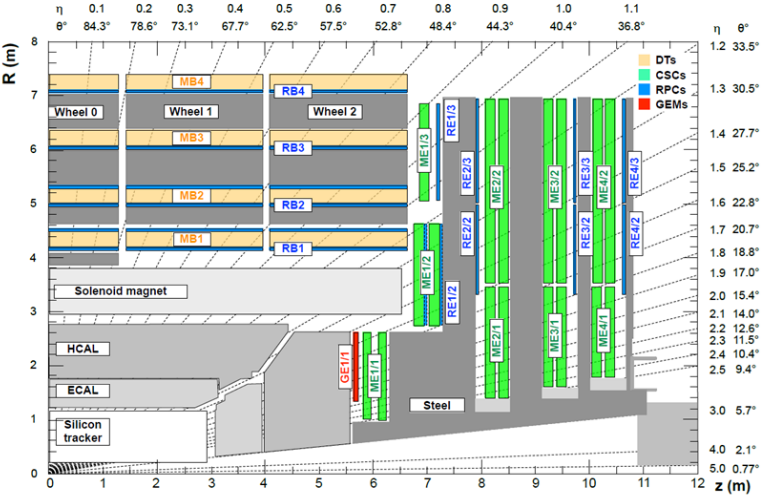

Figure 3.12. Schematic view in the r-z plane of a CMS detector quadrant, showing location of DTs, CSCs, RPCs and GEMs [86].

As fewer muons are expected in the barrel region, DTs are placed there and cover up to $|\eta| < 1.2$. As the name suggests, they consist of drift chambers with rectangular cells positioned in between the magnets return yoke. They provide spatial measurements that can also be used in triggering. There are four concentric cylinders around the beam line with, the inner three having 60 drift chambers and the outer one having 70 chambers [87]. The anode wires are made of gold-plated stainless steel and their length is approximately 2.4 m with maximum drift of 21 mm. The cathode strips are placed on the side walls of the tube, and additional electrode strips at the top and bottom of each tube help shape the drift field. The tubes are filled with a mixture of Ar and CO_2. The layers of a DT have an offset of half of the width to ensure high time (2 ns) and spatial resolution of 100 µm and 150 µm in the transverse and longitudinal directions, respectively [86].

In the endcap region, a greater muon rate is expected, and the magnetic field is not homogeneous. Therefore, CSCs are chosen due to their fast response, fine segmentation, and radiation resistance [88]. The CSCs have a faster response time than DTs while the time resolution remains similar and is around 3 ns [86]. The CSCs cover $0.9 < |\eta| < 2.4$ and the chambers are placed perpendicular to the beam with cathode strips running radially outward and anode strips perpendicular to the cathodes. Moreover, in total there are 468 CSCs, each trapezoidal with six anode wire planes intertwined with seven cathode planes. The CSC extends the muon triggering capabilities in the endcap region. CSCs are filled with a mixture of Ar, CO_2 and CF_4. The provided spatial resolution ranges from 45 µm to 150 µm.

In total, 480 RPCs are installed in the barrel and 576 RPCs in the endcap region to provide the trigger with complementing redundant information, as well as to achieve a good measurement of transverse momentum and timing. Their time resolution is around 1.5 ns [86]. They are gaseous parallel-plate or double gap detectors operated in avalanche mode [89]. Graphite electrodes and copper readout planes and a gas mixture of $C_2H_2F_4$, C_4H_{10} and SF_4 are used. Each gas gap is 2 mm wide. The barrel part consists of five wheels, each consisting of six layers, while endcaps have four discs each. RPCs cover up to $|\eta| < 1.9$, their spatial resolution is quoted around 0.8 cm - 1.3 cm. They complement the muon trigger in the endcap region.

Finally, a GEM is located in front of the inner ring of the CSC in the forward region. It was added for Run 3 operations with the HL-LHC in mind to contribute in maintaining an adequate pattern recognition and efficient muon reconstruction. The GEM is a triple-layer gas electron multiplier detector covering $1.55 < |\eta| < 2.18$ and is the first of three layers to be installed for the Run 4 [85]. The bottom of a GEM chamber is a circuit board holding the copper drift electrode while the top is the readout board consisting of radially orientated readout strips. There are 128 strips in each chamber and three GEM foils that amplify the ionization signal which all together allows for charge multiplication of up to 10^5. The foils are made from a copper layer with periodic grid, or more precisely – holes, surrounded by a layer of polyimide. The GEMs are filled with a mixture of Ar and CO_2. The time resolution is around 5 ns while the spatial resolution is around 30 µm to 100 µm.

Broadly speaking, muons that traverse the muon system ionize the gas in the chambers, which eventually causes electric signals to be produced on the wires and strips, which are read out by the electronics. Each readout has a precise location associated to it and thus it can be used by algorithms when reconstructing muons. In the case of multi-layer detector, signals in each layer can be combined to form a track segment within the chamber.

3.3.7. Trigger System

The current LHC beam crossing interval for *pp* collisions is 25 ns which corresponds to a crossing frequency of 40 MHz, or in other words, 40 million collisions per second. Even with a conservative number of simultaneous collisions per crossing it would be impossible to store and process the large amount of data created by the final state particles. Ergo, a significant but well-informed rate reduction has to be done, selecting to store only the potentially interesting events and forever rejecting the rest. It is achieved by the trigger system which consists of two steps – Level-1 (L1) trigger and the HLT – which reduce the event rate to ≈100 kHz and to ≈1 kHz, respectively.

The L1 trigger is hardware-based, it is implemented in the processor field-programmable gate arrays (FPGAs) that are mounted on electronic boards, as it has to be quick and robust, yet be ready to target a wide spectrum of desirable event topologies. It uses coarse data from the calorimeters, and muon system that provide information on physics object candidates while holding the high-resolution data in the memory pipeline in the front-

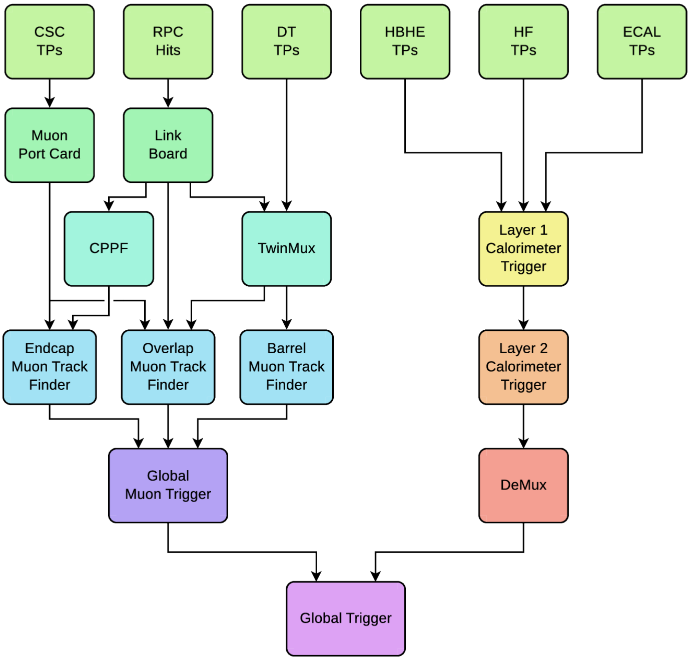

Figure 3.13. Level-1 trigger architecture, labels in the diagram correspond to trigger primitives (TPs), concentration preprocessing and fan-out (CPPF), demultiplexing card (DeMux) [90].

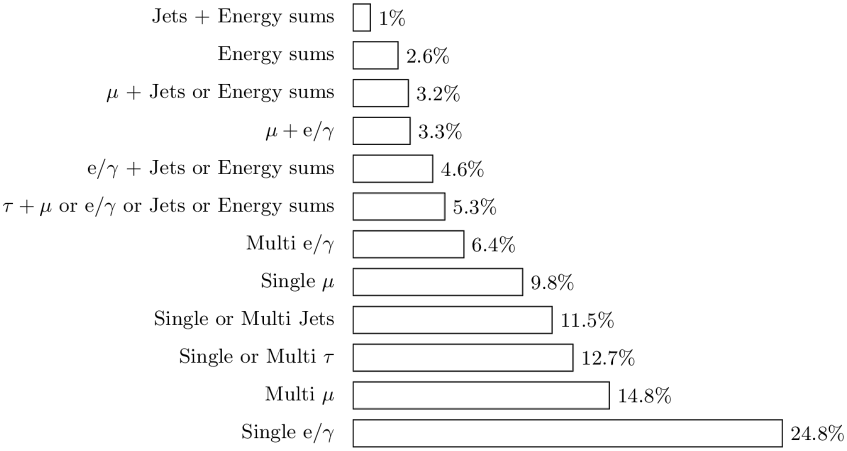

Figure 3.14. Fractions of the 100 kHz rate allocation for single and multi-object triggers and cross triggers in a typical CMS physics menu during Run 2 [90].

end electronics. The decision is generated on the basis of the multiplicity and kinematic information of various candidates. If a positive decision is made, the complete detector data are read out for transfer to the HLT [90]. Schematically its architecture is shown in Fig. 3.13, showing its local, regional, and global trigger components.

At the bottom of the chain are the local components – the muon trigger gathers information based on track segments in the muon system and the calorimeter trigger gathers information based on the energy deposits in the calorimeter towers. This information is transferred to a regional trigger via high-speed serial links. Regional triggers combine this input and use pattern recognition to sort and rank trigger objects, examples of favoured objects are shown on the upwards flowing lines. Finally, the global subtriggers transfer the best candidates to the top of the hierarchy for the final decision.

The global trigger's decision is chosen from a given "menu" with various "seeds" and can be chosen before or during data-taking. Any event that does not satisfy any seed is forever rejected. Typical criteria include the number of specific objects (e.g., leptons), thresholds on the transverse momenta, pseudorapidity, as background processes tend to have softer transverse momentum and higher pseudorapidity. Fig. 3.14 shows the fraction of the 100 kHz rate allocated for each trigger type in a typical menu. The rate of the trigger seed can be further suppressed by applying a "prescale". A prescale of N means that only 1/N of the passing events is accepted.

The trigger system's hardware was upgraded in LS1 to favour industry standard solutions, however, more prominent are the algorithmic upgrades made for Run 3. As the Run 3 physics programme is broader, several new algorithmic approaches were proposed, some also based on machine learning (ML) techniques within the FPGA. Moreover, for Run 3 an exciting scouting system was commissioned allowing to read out unfiltered data.

When the L1 trigger has selected a potentially interesting event, it is passed to the next filtering stage – the HLT. The HLT is software-based, running on a farm of commercial computers, which uses complete high-resolution data and performs complex calculations with usually higher thresholds and requirements [91]. The HLT selects data based on the chosen HLT "paths" available within the selected trigger "menu". A "path" is a set of algorithmic rules that reconstruct and select objects. After an event has passed the HLT, only high-level physics objects will be stored on the disc, no raw detector channel data are stored for offline analysis in the CERN Tier-0 in tape format.

The HLTs selecting similar physics object topologies are grouped into primary datasets for offline processing. The paths are classified as primary or complementary. Primary paths are used for analysis and usually have higher level for acceptance, while complementary paths are used for calibration and efficiency measurements, thus are looser. Complementary paths are often "prescaled", meaning that only a fraction of events that pass the HLT are accepted for storage, thus reducing the storage rate.

The HLT is computationally heavy, given that around 200 algorithms are run. Fig. 3.15 displays a pie chart with central processing unit (CPU) time distribution per event spent

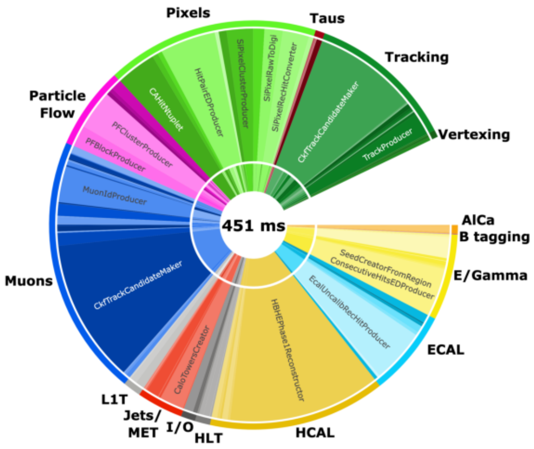

Figure 3.15. Pie chart distribution of the CPU time per event spent by the HLT for different parts of the event reconstruction [91].

by the HLT. Individual parts are grouped by detector and physics object, while the empty slice accounts for the time spent outside of the individual algorithms. The average processing time sets an upper limit on the processing capacity of 130 kHz which exceeds the nominal value. Lately, intensive studies and optimisation campaigns are performed to incorporate graphical processing unit (GPU) where possible to speed up processing.

In addition, non-standard usage of the trigger system is available for the CMS detector, the so-called data scouting and data parking [92]. Data scouting uses significantly reduced HLT thresholds and stores an incomplete event information with a trade of very high data rates. Data parking involves storing large amounts of raw detector data collected by algorithms with reduced trigger thresholds to be processed later. Both approaches were already available for Run 1 and Run 2, however, benefiting from the overall advancement in technologies, and the adaption of parallel processing, they have been used more widely in Run 3. This in turn has allowed to explore phase-spaces otherwise unavailable at the CMS detector. This Thesis has not directly benefited from data parking or scouting, however, it would benefit by any improvements in the techniques of object identification available thanks to the unique datasets.

3.3.8. Detector Control and Safety System

Having the right detecting material alone is not sufficient to gather high quality physics data. We need to be able to control the detector in an optimal, reliable, and safe manner, starting from “turning it on/off” to optimising its performance. The main goal of the DCS is to bring the detector in a state, where it can collect physics data, while the DSS is responsible for protecting the detector and its equipment from various hazards. In the CMS experiment, these two systems are separated while they often share data from the same probes.

The DSS is a self-contained system, that uses hard-wired probes controlled by programmable logical controllers (PLCs) that can quickly act on observed data, e.g. by interlocking the power supplies. The system is designed to keep the detector safe, however, it is achieved in a quick and foolproof way which often is harsh on the electronics. Therefore, a software-based safety layer is implemented with safety thresholds that would allow for a safe detector shutdown if there are signs of potential hazards. This, however, is achieved by the DCS.

The DCS scope reaches beyond just the control of CMS subsystems, it monitors and controls the experimental hall as well as performs the communication with external systems such as the accelerator. Therefore, it performs the bookkeeping of detector's environment. It also provides a graphical user interface, and, in fact, has to be very user friendly as the whole detector is ran by a small and ever-changing shift crew, out of which a single brave shifter at any given time has to operate the control system. The context diagram of a DCS can be seen in Fig. 3.16.

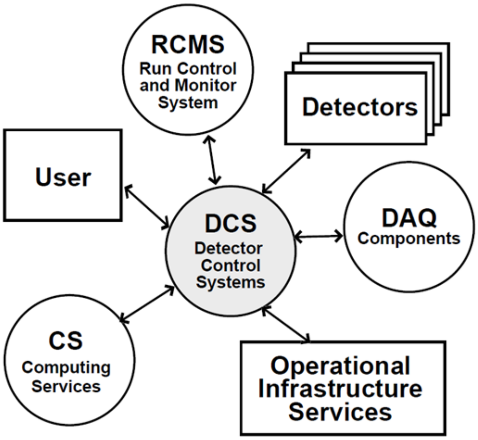

Figure 3.16. The context diagram of a DCS [93].

The DCS brings the detector into a running condition, translating system's high-level commands into low-level actions for the hardware. To streamline everyday operation and reduce human error, the system employs automatic actions as much as possible. However, a great amount of work goes into designing a precise, representative and reliable system. The system is hierarchical and modular, each subsystem can be operated individually, yet it can easily be connected to the central DCS supervisor hierarchy. Running individually allows for easier maintenance, calibration, or even troubleshooting. This is a purely logical structure, implemented only in software, more details are given in Chapter 5.

3.3.9. Phase-II Upgrade and the MIP Timing Detector

Just as the accelerator machine will enter its Phase-II, all detectors will undergo serious and ambitious upgrades to get the most out of the HL-LHC and the opportunities it will bring. The CMS and ATLAS collaborations will perform the majority of detector upgrades in the LS3, while for ALICE and LHCb collaborations the severe detector upgrades are planned for the LS4. With increasing luminosity, an increase of simultaneous collisions is expected. PU of 200 is anticipated, and to tackle the challenges originating from this increase, the CMS detector will have a higher geometric coverage and higher resolution and granularity. Moreover, it will use precision timing and support higher data rates. Existing detectors will evolve, new ones will be built (are being built), and several improvements in the read-out systems, such as the L1 trigger, are also expected.

An increase in luminosity brings an increase in radiation damage. Therefore, the current tracker system will be replaced by a radiation hard two part system (inner tracker and outer tracker) capable of dealing with the high hit rate [94]. The detector will be extended in the forward direction covering $2.5 < |\eta| < 4.0$. Overall, a simpler layout is expected for the outer tracker, while the inner tracker will have inclined modules, which will allow for a reduced material budget. To extend the triggering capabilities, in Phase-II the tracker will contribute to the L1 trigger.

Just outside the outer tracker will be a new detector for CMS Phase-II, which will provide a completely new capability for the CMS – precision timing for MIPs [4]. The MIP Timing Detector (MTD) is expected to provide timing resolution for single charged tracks of 30 ps to 40 ps resolution at the start of operation, degrading due to radiation damage to 60 ps to 70 ps by its end-of-life. It will also contribute to charged hadron identification. As part of this Thesis is dedicated to work related to the MTD, it is described in more detail further in this section.

The calorimeters will split into separate barrel and endcap systems, with the new High Granularity Calorimeters (HGCAL) in CMS's endcaps. These will be impressive imaging calorimeters that will provide the opportunity to study the jet substructure, long-lived particles, and not only. Moreover, there is a very ambitious plan to use the endcap region for triggering. Although HGCAL will be under super harsh conditions dealing with huge PU, several advancements in the trigger strategy and the overall design of the subdetector is expected to facilitate event triggering. The HGCAL will combine layers for the electromagnetic calorimeter and layers for the hadronic calorimeter. The high granularity will be achieved by hexagonal modules based on Si sensors in high radiation regions and scintillating tiles in low-radiation regions. It will be a cold system, maintained at $-30\,^\circ$C, covering $1.5 < |\eta| < 3.0$ [95]. The electromagnetic parts will use Pb, Cu and Cu-W absorbers while in the hadronic parts the absorber layers will be made out of steel.

Of course, the remaining calorimeter in the barrel region will also undergo several changes, mainly to increase the crystal granularity, improve readout, and upgrade the laser monitoring system [96]. By upgrading the front-end electronics they will achieve an increased time resolution.

The muon systems are planning to update their readout electronics, both for the front-end and the back-end. For example, the upgraded RPC's electronics will allow to lower the time resolution down to 1.5 ns. The main focus of the Phase-II upgrade for the muon system is the forward region. Consequently, the coverage will be extended to $|\eta| = 3$ by installing additional chambers. The upgrade will provide improved RPC stations, and three new GEM stations [97]. Although not described in detail here, the muon systems is planning to undergo a complex upgrade procedure.

Quite impressive changes are expected for the Data Acquisition (DAQ) system, especially the connected trigger system [98]. The L1 trigger will have more complete information available having track information from the tracker while keeping the latency to no more than 12.5 µs. It will be able to trigger on displaced muons and long-lived particles. Moreover, the L1 trigger is expected to have complex layers able to run several advanced algorithms, including but not limited to ML algorithms for particle identification and reconstruction. Regarding the HLT, an increased output of 7.5 kHz is expected.

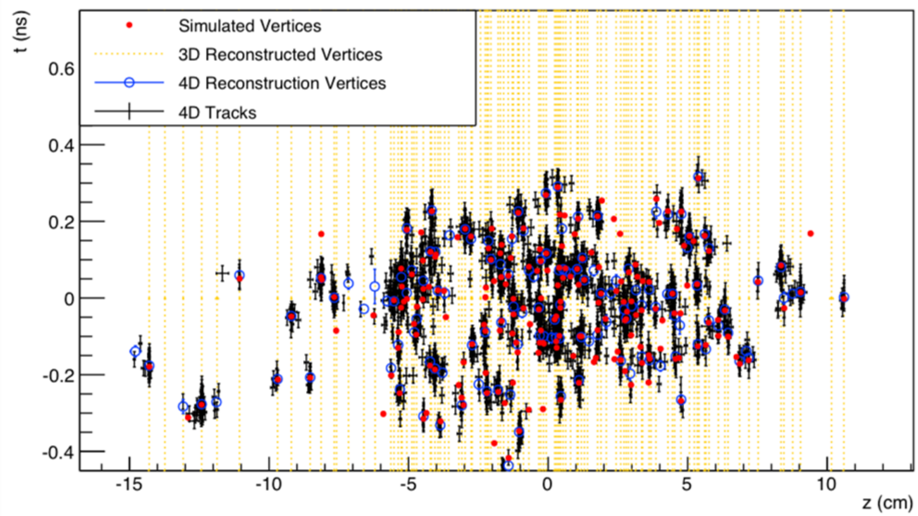

Figure 3.17. Simulated and reconstructed vertices in a bunch crossing with PU of 200 assuming a MTD with 30 ps time resolution covering the barrel and endcaps [4].

Going back to one of Phase-II newcomers, MTD's main goal is to provide precision timing for charged particles, thus allowing to mitigate the PU. A great example of this is shown in Fig. 3.17, where both the spatial and the time coordinates are shown for a bunch crossing. As LHC proton bunches are not exactly point-like, collisions that can happen during a bunch crossing are spread over time with a root mean square close to 200 ps. Therefore, additional timing information can help unravel the complex aftermath of collisions taking place. Assuming a track-time reconstruction efficiency of 85 %, the MTD could halve the wrong track associations [4], thus the reconstruction conditions would be closer to Phase-I operations.

The MTD will help with particle identification, both indirectly and directly. The MTD indirectly helps by increasing the efficiency of PU track removal from particle isolation cones which will help with isolated lepton identification. However, the MTD will also have a direct impact, as the layers will provide time-of-flight measurements, thus allowing for improved charged hadron identification. The MTD will consist of two systems – the barrel timing layer (BTL) and the endcap timing layer (ETL), as can be seen in Fig. 3.18. To mitigate the dark current and to increase the signal over background ratio, the detector will be cooled to around $-30\,^{\circ}\mathrm{C}$ using a two-phase CO_2 flow. Due to the geometry, both systems are experiencing different levels of irradiation, and have converged on using different sensors and other solutions to deal with possible complications.

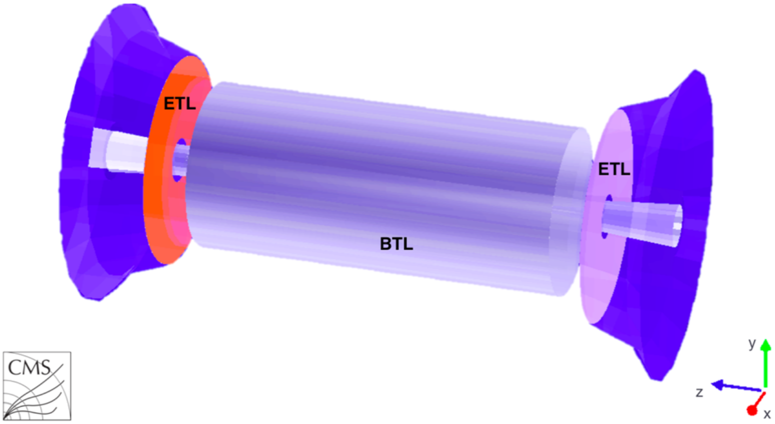

Figure 3.18. A schematic view of MTD's geometry, showing its barrel and endcaps part [4].

The BTL will be a single-layer, cylindrical detector covering $|\eta| < 1.48$ squeezed within the 45 mm gap between the outer tracker and the ECAL at a radial distance of approximately 1 m from the beam axis. The expected timing resolution per track is 30 ps to 65 ps. It will use LYSO:Ce scintillating crystal bars and a SiPM readout on both ends. 16 elongated crystals form an array and two arrays form a BTL detector module (DM) which is encased in a copper housing. Additional cooling of the SiPMs is achieved with thermoelectric coolers (TCs). Twelve DMs form a readout unit, six readout units form a tray and all together 72 (two in the z times 36 in the ϕ direction) trays comprise the BTL. The layout is an optimisation between covering a large area, not clustering it with service channels, and, of course, cost [99].

As noted, TCs are used to cool the sensors, as one of the main challenges for the SiPMs is the increase of the leakage current with increasing radiation dose. This will also be tackled with dedicated annealing in between the periods of data-taking. The generated heat will be carried away via thin `316L` low carbon steel tubing containing the two-phase CO_2 flow. Moreover, the MTD will share the cold volume with the tracker.

For the forward region a different approach is chosen. The ETL will be a two disc system placed in both endcaps, thus allowing for up to two hits per track. It will cover $1.6 < |\eta| < 3.0$, and is expected to be less than 99 mm thick, siting on the HGCAL's nose. The ETL consists of low gain avalanche diodes (LGADs) as sensors, grouped in 16×16 arrays, bump-bounded to a designated chip. The expected timing resolution per track is 35 ps. This is mainly achieved with the doubled layers and a different sensor solution which is more radiation hard. Here, the timing degradation is combatted with higher bias voltage for the sensors, however, limitations occur due to spark damage.

It is foreseen that the ETL will be serviced in between running periods, while the BTL will most likely lack such a luxury. Therefore, the design and operation solutions have to be thoroughly thought out. An effective control and safety system will be absolutely crucial for effective operations.

3.4. Summary

This chapter described the unique experimental environment this Thesis benefits from. The CERN's accelerator complex with its crown jewel the LHC was introduced, thus explaining where the *pp* collisions take place. Afterwards, the CMS detector with all its subdetectors was presented, not only characterising its current status but also future upgrades. This chapter has allowed to get accustomed to the many acronyms of CMS, also including its coordinate system.

The next step is to translate the performance of the CMS detector into reliable physics objects such as charged leptons, photons, jets, and MET. Therefore, the following chapter details the reconstruction algorithms and calibration procedures used in CMS. These procedures transform detector-level information into physics objects suitable for analysis, allowing the ingenuity of the detector and all its upgrades to shine through.

4. PHYSICS OBJECT RECONSTRUCTION AND IDENTIFICATION

As particles have traversed the CMS detector, leaving their signatures in different layers, and the trigger system has selected this event as potentially interesting, the whole detector information can be used to interpret these signatures as “physics objects”. Low-level objects such as tracks and energy clusters are correlated to form high-level objects such as electrons or muons, which in turn can be grouped to build even more complex objects, such as jets. This chapter will focus on electrons, muons, jets and MET (carried away by neutrinos) as they are important for the $HH \to WW^*ZZ^*$ analysis described in Chapter 6; however, with data collected by the CMS detector it is possible to reconstruct also other physics objects, e.g. photons.

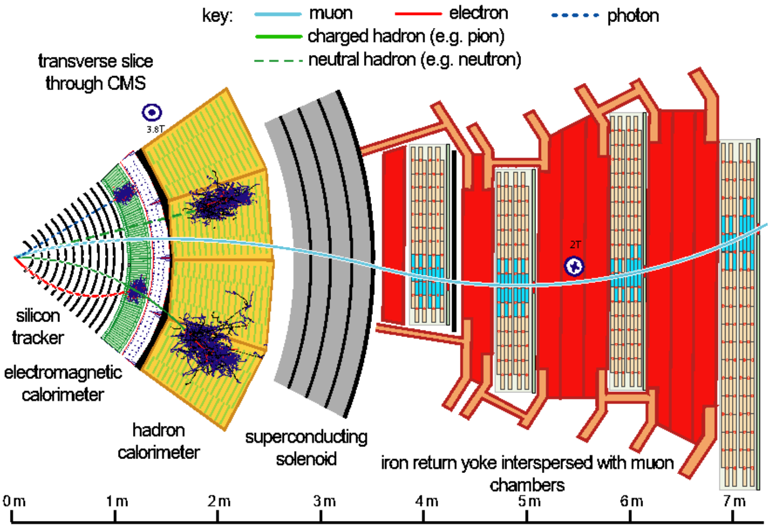

Figure 4.1. Several particle interactions and typical signatures in a transverse slice of the CMS detector’s sector [100].

In Fig. 4.1, a slice of the transverse cross section of the CMS detector is shown, highlighting various physics objects and their typical signatures. Muons traverse the entire detector and often escape it altogether, however, as charged particles they leave signal in the traversed silicon tracker layers and the muon chambers. These signals or hits can be grouped to form tracks that mark their trajectory and are used to extrapolate to their origin or vertex. Electrons leave hits in the tracker and are absorbed in the ECAL, thus the main information for their reconstruction is provided by the ECAL. Both charged and neutral hadrons lose part of their energy in the ECAL and are absorbed in the HCAL. Photons leave no mark in the tracker while they are absorbed in the ECAL. Finally, neutrinos escape the detector undetected. However, their energy can be estimated by the

MET. In hadron colliders, it is common to talk about jets – hadronised quarks and gluons, manifesting in cone-shaped objects, inclusively measured by the calorimeters. However, to deduce the origin or content of the jet, e.g. a b quark, information from the tracker is needed, as hadrons containing b quarks tend to have a longer lifetime, thus producing a more displaced SV. Such information allows to tag if the jet has originated from light quarks, or from c or b quarks.

The CMS uses the particle flow (PF) approach [100] which correlates the signal from all subdetectors to create an improved event reconstruction. As mentioned before, its low-level reconstruction objects are charged particle tracks in the tracker and energy clusters in the calorimeters. This holistic approach has enabled CMS to deliver such great results.

The reconstruction starts by finding charged particle tracks and vertices. A combinatorial track finder (CTF) based on Kalman filtering (KF) [101] is used to reconstruct the tracks in three stages: the generation of track seeds, the recognition of tracks and the fitting of the tracks. Good tracks have marked at least two consecutive Pixel layers, have at least eight hits in total, and miss no more than one hit along the way. The CTF is applied iteratively starting with seeding the tracks most compatible with the primary vertex (PV) and highest goodness-of-fit value. When the reconstruction is completed for a track, its hits are masked to avoid double counting and the CTF is applied again with loosened requirements for seeds. Incoming particles can interact with the detector material altering their initial trajectory or producing SVs. A dedicated algorithm is applied to link common secondary particle tracks to find SVs within the tracker volume. The track reconstruction efficiency for charged pions above 1 GeV is around 70 % to 80 %, while for isolated muons it is around 99 %. Increasing reconstruction efficiency while keeping the misreconstruction rate low is critical for the overall PF event reconstruction, as charged hadrons misreconstructed as neutral could cause serious degradation in jet reconstruction.

Similarly intricate is the calorimeter clustering algorithm which not only detects and measures the energy and direction of photons and neutral hadrons, separates neutral particle energy deposits from charged particle deposits, reconstructs and identifies electrons and their accompanying bremsstrahlung photons, but also measures charged hadron energy. The energy clustering is performed separately in the barrel and the endcap region, and is carried out in three steps – finding the seeds, assembling topological clusters, and finally, reconstructing the energy cluster. Cells with energy deposits surpassing a given threshold are identified as the seeds for an energy cluster, while topological clusters are created by aggregating several neighbouring cells. Then a Gaussian-mixture algorithm is used to reconstruct energy clusters within topological clusters. Finding many energy clusters within a topological cluster, is typical for a hadron shower.

After successful reconstruction of tracks and clusters, they are passed to a linking algorithm to test any pair of elements to form a physics object. First, muon candidates are built, and their corresponding hits are masked in the following steps. Second, electron candidates and their emitted photons are built, their tracks and energy clusters are masked.

Finally, hadrons from jet fragmentation and hadronisation and non-isolated photons are reconstructed. Particle object reconstruction and identification in the CMS experiment is a well tested and trained set of algorithms, however, a non-zero probability of misreconstruction or misidentification exists. This is checked by an event post-processor which uses anomalously large MET as one of the probes. The algorithm has undergone several stages of improvements, increasing its robustness and reliability, however, minor errors can be brought in by cosmic muons traversing the CMS, a wrong association of inner and outer tracks, muon decay in flight, or simply particle misidentification.

4.1. Muon Reconstruction and Identification

Due to the design of the CMS detector, muons can be identified and reconstructed with high efficiency through the full acceptance of the detector, because other particles are absorbed before the muon stations. To further improve the efficiency of muon identification up to 99 %, three reconstruction methods are used forming standalone, global, and tracker muon candidates [102]. "Standalone" muons are reconstructed using hits within only a DT or a CSC as seeds and then hits along the potential trajectory from all DTs, CSCs, RPCs (and GEMs) are used by a KF to propose and characterise a trajectory. "Global" muons are formed when each standalone muon track is matched to a track in the inner tracker. They are built "outside-in". For muons with high transverse momentum, this definition is more efficient than just the standalone definition. Lastly, the tracker muons are reconstructed from hits in the tracker and extrapolated to look for at least one compatible hit in the muon system. They are built "inside-out". Therefore, the tracker muon definition is more suitable for low-momentum muons. When the tracker and the global muon candidate tracks match in the inner detector, they are merged to save only one definition of the object. If a muon is reconstructed only as a "standalone" muon, it is considered lower quality and rarely used in physics analyses.

Hits associated to the muon candidate allow to reconstruct its properties. For example, to determine muon momentum Tune-P algorithm [103] is used with several refits taking information from several parts of the track and evaluating their goodness-of-fit. The highest quality fit that reduces the transverse momentum imbalance is chosen. To distinguish between prompt muons and muons that come from weak decays (being part of a jet), an isolation criterion is defined, where the transverse momentum of the muon is compared to the total energy in a geometrical cone surrounding the muon. The track based approach sums the reconstructed tracks within the cone while the PF approach uses information from charged and neutral PF candidates within the cone. The typical cone size is $\Delta R < 0.4$, however, it can be varied, as an example, depending on the transverse momentum of the muon.

Moreover, muon object quality is characterised with its track's fit – hits per track, the alignment, and fit quality, allowing to create an identifier (ID) ranking that balances between efficiency and purity. Several working points (WPs) are defined: loose, medium, tight, and soft, and high momentum muon ID. As an example, medium muon ID is designed to identify prompt muons from the PV as well as muons coming from flavour decays. It is tuned to have an overall efficiency of 99.5 % for muons originating from W or Z boson decays [102]. The muon candidate is selected by the PF algorithm and is either a tracker or a global muon. By having requirements on segment quality and goodness-of-fit, it aims to keep the misidentification of charged hadrons as muons as low as possible.

4.2. Electron Reconstruction

As electrons can interact with the tracker material, an incoming electron might emit bremsstrahlung photons which have a high probability to convert into an electron-positron pair. Thus, by the time the primary electron reaches the ECAL it may no longer be a single particle, but rather a shower of several electrons and photons. The energy deposited by electrons and bremsstrahlung photons is grouped into ECAL superclusters, and dedicated algorithms are used to combine clusters to recover the energy of the primary electron. Additionally, the energy lost as a result of the bremsstrahlung photons is taken into account. Simulations predict that in high-η regions the photon conversion before the last tracker layer is as high as 60 % [104]. Moreover, if the photon direction is tangent to the electron track, a link is created in the data reflecting it.

The electron reconstruction algorithm can be ECAL-based or tracker-based. Previously mentioned ECAL superclusters are used as track seeds in the ECAL-based track reconstruction approach. However, this method is effective only for well isolated electrons with high transverse energy. For electrons in jets or simply low-momentum electrons the tracker-based seeding is used, where tracks are used to look for compatible ECAL superclusters. In either case, the electron track parameters are found using Gaussian sum filters (GSF) [105] as these better account for the lost energy via bremsstrahlung. As an example, the electron charge (thus, if it is an electron or a positron) is determined by the sign of the curvature of the GSF track.

Electron candidates are constructed associating the GSF tracks with the ECAL superclusters. A dedicated boosted decision tree (BDT) [106] is trained to characterise the quality of associated objects – it combines track information, supercluster observables, and specific matching variables. Reconstructed electron candidates are required to pass a loose ID criterion to ensure high identification efficiency for genuine electrons. Otherwise, photons and hadrons within jets could be wrongly associated causing serious mismeasurement. A dedicated BDT is used to classify electrons. These algorithms can be trained for isolated or non-isolated electrons and take into account various tracker-related variables, shower-shape variables, as well as ratios of them. It can be based either on a set of sequential requirements or on a multivariate algorithm (MVA) discriminant.

Similarly as for muons, isolation criteria can be used to distinguish between prompt and background electrons. The sum of the reconstructed energy within a cone around the electron is compared to the electron's energy. Usually $\Delta R = 0.3$ is used and a veto region within the cone is defined to exclude the electron's contribution. Additionally, the narrow shape of the electromagnetic shower in the ECAL can be used as a discriminant against electrons coming from jets. An absence of hits in the innermost layers of the tracker help to reject electrons coming from photon conversion.

Electron energy is corrected as systematic variations of the energy measurements are present in the ECAL either due to the lost shower leakage, intermodule gaps, or simply detector ageing. An MVA technique is used to correct the energy estimation. Also, the energy scale and smearing are corrected on the basis of the comparison between the data and the simulation.

4.3. Jet Reconstruction

Quarks and gluons produced in the collisions undergo a fragmentation and hadronisation process within the detector, resulting in the generation of a collimated spray of particles termed a jet. Jets are reconstructed with the anti-$\mathrm{k_T}$ algorithm [107] that clusters PF candidates within a specific distance parameter. It is collinear and infrared safe. Collinear – a narrowly splitting particle does not create a new jet, and infrared safe – radiation at low momentum does not produce new jets. The algorithm operates with the distance between entities, e.g., particle candidates or anti-$\mathrm{k_T}$ pseudojets, d_{ij}, defined in Eq. (4.1), and the distance between the entity candidate and the beam, d_{iB}, defined in Eq. (4.2):

$$d_{ij} = \min(k_{ti}^{2p}, k_{tj}^{2p})\frac{\Delta_{ij}^2}{R^2}, \tag{4.1}$$

$$d_{iB} = k_{ti}^{2p}, \tag{4.2}$$

where $\Delta_{ij}^2 = (y_i - y_j)^2 + (\phi_i - \phi_j)^2$, k_{ti} is the transverse momentum of the particle i, y_i is the rapidity of the particle i, ϕ_i is the azimuth of the particle i, R is the radius of the jet, and p is the relative power of the energy versus the geometrical scales. By default, in the anti-$\mathrm{k_T}$ algorithm $p = -1$. This allows to build jets around the hardest particles. The algorithm iteratively identifies the smallest of distances, if the distance is between two entities, then they are recombined into a new pseudojet, while if the distance is with the beam, the entity is called a jet and removed from the algorithm. In the end, no entities are left. From the analysis standpoint, the distance parameter R can be varied to consider wider or narrower jets. This is denoted in their object name, for example, AK4 jets have a distance parameter of $R = 0.4$.

Several techniques are applied before jet clustering to mitigate the PU contribution when forming jets [108]. One technique is the charged hadron subtraction (CHS) [100], which excludes charged particles associated with PU vertices based on tracking information. In this method, the neutral particles originating from the PU are mitigated only by applying an event-by-event jet-area-based correction. Another is the pileup per particle identification (PUPPI) algorithm [109], which builds on the CHS method. It uses local shape information, as well as tracking information, to add a weight corresponding to the probability that the particle has come from the PV which is used to reweigh the four-momentum of each candidate. The recommended jet collection has changed between Run 2 and Run 3. In Run 2, it was AK4+CHS while for Run 3 – AK4+PUPPI.

The kinematic differences between leptons coming from the electroweak decay of Z and W bosons, and jets allow to use lepton isolation as a great handle for selecting prompt leptons and rejecting leptons in jets produced from decaying hadrons. The isolation is quantified by estimating the total transverse momentum of particles emitted around the direction of the lepton. Therefore, ΔR region around an object candidate is used by multiple algorithms.

The CMS apparatus allows to identify whether the jet forms from the hadronisation of a heavy-flavour quark such as b, c or light-flavour quarks such as u, d, s. Hadrons containing b quarks have a longer average lifetime than their light-quark peers, thus can travel longer distances within the detector, producing a further-displaced SV. Moreover, on average, b quark jets will have a higher number of associated tracks. This property has been used to design several classifiers that can tag the jet origin, such as the `DeepJet` [110], that considers the full information of all jet constituents, charged and neutral particles, and even global parameters such as the number of vertices.

The jet energy scale and resolution corrections are derived from simulation studies to correct the average energy of a jet to the truth-level jet. The corrections also account for PU and non-linearity in the detector response. As jet momentum is calculated as a vectorial sum of all particle momenta within a cone, it is a good but not perfect estimate of jet's momentum; thus, several corrections are applied sequentially. First, the PU offset is subtracted, second, the detector response is corrected from simulations, and third, residual corrections are applied to minimise the differences between the data and simulation. Finally, optional jet flavour composition corrections can be applied. Each of the corrections can be seen as a reweighing of jet constituent's momenta, therefore, the corrections are usually binned in energy density, jet area, transverse momentum, and pseudorapidity.

4.4. Missing Transverse Momentum Reconstruction

Thanks to momentum conservation and the fact that in the transverse plane it is zero before a collision, it is possible to estimate the energy carried away by particles that do not interact with the CMS detector, such as neutrinos. It is done by reconstructing the MET by vectorially summing the transverse momenta of the reconstructed objects and then accounting for any jet energy corrections needed to be applied on top, as shown in Eq. (4.3). Any imbalance is seen as MET.

$$\vec{p}_T^{\,miss} = -\sum_{i}^{N_{particles}} \vec{p}_{T,i} - \sum_{j}^{N_{jets}} (\vec{p}_{T,\,j}^{\,corr} - \vec{p}_{T,j}) \tag{4.3}$$

4.5. Event Simulation with Monte Carlo Generators

MC simulations are the backbone for signal and background modelling, event selection and optimisation, as well as the development of various methods. These simulations reproduce the whole chain of particle collision, starting from parton level interactions until a complete detector response. Thus, allowing for a quantitative comparison between theory with controlled assumptions and the beautifully random and real experiment.

At first glance, particle collisions might have a simple structure, yet we rarely are talking about just a few final states, and the necessary calculations stack up. The MC event generators help with the calculations, dividing them into consequential steps. Their goal is to use computing power to generate events to such a detailed level as could be observed by an ideal detector. As particles behave probabilistically, meaning, individual outcome cannot be precisely predicted but patterns emerge statistically over many observations, generators sample all relevant variables according to the desired probability distributions, thus ensuring randomness in the final event.

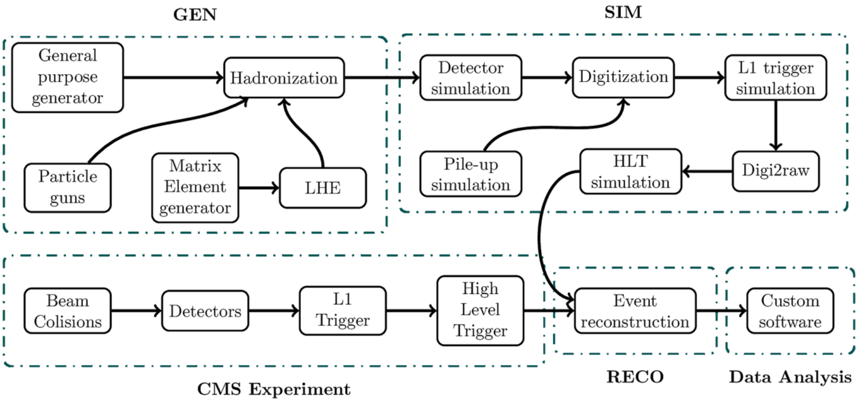

Figure 4.2. The main steps in the production chain of simulated data [111], following event generation (GEN), simulation (SIM), and reconstruction (RECO).

The main steps of production of a CMS dataset are summarised in Fig. 4.2, showing the steps for a MC simulation at the top and for data at the bottom. The MC simulation starts with generating the beam collision, then undergoes simulation of the detector and its electronics, and finally, the event reconstruction. Afterwards, the output data can be analysed. These production steps are further detailed below.

The event generation begins with the simulation of the hard scattering process of the incoming partons (quarks or gluons) from each proton that produces outgoing partons. The probability of the given interaction is computed from matrix elements and can be done with various precision. The LO calculates basic tree-level interactions, the NLO includes one-loop correction, and each "Next-to" adds another level of correction. Generally, higher order corrections improve the agreement between theory and data. However, they are more computationally heavy.

A multitude of dedicated generators are available and customisable for various calculations. A few examples are the `MadGraph5 amc@NLO` [112], `Pythia` [113], `Powheg box` [114]. The `Pythia 8` is a general purpose MC event generator, implemented in C++, but also available with a Python interface, which provides models for the evolution of particle interaction, starting from hard scattering to decaying into complex final states. Although it provides results only in LO precision, it is widely used to simulate events in various colliders. The `MadGraph5 amc@NLO` can generate multi-parton matrix elements in LO or NLO. The `MadGraph5` part performs the hard scattering, while the `amc@nlo` focusses on matching and merging these events to parton showers. It is a great choice for complex final states and also has a Python interface. The `Powheg` produces NLO level events with only positive weights and interfaces them with parton showers. The `Powheg box` is a framework that automates the process of implementing the `Powheg` method for different processes, such as `ggHH` [115].

Generators need specific input data. As the momenta of quarks and gluons inside the proton are not constant over time, they can be described by PDFs which characterises the probability of finding a parton with a certain momentum at a given scale. These functions have been derived for various applications, e.g. targeting pp or other types of collisions, for experiments at the LHC or at other machines. They range in data sets, fit methods, uncertainty treatments, and overall usage. The uncertainty of a PDF must be propagated to the final result, therefore, it needs to be well understood. In the case of `Pythia`, "tunes" are used to fit the experimental data. These are a set of conditions for various processes like parton showering, hadronisation, and underlying event modelling. Often they are tied to a specific `Pythia` version and have target experiments. Both PDFs and tunes used for the generation of the MC samples used in this Thesis are summarised in Section 6.3.

After the hard scattering, the outgoing coloured partons undergo parton showering. The radiation process is complex and includes both the initial-state radiation (ISR) and final-state radiation (FSR). The first emits radiation before the hard scattering, while the second radiates gluons which in turn form jet-like structures. This is a crucial step often performed by `Pythia` or `Herwig++` [116]. Generators have various hadronisation models which can either use string or cluster modelling. At this level, the particles are called "generator-level" or even more poetically as "truth-level" particles, as afterwards they meet the "reality".

Alongside the primary hard interaction, additional or overlapping events can take place. The most intuitive are simultaneous soft scatterings or simply beam remnants. Moreover, as mentioned in Section 3.3, there is a multitude of simultaneous collisions taking place each bunch crossing, the PU. It is modelled and included in the simulated sample. This contaminates object reconstruction, therefore, its modelling is crucial. Usually, minimum-biased events are overlaid onto the primary MC event. The PU distribution is scaled to match the PU profile observed in the data.

The next processing step involves understanding how such an event would be seen in the detector. This is done by the `Geant4` [117] passing the event through a model of the CMS detector. The model outputs a raw detector-like response. The `Geant4` simulates the passage of particles through matter, meaning it models energy loss through ionisation, bremsstrahlung, and showering, and it also tracks the particle as it traverses various layers through the CMS's magnetic field, and can simulate detector-specific properties, such as the resolution and response time, and the pulse shape for various sensors. After the modelling, the response is digitalised by introducing electronic noise and other detector response limitations to mimic the raw detector output. Clearly, the modelling is very time consuming as the CMS model needs to be very precise and reflect the exact detector geometry, its material budget, and operations. However, for quick studies, fast simulations can be performed rudimentary simplifying the geometry at the price of time and accuracy.

Finally, the "raw detector response" is fed through the standard CMS reconstruction chain just as the real data. This means emulating the L1, then HLT, reconstructing tracks, clustering calorimeter energy deposits, employing PF and identifying objects. The beauty of simulated data is that the generator-level or the truth-level information will always be available, thus allowing to validate or simply to compare object reconstruction, event categorisation, to dig into the origin of the particle and much more.

Many of these steps can be performed using the CMSSW, where each version already contains a predefined version stack of external packages, `Pythia` tune and PDF set support, and calibration and alignment constants. Specific global tags indicate the ideal intent for each version. Moreover, the CMS experiment uses custom data formats that are based on `ROOT` trees, and specific CMSSW versions support specific data formats. Overall, the file formats range from analysis object data (AOD) (and contain complete reconstruction information) to NanoAOD (skimmed, light, and the current *industry standard*) [118].

Clearly data processing and production is a computationally intensive task, therefore, various ideas on how to cleverly reduce the computational complexity have been developed, starting from not saving seemingly uninteresting events, optimising the processing or carefully deciding on how detailed simulations are needed. As an example, it is possible to generate an inclusive MC sample, one spanning the full kinematic coverage, while it might be useless to populate the phase-space outside the detector's fiducial space. In contrast to the inclusive samples, one can generate just a slice of the inclusive phase-space, better populating scenarios where the inclusive sample would need to be gigantic to sufficiently cover it. In such a case, attention would need to be made not to overlap the samples when merging multiple of them together.

Overall, very little of this all could be possible without the infrastructure of the Worldwide LHC Computing Grid (WLCG) [119], where a network of hundreds of computing centres across tens of countries, analyse, distribute, extract and process all the collision data and simulation. It is a distributed and tiered solution, where Tier-0 is CERN's Data Centre, which deals with initial raw data storage, some prompt reconstruction and distribution to Tier-1 centres. Tier-1s store tape backups, do large-scale reprocessing and distribute to Tier-2s, which mostly provide resources to end-users, deals with MC production and smaller reproduction. Finally, Tier-3s are the smallest entities dealing with very specific tasks for groups or individuals. Overall, this grid allows for great functionality as it provides easy access to the distributed data without the need to know the exact location of the file. It additionally servers as a middleware for job scheduling with `CRAB` or `HTCondor`.

4.6. Summary

This chapter was dedicated to physics objects reconstruction and identification. As detecting an electronic signal in a detector's layer is just one of many sequential steps needed to characterise a particle collision. It introduced the overall approach used in the CMS of particle detection, the PF. Then described how leptons, jets and MET are reconstructed in the detector. These physics objects will be crucial for the Thesis analysis. Finally, event simulation was introduced to complement the experimentally gathered data.

As the LHC progresses toward higher luminosities, maintaining the performance of physics object reconstruction becomes increasingly demanding. Therefore, detector upgrades and associated technical developments are essential to preserve reconstruction efficiency and resolution under challenging operating conditions, described in the previous chapter. Thus, the next chapter presents the technical work undertaken as part of this Thesis, focussing on the development and operation of control systems for a MTD test-stand in preparation for the Phase II CMS detector upgrades.

5. BUILDING A DETECTOR CONTROL SYSTEM FOR THE MTD TEST-STAND

As mentioned in Section 3.3.9, the MTD is one of the new detectors currently under construction for the HL-LHC era at the CMS detector. It will provide high-precision timing information, crucial for unravelling the complex collision aftermath provided by the upgraded accelerator complex. Logically it can be divided into two parts – the BTL and the ETL. Due to the different experimental challenges, both parts have adapted different technical solutions, thus, each will have a different set of commands and different evaluations of states to define when the apparatus is in a safe state for physics data-taking. However, it is foreseen that the MTD will have a shared DCS, logically partitioned to represent the hardware differences. Such an approach is common in the CMS experiment.

With increased attention to upgrade activities and the approaching LS3, it has been high time to work on the prototype for the MTD's DCS, constructing and testing various aspects of it. Therefore, a DCS was built in full compliance with the requirements of the CMS Central DCS team for one of the MTD test-stands, designed for testing of a full-size BTL tray. Although with limited functionality, it serves as the first prototype for the final MTD's DCS, and, moreover, facilitates data-taking vital for a successful development, assembly and commissioning of the BTL.

This chapter describes the extensive work on the prototype, which was the main priority during the first half of the Thesis studies. Although the control system is built for a test-stand, it is nonetheless denoted as a DCS. Section 5.1 describes the philosophy of CMS DCS architecture to later highlight the similarities and future developments of the created DCS. Section 5.2 introduces the test-stand noting what is being controlled and monitored, while Section 5.3 summarises its functional requirements and limitations. Section 5.4 notes its overall architecture and specific implementation details, while Section 5.5 summarises the project's prospects.

5.1. Building a DCS at the LHC

To embrace the challenges posed by working within a large collaboration, the Joint Controls Project (JCOP) was created in the end of 1997 to address the common aspects of the DCSs of the LHC experiments [120]. This allowed for a more efficient development, management, and maintenance of control system related aspects. It was agreed to use the supervisory controls and data acquisition (SCADA) development environment, and `WinCC OA` (initially called `PVSS`) as the main development tool. `WinCC OA` is a well-established, robust commercial solution that already supports basic functionalities and has potential for future development. It provides connectivity to databases, networks, and hardware, as well as offers tools for building a graphical user interface, amongst other key functionalities. Within `WinCC OA`, process variables are represented as data points that can be organized in structures called data point types, allowing to build customised representations. With the help of the JCOP, various technology standards were agreed on, such as communication protocols, the choice of standard PLCs and standard field buses. In addition, a CERN-wide JCOP framework was created to provide a set of guidelines, dedicated tools, and sets of common software components for controlling devices. A well-designed and packaged component not only reduces the development effort, but also hides the complexity of the underlying tools.

It was agreed to use the Finite State Machine (FSM) concept. The FSM toolkit builds on the State Manager Interface (SMI) built for one of LEP experiments, DELPHI (DEtector with Lepton, Photon and Hadron Identification) [121]. It allows to approximate the system in logical objects that behave as a finite state machine, meaning the system can be in only a finite number of states at any given time. In each state, it can accept commands that trigger actions and possibly lead to a change of state. The system is organised in a hierarchical structure and forms subsystems that fit logically together [122], and with its nodes allow for integrated controls. There are two types of nodes – device units (DUs) and control units (CUs). DUs are capable of driving the corresponding equipment or hardware devices, while CUs correspond to a logical object that behaves as an FSM. In general, states flow up and are summarised by each next level, while commands flow down, as shown in Fig. 5.1.

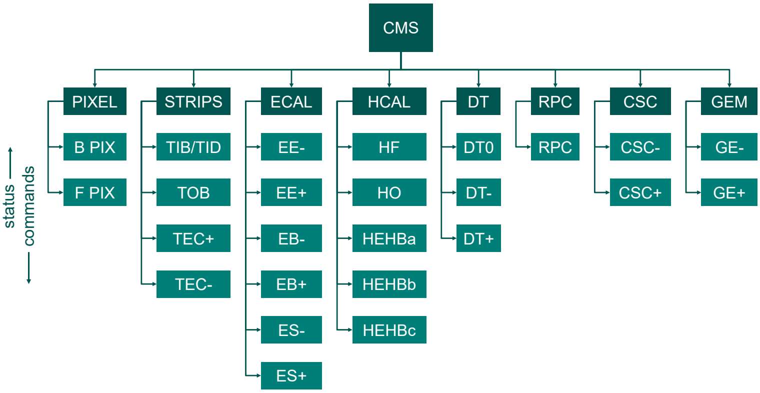

Figure 5.1. CMS DCS FSM tree showing the top supervisor node for physics data-taking, as well as two more layers of nodes representing subdetector DCSs. This is not a complete representation as each subsystem has more nodes in the lower levels.

One of the main strengths of an FSM tree is its complete automation. Actions provide a mechanism for routine procedures, thus making them more efficient and less error prone. The FSM tree allows for more intuitive error handling and detection. As it is rule-based, the recovery from a known problem can be automated or altogether avoided in advance.

It starts bottom-up and each subsystem is tasked to recover its own errors, thus best handling their DUs, their equipment. This allows the error recovery to be scalable and asynchronous.

In the top level, the FSM can have one of the four states:

- ON: when the system is ready to collect data.
- STANDBY: the system is partly ON but not ready to collect data. This could, for example, mean that a part of the detector has the low-voltage components turned ON, but the high-voltage components, e.g., the sensors, are not yet powered.
- OFF: when all parts of the system are powered off.
- ERROR: human intervention is required.

One can provide commands to transition to ON, OFF or STANDBY state, while ERROR is always evaluated. When a higher level node commands to "turn on" the lower level nodes translate the corresponding command into specific actions, and following these actions DUs control the hardware. In return, the states of lower levels are summarised and thus define the state of the upper level.

As already was shown in Fig. 5.1, the CMS DCS's FSM is a hierarchy tree with the central supervisor as the top node. The supervisor is commanded by the LHC state change, thus it can automatically switch ON or OFF. The top node's children are subdetectors with their DCSs. The main CMS supervisor node responsible for physics data-taking is shown together with each subdetector's DCS. For simplicity, only the first level of nodes is shown for each subdetector. Hardware-wise, the CMS DCS computing infrastructure consists of several server nodes with uninterrupted power sources and redundant peers for smooth problem handling. Software-wise, it is organised as an incremental software stack including the `WinCC OA`, the JCOP framework, the CMS framework and detector specific software.

The CMS framework is an extension of the JCOP framework, summarising and centralising CMS-specific functionality. It encapsulates CMS specific redundancy and detector protection mechanism, extends alert handling and display, and automates the set-up of open platform communications (OPC) server tools (these servers act as standard interface to e.g. PLCs or power supplies), and not only. The subdetector specific software includes subsystem specific functionality, device definition and layout. If the CMS framework is maintained by the central team, the subdetector software is maintained and developed by a team in each subsystem, however, if their component is generic enough and could benefit other groups it can be easily shared.

5.2. The Test-stand

Testing and validating is a natural process for any detector system, and many test-stands can exist for one detector. Each test-stand can investigate individual components or the interlink among several of them. The MTD test-stand in question is a full-scale test-stand for a single BTL tray and is located in the tracker integration facility (TIF) at CERN. As mentioned in Section 3.3.9, a BTL tray is the largest subcomponent of the barrel part of the MTD, as 72 trays create the entire BTL. This test-stand was initially created for cooling tests, but has evolved over time to facilitate a wide variety of tests. The research questions to answer include the optimal flow-rate and temperature in various operating settings and tray positions; the power dissipation of the sensing models; the operation of thermoelectric coolers (TCs) in various operating settings; as well as the powering sequence of the on-tray electronics. This test-stand also allows to optimise the final positioning of the probes needed for the DSS system, as well as to find safe operating limits for the tray.

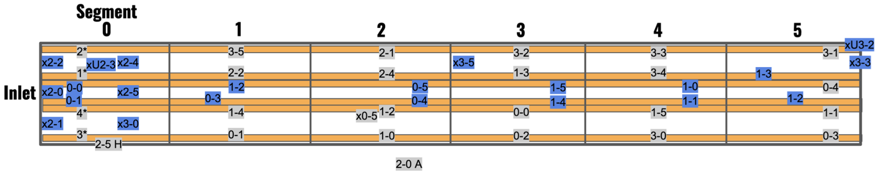

Figure 5.2. A schematic representation of the BTL tray cooling test-stand, indicating the segment numbering, gas inlet, and noting microstrip heaters in yellow. Gray and blue boxes represent a possible layout of various sensors.

This test-stand is a full-size prototype and a schematic representation of it is shown in Fig. 5.2. It is approximately 40 cm wide, approximately 250 cm long and around 40 mm thick, logically it is sectioned into six readout units or segments. It is made of an aluminium plate with etched pathways for steel pipes installed for the CO_2 cooling. The two-phase CO_2 cooling is provided by TIF's CO_2 plants 6th loop, thus making it possible to adjust both the flow-rate and the temperature of the liquid CO_2 with the lowest temperature reaching around $-35\,^{\circ}\mathrm{C}$. The tray can be rotated axially to mimic any tray positions and possibly test for any dry-outs, thus the insulating cover is relatively large; however, it allows to have an enclosed volume that can be flushed with dry air to lower the dew-point and to avoid the accumulation of moisture. In addition, a layer of isolation is applied just on top of the tray, as expected in the design.

In the first iteration of the test-stand, it consisted of only the tray with its cooling network. In the second step, load simulating resistive strip heaters were placed on each segment (six per tray, as can be seen in Fig. 5.2, each corresponding to one readout unit). In the third iteration, the simulating heaters were removed from one segment and replaced with real sensor modules. More precisely, the replacement mimicked one half of the readout unit, consisting of a mock-up concentrator card and a front-end board with pre-series SiPMs and LYSO crystals (a Cerium doped Lutetium-based scintillation crystal). All heaters and modules (and their TCs) were powered by laboratory power supplies, allowing for easy testing. A relay system was attached to cut the power to these supplies if the situation required it.

5.3. DCS Requirements and Design Choices

Several functional, performance, and safety requirements were set for this DCS. Regarding the functional requirements, the very first and most important ones imposed by the team performing the tests were the monitoring and data logging. The average testing sessions span several hours or even days, within which the DCS has to provide reliable, uninterrupted monitoring, and archiving of the probe measurements and environmental data. These data sources are below 100, so not too excessive. The combination of long time periods for the temperature equalisation combined with the importance of being able to record the fast-paced response to the varying environmental conditions calls for the ability to have several data-taking regimes. In addition, an alarm system was needed. This functionality mainly had to inform if the connexion with any of the hardware devices was lost for a prolonged period, exceeding the maximum latency. However, it also provided information on the status of connexion with databases used for data storing. The databases used are not local and are built following the central guidelines. A functionality put in a “wish-list” is the control of the power supplies and the modules. However, this has not been possible in the current test-stand scenarios and is reserved for future evolutions as described in Section 5.5.

Regarding performance requirements, the DCS must be running 24/7 and be able to self-recover after unlikely situations of lost power. The probes need to be read in continuously while the archiving should take place only when triggered by a criteria (mostly chosen as a relative change in the value rather than a time interval). Due to limited local buffers, the latency must not exceed a predefined limit for optimal operations. In general, a good balance should be found between the abundance of data and the usability of the data. The graphical user interface must be intuitive, efficient in computing and follow the standards present in the CMS collaboration.

The safety criteria set for the system are rather loose and require an operator for the safe supervision of the states. No hardware or software redundancy is created for the DCS. As control functions are limited, safety measures are not fail-safe and mainly are in the form of alarms as mentioned above. The integration of a relay system allowed to cut the power to the power supplies, however, this is done in a harsh way and does not allow for soft shut down. At the same time, for the initial tests, this was sufficient.

5.4. DCS Architecture

A standard DCS architecture is chosen. Hardware-wise a standard Siemens Simatic S7-1200 PLC is used, and connected to the DCS project using the S7 communication protocol. Only a few channels of all available are used, as two humidity sensors and four temperature sensors are connected through it. As the system evolved, four pressure sensors were added near the CO_2 inlet and outlet to characterise the pressure drop achieved. These sensors can be used in the hardware interlock that opens a relay system. The test-stand uses laboratory-grade power supplies to power the micro-strip heaters, sensing modules, and their TCs. In terms of DCS, this is not ideal because these supplies do not support automated control. To provide at least a basic safety system, the power supply power cable was connected via the relay system controlled by the PLC. Thus, allowing to open the circuit and cut the power to the heaters and coolers if needed. Additional sensing within the cold volume is done with 72 temperature sensors connected through three massive temperature readout system (MTRS) cards. For connectivity to the project, Modbus is used. Both the PLC and the MTRS is connected via an Ethernet cable to a switch providing access to hardware. Initially, the software project was running in a physical blade hosting Windows Server 2016, however, after an internet switch became faulty, the project was moved to a virtual machine, hosting a Windows Server 2022, following the latest recommendations. The graphical interface of the project is made available for all `MTD_Operators` via the `CMS Terminal server`.

The software part of the control framework is built using the `WinCC-OA` tool, using the version and patch recommended by the Central DCS team. The project is built following the CMS production standards, which has allowed to benefit from central tools and infrastructure. Several JCOP and CMS functional components are used, to implement common functionality and connectivity with various device types. To translate various necessary aspects of the test-stand, a set of MTD specific functional components was newly built, as summarised in Table 5.1.

The building of this prototype project has been a team effort, initially led and always supervised by the field's experts. For the author of this Thesis, it was a great learning experience, and her contribution to the project evolved over time. It started with creating the graphical user interface panels for various components wherever it was needed. It encapsulated both the graphical design, designing and optimising the functionality, and reusing or creating new scripts and libraries to support the said functionalities. In Fig. 5.3, some of the panels for the MTD TIF DCS project are shown, all panels shown here are made by the author of this Thesis; however, does not represent the full set created. The only component for which she did not create the graphical interface was the `CMS_MTD_ILK`, as it is the latest addition to the set of components, already delivered by the following expert. For the design of this component, the author of this Thesis took on a supervisory role, as it was the onboarding project of the following MTD DCS expert.

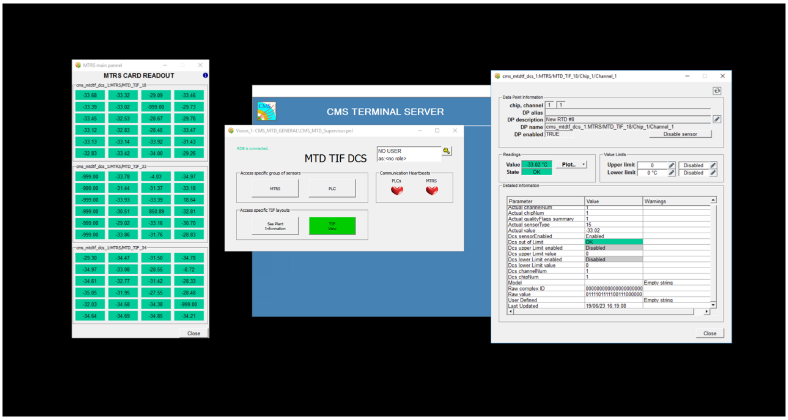

(a) supervisor panel together with MTRS detailed panels

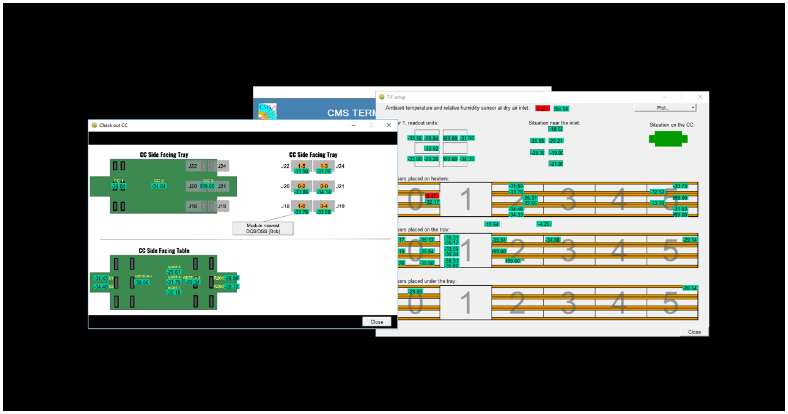

(b) TIF's view

(c) plant's view

Figure 5.3. A screenshot of the main MTD TIF DCS's graphical interface panels.

Table 5.1

Functional components created for the MTD TIF DCS project

Component	Description
`CMS_MTD_TIF_BASE`	Ensures connexion to the configuration and conditions databases
`CMS_MTD_GENERAL`	Hosts supervisory panel as well as the heartbeat panels for hardware, indicating the connexion and latency to the PLC and MTRS
`CMS_MTD_AC`	Handles the access control, people with role of `MTD_Operator` have access rights to the project, while `MTD_Expert` have rights to alter the project
`CMS_MTD_PLC`	Ensures the MTD specific PLC configurations to be installed
`CMS_MTD_MTRS`	Ensures the MTD specific MTRS configurations
`CMS_MTD_DIP`	Accesses published information of the CO_2 plant, such as the flow-rate, temperature
`CMS_MTD_RDB_SMOOTHING`	Allows to record data without any smoothing applied for intensive testing over short periods
`CMS_MTD_ILK`	Provides a software level interlock, allowing to use MTRS probes for opening the relays

With evolving knowledge of how a functional component has to be designed and packaged, the author of this Thesis followed the full creation cycle to create the `CMS_MTD_DIP` and `CMS_MTD_RDB_SMOOTHING` components. The first component accesses the CO_2 plant's published data, the environment data via the data interchange protocol (DIP) [123], that extends distributed information management (DIM), a protocol created at CERN [124]. The creation of this package allowed to deepen the understanding of creating a new data point type, data point creation and loading to the configuration database, appending a manager, and of course, creating a functional graphical user interface. All of the above were performed by the author of this Thesis with quality control provided by the CMS Central DCS team. The second component allows to alter the smoothing of the data archiving for various probes. The work on this component provided a great learning opportunity for creating dedicated scripts that use data from various data points, designing a new manager, and new data point types.

Other maintenance and upkeep tasks were also performed throughout the project development carried out by the author of this Thesis. These included the updates of graphical interfaces, the inclusion of new data points and their types, as well as the update of the project from `WinCC-OA 3.16` to `WinCC-OA 3.19`, ensuring compatibility for all components. This work allowed to practise working with various centralised tools, and practice the DCS building philosophy adapted within the CMS collaboration. In parallel to the TIF's DCS project, another training project was created further exploring various DCS aspects not yet available in the TIF's project, such as the FSM. Also, as mentioned above, knowledge transfer was ensured for the following DCS expert.

5.4.1. Limitations of the Current DCS

Clearly, the test-stand is more limited than a full detector, both in complexity and scale. The tray has only around 100 sensing channels, while detectors might have millions of channels. If for an operational detector the placement of probes and devices is well set in stone, then for a test-stand, changes, e.g. in the positioning of the sensors, can take place within a few days, and the system must promptly reflect them. Moreover, several new sensors might be added or removed along the course of testing, calling for a flexibility of the DCS.

The team performing the tests at the test-stand is small and operations are centrally organised, thus no self-impeding or overlapping interventions are taking place. At the same time, as no formal operator roles are defined in the test-stand environment, responsibility for monitoring the alarms and reacting to such conditions is not explicitly assigned. In practice, this limitation is mitigated by the presence of expert users during operation. Moreover, due to the ever-changing test-stand setup, several alarms do not give clear instructions how to mitigate them, and an extended knowledge is required.

As discussed before, the control aspect of the DCS is not present. However, the choice of standardised hardware (PLCs, MTRSs) will allow for smooth transitioning to automation when the non-standardised hardware (laboratory power supplies) will be exchanged. The same goes also for the chosen communication standards, they facilitate an easy expansion of the prototype system. A note worth making is that although the project has been built following the CMS standards, e.g. the redundancy is not met. There is no redundant peer hosting the project, able to take over if the main peer undergoes a fault. However, due to the nature of the tests and the maturity of the project, this was allowed and sufficient.

5.4.2. Impact on Detector Testing and Development

The DCS project has been vital for a successful development, assembly, and commissioning of the BTL. The system allowed to collect data characterising optimal cooling setting, power consumption by the TCs, sensor placement, and attachment style. In addition to many internal presentations and contributions to internal documents, a CMS Detector Performance Summary was published about the results of the thermal tests performed using this test-stand and its DCS, the BTL cooling setup at TIF [125].

Regarding the DCS prototype, many important lessons have been learnt. The whole MTD group has benefited from not just having a DCS project that facilitates data reading and provides the first steps towards automatisation, but a project built following the central guidelines. This is essential for the optimal design of the final DCS, understanding of the overall procedure, and best-practices. Moreover, having centralised backups of the components, and the project image, as well as globally supported databases, provides an increased security for the tests carried out with the test-stand. Also, beyond the software-value, the work performed on the prototype system has allowed to train (and will allow to train many more) in-house DCS experts necessary for the MTD operation.

5.5. Prospects of the Project

The initial DCS prototype met the necessary goals set by the team working on the test-stand, it has served as a good testing ground for many features, design choices, and functionalities that could benefit any further system, as was mentioned above. Moreover, the project is expected to evolve into the first DCS prototype towards the final detector, as more functionality becomes available. The current DCS project will be used to further develop three important aspects for controlling the MTD. They are expanded below, indicating the introduced functionalities.

Firstly, the controlling sequence needs to be designed and tested. This scenario becomes available upon the arrival of dedicated power supplies. From the test-stand point of view, this will provide the opportunity to test the component powering as intended in the final detector. Various tests will become available – finding the most optimal powering sequence, designing the ramping up and down of the voltage, evaluating the necessary power for various conditions, and estimating any losses, as well as figuring out the placement of the power cables. DCS-wise, it will be possible to work with the designated components, implementing the power supplies as data points, having the ability to control and monitor them via the DCS. This will allow to build the first prototypes of the FSM, design and test out basic functionality with automated actions, such as “turning on”, etc. This scenario could be further investigated by populating the full tray with sensor modules, thus analysing collective behaviour, defining annealing, standby, and data-taking regimes.

Secondly, the communication with the DAQ system needs to be tested. This second scenario becomes available upon collaboration with the DAQ team and having a unified test-stand to investigate the interplay between the DCS and the DAQ. Here, both from the test-stand and the DCS point of view the main gain will be streamlining the intercommunication between both systems. This will allow to define clear boundaries of each system’s responsibility, test and improve the efficiency of their communication. These tests will highlight how both teams will need to collaborate to take the most out of the limited information within the limited bandwidth available from the detector.

Finally, to create the first iteration of the DCS for the final detector, the collective behaviour within a supertray needs to be researched. Thus, the third scenario is expanding this test-stand to a supertray unit. A supertray is a set of six neighbouring trays that share the same cooling loop. Test-stand-wise, this allows to study and investigate the collective behaviour of a set of trays, explore the mechanical solutions, communication interfaces, and similar. As an example, such a system will provide ample room for testing on the uniformity of cooling and our ability to correctly characterise it with the available probes. From the DCS point of view, this setup will allow testing the scalability of the project, and will provide ample ground for testing various aspects of the FSM, as well as alarm design and automated control. This will provide an even more complete testing ground for various DSS aspects. As an example, parts of the supertray could be forced to exit the desired running ranges, forcing the system to act.

5.6. Summary

After the general introduction of the CMS detector and how it detects and reconstructs physics objects in the previous chapters, this chapter opens up on specific details about the DCSs, which are often taken for granted. It gives an introduction to the intricacy of building a DCS for a detector at the LHC. It describes the main tools and the main concepts that are being followed. Finally, it presents the adventures of building a DCS for a MTD test-stand and provides an outlook for the future of this project.

At this point of the Thesis, the theoretical motivation has been introduced, the experimental environment outlined, physics objects reconstruction explained, and the work on future upgrades has been presented. Thus, building on this foundation, the following chapter introduces the core building blocks of the HH analysis presented in this Thesis, including event selection, background modelling, and categorisation strategies.

6. BUILDING BLOCKS OF THE NON-RESONANT HIGGS BOSON PAIR PRODUCTION IN WWZZ DECAY CHANNEL ANALYSIS

An important part of this Thesis is the design and development of a new CMS analysis focused on the non-resonant HH production in the $HH \to WW^*ZZ^*$ decay channel. Because there was no previous CMS analysis of this channel, dedicated event selection and categorisation strategies, signal modelling, and background estimation strategies were designed and implemented from the first principles. The analysis workflows were optimised to ensure accurate signal modelling and to quantify the dominant experimental uncertainties. This chapter is dedicated to summarising the many building blocks of this analysis and in places providing a sneak peak on the windy road that led to the final selection or implementation technique. This journey span more than two years and was the primary focus during the final years of the author's doctoral studies.

After a brief introduction in Section 6.1 on the importance and possible opportunities brought by the $HH \to WW^*ZZ^*$ decay channel, the analysed dataset is summarised in Section 6.2 with the choice of simulations motivated in Section 6.3, also explicitly explaining why a new sample generation was needed. To dive deeper into the amazing quest of building a new analysis, the description of the design of the signal region is expanded in Section 6.4. It summarises object selection and calibration, event categorisation, and the need for a stronger signal classifier, which lead to the training of a dedicated ML algorithm. Alongside the final solutions, several in between steps are shown to better motivate the chosen approach. Then, in Section 6.5, an overarching look is given into the acceptance of other HH signals in the developed signal region. In Section 6.6, an overall data and MC agreement in control regions is shown, verifying the background modelling. Finally, possible sources of uncertainties are estimated in Section 6.7 and the measurement is described in Section 6.8. All this is necessary to build a stable and robust framework with which the final results can be obtained and further described in the next chapter, Chapter 7.

6.1. Motivation to Target the WWZZ Decay Channel

Each analysed HH decay channel opens a new window into the Higgs sector. While several HH decay modes have been studied extensively, other final states remain largely unexplored due to their experimental complexity or lower BR. As can be compared in Fig. 2.11 in Chapter 2, the $HH \to WW^*ZZ^*$ channel has a BR of only around 1 %. Thus, its appeal must come from another property of the channel.

In this decay channel, one Higgs boson decays into a pair of W bosons, while the other decays into a pair of Z bosons. Moreover, within the pair, one vector boson is on-shell while the other is off-shell. Neither can be detected in our detector; however, several of their final-state products can be detected. Figure 6.1 shows all the possible decays of $HH \rightarrow WW^*ZZ^*$. There is a mixture of charged leptons, quarks, and neutrinos, where from the hadronised quarks we expect jets and from neutrinos we expect MET in our detector. At the same time, final states with charged leptons offer a good signal-to-background ratio as they have clean and isolated leptons, yet it is clearly visible that such states have a lower BR than their hadronic siblings.

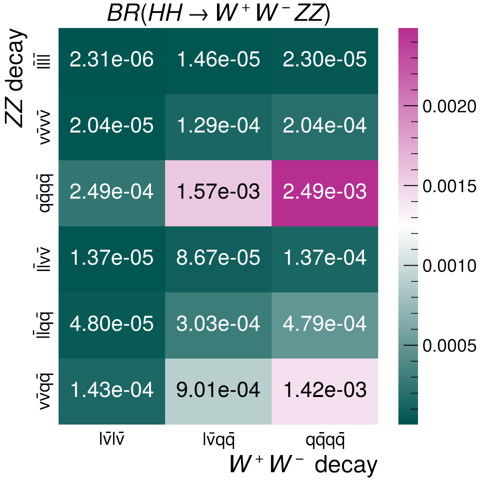

Figure 6.1. Possible decays of a HH through the WWZZ decay channel.

For the initial analysis, it was decided to check the sensitivity of the decay channels and construct analysis categories that would target some of these final states. For more convenient and reliable reconstruction, decays with $Z \rightarrow \nu\nu$ (for simplicity hereinafter notations for antiparticles, electric charges, and on-shell/off-shell is mostly omitted) contribution were omitted since a significant amount of the energy would be carried away by neutrinos and it would be difficult to confidently measure it with our detector. Seven potential categories were created, labelled based on the expected lepton multiplicity:

2.1. category targets $WW \rightarrow l\nu l\nu$ and $ZZ \rightarrow qqqq$. As leptons come from W bosons, it is decided to target opposite flavour decays to reduce the QCD background and require $m_{ll} > 12$ GeV for opposite charge lepton pairs. To target Z boson hadronic decays, at least two jets are expected in the event, as well as MET, $E_T > 30$ GeV, due to neutrinos.

2.2. category targets $WW \rightarrow qqqq$ and $ZZ \rightarrow llqq$. As both leptons come from a Z boson decay, an opposite sign (electric charge) same flavour (OSSF) lepton pair is expected with a loose invariant mass window, $m_{ll} \in (25, 120)$ GeV. To account for the hadronic decays of W bosons and the other Z boson, at least four jets are required.

3. category targets $WW \to l\nu qq$ and $ZZ \to llqq$. To target the lepton pair coming from the Z boson decay, a loose mass window is imposed on the OSSF pair, requiring $m_{ll} \in (25, 120)$ GeV. At least three jets are expected and $E_T > 20$ GeV complements the W boson semileptonic decay.

4.1. category targets $WW \to l\nu l\nu$ and $ZZ \to llqq$. One opposite sign (electric charge) opposite flavour (OSOF) and one OSSF lepton pair is expected. One of the pairs need to pass the loose mass window, $m_{ll} \in (25, 120)$ GeV, while the other is required to have $m_{ll} > 12$ GeV. $E_T > 30$ GeV complements the W boson semileptonic decays and the requirement for at least two jets complements the hadronic decays of the Z boson.

4.2. category targets $WW \to qqqq$ and $ZZ \to llll$. Two OSSF lepton pairs are required. Of both pairs only one needs to pass the tight mass window, $m_{ll} \in (60, 120)$ GeV while the other has to pass $m_{ll} > 12$ GeV. At least two jets are expected from the hadronic decays of the W bosons.

5. category targets $WW \to l\nu qq$ and $ZZ \to llll$. Two OSSF lepton pairs are expected and one of them has to pass the tight mass window, $m_{ll} \in (60, 120)$ GeV while the other has to pass $m_{ll} > 12$ GeV; $E_T > 20$ GeV is expected from the semi-leptonic decay of the W boson.

6. category is designed for $WW \to l\nu l\nu$ and $ZZ \to llll$. To loosen the selection, however, only two OSSF pairs are required similarly as in the five lepton case; $E_T > 20$ GeV is required.

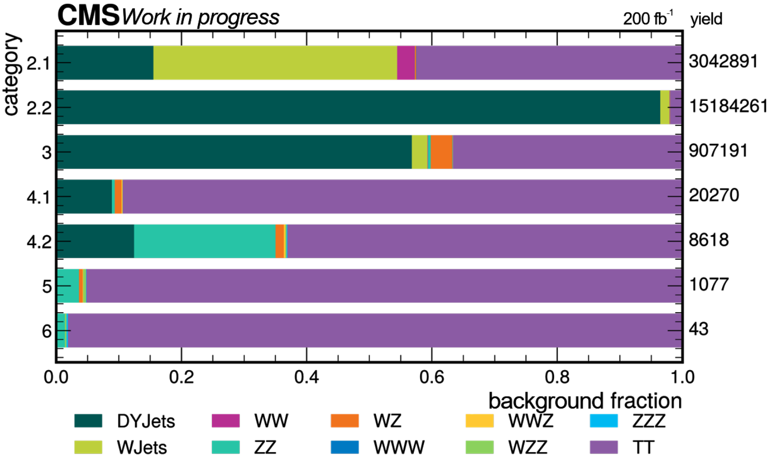

Figure 6.2. Background distribution in possible analysis categories, 2018 MC example for initial estimates, extrapolated to 200 fb^{-1}.

To paint the picture, an early study of background estimations per possible categories are shown in Fig. 6.2. The example uses 2018 MC, but the luminosity is extrapolated to the expected 200 fb^{-1}. Firstly, it can be seen that each next lepton multiplicity has on average an order of magnitude lower overall yield. Secondly, the main backgrounds are DY (more prominent in low lepton multiplicities) and $t\bar{t}$ (more prominent in high lepton multiplicities), subdominant are diboson backgrounds. Thirdly, if the signal contribution was displayed in the figure, it would not be noticeable, as its yield is several orders lower. This can be compared in Table 6.1 where the expected signal and background event yields per category are shown for comparison. In the most populated category, 2.2, the expected signal for 200 fb^{-1} is almost 1.5 events, while for category 6 it is 0.004 events.

Table 6.1

Expected event yield for 200 fb^{-1} based on the initial studies

Category	Decay channel	Signal yield, events	Background yield, events
2.1	$HH \to WWZZ \to l\nu l\nu\ qqqq$	0.605	3042891
2.2	$HH \to WWZZ \to qqqq\ llqq$	1.486	15184261
3	$HH \to WWZZ \to l\nu qq\ llqq$	0.915	907191
4.1	$HH \to WWZZ \to l\nu l\nu\ llqq$	0.083	20270
4.2	$HH \to WWZZ \to qqqq\ llll$	0.093	8618
5	$HH \to WWZZ \to l\nu qq\ llll$	0.029	1077
6	$HH \to WWZZ \to l\nu l\nu\ llll$	0.004	43

Therefore, the rarity of $HH \to WW^*ZZ^*$ makes this search very challenging. Targeting two-lepton final states is extremely difficult as signal events drown in the $t\bar{t}$, QCD, and DY backgrounds, while targeting five- and six-lepton final states would give conveniently clean signatures, however, the data-taking would need to be very long to collect a sufficient amount of it. Thus, the initial feasibility analysis focusses on the final states of the three and four leptons. Of these, the four-lepton case was developed in this Thesis and is outlined in detail in the following chapter. The three-lepton case with a partial dataset is developed in a parallel analysis, see Ref. [126]. To provide a broader picture, the three-lepton category will be introduced before providing projections of the combination of the results for these categories in Chapter 7.

Regarding the four-lepton categories, three $HH \to WW^*ZZ^*$ decays can produce four leptons, which are (in order of decreasing BRs):

1. where both W bosons decay semi leptonically, $W \to l\nu$, and one Z boson decays leptonically, $Z \to ll$, while the other decays hadronically, $Z \to qq$;
2. where both W bosons decay hadronically, $W \to qq$, and both Z bosons decay leptonically, $Z \to ll$;
3. where both W bosons decay semi leptonically, $W \to l\nu$, and one Z boson decays leptonically, $Z \to ll$, while the other decays to a pair of neutrinos, $Z \to \nu\nu$.

The BR of the third decay channel is comparable with the five-lepton final state's BR, and since a significant amount of the energy would be carried away by neutrinos, it would be difficult to confidently measure it with our detector. Thus, event selection has been developed with the first and second decay channels in mind, creating categories 4.1 and 4.2. The corresponding Feynman diagrams can be seen in Fig. 6.3.

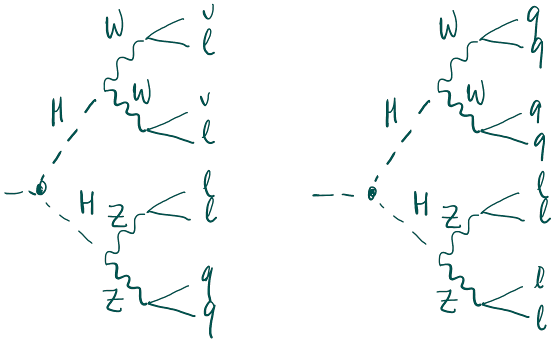

Figure 6.3. Feynman diagrams for the considered HH decays through WW^*ZZ^* with four leptons in the final state, (1) *vlvl llqq* case, category 4.1, on the left and (2) *qqqq llll* case, category 4.2, on the right.

As hinted by Fig. 6.2, the simplified characteristics (number of leptons, jets) of the HH channel $HH \to WW^*ZZ^* \to 4l$ are not unique, therefore, this search suffers from various background sources, both irreducible and reducible. Irreducible sources have an identical final state set, while reducible appear the same because of a misreconstruction or misidentification. Clearly, processes with a large cross section are more potential threats. Thus, background processes include the production of vector bosons with additional jets, including vector boson production in association with top quark pair, single and pair production of top quarks, as well as diboson and triboson production, and other even rarer processes. An example of the Feynman diagrams for pair production of top quarks, and diboson and triboson production is shown in Fig. 6.4. These clearly show the production of

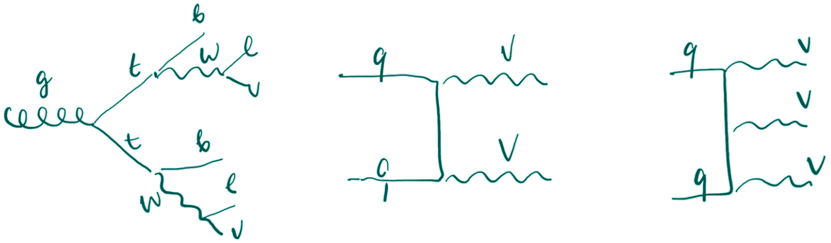

Figure 6.4. The Feynman diagrams for $t\bar{t}$ background on the left, VV production in the middle and VVV production on the right.

vector bosons and how, in combination with additional jets, events with their final states could be misidentified as coming from the $HH \to WW^*ZZ^* \to 4l$ decay. Additionally, this search considers single-Higgs boson production as a background source. Several Feynman diagrams were already shown in Chapter 2. Both event pre-selection, physics object choice and event categorisation should disfavour events coming from backgrounds, with a moderate impact on the signal efficiency.

6.2. Data Samples

The analysed data have been collected with the CMS detector during two pp data-taking periods – full Run 2 (2016, 2017, and 2018) and early Run 3 (2022 and 2023). To target the HH channel $HH \to WW^*ZZ^* \to 4l$, data events with electrons and muons are selected and analysed if they pass one of the corresponding trigger paths described in Section 6.4. Only data certified with the Golden standard are used in this work. These samples correspond to about 200 fb^{-1}, as can be seen in the summary Table 6.2. Overall, Run 2 provides more luminosity than the early Run 3, as the year with the highest integrated luminosity, 2018, concludes the Run 2. For brevity, throughout the following sections, only one example from a randomly chosen era will be shown, however, figures and tables have been made for each era, combined per year, then Run, and finally the whole period analysed. Here, "era" refers to a given data-taking period with stable data-taking conditions.

As was introduced in Section 3.3, the two data-taking Runs have slightly different parameters. As an example, the PU profile has changed and the average PU had steadily grown from 27 in 2016 to 52 in 2023. Although clearly the most exciting change is the increase in the centre-of-mass energy from 13 TeV for Run 2 to 13.6 TeV for Run 3.

Table 6.2

Integrated luminosity, its uncertainty, average PU and the centre-of-mass energy ($\sqrt{s}$) across years analysed in this Thesis

Year	Int. luminosity, fb^{-1}	Lum. uncertainty, %	Avg. pileup	$\sqrt{s}$, TeV 7	Run
2016	36.31	1.2	27	13	2
2017	41.48	1.7	38	13	2
2018	59.83	2.5	37	13	2
2022	34.75	1.3	46	13.6	3
2023	27.86	1.4	52	13.6	3

Due to drastic changes in the detector, the 2016, 2022 and 2023 data-taking periods have been split into two eras per year that require dedicated data analysis or handling. In mid 2016 it was noticed that the `APV25` readout chip drain speed was saturated, causing wrongful amplification, thus it had to be changed to correct the readouts [127]. These `APV25` are the readout chips used for silicon microstrips in the CMS tracker, and the saturation error was corrected by adjusting the preamplifier feedback voltage bias (VFP). These eras split into "pre-VFP" (aka "APV") and "post-VFP" periods and cover 20.2 fb^{-1} and 16.6 fb^{-1}, respectively. The 2022 data-taking year was split due to a cooling leak in the forward ECAL endcap, which made around 7 % of it unusable, thus requiring a separate simulation and calibration procedure [128]. These eras are named `2022` and `2022EE` and cover 8.08 fb^{-1} and 26.67 fb^{-1}, respectively. 2023 was split because several modules covering around 23 degrees in ϕ in the Barrel Pixel became inoperable due to an issue distributing the LHC clock signal [128]. The tracking possibility was lost in this area, thus a dedicated correction was needed. These eras are named `2023` and `2023BPix`, and cover 18.41 fb^{-1} and 9.45 fb^{-1}, respectively. Although these challenges might come across as serious, the data collected by the CMS detector remain state-of-the-art and many detailed studies were performed to understand the exact implication of each obstacle, making the simulations and reconstructions even more precise and well motivated.

The majority of the Run 2 samples used in this Thesis are ultra legacy (UL) quality. The UL quality indicates the final, fully reprocessed version of the CMS Run 2 dataset. While for the Run 3 the re-reconstructed quality is the highest available for this Thesis timeline. This already includes a reprocessing with several improvements, but might not be the final available version. To remain consistent, the recommended NanoAOD version (v9) is used for Run 2 datasets, while for the Run 3 the NanoAOD version 12 is chosen as the recommended one. Single and double lepton primary datasets are chosen for data selection in this Thesis. To avoid possible overlap when selecting the same event from different primary datasets, a dedicated selection algorithm is based on the triggered trigger paths as described in Section 6.4.

6.3. Monte Carlo Simulations and their Reweighing

MC simulations are used to model the signal, HH production, as well as the background processes. Precise modelling of the physical process is crucial in not only understanding the processes studied but also in designing a targeted analysis framework. Therefore, the most precise, collaboration-wide approved, and in general state-of-the-art generators are used. To further mitigate mis-modelling of e.g. detector response, a dedicated weight to each MC event is applied.

Section 4.5 describes event generators in more detail, however, it is worth noting that this Thesis has used LO and NLO (or even higher when possible) samples generated by `MadGraph5_amc@nlo` [112], `Powheg v1.0` or `Powheg v2.0` [114], [115], [129], [130], [131], while hadronisation has always been done using `Pythia` [113]. A short summary is shown in Table 6.3, including the signal considered, decay modes allowed, generators used, and the used cross section for further calculations. The related theoretical uncertainties in the cross section are given in Section 6.7. In the table `MadGraph5_amc@nlo` is shortened

Table 6.3

List of MC samples used in estimating signal and background contributions, generators used for their production, cross section used for Run 2 eras and Run 3 eras; † has an extra restriction on $4 < m_{ll} < 50$ GeV, and †† has an extra restriction on $m_{ll} > 50$ GeV; “N/A” indicates the sample was not available in the given Run

Process	Decay modes	Generators	$\sigma^{\text{Run 2}}$, pb	$\sigma^{\text{Run 3}}$, pb
ggFHH	$HH \to VV^*VV^*$	PW	1.87e-03	2.07e-03
ggFHH	$HH \to bb\tau\tau$	PW+MG5@LO	2.46e-03	2.46e-03
ggFHH	$HH \to bbZZ^*$	PW	4.92e-06	4.92e-06
ggFHH	$HH \to \tau\tau VV^*$	PW	9.42e-04	1.04e-03
ggFHH	$HH \to \tau\tau\tau\tau$	PW	1.20e-04	1.33e-04
ggFH	$H \to ZZ \to 4l$	PW/PW2+JHUGen	0.013	0.014
VBFH	$H \to ZZ \to 4l$	PW/PW2+JHUGen	1.04e-03	1.12e-03
W^-H	$H \to ZZ \to 4l$	PW/PW2+MiNLO+JHUGen	1.46e-04	1.56e-04
W^+H	$H \to ZZ \to 4l$	PW/PW2+MiNLO+JHUGen	2.31e-04	2.44e-04
ZH	$H \to ZZ \to 4l$	PW/PW2+MiNLO+JHUGen	6.25e-04	7.75e-04
$t\bar{t}H$	$H \to ZZ \to 4l$	PW/PW2+JHUGen	1.39e-04	1.56e-04
$b\bar{b}H$	$H \to ZZ \to 4l$	PW/PW2+JHUGen	1.34e-04	1.45e-04
$t\bar{t}WH$	all	MG5@LO	1.14e-03	N/A
$t\bar{t}ZH$	all	MG5@LO	1.13e-03	N/A
$Z/\gamma^* + j$	$2l$	MG5@NLO+FXFX	360	386
$t\bar{t} + j$	$2l2\nu$	PW/MG5@NLO+FXFX	88.3	95.5
t or $\bar{t}[tWll]$	all	MG5@LO	0.011	N/A
t or $\bar{t}[tZq]$	all	MG5@NLO	0.076	N/A
tW^-	$2l2\nu$	PW	N/A	36.0
$\bar{t}W^+$	$2l2\nu$	PW	N/A	36.0
$t\bar{t}\gamma + j$	all	MG5@NLO+FXFX(+MS)	3.76	4.22
$t\bar{t}\gamma$	all	MG5@LO	1.50	N/A
$WZ\gamma$	$W \to l\nu,\ Z \to 2q$	MG5@NLO	0.043	0.084
$t\bar{t}W + j$	$W \to l\nu$	MG5@NLO+FXFX+MS	0.216	N/A
$t\bar{t}WW$	all	MG5@LO(+MS)	7.00e-03	8.20e-03
$t\bar{t}WZ$	all	MG5@LO	2.45e-03	2.71e-03
$t\bar{t}ZZ$	all	MG5@LO(+MS)	2.45e-03	1.58e-03
$t\bar{t}Z$	$Z \to 2l$	MG5@NLO	0.075	N/A
$t\bar{t}Z$ †	$Z \to 2l$	MG5@NLO	N/A	0.086
$t\bar{t}Z$ ††	$Z \to 2l$	MG5@NLO	N/A	0.039
WW	$2l2\nu$	PW	11.1	11.8
WZ	$3l\nu$	PW+MG5@NLO+FXFX	5.21	4.92
ZZ	$4l$	PW	1.32	1.39
WWW	all	MG5@NLO(+MS)	0.216	0.233
WWZ	all	MG5@NLO	0.171	0.185
WZZ	all	MG5@NLO	0.057	0.062
ZZZ	all	MG5@NLO	0.015	0.016
$t\bar{t}t\bar{t}$	all	MG5@NLO	8.21e-03	9.65e-03
$WWZZ$	all	MG5@LO	4.44e-04	4.91e-04

to `MG5@NLO`, and if the Frederix–Frixione merging scheme [132] is used, it is denoted accordingly. If only LO matching is performed, it is denoted with `MG5@LO`. Moreover, several resonances that have been generated with `MadGraph5_amc@nlo` are decayed with `MadSpin` [133]. In such a case, it is indicated with `+MS` in the table. A multiple of Higgs boson samples have used Johns Hopkins University (JHU) generator [134] to decay the Higgs boson, in the table this is denoted with `JHUGen`. If `Powheg v1.0` is used, it is denoted as `PW`, while in the `Powheg v2.0` case it is denoted as `PW2`. If the version has changed across eras, it is denoted with a slash. When `Powheg` is extended with `MiNLO` [135] to handle processes with associated jets, it is noted accordingly. Regarding `Pythia`, the most comprehensive and modern event "tune" developed for CMS is used: CP5 [136]. This tune is a specific set of parameters optimized to fit experimental data, it controls how underlying event modelling is done. Currently, it is considered the golden standard for Run 2 and Run 3 eras. It uses `NNPDF3.1 NNLO` [137] PDF set. The quoted cross sections are gathered from the centralised cross section database [138] or the recommended theory calculations [139], [140], [141].

As stated before, low-level inaccuracies are corrected using per-event weights rather than making the event simulation more complicated or detailed. Such an example is PU reweighing. As event generation is a lengthy process, more often than not the central event production starts before the precise PU distribution is known. Therefore, afterward, a weight per-event is calculated as a ratio between the PU distribution in the data and in the MC. Usually, the PU is calculated from the number of reconstructed PVs or from the instantaneous luminosity measured per bunch crossing. As detector response differs with various PU, it is crucial to calculate it correctly to account for its contribution.

In general, if events with jets and leptons are targeted, each event gets an assigned weight as in Eq. (6.1):

$$w_{event} = \frac{L_{int} \cdot \sigma \cdot \mathcal{BR} \cdot w_{PU} \cdot SF_{leptons} \cdot SF_{jets} \cdot w_{generator}}{\sum w_{generator}}, \tag{6.1}$$

where L_{int} is the integrated luminosity we want to scale the simulation to, σ is the simulated sample's cross section and $\mathcal{BR}$ is the branching ratio of the simulated events (e.g. if the simulation is generated for a subset of possible decays as in the HH decay into four vector bosons, rather than everything), w_{PU} is pileup weight, $SF_{leptons}$ is the scale factor (SF) for leptons (all four lepton SF multiplied) and SF_{jets} is the SF for jets, finally $w_{generator}$ is the weight coming from the event generator. This formula is somewhat intuitive, as we want to scale the simulation in a reliable fashion. We need to know to what amount of data it needs to be scaled (L_{int}), what is the average rate for this production ($\sigma \cdot \mathcal{BR}$), what is the relative importance for this simulated event $\left(\frac{w_{generator}}{\sum w_{generator}}\right)$ and what are other (minor) corrections still needed for the simulation.

SFs are needed to align the efficiency of e.g. lepton identification in simulations and in the data, as minor modelling imperfections always exist. These are derived from a dedicated region, that is orthogonal to or severely depleted of the signal. Let us take lepton identification SFs as an example. They are calculated using the "Tag and Probe" (TnP) method [142] and pure samples of $Z \to l^- l^+$ (or J/Ψ in the case of low transverse momentum measurement, such as described in Ref. [143]) events are used, meaning selected leptons are the same flavour but opposite charge (OSSF). One lepton of the pair is called the "tag" and it has to satisfy trigger requirements, as well as tight identification and isolation criteria. The other lepton in the pair is called the "probe" and it is tested against a loose selection, corresponding to the efficiency measurement at hand. If the probe passes the selection, the whole event is categorised to "pass" and if the test fails, the whole event is categorised as "fail". The efficiency, ε, is defined as the ratio of the number of passing events, N_P, over the total number of events, also including the failing events, N_F. It is calculated using Eq. (6.2).

$$\varepsilon = \frac{N_P}{N_P + N_F} \tag{6.2}$$

When the selection, for example, in a tight mass window around the Z boson invariant mass peak, is pure enough, a simple cut-and-count approach can be used. However, if the background contribution is sizeable, both the passing and failing event distributions can be fitted against a signal and background model, and the true signal yield can be extracted from the fit. Usually the background is modelled as an exponential decay, while the signal peak is characterised by a Double Sided Crystal Ball function. Due to varying kinematics, efficiency usually is extracted in (p_T, η) regions or bins, while an even finer binning can take place if enough statistics are provided. Finally, the SF is calculated as the ratio of the efficiency in data and MC simulations in each of the test bin as shown in Eq. (6.3):

$$SF(p_T, \eta) = \frac{\varepsilon(p_T, \eta)_{data}}{\varepsilon(p_T, \eta)_{MC}}, \tag{6.3}$$

where ε_{data} – is the lepton selection efficiency in the data and ε_{MC} in the MC simulations. The SFs for centrally supported IDs are provided centrally by the CMS collaboration, however, if the object selection is more complex or uses a different WP, the SFs need to be derived individually for each analysis.

As jets undergo a complex correction process (further described in Section 6.4.2), no additional SFs are applied for their generic IDs. At the same time, dedicated SFs are needed when applying the PU ID (recommended for Run 2 jets with $p_T < 50$ GeV). Moreover, as this Thesis analysis benefits from b-tagging, the discrepancies in the b-tagging between data and MC need to be addressed, and a per-event weight needs to be applied. This and the exact IDs and WPs used for each object are described in detail in Section 6.4.1 and Section 6.4.2.

Moreover, Eq. (6.1) is extended by adding another weight for 2016 and 2017 data-taking period due to the L1 pre-firing [90]. In these years, a gradual timing shift of the

ECAL caused by radiation damage was not adequately compensated online. Over time, the most affected high-$|\eta|$ regions caused a wrongful association of the energy deposit with the previous bunch crossing, causing the L1 to pre-fire. As two consecutive bunch crossings are prohibited from firing, this association vetoed the original bunch crossing from firing, leading to inefficiencies in the trigger. The weight, w, is calculated using Eq. (6.4) where the pre-firing probability, P, is evaluated in an unbiased and unprefirable dataset. The overall magnitude of the correction is estimated below 4 %, and it is more prominent for objects with high-$|\eta|$ and high-p_T.

$$w = 1 - P(\eta, p_T) \tag{6.4}$$

6.3.1. Producing Filtered Signal Sample

At the beginning of this Thesis, the main signal sample available for signal evaluation was an inclusive $HH \to VV^*VV^*$. It includes $HH \to WW^*WW^*$, $HH \to ZZ^*ZZ^*$, and the Thesis favourite $HH \to WW^*ZZ^*$. The sample is heavily dominated by the $WWWW$ decay, as $\mathcal{BR}(4W) \approx 4 \cdot \mathcal{BR}(2W2Z)$ and $\mathcal{BR}(4W) \approx 67 \cdot \mathcal{BR}(4Z)$. Moreover, when selecting four leptons, the remaining statistics might have been enough to estimate the total yield, but were not sufficient to train any signal extracting algorithms. Therefore, a private production for $HH \to WW^*ZZ^* \to 4l$ was launched to motivate a request for central production of such filtered samples for training purposes.

This private production closely followed the inclusive sample's production steps but with an additional generator-filter on the daughter particles, and additionally suppressing the $Z \to \nu\nu$ decay. Meaning, the same gridpack (precomputed datasets necessary to accelerate the generation, the main key computational elements) was used and the same production sequence was followed, while significantly increasing statistics. Two filters were explored, (a) one which filters for exactly four true level leptons and (b) one which filters for at least four truth-level leptons. In the private production, (a) was chosen to quicker acquire the needed statistics.

Table 6.4 shows the comparison for queries of four truth-level lepton events in the filtered and in the inclusive samples, an example of a file from 2018 MC dataset is chosen. It can be seen that in the inclusive sample four truth-level lepton events make up only sub-1 % contribution, moreover, more than a half of them come from the $HH \to WW^*WW^*$ decay, therefore, explicitly targeting four-lepton events gives the highest improvement, and targeting $HH \to WW^*ZZ^*$ decay gives only a marginal advantage. However, when analysing the statistics for reconstruction-level leptons, in the case of filtered production, around 80 % of generated events have at least four reconstructed leptons, of which 10 % pass the pre-selection phase-space, while in the inclusive sample around 10 % have at least four leptons, of which only around 4 % pass the pre-selection. More details on the pre-selection are described in Section 6.4.

Table 6.4

Comparison of the inclusive and filtered 2018 Run 2 sample four truth-level lepton events (example of one file), where N_l , N_q, N_ν, and N_τ correspond to the number of generated charged leptons (muons or electrons), jets, neutrinos and taus from the W and Z decays, sorted by the most common, vector boson decays given as example

Decay	N_l	N_q	N_ν	N_τ	% of incl.	% of filt.	VV* Decay	VV* decay
WW^*WW^*	4	0	4	0	0.178	-	$l\nu l\nu$	$l\nu l\nu$
WW^*ZZ^*	4	2	2	0	0.106	59.03	$l\nu l\nu$	$llqq$
WW^*ZZ^*	4	4	0	0	0.041	28.35	$qqqq$	$llll$
WW^*ZZ^*	4	0	4	0	0.011	-	$\nu\nu\nu\nu$	$llll$
WW^*ZZ^*	4	2	1	1	0.005	9.08	$\tau\nu qq$	$llll$
WW^*ZZ^*	4	0	2	2	0.005	3.55	$l\nu l\nu$	$\tau\tau ll$
ZZ^*ZZ^*	4	4	0	0	0.017	-	$qqqq$	$llll$
ZZ^*ZZ^*	4	2	2	0	0.017	-	$qq\nu\nu$	$llll$
ZZ^*ZZ^*	4	2	0	2	0.011	-	$\tau\tau\nu\nu$	$llll$

These findings strongly motivated central filtered sample production, allowing to train the signal extracting algorithm on centrally approved samples. Moreover, to envision possible extensions to the analysis, the centrally produced filtered sample was chosen to cover not only four but also more leptons in final states (option (b)). If not useful for further expansion, then at least it would allow for similar downward migration, as in the inclusive sample.

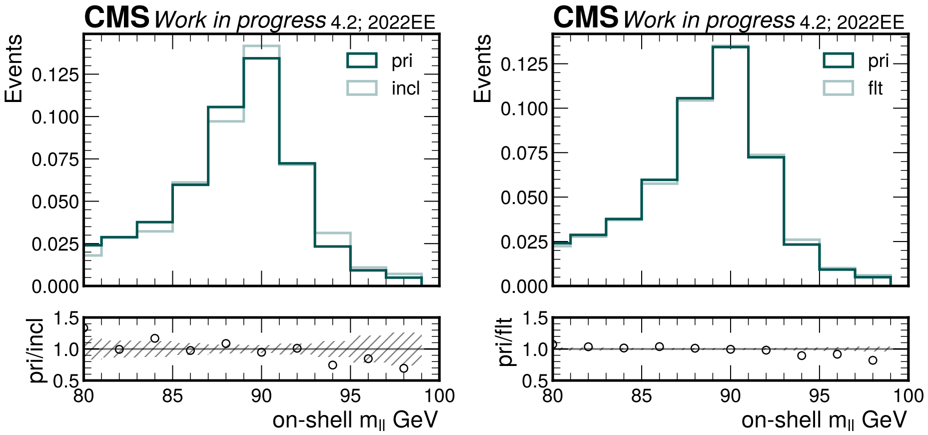

(a) private filtered vs central inclusive production (b) private filtered vs central filtered production

Figure 6.5. Comparison between the private filtered production ("pri"), central filtered production ("flt") and central inclusive sample production ("incl"), example for 2022EE period, 4.2 category on-shell m_{ll}.

In an example of 2022EE era's MC, a comparison of the on-shell m_{ll} for the category 4.2 are shown in Fig. 6.5. In Figure 6.5a the privately produced filtered sample and the inclusive sample are compared, while the privately produced filtered and the centrally produced filtered samples are compared in Fig. 6.5b. Most statistical fluctuations and differences are within the uncertainties, while there is a slight underproduction of the privately generated sample in the high-tail of the on-shell m_{ll} distribution. Overall, the slight differences could be attributed to the missing $Z \rightarrow \nu\nu$ decay in the filtered and private sample; however, the underproduction of the private sample most likely is due to it targeting exactly four truth-level leptons rather than at least four.

6.4. Designing the Signal Region

Events must pass several stages of selection before being considered in the signal region (SR) of this analysis. The very first step is the trigger selection, which aims to find events that might be coming from a HH decay amongst all other possibilities. Afterwards, object selection is performed and events are categorised based on several object kinematics or candidate parameters, and finally a BDT outputs a discriminant value accepting or rejecting the event in the SR. Each stage aims to target the signal while rejecting background processes as much as possible.

First of all, events are selected if single-, double- or, where available, triple-lepton HLT paths have been triggered. Single-electron HLT paths require $p_T > 25$ GeV or even $p_T > 40$ GeV depending on the year, while single-muon HLT paths have requirements of $p_T > 22$ GeV or $p_T > 24$ GeV. Both double- and triple-lepton HLT paths can have a cascading set of requirements, e.g., the leading lepton has to satisfy $p_T > 23$ GeV while the subleading $p_T > 12$ GeV, or both leptons have to satisfy the same threshold, e.g. $p_T > 33$ GeV. These trigger paths can be for the same flavour, e.g., targeting three electrons, or mixed flavour, e.g., requiring one muon and two electrons. In the one-lepton HLT path case, the leptons have tight online selection, while for two and three-lepton case, this selection is loose or very (very) loose to not sacrifice the selection efficiency.

Paths are used in an “OR” combination, allowing for a better event coverage. The available trigger paths have changed over the years, as an example, in Run 3 there are no more three-electron triggers available while such paths existed in Run 2. Overall, due to a more precise muon detection within the detector, muon triggers have lower uncertainties, so it would make sense to prioritise them over the electron triggers. However, as an “OR” of the paths is used, this does not make much difference.

The trigger efficiency for selecting $HH \rightarrow WW^*ZZ^* \rightarrow 4l$ events is shown in Fig. 6.6, where the ratio of selected and total events is shown for each period analysed. The uncertainties correspond to the number of selected events rather than the properties attributed to each trigger. For 2023 year, a slightly lower efficiency is reached, yet within uncertainties the trigger efficiency on selecting the signal is very high across all years, around 98 %.

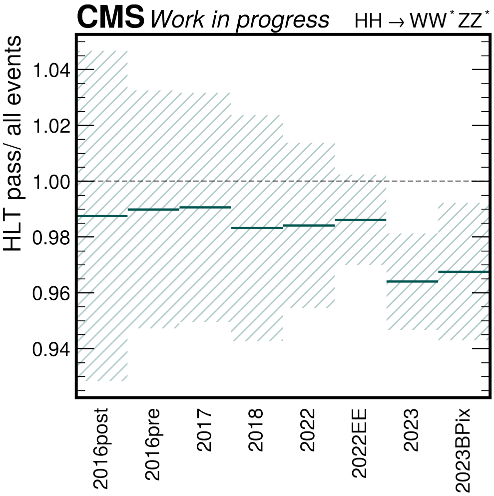

Figure 6.6. Ratio of $HH \to WW^*ZZ^*$ events that have passed the HLT "OR" over the total number of events in the main signal sample, across analysed eras.

When selecting events from experimental data, that is, from several primary datasets, attention is paid to not double count them. Each event is tested within each of the primary datasets and is selected:

- from `DoubleEG`/ `EGamma`, if it passes at least one of the selected di/tri-electron triggers;
- from `Muon`/ `DoubleMuon`, if it passes the di/tri-muon triggers and fails the di/tri-electron triggers;
- from `MuonEG`, if it passes the muon-electron and fails the di/tri-electron and di/tri-muon triggers;
- from `SingleElectron`/ `EGamma`, if it passes the single-electron trigger and fails all of the above triggers;
- from `SingleMuon`/ `Muon`, if it passes the single-muon trigger and fails all of the above triggers.

6.4.1. Lepton Selection and Calibration

After the event has passed the trigger selection, the physics object selection comes. This being a completely new study, gave the opportunity to design the desired selection. This in turn meant launching several studies regarding the choice of lepton IDs, additional quality criteria, various isolation parameters, anything that would draw a clear separation between signal and background leptons.

This Thesis is not explicitly targeting taus or neutrinos, therefore, only three main physics objects are considered – muons, electrons, and jets. Although the studies for their selection were performed in parallel, for pedagogical reasons, they will be discussed by type rather than by time. Very initial studies (see Fig. 6.2) showed that even for the four-lepton category $t\bar{t}$ and DY are concerning backgrounds, therefore, extra attention was paid to reduce their acceptance. One of the methods was to compare lepton transverse momentum distributions. Signal leptons are expected to be slightly boosted due to the Higgs decays, at the same time, it is known that one of the vector bosons always is off-shell, thus producing low-p_T leptons. Also, many background processes would have leptons with a softer p_T spectrum overall.

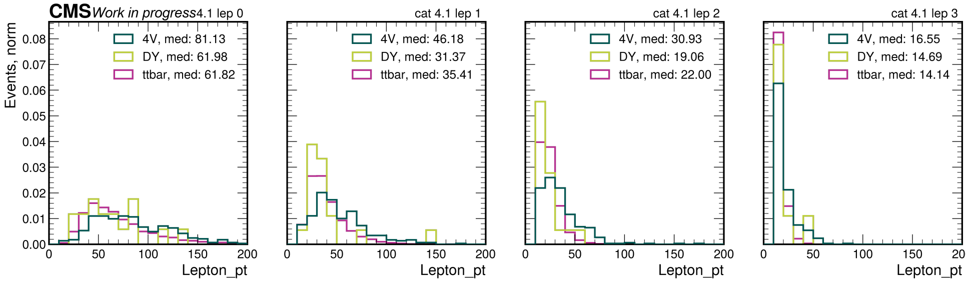

(a) category 4.1

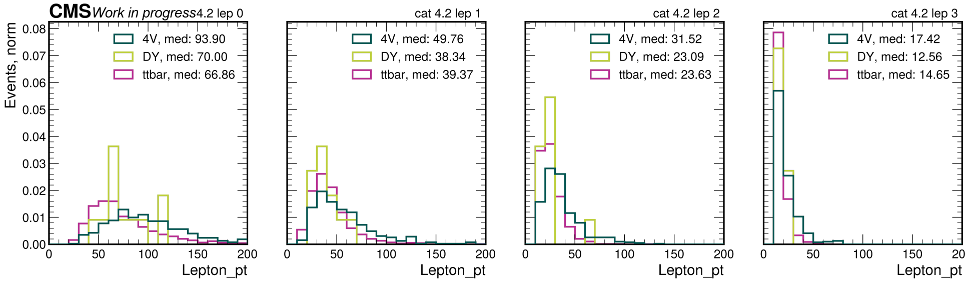

(b) category 4.2

Figure 6.7. Lepton transverse momentum shape comparison for the signal ("4V"), and two leading backgrounds, the left-most subfigure shows the shapes for the leading lepton while the right-most subfigure shows it for the softest lepton in the event; value indicates the mean of the distribution, 2022EE MC.

Thus, the transverse momentum distributions were compared for the signal and main background processes to see if a higher transverse momentum threshold requirement on the leading or the sub-leading lepton could help in rejecting the backgrounds. This is done for leptons selected with a loose ID provided centrally and restricted within $|\eta| < 2.4$, and additionally requiring $p_T > 10$ GeV. A comparison is shown in Fig. 6.7, where each subfigure displays the p_T shape of the leading, sub-leading, sub-sub-leading and the softest lepton (w.r.t. p_T). It can be seen that the mean value of the distribution is higher for the signal sample, thus several thresholds for each lepton's transverse momentum were examined. To compare each improvement in early analysis stages, a proxy of statistical significance was used. As a background-dominated scenario is explored, a naive significance is used and defined as $S/\sqrt{B}$ where S is the signal yield and B is the background yield. Thus, allowing to compare the signal over the background fluctuation in a fast and intuitive approach.

To get ahead of the next few paragraphs, Table 6.5 summarises just a few of the examined scenarios, already comparing it with the final selection. Raising the leading and sub-leading leptons p_T threshold gave a significant overall improvement, while changing the third lepton's threshold provided only marginal changes. Thus, it was decided to impose only an additional $p_T > 25$ GeV on the leading lepton and $p_T > 15$ GeV on the sub-leading lepton (first column in Table 6.5). This requirement is looser than the p_T thresholds imposed by single lepton HLT paths, however, tighter than the majority of double-lepton paths and all triple-lepton paths, thus not introducing a significant bias.

Table 6.5

The comparison of statistical significance ($S/\sqrt{B}$) per transverse momentum thresholds per lepton, per category, estimated from 2022EE MC sample and extrapolated to 200 fb^{-1}

Category	25/15/(10)	25/15/12/(10)	25/15/15/(10)
4.1	1.66e-03	1.66e-03	1.69e-03
4.2	9.16e-04	9.17e-04	9.19e-04

These requirements helped, but $t\bar{t}$ still remained a huge issue. As top quarks decay through the weak interaction, producing a W boson and a b quark, it was decided to see how effective could be the rejection of events with b-tagged jets or leptons decaying from the top quark via a W boson. For leptons, applying another ID was the most impactful. This ID had been designed for the $t\bar{t}H$ analysis [144] and helps targeting leptons coming from the H boson rather than the (anti-) top quark. The MVA discriminator was trained with `TMVA` [145] on prompt leptons from an inclusive $t\bar{t}Z$ sample as signal and leptons from semi-leptonic $t\bar{t}$+jets decays as background. Six centrally provided WPs are provided, ranging from very loose to extra tight definition.

Table 6.6

The comparison of statistical significance ($S/\sqrt{B}$) per ttH MVA WPs per category, estimated from 2022EE MC sample and extrapolated to 200 fb^{-1}

Category	No ttH ID	WP loose	WP medium	WP tight	WP 4W
4.1	1.55e-03	1.66e-03	1.54e-03	1.54e-03	1.82e-03
4.2	8.39e-04	9.16e-04	8.69e-04	8.20e-04	8.51e-04

Upon investigating which WP to choose, it was noticed that the CMS HH multilepton analysis [34] had introduced its own (4W). Thus, it was added for evaluation. The comparison of statistical significance is given in Table 6.6 for the investigated WPs. Although WP 4W gave a higher significance in the category 4.1, a more conservative approach of selecting centrally approved WP-loose was chosen. The conservativeness will allow for a more streamlined combination with other $HH \to WW^{*}ZZ^{*}$ analysis channels.

Next, there were studies on the implementation of various quality cuts. Several lepton isolation criteria, thresholds on the IPs along the beam line and in the transverse plane, numerous characteristics for deposited energy amongst other criteria were compared. However, these are reported only in the final configuration not to overwhelm the reader any further. The final requirement set is summarised in Table 6.7 for electron selection and in Table 6.8 for muon selection.

Table 6.7

Electron selection

Observable	Description	Value
p_T any	transverse momentum	> 10 GeV
$\lvert\eta\rvert$	abs. pseudorapidity	< 2.5
$\lvert d_{xy}\rvert$	abs. IP in xy plane	< 0.05 cm
d_z	IP along the beam line	< 0.1 cm
d/σ_d	3D IP	< 8
I_r	isolation criteria	$< 0.4 \cdot p_T$
$\sigma_{i\eta i\eta}$	electron supercluster shape	$\{0.011/0.030\}$
H/E	H (E) energy deposited in the HCAL (ECAL)	< 0.1
1/E-1/p	E – cluster energy, p – track momentum	$>$ -0.04
conv.	photon conversion rejection	True
miss.	missing inner hits in tracker	$= 0$
ID	`mvaFall17V2noIso_WP[L/90]` ID	$\geq$ WP-loose/WP-90
ID	`MVA ttH`	$\geq$ WP-loose

Table 6.8

Muon selection

Observable	Description	Value
p_T any	transverse momentum	> 10 GeV
$\lvert\eta\rvert$	abs. pseudorapidity	< 2.4
$\lvert d_{xy}\rvert$	abs. IP in xy plane	< 0.05 cm
d_z	IP along the beam line	< 0.1 cm
d/σ_d	3D IP	< 8
I_r	isolation criteria	$< 0.4 \cdot p_T$
ID	PF muon ID	$\geq$WP-medium
ID	`MVA ttH`	$\geq$WP-loose

As for the final lepton selection, their kinematic properties such as transverse momentum, p_T, and pseudorapidity, η, are used to select good physics objects. These parameters are chosen to cover the detector region where good identification and reconstruction is possible. Also, the so-called IPs are used: $|d_{xy}|$ – absolute distance with respect to the PV in xy plane, d_z – the distance along the beam line and d/σ_d – the significance of the 3D IP with respect to the PV. These allow to disadvantage particles originating from SVs and cosmic muons.

Electrons and muons coming from signal events are expected to be isolated, while misidentified leptons or leptons coming from background processes are often reconstructed within jets or simply have other objects near them. Therefore, mini-isolation criteria, I_r, defined in Eq. (6.5) is used.

$$I_r = \sum_{charged} p_T + \max\left(0, \sum_{neutral} p_T - \rho A \left(\frac{R}{0.3}\right)^2\right), \tag{6.5}$$

where the scalar sum of transverse momenta of charged hadrons and the scalar sum of transverse momenta of neutral hadrons and photons are used, here PU is accounted for with the ρA variable: ρ is the event-specific average PU energy density per unit area in the $\phi - \eta$ plane and A is the effective area specific to the given type of isolation, lastly R is the radius of interaction cone for which the isolation has to be calculated. This method is called “mini” because, as shown in Eq. (6.6), R shrinks as lepton’s transverse momentum increases, this allows for increased efficiency for boosted topology reconstruction and proved superior than other isolation requirements tested. A value of 0.4 corresponds to a loose WP.

$$R = \begin{cases} 0.05 & \text{if } \ p_T > 200 \text{ GeV} \\ 10 \text{ GeV}/p_T & \text{if } \ 50 \text{ GeV} < p_T < 200 \text{ GeV} \\ 0.20 & \text{if } \ p_T < 50 \text{ GeV} \end{cases} \tag{6.6}$$

Additionally, for electrons, the objects need to satisfy a set of conditions to mimic the electron identification criteria applied at the trigger level, thus ensuring a high probability that the selected object is a prompt lepton. First, the electron supercluster shape in η-direction ($\sigma_{i\eta i\eta}$) must be below a certain value. Two values are shown in the table that represent the expected values in the ECAL barrel and in the ECAL endcap region, respectively. To reduce fake electron acceptance, H/E and $(1/E - 1/p)$ are used, where H/E is the ratio of electron’s energy deposited in the HCAL to the energy in the ECAL. And $(1/E - 1/p)$ shows the difference between the inverse of the energy of the electron cluster and the inverse of its track momentum. Moreover, photon conversion to electrons should be rejected and there should be no missing inner hits even more ensuring a high quality track and its reconstruction, thus having a low probability of misidentification.

Equally important for both electrons and muons is to pass a dedicated identification criterion. For electrons `EGamma POG` (Electron and photon physics object group) has created a MVA trained on MC samples of DY with jets which effectively sorts true electrons and electrons coming from jet backgrounds. Training is carried out using `xgboost` [146] and performed in six (p_T, η) categories and also offers a criteria with isolation parameters included. There is a slight difference for the ID used for Run 2 and Run 3 years in this analysis, for Run 2 `mvaFall17V2noIso_WPL` is used while for Run 3 `mvaNoIso_WP90`. The loose WP (WPL) corresponds to around 98 % signal efficiency for electrons with $p_T > 10$ GeV and would have been preferred over WP90 which has only 90 % signal efficiency. Sadly, it was not available within this Thesis timeline. For muons, `Muon POG` (muon physics object group) have developed a criterion to distinguish prompt muons from fakes, this cut-based ID has been trained on muons coming from W decays. A loose muon criterion with 99.5 % signal efficiency for muons with $p_T > 20$ GeV is chosen (`mediumId`). This ID does not include explicit isolation criteria.

To improve object modelling, electron residual energy scale and resolution corrections are applied. Similarly muon momentum and scale corrections are also applied before selecting any object, as it is possible to model the object with higher resolution than our detector can detect. Finally, since lepton identification and reconstruction efficiency differ in data and MC, dedicated SFs are used for each object. The lepton SFs are calculated with Eq. (6.3) and, as mentioned previously, are calculated in regions of transverse momentum and pseudorapidity due to lepton varying kinematics.

6.4.2. Jet and Missing Transverse Energy Selection and Calibration

Due to the hadronic decays of vector bosons in the $HH \rightarrow WW^*ZZ^* \rightarrow 4l$ decay channel, jets are equally important as leptons for this analysis. Ideally, the category 4.1 would expect two jets, while the category 4.2 would expect four. Sadly, jet reconstruction and identification is not a trivial task, and even with the CMS detector it is not as straightforward. Therefore, looser selection for jets is required to allow more effective signal acceptance. Moreover, in the decay channel, where $W \rightarrow l\nu$, a part of the energy is carried away by neutrinos. The CMS detector is not designed to detect them, their presence can be evaluated only inexplicitly, since some MET must be accounted for in the detector. Also, for the requirement on the MET, a rather loose selection is applied.

An analogous study of jet transverse momentum distributions was performed to see if any differences in the shapes for background and signal jets could provide a good discriminator. Within an event, jets are sorted by their transverse momentum in a decreasing manner, and as can be seen in the example for the category 4.1 in Fig. 6.8, the signal jets are on average softer, indicating that the transverse momentum threshold should be as low as possible. At the same time, low-p_T jets are very difficult to reconstruct and identify confidently in our detector, and often the available modelling does not describe the data well. Thus, a compromise was reached to increase the transverse momentum threshold to 25 GeV for each jet. The reasoning for this decision will be expanded further in this section.

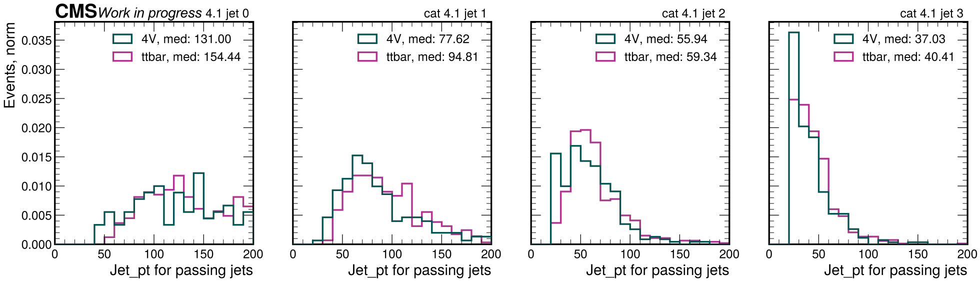

Figure 6.8. Comparison between jet transverse momentum shapes for the leading and sub-leading jets for the signal ("4V") and $t\bar{t}$ background, example for the category 4.1, 2022EE MC; value indicates the mean of the distribution.

Combatting the $t\bar{t}$ background was still a priority, therefore jet tagging was used. As mentioned in Section 4.3, due to different event topologies reconstructed jet flavour can be classified using jet kinematic information, therefore this Thesis benefits from vetoing jets with heavy flavour. Dedicated deep neural networks (DNNs) have been trained and maintained by the `BTV POG` (b-tagging and vertexing physics object group). These DNNs have been trained on QCD multijets and fully hadronic $t\bar{t}$ events and allow to assign a probability that a jet has a b quark origin. The recommended tagger `DeepJet` [110] was used and its WPs were tested to find the most optimal for this analysis. In the end, WP-loose was chosen, which has around 90 % b-tagging efficiency for b jets and around 10 % mis-tagging efficiency for light jets. Thus, the events are rejected if there is at least one jet that passes the lowest WP of the `btagDeepFlavB`. This requirement, together with other lepton related requirements, have allowed to significantly reduce $t\bar{t}$ influence as will be shown in the next section.

Table 6.9

Jet selection, with (*) marked requirements that are applied for Run 2 period only

Observable	Description	Value
p_T	transverse momentum	> 25 GeV
$\lvert\eta\rvert$	pseudorapidity	< 2.4
`btagDeepFlavB`	b-tagger	< WP-loose
jet ID	jet quality ID	True
jet PU ID*	PU rejection	True
overlap	rejected if an ID'd lepton in $\Delta R < 0.4$	True

Table 6.9 summarises the final selection for jets. Jets are mainly selected based on their kinematic parameters transverse momentum, p_T, and pseudorapidity, η. If a jet is near ($\Delta R < 0.4$) a lepton that has passed the default ID, it is considered that it overlap the lepton, and the jet is discarded. Moreover, jets are required to pass the tight jet ID. This ID has a signal efficiency of more than 98 % and background rejection greater than 98 %. For Run 2 jets with transverse momentum below 50 GeV, an additional PU ID is

applied to help separate signal jets from PU jets. This ID has a signal efficiency higher than 95 % throughout the entire detector region, regardless of the average PU. As the default jet collection has changed in Run 3, currently there is no need to apply a similar ID, therefore, the entry in Table 6.9 is marked with a star.

Regarding jet corrections, the recommendations of `JetMET POG` (Jet and missing transverse energy physics object group) are followed. The most up to date jet energy corrections (JECs) are applied and jet energy resolution (JER) in MC is smeared accordingly as introduced in Chapter 4. Moreover, to avoid problematic regions with anomalous “hot” or “cold” jet activity, a dedicated veto map is applied. This rejects jets that fall in this region (recommended approach for Run 2) or rejects the whole event (recommended approach for Run 3) if a jet has landed in the vetoed region. These maps are produced centrally and their usage is encouraged for Run 2 analysis and mandatory for Run 3.

As mentioned before, for jets, a slightly different SF is designed to account for different b jet identification (or tagging) and mis-identification efficiency. Jet SFs are calculated in regions of transverse momentum, pseudorapidity, and flavour. As this analysis deals only with non b-tagged jets, the SF formula simplifies to Eq. (6.7):

$$SF_{jets} = \prod_{j} \frac{1 - SF_j(p_T, \eta, \text{flav})\varepsilon_j(p_T, \eta, \text{flav})}{1 - \varepsilon_j(p_T, \eta, \text{flav})}, \tag{6.7}$$

where j corresponds to jets failing b-tagging, $\varepsilon_j = \dfrac{N_{\text{b-tagged jets}}}{N_{\text{total jets}}}$ is the b-tagging efficiency obtained from simulation, or simply put, the fraction of jets passing a certain WP, SF_j is a SF for a certain WP. For an example, in the case of light flavoured jets, the b-tagging efficiency, ε_j, should be close to zero, as higher values would indicate misidentification. Therefore, for light jets the SF_{jets} is very close to unity, while in the case of true b jets, the eventual SF should be influenced.

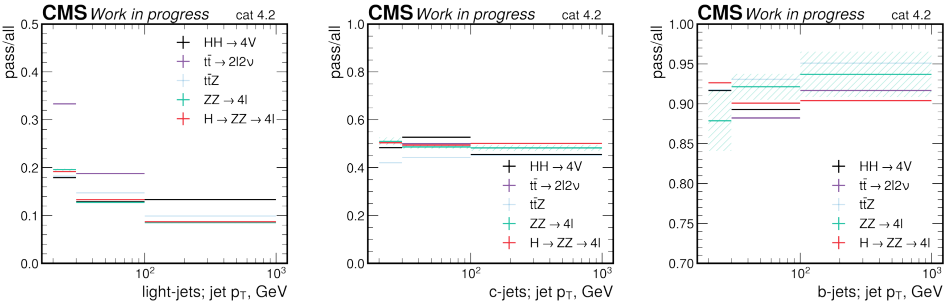

Figure 6.9. b-tagging MC efficiencies across jet transverse momentum for various processes, for light jets, c-jets, b jets, example for the category 4.2, 2022EE MC.

The b-tagging efficiency in MC is calculated in analysis phase-space without applying the veto on b-tagged jets. Due to the limited statistics, these are calculated from three MC samples – (a) $HH \to VVVV$ and applied to Higgs boson pair samples, (b) $H \to ZZ \to 4l$ and applied to single-Higgs boson backgrounds and (c) $ZZ \to 4l$ and applied to other backgrounds. ZZ is chosen as the universal sample due to it being one of the main backgrounds and within each year, these samples are rich in statistics (in comparison to $t\bar{t}$ which provides just a few MC events in the SR). An example of b-tagging MC efficiencies calculated for the `2022EE` era are shown in Fig. 6.9 across a selection of processes for light jets, c-tagged jets, and b-tagged jets, respectively. Not to oversaturate the figure only uncertainties from the ZZ sample are shown.

The final efficiency maps are calculated across p_T and $|\eta|$, and an example from the `2022EE` era's MC for light jets are shown in Fig. 6.10. Here, the transverse momentum is binned starting from 20 GeV, showing that at low-p_T and high-$|\eta|$ regions the efficiencies for light jets are larger. That means that mis-tagging is greater. Therefore, it was decided to sacrifice signal sensitivity and increase the jet transverse momentum threshold to 25 GeV to skew further away from the problem areas. The lost fraction of the signal varies depending on the era analysed, ranging from 30 % in the 2023 dataset to 40 % in 2018.

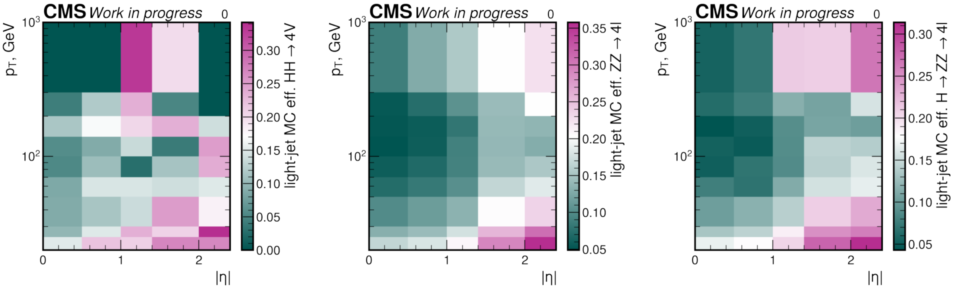

Figure 6.10. b-tagging MC efficiencies across jet transverse momentum and pseudorapidity for light jets (0), 2022EE.

Regarding the MET, the default one is selected in each period – PF MET in Run 2 and PUPPI MET in Run 3. This quantity has the Type-I correction applied. The Type-I correction simply propagates the JECs to the MET. If the recommended JEC version has changed since the production, the Type-I correction is recalculated with the up to date correction set. An additional correction is applied within the analysis propagating jet smearing. Thus, MET is recalculated after the jet smearing in MC.

6.4.3. Event Categorisation

As introduced previously, this Thesis focusses on two out of three four-lepton decay channels. To target these two different final states, two subcategories are designed – the subcategory 4.1 that targets the $HH \to WWZZ \to l\nu l\nu\ llqq$ decay channel and the subcategory 4.2 that targets the $HH \to WWZZ \to qqqq\ llll$ decay channel. For simplicity throughout this Thesis, subcategories are denoted as categories. If the event satisfies trigger selection described in Section 6.2 and four leptons pass the criteria described in Section 6.4.1, then the next step is the categorisation of events. Here, the event is sequentially tested against requirements shown in Fig. 6.11. After the event has passed either of the sequences, it is referred to as in the pre-selection phase.

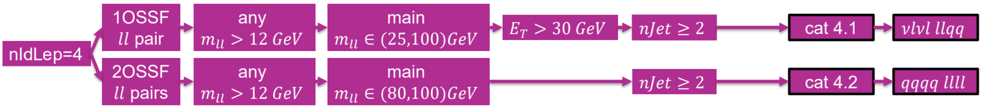

Figure 6.11. Sequential event categorisation for four-lepton categories.

In the category 4.1, two di-lepton pairs are constructed – one OSSF ll pair and one OSOF ll pair. Both pairs are required to have $m_{ll} > 12$ GeV and one must pass the loose invariant mass window of $m_{ll} \in (25, 100)$ GeV. As both W bosons are expected to have neutrinos in the decay, the missing energy must exceed $E_T > 30$ GeV. In addition, the event should have at least two jets to account for the hadronically decaying Z.

In the category 4.2 two OSSFs ll pairs are built, both are required to satisfy at least $m_{ll} > 12$ GeV and one pair must pass the tight mass window targeting the on-shell Z decay with $m_{ll} \in (80, 100)$ GeV. To account for the hadronically decaying W bosons, the event should ideally have at least four jets, giving room for reconstruction errors. In fact, if pairing of leptons would allow the event to be classified either in category 4.1 or category 4.2, the 4.2 definition is preferred. The lepton pairing is always done in the most optimistic way, e.g., choosing combinations that favour both pairs to have $m_{ll} > 12$ GeV. Initial studies used a looser lepton invariant mass window of $m_{ll} \in (60, 120)$ GeV, however, tightening it to $m_{ll} \in (80, 100)$ GeV provided a medium improvement in the statistical significance. Moreover, such a mass window will help in the HH combination, as it is inverted to the one used in the $HH \to WW^*WW^* \to 4l$ search channel.

Requiring exactly four jets in the category 4.2 proved to be inefficient. Several studies were performed to compare the statistical significance of jet multiplicity above one, two, three, and four jets in the pre-selection stage and propagating this data input to the BDT stage (described in detail in Section 6.4.4). It was found that requiring the event to have at least two non b-tagged jets gave the highest statistical significance, while providing enough training data for the BDT model. For the category 4.1, targeting two jets proved to be effective. When this requirement was reduced to requiring at least one non b-tagged jet, the statistical significance was increased in the pre-selection stage, however, the BDT was not as effective at rejecting the background. Thus, the initial requirement of non b-tagged jet multiplicity remained. Since this study, the requirement for the transverse momentum of jets had to be increased. The reevaluation of the BDT sensitivity studies for other jet multiplicities and possible changes remains outside the scope of this Thesis, however, are taken into account in the accompanying physics analysis summary.

No requirement is set on the invariant mass of the jet system, as early studies did not show a strong separation power for it. However, such a variable is included as a feature in the trained BDT. Similarly, also no requirements on the angles between jets and/or leptons are set in the pre-selection phase, but these variables are provided as features for the BDT. For more details, see Section 6.4.4.

To verify whether lepton pairing is done as expected, a truth-level lepton parent study was performed. Fig. 6.12 shows the average parent `pdgId`. Meaning, if a pair has parent `pdgId=23`, both leptons have come from a Z boson, however, if it is 23.5 one parent is a Z boson, while the other one is a W boson. Ideally, the lepton pairing would be done so no cross association is present (no average parent `pdgId`=23.5), moreover, the category 4.2 would peak only at 23, while 4.1 would have both 23 and 24 (Z boson parents and W boson parents). Clearly, the distinction is not as pronounced, but category 4.2 is more effective at selecting leptons from Z boson than the category 4.1. Following alternative pairing studies, it was decided not to include more requirements on the lepton pair, such as the angular distance between them, to improve the pairing in the pre-selection phase but rather to provide this information in later steps.

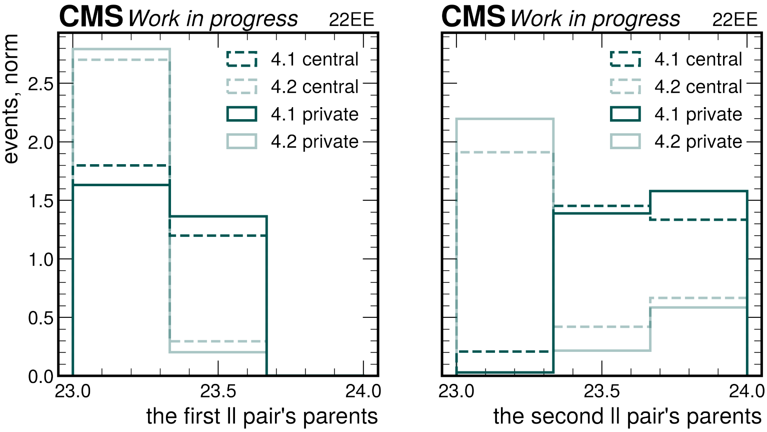

Figure 6.12. Lepton parent study in four lepton categories, example from 2022EE comparing signal from the inclusive (central) and filtered (private) samples across both categories.

The event migration between lepton multiplicities was investigated by studying the number of truth-level leptons in the event. It was found that both upward and downward migrations were introduced by misreconstruction and/or misidentification. Upward migration might occur when a non-prompt lepton passes signal requirements or a jet is wrongfully reconstructed as a lepton that passes the requirements. Downwards migration can happen if a prompt lepton does not pass the requirements (e.g. chooses phase-space outside of the detectors fiducial space), thus is lost or coincides with a jet, making it impossible to distinguish the two originating objects. As events with higher lepton multiplicities are rarer, three-lepton events are the main contamination in four-lepton categories.

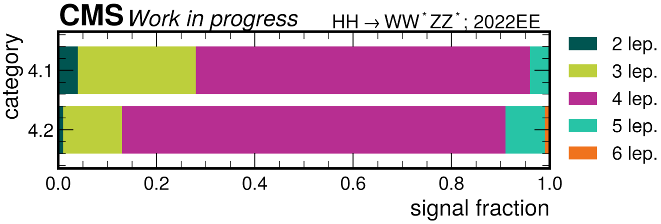

Figure 6.13. Truth-level lepton multiplicities found in an event with four reconstruction-level leptons, example from 2022EE eras signal sample.

Figure 6.13 shows what signal ($HH \to WW^*ZZ^*$) fraction is taken up by various truth-level lepton multiplicities. In category 4.1, around 68 % of $HH \to WW^*ZZ^*$ are true four prompt lepton events, while in the category 4.2 around 78 % are true four prompt lepton events. Overall, this is a satisfying result, as mostly loose WPs are selected for lepton identification. That is, higher acceptance was favoured over purity. Upon evaluating the purity and possible category sensitivity, it was decided not to perform a fake-rate correction or impose further restrictions for the initial analysis. However, this remains a possibility for further improvements.

As the categorisation is defined, it is the time to address the phase-space overlap with the four-lepton category of the CMS HH multilepton analysis [34]. This category (for simplicity further denoted as "4W" category) is built to target the $HH \to WW^*WW^*$, thus a Z boson mass veto is applied, rejecting events where $m_{ll} \in (80, 100)$, where in this Thesis category 4.2 one of the pairs must fall exactly in this mass window, while in the category 4.1 the mass window is looser $m_{ll} \in (25, 100)$. The 4W category does not set any requirements on the number of jets (however, also reject events with loosely b-tagged jets), while for 4.1 and category 4.2 at least two jets need to be present. Also, in the 4W category, the second softest lepton is required to have $p_T > 15$ GeV. It can be concluded that minor phase-space overlap is present, however, it can be dealt with when at the combination stage.

6.4.4. The BDT Classifier

The described object selection and event categorisation targets the signal well, however, it does not discriminate enough events coming from the background processes. Thus, a dedicated observable needs to be constructed which has a strong background discriminating power in favour of the signal. For this analysis, it was decided to obtain it by creating and training a BDT. A BDT is a ML technique that combines a sequence of weak decision trees to form the prediction. Weak in this case signifies that each tree applies very few assumptions about the data and each next tree tries to correct the errors of the previous one. In this Thesis, the BDTs are built using the `XGBoost` (Extreme Gradient Boosting) method [146], and after applying the model to the data, a BDT score distribution is obtained which helps extracting the signal events.

A BDT model is trained per category and per Run. As the BDT score distributions are obtained, a threshold is evaluated separately in each year with the aim of giving the highest sensitivity while taming the MC uncertainty. Thus, after passing the event pre-selection detailed in Section 6.4.3, the event has to pass the final BDT score threshold to be considered in the SR. More on the journey towards it, is summarised in this section.

As the first step, the most optimal input data were investigated for the BDT training. Signal-wise, dedicated filtered samples of $HH \rightarrow WW^*ZZ^*$ with at least four leptons were used. Ideally, a BDT per era would be trained, but as not enough signal events were available in each of the eras, it was decided to build two BDTs – one in each Run, thus combining the events across eras to increase statistics. Before doing this, it was checked that there were no significant differences in the distributions of signal variables across eras. An example of Run 3 can be seen in Fig. 6.14, where a few distributions are compared across eras. The ratio plots at the bottom of each figure show the differences with respect to the `2022EE` era, which had the most statistics. Overall, a good agreement is reached with some tension in high-jet multiplicity in `2023BPix` era which can be attributed to a statistical fluctuation due to the lowest available statistics. Background-wise, another study was performed to see what mixture would give enough statistics to be trained on and would be representative of the pre-selection situation in the categories. Using only the dominant background, ZZ, was quickly ruled out as it did not give enough discriminating power. Similarly, using the background mixture only from the (luminosity) dominant era was ruled out due to low statistics. For the Run 2, the dominant era is `2018`, while for the Run 3 it is the `2022EE` era. Also, using all available events across all eras was ruled out as some samples simply had more statistics, while they were not representing the majority of the event fraction. Thus, a slightly filtered mixture was chosen, where the richest samples

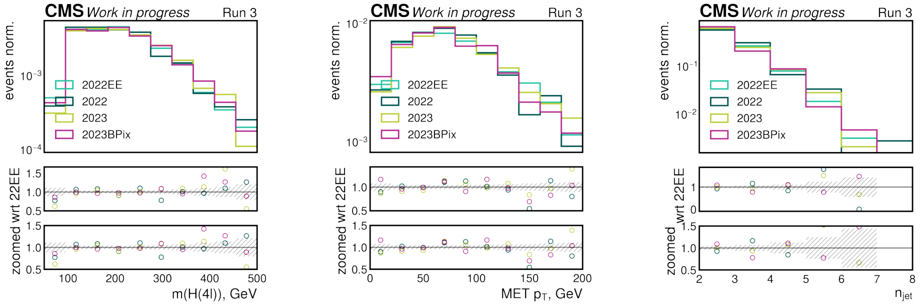

Figure 6.14. Comparison between signal input across years, four lepton invariant mass, missing transverse energy and jet multiplicity, Run 3 example.

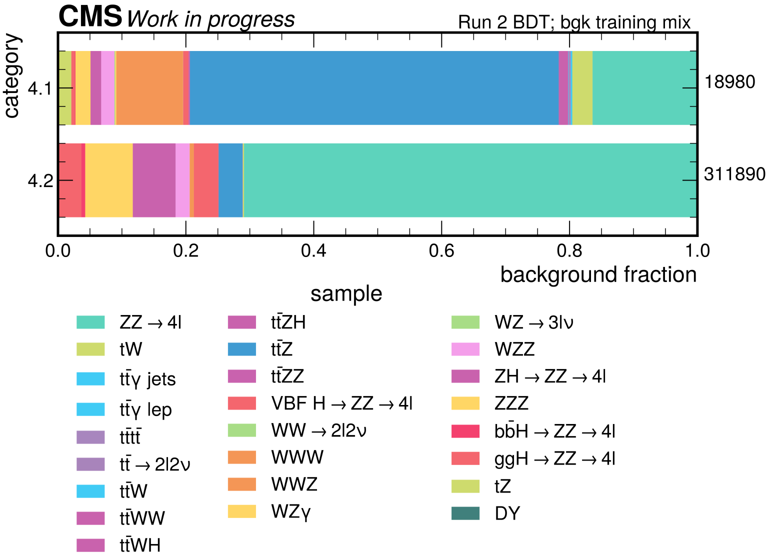

(a) Samples from filtered mixture as the background mixture used for training

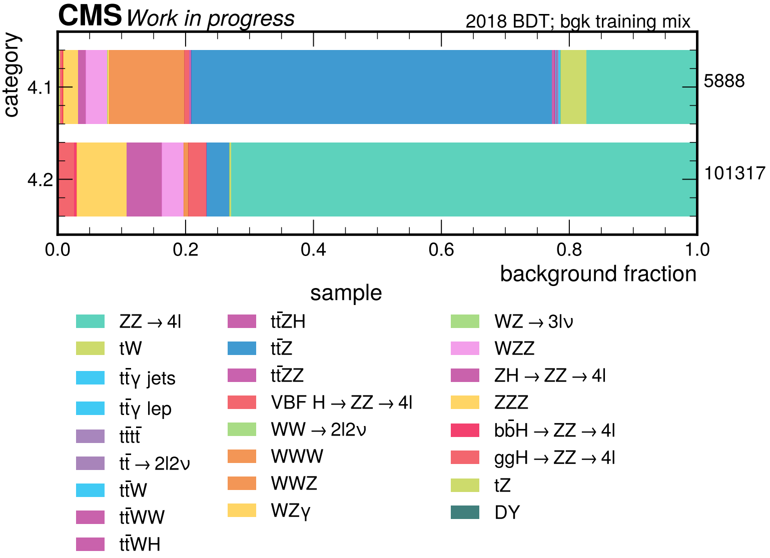

(b) Samples from the dominant era as the background mixture used for training

Figure 6.15. Comparison between background mixture used for training Run 2 BDTs, each colour denotes different samples or sample groups, while the total amount of events are printed on the right.

were chosen only from the most (luminosity) dominant era.

An example for the Run 2 BDT model is shown in Fig. 6.15. Figure 6.15a hows the background mixture obtained using the filtered-mixture approach, while Fig. 6.15b shows the result obtained using only the dominant era. Several things can be concluded upon examining the figure. First, fewer events are available to train the BDT for category 4.1 compared to category 4.2; second, each BDT has a dominant background against which it is trained; third, relative BDT background mixtures in each category are different across the categories; fourth, the relative distribution within the category but between a filtered mixture or only from the dominant era remains practically the same, thus allowing to increase the training, testing, and sampling datasets. Altogether, the filtered mixture approach allows to train a dedicated BDT with sufficient performance as will be shown below.

Furthermore, a study was performed to see if one BDT training could serve both categories. An example of the BDT scores for models trained on various input data can be seen in Fig. 6.16. On the left, the model is trained on data only from category 4.1, on the right on data only from category 4.2, and in the middle a single model has been trained on the data from both categories. It can be seen that both individual models have drastically different shapes, while the combined one is closer to the one of the 4.2-only model, indicating that the information from category 4.1 is lost. With the combined approach there are more events to train on, however, due to slightly different kinematics and unequal number of available events it was ruled out.

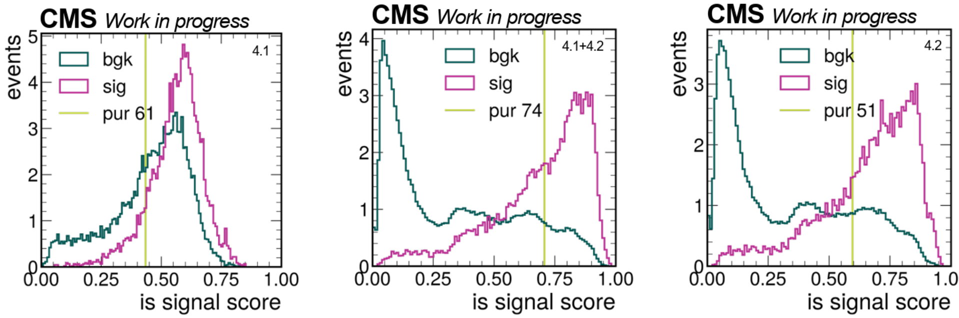

Figure 6.16. BDT score distributions for various BDT input mixtures, only category 4.1 on the left, mix of both categories in the middle and only category 4.2 on the right. Marked in light green is the BDT value threshold providing highest stat. sensitivity.

As the second step, the most impactful input features were investigated. As a BDT was chosen instead of a DNN, high-level physics-inspired event features were created rather than choosing some of the low-level variables. These high-level inputs should allow the BDT to recognise kinematic quirks specific for signal events and not as common in the background. Minimal and maximal angular distances between lepton-lepton, lepton-jet distances per lepton, Higgs candidate related features when the candidate is built from

Table 6.10

Overview of the final BDT input features for the category 4.1 (in column 4.1) and the category 4.2 (in column 4.2) marking in which Run's BDT it has been used

Feature	4.1	4.2	Description
$\max(\Delta R(E_T j_i))$	3		maximal angular distance between MET and a jet
$\min(\Delta R(E_T j_i))$	2; 3		minimal angular distance between MET and a jet
$\max(\Delta R(l_2 j))$	2		maximal angular distance for the sub-sub-leading lepton and its closest jet
$\min(\Delta R(l_0 j))$	2; 3	2; 3	minimal angular distance for the leading lepton and its closest jet
$\min(\Delta R(l_1 j))$	2; 3	2; 3	minimal angular distance for the sub-leading lepton and its closest jet
$\min(\Delta R(l_2 j))$	2; 3	2; 3	minimal angular distance for the sub-sub-leading lepton and its closest jet
$\min(\Delta R(l_3 j))$	2; 3		minimal angular distance for the softest lepton and its closest jet
$\max(\Delta R(l_0 l_i))$	2; 3	2	maximal angular distance for the leading and another lepton
$\min(\Delta R(l_1 l_i))$	2; 3		maximal angular distance for the sub-leading and another lepton
$\min(\Delta R(l_0 l_i))$	2; 3	2; 3	minimal angular distance for the leading and another lepton
$\min(\Delta R(l_1 l_i))$	2; 3	2; 3	minimal angular distance for the sub-leading and another lepton
$\min(\Delta R(l_2 l_i))$	2; 3	2; 3	minimal angular distance for the sub-sub-leading and another lepton
$\min(\Delta R(l_3 l_i))$	2; 3	2; 3	minimal angular distance for the softest and another lepton
$y(HH)$		2; 3	rapidity for the HH candidate built from leptons and jets
$m(HH)$		2; 3	invariant mass for the HH candidate built from leptons and jets
$m_T(HH)$	2; 3	2; 3	transverse mass for the HH candidate built from leptons and jets
$p_T(HH)$		2; 3	transverse momentum for the HH candidate built from leptons and jets
$\eta(HH(4l))$	3	2	pseudo-rapidity for the HH candidate built from leptons
$m(l_1 l_2)$	2; 3	2; 3	invariant mass for first two leptons
$m(l_3 l_4)$	2; 3	2; 3	invariant mass for last two leptons
$m(H(4l))$	2; 3	2; 3	invariant mass for the Higgs candidate built from leptons
$m(Z)$	2; 3	2; 3	invariant mass for Z candidate, if applicable the on-shell
$m(H(lljj))$		2; 3	invariant mass for the Higgs candidate built from leptons and jets, candidate with mass closest to 125 GeV
$m_T(H(4l))$	2; 3	2; 3	transverse mass for the Higgs candidate built from leptons
$p_T(H(llE_T))$	3	2	transverse momentum for the Higgs candidate built from two leptons and missing transverse energy
$p_T(H(4l))$	2; 3	2; 3	transverse momentum for the Higgs candidate built from leptons
$\max(b_{score})$	2	3	maximal b-tagger score for jet
$\sum(b_{score})$	2		sum of b-tagger scores for jets
$m(jets)$		3	invariant mass for leading jets
$m(W(jj))$	3	2; 3	invariant mass for two jets, candidate with mass closest to $(m_Z + m_W)/2$ is chosen
$m(jj)$		2; 3	invariant mass for two leading jets
$\sum p_T(jets)$	2; 3		scalar sum of leading jet transverse momentum
$\sum \vec{p}_T(jets)$	2; 3	3	vectorial sum of leading jet transverse momentum
$METp_T$	2; 3	2; 3	missing transverse energy
n_{jet}	2	2; 3	number of b-vetoed jets

all four leptons, all jets or mixed (as in the category 4.1), HH candidate related features, jet related features, and global event features were considered as potential BDT input features.

Clearly, not all parameters are equally impactful in training the BDT, and ways to define the minimal sufficient set were explored. This is crucial when dealing with low-statistics samples. In the first step, a model with all the mentioned features was trained and the performance of each features was evaluated based on its gain (average improvement in accuracy brought within each split), cover (relative quantity of observations that pass through the split), weight (times the quantity is used to split), as well as its SHapley Additive exPlanation (SHAP) values [147].

The SHAP values show how much a feature impacts the prediction of a model relative to the baseline. Each dot in the drawn shape signifies an event, the colour of it denotes if the feature of this event has a relatively low or high value. Thus, strongly polar impacts both in the shape and colour tend to be the most impactful. The problem with gain-cover-weight is that their ranking and importance sometimes are not easy to interpret, while the SHAP shapes are more intuitive and visually pleasing.

In the second step, a subset of the highest performing features was chosen and a new, pruned BDT was trained. To optimise the feature set even further, a correlation matrix was examined, assuming that redundant features that exhibit a strong (anti)correlation could be dropped. The selection of the top 25 features was found to be a compromise between the number of features and the sensitivity achieved. The final set for both categories can be seen in Table 6.10 where the features present in each BDT model for Run 3 BDTs are marked with “3”, while the features present in Run 2 models are marked with “2”. It is important to note that both BDTs prefer a slightly different set of top features.

The top 10 highest ranking feature SHAP shapes can be seen in Fig. 6.17 for all BDT models. From comparing the SHAP values of the leading features, we can see that for category 4.2 the BDT strongly benefits from the Higgs boson and the HH candidate features. This is somewhat expected, as all leptons are expected to come from both decaying Z bosons. On the other hand, in category 4.1 the BDT has learnt to recognise angular variables. Overall, multiple features have strongly polar distributions with relatively high impact. It is interesting to note that the ranking of the top 10 performing features slightly differs between Run 2 and Run 3 4.1 BDTs while it remains practically the same for 4.2 BDTs. Moreover, the SHAP shapes are slightly different not only across different category models, but also across different Runs. This is probably due to input statistics rather than explicitly different physics at various centre-of-mass energies.

As the third step, the BDT architecture was optimised using the k-fold cross-validation on sets of hyperparameters to find the most optimal set of values that would give the lowest average error. Regarding the data, 20 % of the input was split off for testing, while validation was performed on the data for each era. In the end, the logarithmic loss

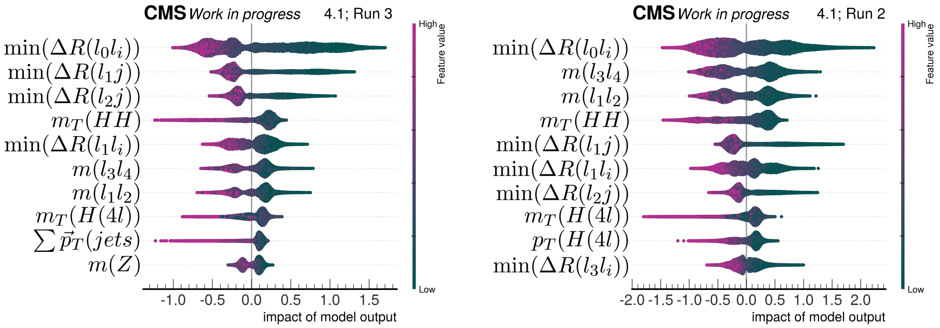

(a) BDT for category 4.1, Run 3

(b) BDT for category 4.1, Run 2

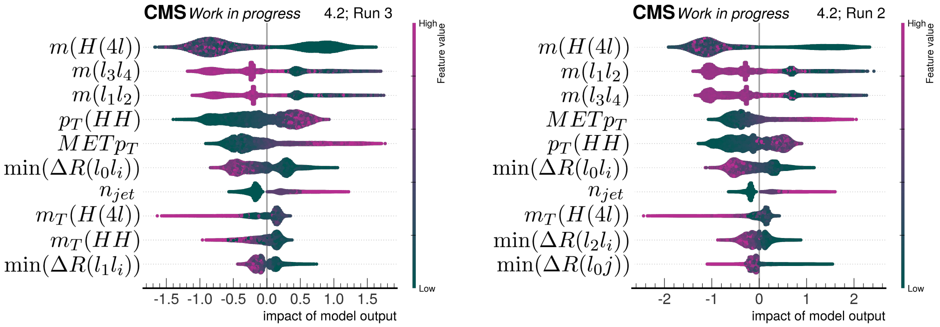

(c) BDT for category 4.2, Run 3

(d) BDT for category 4.2, Run 2

Figure 6.17. Top 10 SHAP values for BDT features.

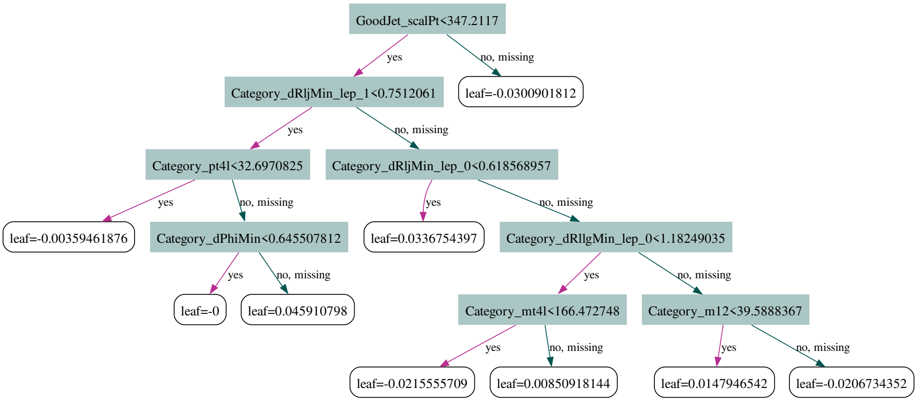

Figure 6.18. 42nd tree in Run 3 BDT model for category 4.1.

between the true value and predicted probability was used to solve the binary problem (if the event is signal-like or not). Regarding the BDT hyperparameters, each model was given 500 boosting rounds or epochs to optimise, while if the BDT had not improved significantly for 15 rounds, it was stopped. The learning rate was set to 0.1 and the maximum depth was set to four trees. The positive weight scale was always adjusted to equal the number of signal and background events for training, meaning, that this parameter changed for each model. Also, γ, which is the minimum loss reduction required to make a further partition on a leaf node of the tree, was adjusted as $\gamma = 5$ for 4.1 models and $\gamma = 20$ for 4.2 models. Similarly, α, which is a level-1 regularization term on weights, was chosen $\alpha = 5$ for 4.1 models and $\alpha = 20$ for 4.2 models. This increase lead to more conservative models.

For evaluating the BDT performance, the receiver operating characteristic (ROC) curve and area under curve (AUC) were used as metrics. The models were designed to have the highest AUCs while keeping both training and testing values similar, so as not to overtrain the model. The final Run 2 BDT model for category 4.1 completed 130 epochs, while Run 2 BDT model for category 4.2 completed 156 epochs. At the same time, Run 3 BDT model for category 4.1 took 74 epochs to train and Run 3 BDT for category 4.2 took 114. Thus, this number amounts to the number of weak learners or trees within each model. An example of the 42nd tree in the Run 3 BDT for category 4.1 is visualised in Fig. 6.18. From the example, it can be seen that the maximal depth of four trees is respected, yet some levels already lead to leafs rather than the next depth.

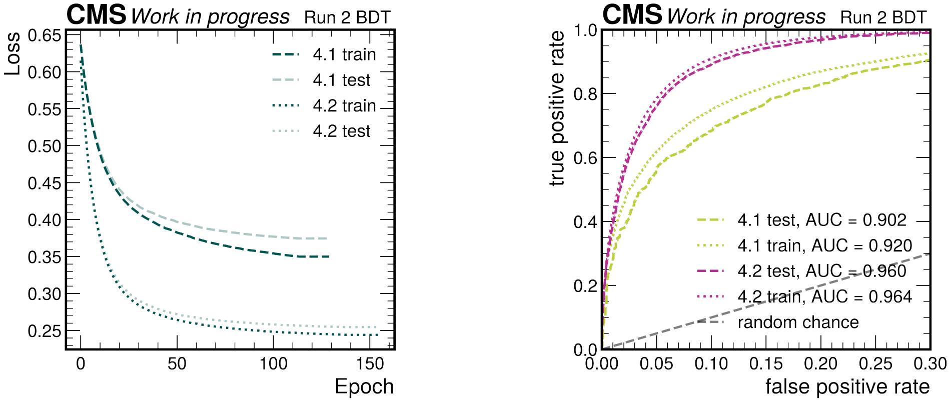

(a) logloss (logarithmic loss between the true value and predicted probability) for testing and training

(b) receiver operating characteristic curve for training and testing samples

Figure 6.19. BDT performance parameters for Run 2 BDTs.

An example of the characteristics described above for Run 2 BDTs are shown in Fig. 6.19. The evolution of the logloss function per each training epoch is shown in Fig. 6.19a for both the training and the testing datasets. For easier comparison, both

4.1 and 4.2 BDTs are plotted together. Firstly, it can be seen that the 4.2 BDT reaches an overall lower loss function values with fewer epochs, however, the 4.1 BDT takes less overall epochs to reach a stable state with no more improvements in reducing the logloss function. Secondly, the optimised function value is lower for the 4.2 BDT than for the 4.1 BDT. Thirdly, the difference between the training and testing datasets increases with each epoch and remains larger for the 4.1 BDT model than for the 4.2 BDT. This can be partly explained by lower statistics, partly by more challenging physics final state to recognise. In Fig. 6.19b, the ROC curve is shown. Overall, 4.2 BDT has a higher AUC and both training and testing AUC are very similar, however, both 4.1 BDT and 4.2 BDT perform significantly better than just a random choice. Comparing the AUCs, it can be seen that the testing sample has slightly worse performance, however, the algorithm is not overtrained.

As the fourth step, a suitable threshold was evaluated on the BDT score to classify an event in the SR. As the overall sensitivity is not as high, this BDT score value signifies that it is more likely to find signal above, rather than below it. And it is not true to say that an event with a BDT score higher than this value is more likely to be signal, rather than background. In the following figures, the BDT score will be denoted as “is signal score”. Further down a clear example with the yields and contributions will be given.

Regarding the choice of the threshold, as MC statistics vary in each era, it was decided against setting a single BDT score value as a threshold for the entire Run, to avoid suffering from high MC uncertainties or weak discriminating power. Thus, a different BDT score threshold has been set for each era. This was done by looking for the highest statistical significance which can be calculated using Eq. (6.8), where S – signal and B – background, and w_i – the weight of the event.

$$sen = \frac{S}{\sqrt{B}} = \frac{\sum w_i^S}{\sqrt{\sum w_i^B}} \tag{6.8}$$

In addition to the highest statistical significance MC can provide, a low relative uncertainty on the signal (calculated as Eq. (6.9)) $S_r < 20$ % in the signal-like region (high tail of the BDT output score) and a reasonable uncertainty on the background $B_r < 36$ % were required. This protects from choosing a threshold above which there are too few events and any decision might be worse than a flip of a coin. Ideally, the binning for this search would be very fine and the relative uncertainty of sensitivity Eq. (6.10) would always be kept below 20 %. However, this proved to be very challenging in some eras because of the statistically limited samples. Thus, a very coarse binning was used.

$$S_r = \frac{dS}{S} = \frac{\sqrt{\sum w_i^2}}{\sum w_i} \tag{6.9}$$

$$\left(\frac{S}{\sqrt{B}}\right)_r = \frac{d(S/\sqrt{B})}{S/\sqrt{B}} = \sqrt{S_r^2 + (1/2 \cdot B_r)^2} \tag{6.10}$$

Two scenarios are shown in Fig. 6.20, (1) when evaluated using only $HH \rightarrow WW^*ZZ^*$ (dark green, Y, solid line) and (2) when the entire contribution of HH decays (light green, +, dashed line). For an easier comparison, the values are normalised with respect to the highest statistical significance calculated from the (1) case, showing their relative evolution. Points present in the graph pass the criteria on relative uncertainty described above, shaded area denotes the uncertainty if this value would be chosen, the marked line shows the point with the highest significance. Missing dots indicate that the criteria are exceeded, while a value of zero indicates division problems. It can be seen that smooth evaluation takes place only in low-BDT score regions where there is a sufficient number of events. Quick climbs or drops in the calculated values and uncertainties can be attributed to the background mixture having a multitude of background sources, where the individual weights can differ in magnitude. A good example is the category 4.1 where both evaluations give different preferred thresholds. For the category 4.2, on the other hand, both methods provide the same preferred cut-off point. However, for both categories, an even more conservative threshold is chosen. In the case for category 4.1, the threshold is chosen as 0.2, while for category 4.2 it is chosen as 0.8, characterising value where no great statistical fluctuations are present.

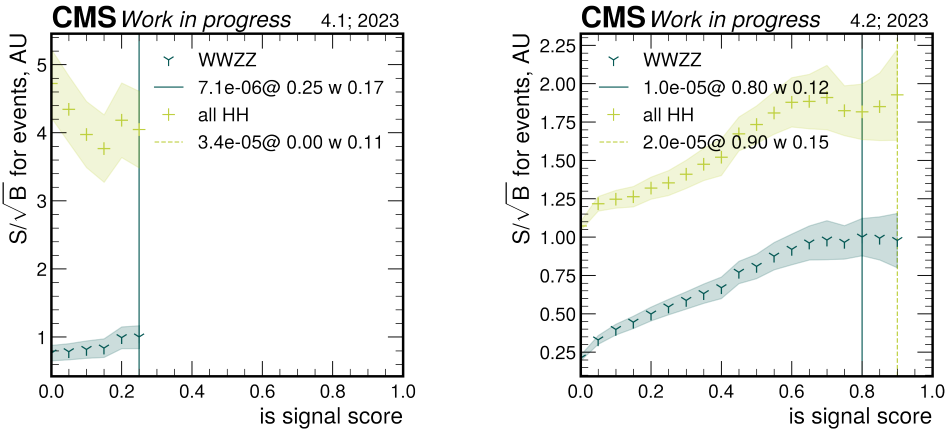

(a) 4.1 statistical significance from BDT signal score, 2023 era

(b) 4.2 statistical significance from BDT signal score, 2023 era

Figure 6.20. Run 2 BDTs applied on 2023, showing statistical significance $(S/\sqrt{B})$ as function of the BDT score threshold, normalised values in arbitrary units (AU) are shown for comparison between evaluation on $HH \rightarrow WW^*ZZ^*$ only (dark green, Y, solid line) and on all HH decays (light green, +, dashed line).

Following this method, the BDT score was binned and a comparison for the back-

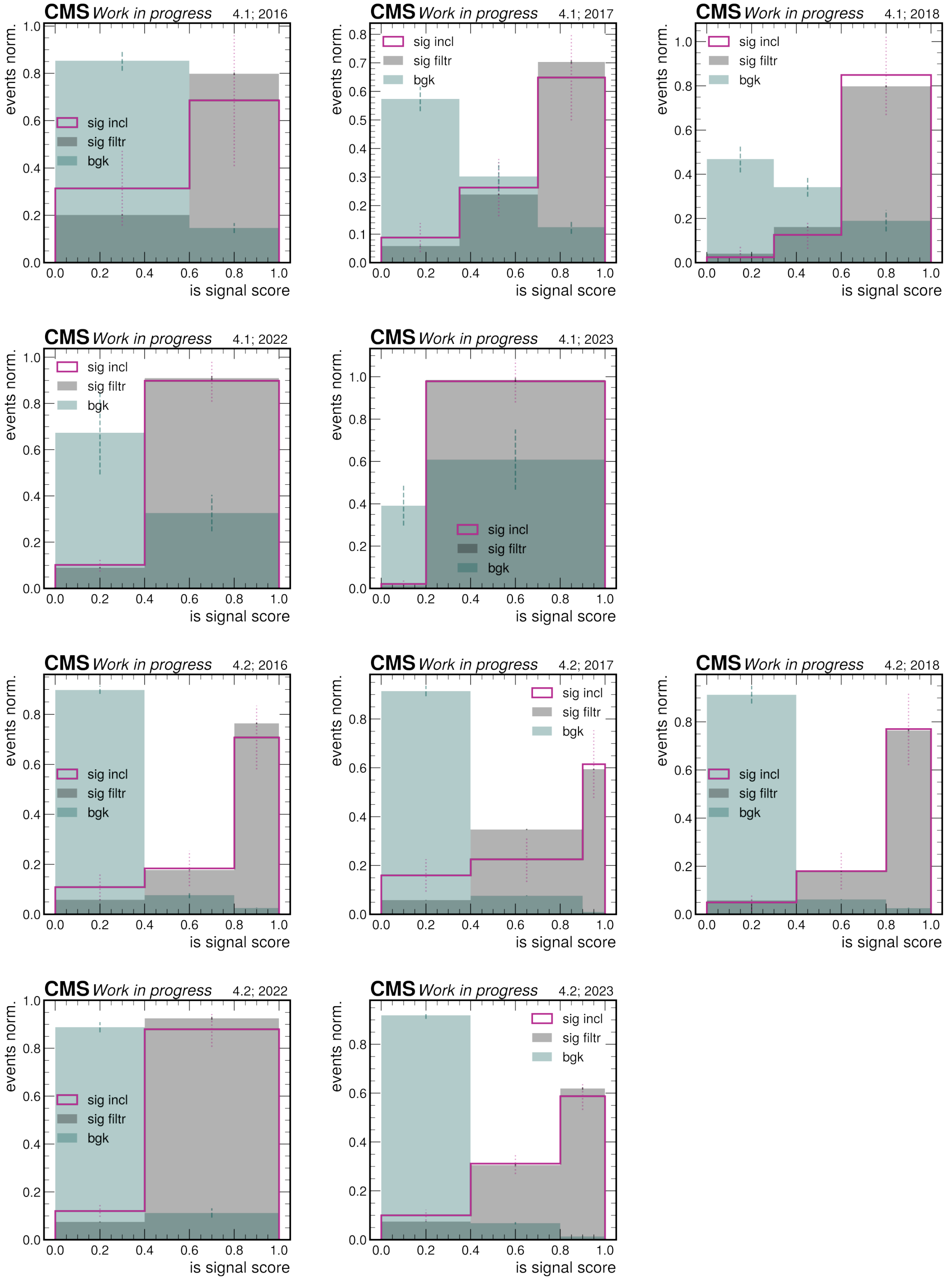

Figure 6.21. Run 2 and Run 3 BDT applied on bothcategories in all eras, showing BDT score for “sig incl” – inclusive $HH \to WW^*ZZ^*$, “sig filtr” – filtered $HH \to WW^*ZZ^*$ on which the model was trained and “bgk” – summed background contribution in era; shapes are weighted by event weight and normalised to unity.

ground (“bgk”), the $HH \to WW^*ZZ^*$ contribution from the inclusive signal sample used for evaluation (“sig incl”), and the filtered signal used for training (“sig filtr”) per era and category is shown in Fig. 6.21 for both categories. Where not constrained by the MC uncertainty, the low-BDT score region is divided into two or more bins to provide more information on the shape comparison. Events are weighted, and for easier comparison, shapes are normalised to unity. Overall, a good shape agreement between the filtered and inclusive signal samples is reached, as they overlap within uncertainties. In several score bins, the MC uncertainty is relatively high, especially in the category 4.1, which is less populated. At the same time, when comparing the BDT score distributions for category 4.2, a clear signal and background separation is visible.

The final BDT score bin is considered as the SR, thus the BDT score threshold is the bins lowest edge. Table 6.11 summarises BDT score values per category and year, including the corresponding relative uncertainties. It was possible to set a threshold in each of year with the MC statistics being the main limiting factor. On average, category 4.1 has lower BDT score thresholds than category 4.2. However, the evaluation is year-sensitive, as can be seen in 2022, where a lower value had to be set due to the MC uncertainties in both signal and background.

Table 6.11

BDT score value thresholds and the relative uncertainties considered

Cat	Threshold	S_r, %	B_r, %	$(\frac{S}{\sqrt{B}})_r$, %	year
4.1	0.6	15.23	14.53	16.88	2016
4.1	0.7	14.11	18.94	17.00	2017
4.1	0.6	12.22	25.59	17.70	2018
4.1	0.4	7.02	24.27	14.02	2022
4.1	0.2	5.11	23.34	12.74	2023
4.2	0.8	12.85	3.24	12.95	2016
4.2	0.9	17.83	3.70	17.92	2017
4.2	0.8	13.31	7.37	13.81	2018
4.2	0.4	5.15	17.62	10.21	2022
4.2	0.8	8.01	7.93	8.93	2023

Finally, the influence of the BDT score threshold on the final yield is evaluated. An example of the weighted event distribution in each category after pre-selection and after passing the BDT score threshold (thus, becoming the SR) is given in Fig. 6.22. This example is from the 2018 data-taking era, so the yield is extrapolated to 59.74 fb^{-1}. The figure shows what fraction of the category is taken up by each of the process in both categories. As the signal contribution remains in the minority, the total signal yield (and for comparison the total background yield) is printed on the side. Here as the signal contribution is considered not only $HH \to WWZZ$, but also other HH decays as is explained in Section 6.5. After pre-selection, category 4.1 is a rather equal mixture of several samples, with ZZ (in green), $t\bar{t}$ (in light purple), WWZ (in orange) and $t\bar{t}Z$ (in light blue) being somewhat leading. The background yield is around 300 times higher

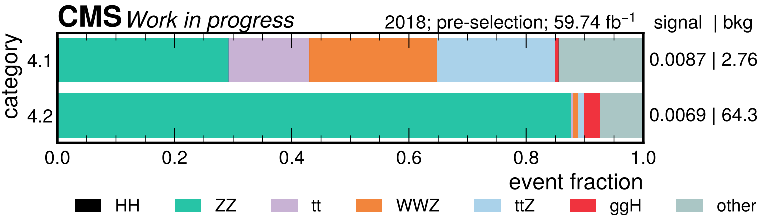

(a) event pre-selection

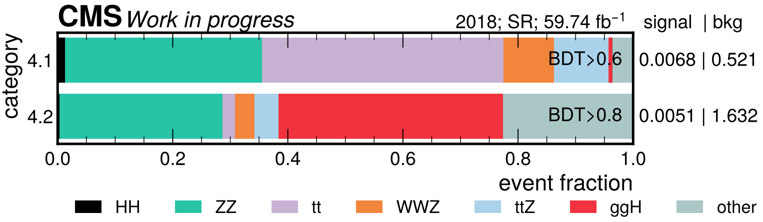

(b) the SR

Figure 6.22. Signal and background contribution for the event fraction in the analysis categories, the total yield for signal and background is shown on the right, example for 2018.

than the signal yield, yet no more than three events are expected. On the other hand, category 4.2 in pre-selection is dominated by ZZ (in light green), and the signal yield is around 10'000 times lower than the background yield, together expecting less than 65 events.

When comparing this to the SRs, it can be seen that the overall yields are significantly reduced. In SR 4.1, less than one event is expected, with the distribution of the MC prediction slightly changed with the dominant becoming the $t\bar{t}$ production. At the same time, the 4.2 BDT works well to reject the ZZ contribution while struggling to reject the $H \rightarrow ZZ$ contribution (in red), thus changing the expected MC distribution. Less than two events are expected in this SR after the full selection. More detailed results are shown in Section 6.8. Performance-wise, the 4.1 BDT reduced the signal contribution by 22 % while reducing the background by around 81 % and 4.2 BDT reduced the signal contribution by 26 % while reducing the background by around 97 %. Similar results are reached in other years, however, the 4.1 BDT model for Run 3 performs better in rejecting the $t\bar{t}$ contribution.

During the early stages of the BDT testing, the strategy to choose input data (or, equivalently, to define event categories) was still in development. The object selection ranged from requiring very loose to very tight criteria, before ultimately converging on the relatively loose object selection outlined in Section 6.4.1 and Section 6.4.2. Also the event categorisation underwent major construction works, mainly regarding the number of necessary jets, until landing on the selection described in Section 6.4.3.

Subsequently, after examining the performance of the final BDTs, several follow-up studies were conducted to investigate whether pre-selection could be relaxed even further. The aim was to allow more signal and background events to enter into the categories, thereby increasing the training statistics for the BDTs and potentially improving their ability to distinguish signal events. These checks were performed using the `2022EE` MC sample, and several of the tested configurations are summarised in Table 6.12, where the comparison metric ($S/\sqrt{B}$) is normalised to the default selection.

Table 6.12

Comparison of normalised $S/\sqrt{B}$ and its relative uncertainty for various event loosening scenarios

Cat. 4.1	Unc. 4.1	Cat. 4.2	Unc. 4.2	Scenario
1.000	16.3 %	1.000	12.3 %	baseline: object and event definition as described in this chapter
1.042	12.4 %	1.141	8.2 %	events with b-tagged jets are not rejected, however, only b-vetoed jets are used in building objects
1.047	16.9 %	1.010	11.7 %	p_T requirement for softest two leptons is loosened to 7 GeV
1.025	16.6 %	1.000	12.3 %	MET requirement is not applied for category 4.1
0.934	18.8 %	0.916	12.7 %	ttH MVA requirement is lifted from muons and electrons
0.873	14.6 %	0.855	11.1 %	a loosened number of jets are required (only at least 1 jet)
0.865	18.6 %	0.973	12.8 %	loosened lepton IDs are chosen: for electrons `WP80`; and for muons `isPFcand`
0.748	13.4 %	0.797	9.3 %	no minimum number of b-vetoed jets is required

The most significant gain is reached when events with b-tagged jets are not rejected. The main advantage is the increase in statistics. This selection allows to increase the training dataset by 36 % and 62 % for signal in the 4.1 and the 4.2 categories, respectively, while for background there is a 122 % and 27 % increase for the 4.1 and 4.2 categories, respectively. The AUC for false positive versus true positive is 0.886 and 0.923, for the 4.1 and 4.2 categories, respectively, just slightly more performative than in the baseline case. The top-performing features remain unchanged, although their SHAP shapes change. As interesting as this finding was, it was not implemented because the overall gain in sensitivity was too small to create such a stark difference for only one of the analysis categories. Moreover, by not rejecting events with b jets, a higher overlap would be present with the $HH \to bbZZ \to 4l$ analysis.

Similarly, it was explored if softening the softest lepton transverse momentum requirements would allow to increase the sensitivity for signal events. This selection allowed to increase the training dataset by 12 % and 16 % for signal in the 4.1 and 4.2 categories, respectively, while for background there was an 11 % and 15 % increase in the 4.1 and 4.2 categories, respectively. The AUC for false positive versus true positive is 0.838 and 0.909 for the category 4.1 and the category 4.2, respectively, just slightly less performative as in the baseline case. As the overall gain in the statistical significance was below 5 %, this loosening proposal was not implemented, more so because the SFs of low-p_T have relatively high uncertainties, thus the miniscule gain might be eaten up by them.

In addition, other scenarios did not provide a significant improvement. Lifting the ttH MVA for leptons would allow to simplify the selection process, however, the slight loss in the statistical significance and the more pronounced dominance of the $t\bar{t}$ background was against implementing this change. Neither loosening or lifting the requirement for jet multiplicity, and loosening the lepton IDs brought any gain in the statistical significance, thus neither were adapted. This unresponsiveness to loosening the jet requirement for the BDT trained for the category 4.1 came as a surprise, as initial studies at the pre-selection stage had hinted possible improvements.

6.5. Considering Other HH Contributions

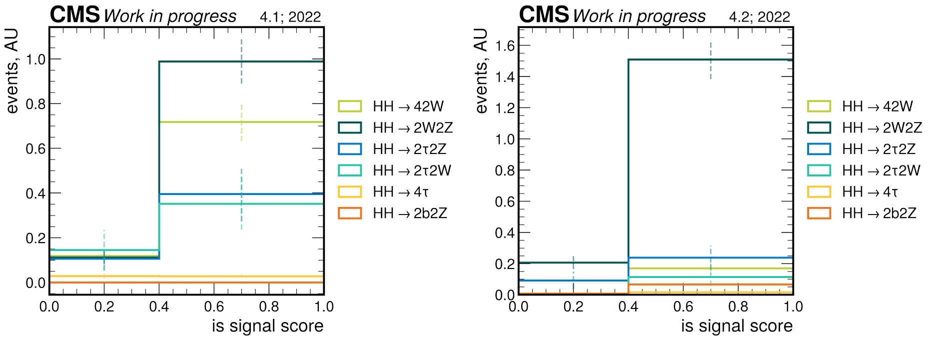

(a) category 4.1

(b) category 4.2

Figure 6.23. The BDT score distribution for various HH decays, example from year 2022, shapes are scaled to arbitrary luminosity for easier comparison.

Four leptons and at least two jets are not a unique signature of the $HH \rightarrow WW^*ZZ^*$ analysis, as other HH decay channels can also lead to it, as an example $HH \rightarrow WW^*WW^*$ or $HH \rightarrow b\bar{b}ZZ^*$. Moreover, some of the other decay channels have even larger BRs, thus making it more likely that an event with such a signature has not come from the $HH \rightarrow WW^*ZZ^*$ decay. Although the event categorisation and the BDT training is designed to target the $HH \rightarrow WW^*ZZ^*$ decay, other HH contributions have to be evaluated to properly account for them in the limit evaluation and with future combination in mind, to account for any possible overlap with other analysis. In Fig. 6.23, an example of the BDT response for various HH decay channels is shown for 2022 data-taking period. In all cases more events favour the high score region.

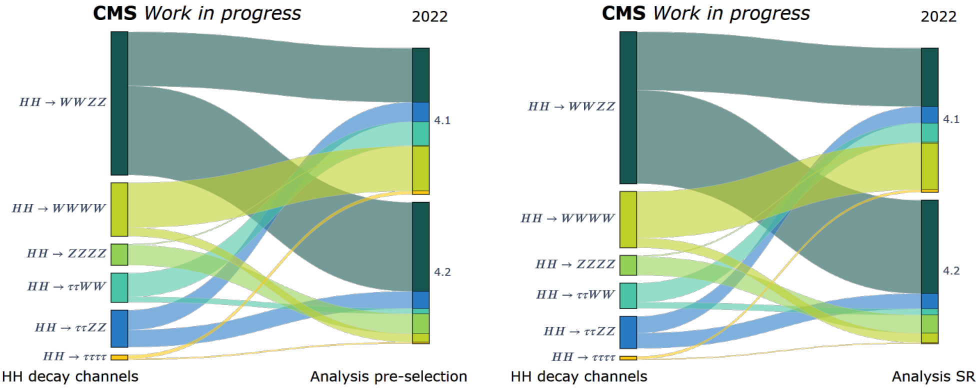

(a) Pre-selection (b) Signal region

Figure 6.24. Relative comparison for HH signal event from several HH decay modes satisfying the pre-selection requirements and after applying the BDT threshold, example from the 2022 data-taking year.

To clearly visualise the content of the categories Fig. 6.24 is constructed, where in Fig. 6.24a the pre-selection contents are shown in each category, and in Fig. 6.24b the SR is shown. Each figure shows the flow of events from various HH decays into the analysis categories, thus showing the relative comparison. At the same time, the expected events for 34.75 fb^{-1} are shown in Table 6.13, where the yields are extrapolated from MC simulations created for the 2022 era only and at this stage should be viewed purely for comparison. It also includes the relative contribution to the SR.

Table 6.13

Expected signal contribution in analysis categories, evaluated from 2022 MC and extrapolated to 34.75 fb^{-1}, showing the HH decay mode, the signal yield in each SR and the relative contribution of each decay mode within the SR

HH decay mode	SR 4.1, events	rel. in 4.1	SR4.2, events	rel. in 4.2
$HH \to WWZZ$	$(1.56 \pm 0.13) \cdot 10^{-3}$	0.41	$(2.50 \pm 0.17) \cdot 10^{-3}$	0.63
$HH \to WWWW$	$(1.24 \pm 0.12) \cdot 10^{-3}$	0.32	$(2.52 \pm 0.54) \cdot 10^{-4}$	0.06
$HH \to ZZZZ$	$(2.93 \pm 1.75) \cdot 10^{-5}$	<0.01	$(4.88 \pm 0.73) \cdot 10^{-4}$	0.12
$HH \to \tau\tau WW$	$(5.09 \pm 1.29) \cdot 10^{-4}$	0.13	$(1.64 \pm 0.66) \cdot 10^{-4}$	0.04
$HH \to \tau\tau ZZ$	$(4.44 \pm 1.26) \cdot 10^{-4}$	0.12	$(4.06 \pm 1.09) \cdot 10^{-4}$	0.10
$HH \to \tau\tau\tau\tau$	$(6.51 \pm 1.97) \cdot 10^{-5}$	0.02	$(2.21 \pm 1.09) \cdot 10^{-5}$	<0.01
$HH \to bbZZ$	-	-	$(1.23 \pm 0.08) \cdot 10^{-4}$	0.03

The majority of $HH \to WW^*WW^*$, $HH \to WW^*\tau\tau$ and $HH \to \tau^+\tau^-\tau^+\tau^-$ caught by this analysis favours category 4.1, while the majority of $HH \to ZZ^*ZZ^*$ and $HH \to bbZZ^*$ favours category 4.2, and $HH \to \tau^+\tau^-ZZ^*$ is spread equally between the two. The leading HH contribution in each SR is $HH \to WW^*ZZ^*$, in category 4.1 it occupies around 41 % while in 4.2 it occupies around 63 %. After pre-selection $HH \to WW^*WW^*$ is of similar contribution as $HH \to WW^*ZZ^*$ in the category 4.1, as $\mathcal{BR}(HH \to WW^*WW^*) \approx 4\mathcal{BR}(HH \to WW^*ZZ^*)$, while after the full selection it is reduced to around 32 %. While $HH \to WW^*\tau^+\tau^-$ with its three times larger BR is the third leading contribution, and together with $HH \to \tau^+\tau^-ZZ^*$ contributes almost 25 %.

At the same time, in category 4.2 the sub-leading contributions are $HH \to \tau^+\tau^-ZZ^*$ and $HH \to ZZ^*ZZ^*$. Their BR is three and 17 times smaller than the BR for the WW^*ZZ^*, respectively, thus not overwhelming the category and contributing in the order of 10 %. Yet, as category 4.2 is targeting the HH decay channel where one Higgs boson decays into two leptonically decaying Z bosons, it only makes sense to see their contribution.

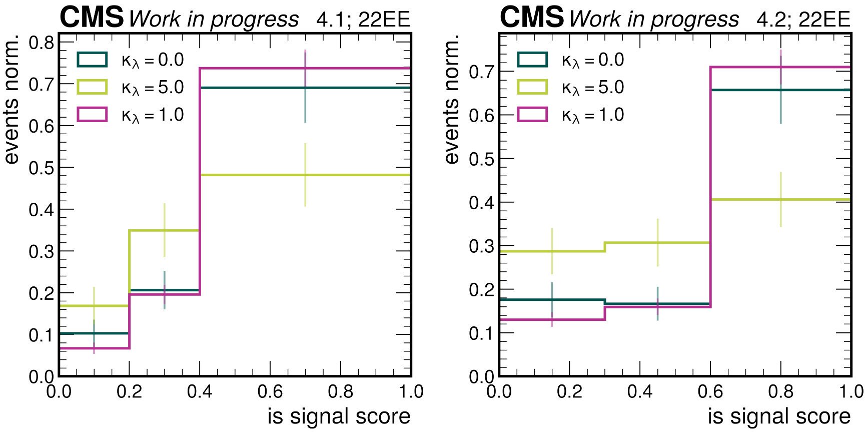

(a) category 4.1

(b) category 4.2

Figure 6.25. BDT score response to other BSM models, example from 2022EE.

The dedicated BDT trained on $HH \to WW^*ZZ^*$ has allowed to keep the sensitivity to HH decays while not sacrificing the $HH \to WW^*ZZ^*$ decay channel. When evaluating the contributions after applying the BDT threshold, the situation is improved as the $HH \to WW^*ZZ^*$ contribution is slightly increased; however, the yield undergoes a significant decrease. These results give a basis for a great question if the final signal-background separation could be done even more effectively. And moreover, should the $HH \to WW^*ZZ^*$ decay channel be analysed separately or in combination with other multilepton decays.

The BDT had been trained with the SM-consistent signal, however, several other BSM model responses were also investigated. In Fig. 6.25, a comparison of the response of the BDT score is shown for the nominal signal (SM-like with $\kappa_\lambda = 1$ in pink), and two BSM alternatives – $\kappa_\lambda = 5$ in light green and $\kappa_\lambda = 0$ in dark green. As expected, these models perform worse, especially $\kappa_\lambda = 5$ gives an almost flat response to the BDT. However, further investigation of BSM models was outside of the timeline of this Thesis, yet could be material for further studies. Dedicated BDTs could not only be evaluated, but trained for several BSM scenarios, thus estimating the possible sensitivity to them. Afterwards, the same analysis strategy could be applied, setting the upper limit, and perhaps performing a κ_λ scan.

6.6. Data and MC Agreement

To validate physics modelling and the constructed categories, data and MC agreement is checked in non-signal regions, the so-called control regions (CRs). Ideally, a CR is constructed as close to the SR as possible, while avoiding or minimising any overlap. Within this region, the distributions of high-level and low-level variables are compared between the data and MC simulations.

After the pre-selection, category 4.2 is clearly dominated by ZZ, while the category 4.1 is a mixture of ZZ, $t\bar{t}$, WWZ and $t\bar{t}Z$ in similar contribution. However, across years there is no clear dominant background after applying the BDT score threshold on the pre-selection in both categories. ZZ retains a significant influence on category 4.2, as well as the single-Higgs related backgrounds, such as ggH. In category 4.1, the dominant backgrounds are ZZ, also $t\bar{t}$, WWZ and $t\bar{t}Z$. Therefore, it was decided to have two CRs per category, they would be very close to the SR, but

- with inverted BDT score threshold (`CRlow`);
- with inverted jet multiplicity requirement (`CRno`).

Clearly the `CRno` provides more statistics than the `CRlow`, however, this phase-space is further away from the SR's phase-space. Also here, the 4.1 category's CRs remain to be a mixture of backgrounds, while 4.2 category's CRs are dominated by ZZ production.

Although an overall good shape agreement was observed across years, within most of 4.2 CRs significant data surplus was noticed, indicating poor MC modelling. As this region is predominantly filled with ZZ production, the fault was searched within it. Upon investigating, it was noticed that the mismodelling could be attributed to poor modelling in high jet multiplicity. The only exception was 2022, which showed great data and MC agreement, however, did not follow the expected scaling compared to other years. Similar findings were observed for the most abundant background in the three-lepton search category, WZ. Since the ZZ sample is modelled using `Powheg` in NLO it should be accurate up to one jet, but the accuracy of further jets coming from parton showers can be less precise. Therefore, a data-driven correction for the ZZ modelling was created based on the transverse momentum of the sub-leading (second) and sub-sub-leading (third) jet,

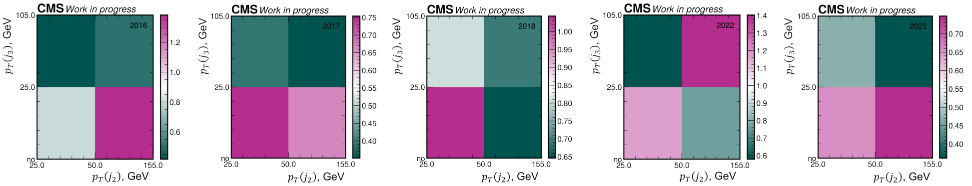

(a) values of the corrections

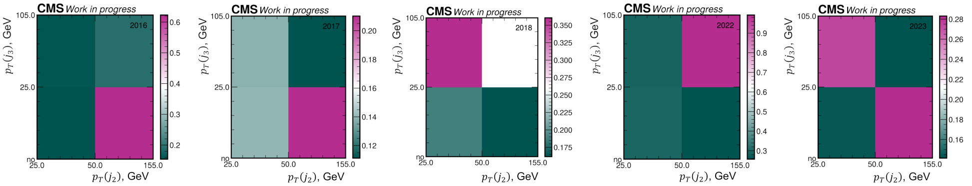

(b) absolute uncertainties

Figure 6.26. The applied data-driven ZZ correction based on the transverse momentum of the first and the second jet from parton showers, "no" indicates events without the second parton jet.

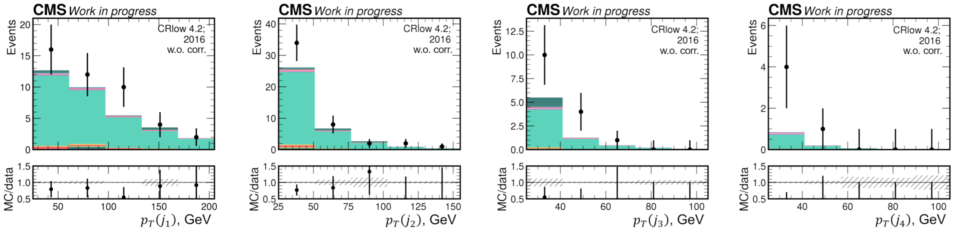

(a) before correction

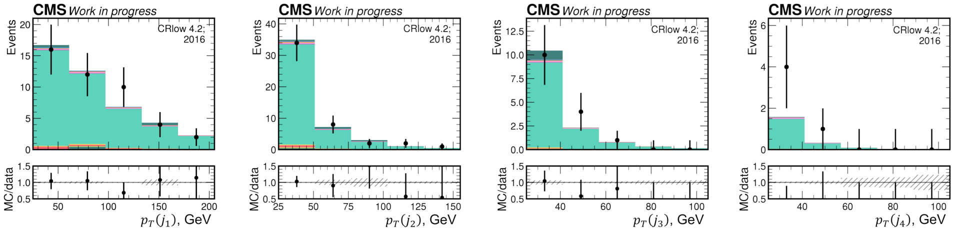

(b) after correction

Figure 6.27. Jet transverse momentum distributions before and after data-driven ZZ modelling correction, example of CRlow 4.2, 2016.

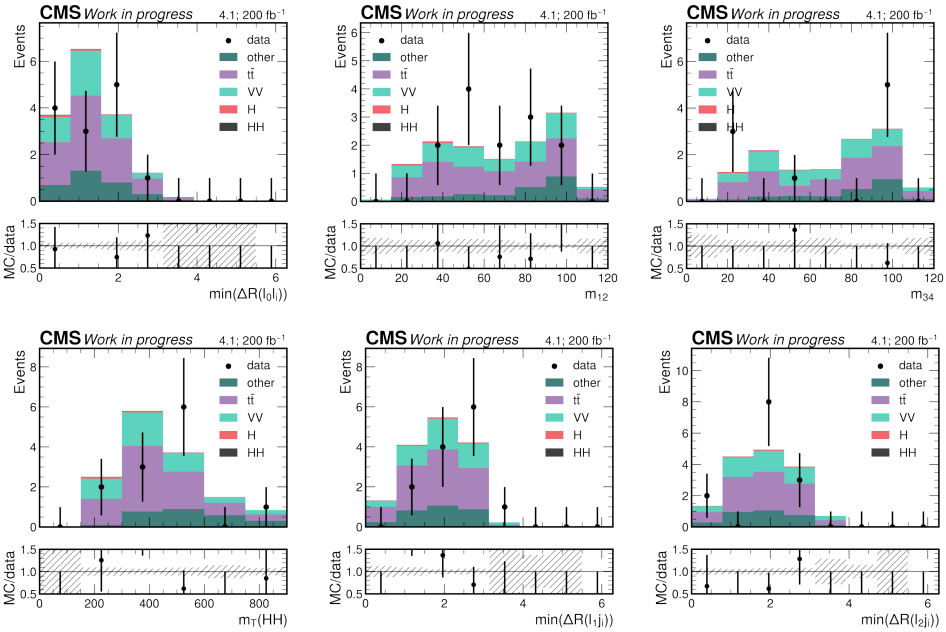

(a) Category 4.1 (SR+CRlow)

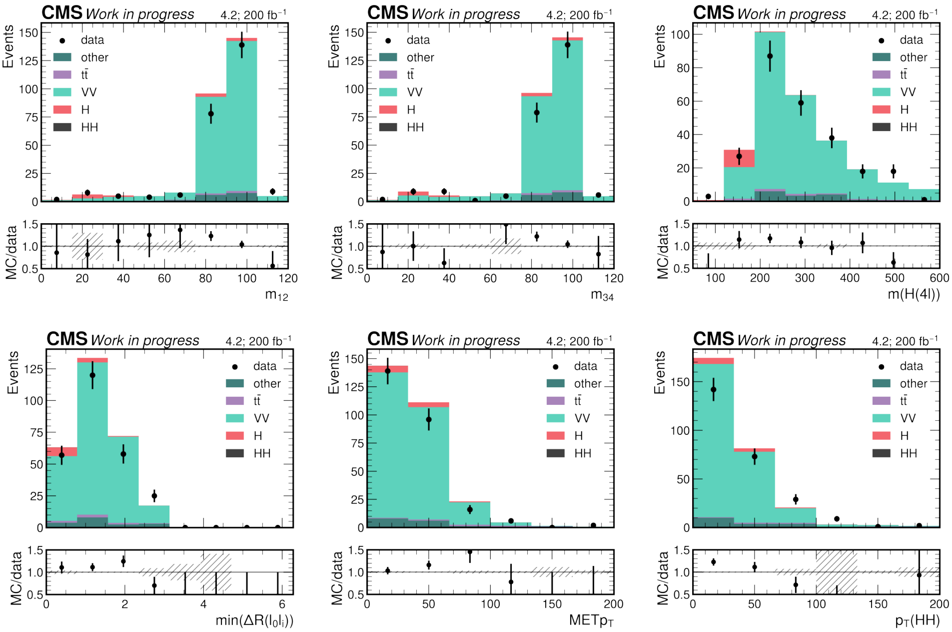

(b) Category 4.2 (SR+CRlow)

Figure 6.28. Most impactful BDT feature data and MC agreement for both categories.

both assumed to be coming from parton showers. As mentioned in Section 6.4.2, jets within an event are arranged in decreasing order of their transverse momentum.

By definition, it is impossible to derive this correction within `CRno`, so `CRlow` was used instead. To achieve ZZ-pure region `4.2 CRlow` was chosen with an additional requirement of $m_{4l} > 150$ GeV to exclude the majority of $ggH \rightarrow ZZ$. The results were evaluated separately in the `CRlow` and in the combined control region `CRlep`, which combines `CRno` and `CRlow`, to increase the statistics. Events were binned by the second and third jet's transverse momentum, also including events without the second parton shower jet. A coarse binning was chosen to reduce the correction's uncertainties mainly caused by just a few events occupying a certain bin. The applied binning:

- transverse momentum of the second leading jet, $p_T(j_2)$: [25., 50., 155.];
- transverse momentum of the third leading jet, $p_T(j_3)$: [no jet, 25., 105.].

The calculated corrections per year can be seen in Fig. 6.26. Afterwards, this correction is applied as a per-event weight to the ZZ contribution in both categories. An example of 4.2 `CRlow` in 2016 data for jet transverse momentum before and after applying the correction is shown in Fig. 6.27. Overall, the data and MC agreement is improved with a slight tension remaining in 2017. An example of data and MC agreement after the application of the ZZ correction is shown in Fig. 6.28. This is shown for the most impactful BDT features with full data for the full category (SR+`CRlow`). Even with the full dataset, the categories remain quite statistically limited, but within uncertainties good data and MC is seen.

6.7. Uncertainty Estimations

No measurement can be quoted without its uncertainty; therefore, the precision of the measurement and the sources of uncertainty must be evaluated. Although this measurement is completely statistically limited, it is necessary to account for potential biases and variations in the measurement. Thus, when improving this measurement with an increase in the amount of statistics, a clear understanding of other nuisance parameters would be complementary.

Each source of imprecision can be viewed as a systematic uncertainty. Many systematic uncertainties affect the event yield of the HH signal and of background processes, while others can influence the distributions of object parameters, constructed observables used for the category definition or the signal extraction. These may come from limited or imperfect knowledge. Uncertainties can arise from both theoretical models (e.g., the uncertainty in the HH production cross section) and experimental factors; thus the sources of systematic uncertainties are divided into two categories – theoretical and experimental uncertainties and are described further in this section.

Theoretical uncertainty sources considered in this Thesis:

- QCD modelling and the choice of the PDF set: to account for other renormalization and factorisation scale values that can be set for the generator, the scale is varied between 0.5 and 2.0, assessing the influence on the generated events. Similarly, to evaluate the choice of the PDF set, the results are reevaluated with alternative sets. This is calculated from the MC samples with the exception of a few samples where the values are taken from the theoretical calculations:
    - ggHH production: 30.77 fb$^{+2.2\ \%}_{-5.0\ \%}$(QCD scale) $\pm$ 2.3 %(PDF + α_S) for $\sqrt{s}$ = 13 TeV and 34.13 fb$^{+2.1\ \%}_{-4.9\ \%}$(QCD scale) $\pm$ 2.3 %(PDF + α_S) for $\sqrt{s} = 13.6$ TeV [139];
    - ggH production: 48.52 pb$^{+4.6\ \%}_{-6.9\ \%}$(theory)$\pm$3.2 %(PDF+α_S) for $\sqrt{s} = 13$ TeV [140] and 52.17 pb$^{+4.6\ \%}_{-6.7\ \%}$(theory) $\pm$ 3.2 %(PDF + α_S) for $\sqrt{s} = 13.6$ TeV [148];
    - $t\bar{t}$ production: 833.9 pb$^{+2.5\ \%}_{-3.6\ \%}$(QCD scale)$\pm$2.5 %(PDF+α_S) for $\sqrt{s} = 13$ TeV and 923.6 pb$^{+2.4\ \%}_{-3.6\ \%}$(QCD scale) $\pm$ 2.5 %(PDF + α_S) for $\sqrt{s} = 13.6$ TeV [141].

- the cross section of simulations: mainly the cross sections and their corresponding uncertainties are taken from the Cross Section database [138], with the exception of ggHH, ggH and $t\bar{t}$ for which the values are quoted above.

- the $\mathcal{BR}(HH \to VVVV)$ is known with an uncertainty of 6.8 % while the $\mathcal{BR}(H \to ZZ \to 4l)$ with an uncertainty of 2 % [24].

Experimental uncertainty sources considered in this Thesis:

- integrated luminosity measurement: integrated luminosity is measured from Van-der-Meer scans, and its uncertainty is evaluated based on its stability and detector response. The associated uncertainties have an uncorrelated component unique for each data-taking year, as well as two correlated components across 2016 - 2018 (3.5 % in total) and 2017 - 2018 (0.8 % in total) years [149]. The associated uncorrelated uncertainties are 1 % for 2016 [150], 2 % for 2017 [151], 1.5 % for 2018 [152], 1.4 % for 2022 [153] and 1.3 % for 2023 [154].

- pileup: the associated uncertainty on the PU reweighing is estimated by varying the total inelastic pp cross section by its uncertainty of 4.6 %, then propagating it to the PU weights of the MC events. The resulting effect is an uncertainty of < 5 % in the SRs, it is treated as correlated across all categories and channels for each year.

- lepton reconstruction and selection: as mentioned before, lepton reconstruction, identification (and isolation) efficiency has been measured separately in Z boson enriched regions for the applied IDs. The SFs are varied up and down, evaluating the change in the final event yield. These uncertainties are divided for muons and electrons, correlated among processes, and uncorrelated between Runs. The associated uncertainties with muon ID is less than 1 % while the associated uncertainty with electron ID is below 10 % and are mainly inflated due to low transverse momentum electrons.

- lepton energy scale and mass resolution: energy scales of both muons and electrons are known with an uncertainty of less than 1 %.

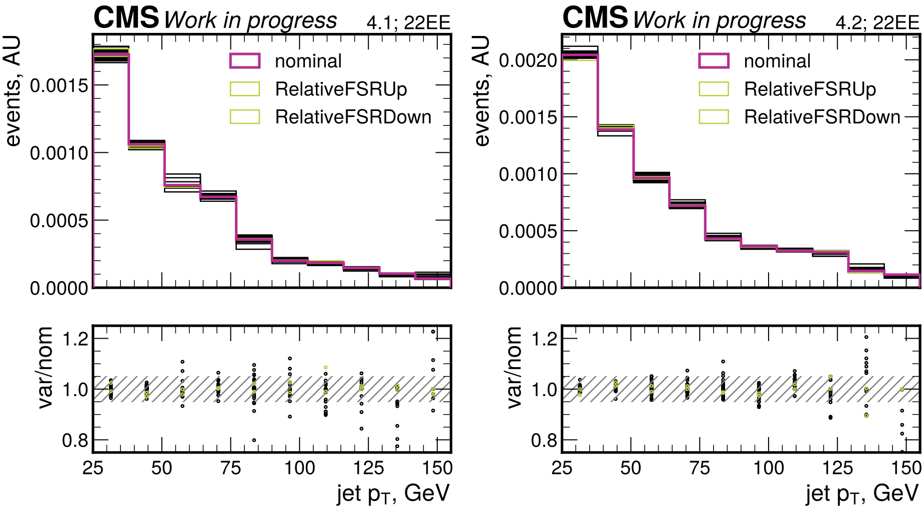

(a) SR 4.1 (b) SR 4.2

Figure 6.29. Nominal jet transverse momentum (in pink) versus jet transverse momentum when several scenarios of jet energy scale (JES) variations are applied (in black). For each variation its contribution shown when JES varied up and down by one standard deviation. The largest variation shown in light green. At the bottom panel a ratio per each variation is shown versus the nominal distribution. 2022EE MC example.

- JES and JER: an extensive calibration process is performed centrally by the CMS to correctly match JES and JER between the data and the simulation. Each analysis is recommended to implement a set of 27 different components on which to evaluate JES modelling in addition to the JER variations. Upon following the complete recipe, it was found that due to the statistically limited nature of this analysis, the variation estimations are too statistically limited to be fully reliable. An example for category 4.1 and category 4.2 are shown in Fig. 6.29 for `2022EE` era on the signal sample. In this sample, 352 and 396 events are available for the category 4.1 and the category 4.2, respectively. In the figure, each variation is shown in black, with the only exception of the highest contributing variation `AbsoluteStat` marked in light green. A higher dispersion is seen for the more statistics limited category 4.1. For the top 10 most impactful scale variations, the relative comparison of the influence

Table 6.14

Top 10 most impactful JES variation shown normalised versus the nominal yield for the down/up shift; example from 2022EE

JES variation	Relative in category 4.1	Relative in category 4.2
AbsoluteStat	0.995/0.967	0.999/1.015
RelativeSample	1.025/0.995	1.007/1.002
FlavorQCD	0.990/1.011	0.995/1.014
TimePtEta	0.998/0.986	1.005/1.001
RelativeBal	1.013/0.992	1.003/1.001
Fragmentation	0.995/0.987	0.999/1.004
RelativeFSR	1.010/0.989	0.999/1.000
PileUpPtRef	0.989/1.000	1.003/1.007
PileUpPtBB	0.995/0.990	1.003/1.002
PileUpDataMC	0.996/1.004	0.995/1.009

on the yield in each category is shown in Table 6.14. It can be seen that the contribution is well below 5 %. Therefore, for this Thesis, only one systematic is applied for a combined JES and JER uncertainty with a conservative value of 5 %.

- b-tagging efficiency and mistag: uncertainties in the b-tagging efficiency can affect the identification of jets originating from b quarks, and the mistag rate for non-b-jets. To evaluate their influence, the central SFs are varied up or down to form correlated and uncorrelated components per jet flavour.

- L1 pre-firing: for 2016 and 2017 an uncertainty in the L1 pre-firing correction are taken into account using the centrally provided weights and their up and down variations in the pre-firing probability. The uncertainty is below 4 %.

- trigger efficiency: the efficiency of signal events to pass the trigger selection is emulated with 1 % uncertainty. It is treated as uncorrelated across years and correlated across processes.

- ZZ MC simulation correction: to account for ZZ simulation mismodelling, a data-driven correction has been applied, and its associated uncertainty has been evaluated by varying the correction up and down by its uncertainty. Overall, the propagated uncertainty is in the order of 5 % to 20 %.

6.8. The Measurement

Currently, the HH production studies are capable of computing only the exclusion limits; therefore, also the main goal of this Thesis is to compute an exclusion limit on the HH signal strength, when approaching it through the $WWZZ$ decay. The limit is calculated using the $\mathrm{CL_S}$ method [27], which is a modified frequentist approach and noted as CL. Following customs, the limit is expressed as a multiplier on the SM cross section value, or on the signal strength, μ, defined as the ratio of the measured cross section and the one predicted by the SM. To calculate either, a statistical model needs to be built.

Statistical analysis based on expected observations is performed with CMS statistical analysis software, `COMBINE` [155]. It provides a command-line interface to many common workflows used in statistical analyses not only in the CMS but in general in high-energy physics. It encapsulates the statistical model using a human-readable configuration file (datacard). It allows building the model using expected observations, running statistical tests on it using both the model and observed data, and finally provides tools for inspecting the model and the tests performed.

The statistical model built by `COMBINE` is denoted as $p(\text{data}; \vec{\Phi})$ and encodes the probability density for the observed data parametrized by the model parameters, $\vec{\Phi}$. The parameter space is divided into parameters of interest, $\vec{\mu}$, and nuisance parameters, $\vec{\nu}$, which in turn are used to model various uncertainties. It is factorized into primary and auxiliary components of the probability as in Eq. (6.11).

$$p(\vec{x}, \vec{y}; \vec{\Phi}) = p(\vec{x}; \vec{\mu}, \vec{\nu}) \prod_k p_k(\vec{y_k}; \vec{\nu_k}), \tag{6.11}$$

where $\vec{x}$ are primary observables brought by the variables containing the parameters of interest, $\vec{y}$ are the auxiliary observables brought by the variables containing the nuisance parameters. Moreover, the $p(\vec{x}; \vec{\mu}, \vec{\nu})$ is the primary observable probability distribution while $p_k(\vec{y_k}; \vec{\nu_k})$ are the probability distributions of the auxiliary observables. Then a likelihood function is constructed as in Eq. (6.12) to determine how probable the observed data are given the built model, therefore it runs over all data entries, d.

$$\mathcal{L}(\vec{\Phi}) = \prod_d p(\vec{x_d}; \vec{\mu}, \vec{\nu}) \prod_k p_k(\vec{y_k}; \vec{\nu_k}) \tag{6.12}$$

Due to the low expected yield, a simple counting experiment is chosen. That is, only the even yield rather than the shape of any variable is considered to distinguish whether the data are consistent with the background-only hypothesis or whether there is evidence for a signal. Thus, this model uses only one primary observable that can be described by a Poisson distribution shown in Eq. (6.13) with the expected value λ.

$$\mathcal{P}(n; \lambda) = \lambda^n \frac{e^{-\lambda}}{n!} \tag{6.13}$$

In the model, uncertainty sources are introduced as a probability density function characterising its best estimate and overall shape of the function. Functions can have log-normal, log-uniform, or gamma distributions. As `COMBINE` expects the nuisance parameters in a functional form, usually log-normal distributions are chosen, thus its function is shown in Eq. (6.14). Each type leads to a different statistical behaviour and is more useful in describing certain nuisances. The log-normal distribution peaks at one, has a longer tail than a Gaussian, and goes to zero as $\theta \to 0$. As it is always positive, it is a natural choice for rates, such as luminosity. In the formula κ denotes the uncertainty and $\tilde{\theta}$ is the best estimate of the nuisance θ.

$$\rho(\theta) = \frac{1}{\sqrt{2\pi}\theta \ln(\kappa)} e^{-\frac{\ln^2(\theta/\tilde{\theta})}{2\ln^2(\kappa)}} \tag{6.14}$$

The test is set up with two SRs and two CRs for constraining the ZZ modelling, resulting in four bins. In each bin, the expected yields or rates are given for the signal and background. For easier manipulation of theoretical uncertainties, backgrounds are subdivided in four subprocess groups: H for single-Higgs related backgrounds, VV for dibosons, mainly the ZZ, t for top quark related backgrounds, mainly $t\bar{t}$, and other backgrounds. Various sources of uncertainty are referred to as nuisance parameters, sometimes slightly misleadingly called “systematics”, and given for each subprocess in the bin. Uncertainties can be set as fully correlated or uncorrelated.

By default, `COMBINE` performs the calculation using the observed data, however, before unblinding, it is also possible to run the calculations using pseudo-data sets to determine the distributions of various statistical quantities, while being blind to the observed data. The pseudo-data case is often referred to as “estimation with toys”. `COMBINE` can produce pseudo-data sets from the statistical model by generating random values of the observables or by producing Asimov data sets where the maximum likelihood estimates are equal to the values used to generate the dataset [156]. The Asimov data sets are used to derive the expected outcome of frequentist calculations, such as in the determination of upper limits and confidence intervals.

A profile likelihood ratio is used as the test statistic, q_μ, which is a common choice to separate the signal from the background. The absolute value of the likelihood rarely is very informative, but a ratio of the function in two different points in the parameter space can be very informative. For computational advantage, the negative sign is preferred to solve a minimising task. For setting an upper limit, a single parameter of interest or signal strength, μ, is used. To avoid unwanted exclusion of small values of μ, the simple ratio is replaced by a piecewise function as shown in Eq. (6.15), where $\hat{\mu}$ is the maximum likelihood estimator for μ and $\hat{\nu}$ are the nuisance parameters that maximise the likelihood function. This definition encapsulates that the HH signal strength is physically non-negative.

$$q_\mu = \begin{cases} -2\log\left(\frac{\mathcal{L}(\mu,\hat{\nu}(\mu))}{\mathcal{L}(\mu=0,\hat{\nu}(\mu=0))}\right) & \hat{\mu} < 0 \\ -2\log\left(\frac{\mathcal{L}(\mu,\hat{\nu}(\mu))}{\mathcal{L}(\hat{\mu},\hat{\nu}(\mu))}\right) & 0 < \hat{\mu} < \mu \\ 0 & \mu < \hat{\mu} \end{cases} \tag{6.15}$$

Again, due to the low expected yields and low expected sensitivity, the `HybridNew` method has been chosen to calculate the upper limit on the signal strength. The `HybridNew` is a frequentist method that provides a more accurate treatment of statistical fluctuations in the low yield cases as it generates pseudo-experiments to evaluate the test statistic distributions, rather than relying on asymptotic approximations. As several sub-results suffered from very low yields, the calculation was performed with `AsymptoticLimits`, which relies on an asymptotic approximation of the test statistic. When comparing the results obtained by both methods, differences below 10 % were seen.

Finally, the CL_s criteria [27], defined as Eq. (6.16), is used to characterise at what CL a limit has been calculated at. Here, p_b corresponds to the background-only hypothesis. The default confidence level is 95 % CL ($\alpha = 0.05$),

$$CL_s = \frac{p_\mu}{1 - p_b} \tag{6.16}$$

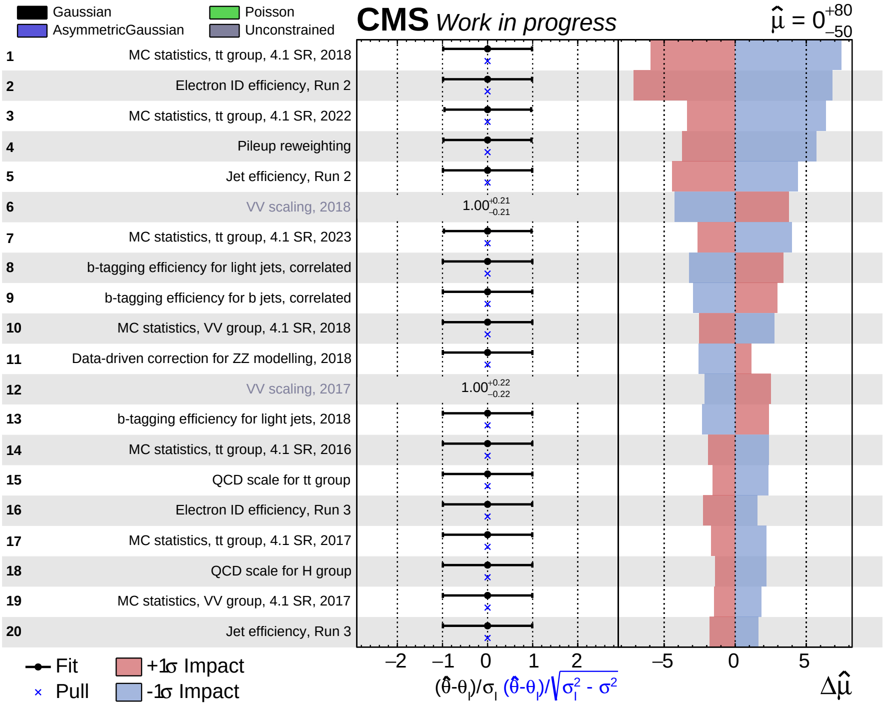

Figure 6.30. The expected ranking of the top 20 nuisance parameters by their impact on the signal strength modifier μ, for the four-lepton categories, combining full Run 2 and early Run 3 data.

The statistics model is tested by evaluating the nuisance impact on the best fit value by simultaneously fitting them and evaluating any pulls. First, the initial global fit is performed, then the nuisance parameter pre-fit is performed followed by per-nuisance conditional fits where each nuisance is shifted by $+1\ \sigma$ and $-1\ \sigma$ (standard deviation, not cross section). These fits simply maximise the likelihood, and no test statistic (with any priors) is applied. The expected impact plots are shown in Fig. 6.30 for the combination of both categories when performing the fit for the full 200 fb^{-1} dataset. The influence on the signal strength is shown. As mentioned before, the fit includes the SRs and CRs (low-BDT score region of pre-selection) and a rate parameter for the ZZ modelling. In the combination, the top three contributing nuisances come from:

- electron ID efficiency;
- PU estimation;
- MC statistics, especially the $t\bar{t}$ group as only a few events are available for evaluation.

Overall, no strong pulls or abnormal influence of the systematics can be seen, thus rendering the model viable.

6.9. Summary

This chapter has been dedicated to summarising the building blocks of the novel $HH \rightarrow WW^{*}ZZ^{*} \rightarrow 4l$ analysis. It started with a general overview of the $WW^{*}ZZ^{*}$ decay channel and why it deserves a dedicated study. It noted the used datasets and simulations, as well as the triggers applied. Moreover, it described the design process of the SRs, including the object selection, event categorisation, and the creation of a new classifier. This chapter showed the expected contribution of other HH decay channels into the analysis categories, before showing the data and MC simulation agreement in CRs. Finally, the measurement technique and the considered uncertainties were detailed.

Now, with the analysis strategy and the methodological framework fully established, the focus turns to the quantitative outcomes of the study. The next chapter presents the results of the statistical analysis, including the observed and expected limits on the HH production cross section and the expected projection of the limit.

7. RESULTS AND PERSPECTIVE

As the building blocks of the $HH \to WW^*ZZ^* \to 4l$ analysis have been summarised, it is time to evaluate the results. To reiterate, the goal of this analysis is to set an upper limit on the HH signal strength, using data collected with the CMS experiment in the full Run 2 and early Run 3 (2022 and 2023) data-taking periods, amounting to 200 fb^{-1}. Thus, in this chapter, the data and MC agreement is shown for regions used for the calculation of the limit. The calculated limit, as well as the likelihood scans are provided for the final combination. In Section 7.1, a projection for the upcoming HL-LHC is provided for the four-lepton category, as well as an estimate is given for the $HH \to WW^*ZZ^*$ channel combination.

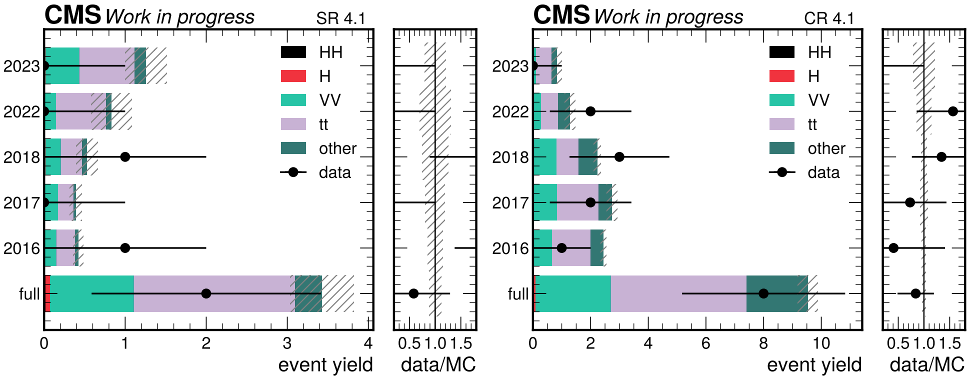

(a) SR 4.1

(b) CRlow 4.1

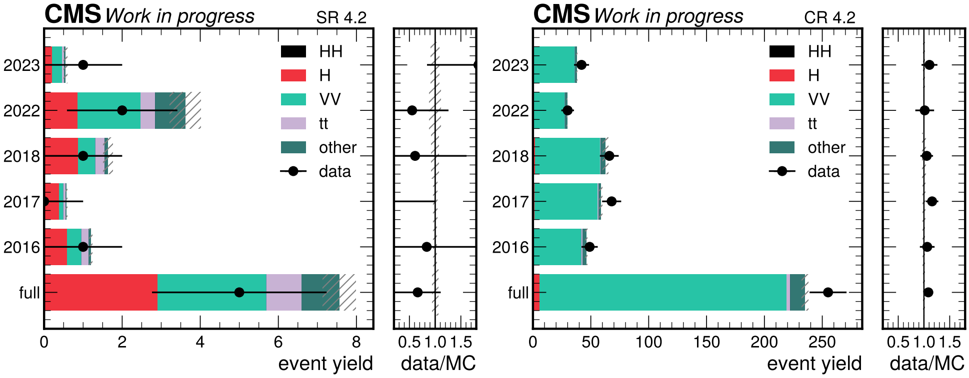

(c) SR 4.2

(d) CRlow 4.2

Figure 7.1. Expected and observed events per year, per SR and CRlow.

A comparison of expected and observed event yield per category is shown in Fig. 7.1. The expected yield of the signal is shown in black, single-Higgs boson backgrounds are shown in red, the diboson backgrounds in light green, the $t\bar{t}$ and single-top backgrounds in light violet, and other background contributions are dark green. Observed data are shown as dots, and in the panel on the right a comparison is shown for the data and MC simulations. As the BDT threshold varies in each year, the expected yield is not proportional to the integrated luminosity. Overall, a good agreement is seen between the data and the simulations.

Less than five events are expected in SR 4.1, however, only two have been observed. In CR 4.1 around eight events are expected and eight are observed. Similarly in the category 4.2, less than eight events were expected and five were observed in the SR, while in the CR around 220 were expected but over 250 were observed. The leading background in SR 4.1 and in CR 4.1 comes from the $t\bar{t}$ group while the leading backgrounds in SR 4.2 come from the single-Higgs group, mainly ggH, followed by the diboson background, mainly ZZ. The diboson background group is the dominant in CR 4.2.

Table 7.1

Observed and expected yields for various processes in the SRs, combined across all years, equalling to around 200 fb^{-1}

Process	SR 4.1, events	SR 4.2, events
HH → 2W2Z (×100)	0.798 ± 0.080	1.136 ± 0.089
HH → 4W (×100)	0.752 ± 0.074	0.117 ± 0.028
HH → 4Z (×100)	0.002 ± 0.002	0.156 ± 0.035
HH → 2W2τ (×100)	0.412 ± 0.059	0.070 ± 0.026
HH → 2Z2τ (×100)	0.183 ± 0.038	0.238 ± 0.048
HH → 4τ (×100)	0.046 ± 0.006	0.006 ± 0.002
HH → 2b2Z (×100)	-	0.043 ± 0.002
total expected signal (×100)	2.19 ± 0.13	1.76 ± 0.11
Higgs boson backgrounds	0.06 ± 0.00	2.90 ± 0.03
dibosons, mainly ZZ	0.97 ± 0.10	2.26 ± 0.06
$t\bar{t}$ (and t) backgrounds	2.77 ± 0.40	0.91 ± 0.23
other backgrounds	0.40 ± 0.02	0.96 ± 0.34
total expected background	4.54 ± 0.42	7.66 ± 0.42
data	2	5

The total expected yields for the signal and background processes in SRs across all five data-taking years are given in Table 7.1. It can be seen that the signal contribution is around 200 times lower than the background contribution in SR 4.1 and around 400 times lower in SR 4.2. This also explains why in the figure shown earlier, the signal contribution is practically invisible. In addition, it is possible to notice that the backgrounds from the $t\bar{t}$ group have a larger statistical uncertainty because fewer events are available for evaluation.

As expected and observed yields have been calculated and possible uncertainties have been evaluated, it is possible to measure the upper limit on the HH signal strength. The expected and observed upper limit on the signal strength of HH production has been calcu-

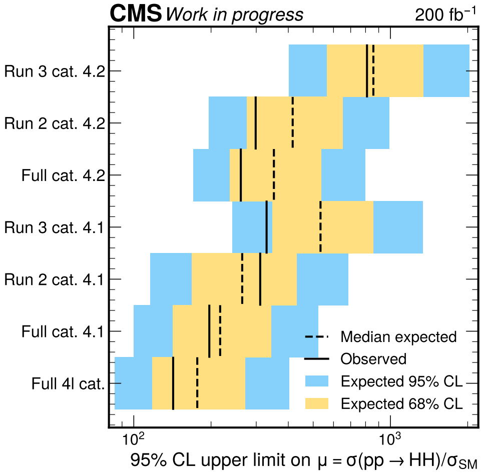

Figure 7.2. Expected and observed upper limits on the signal strength modifier μ per four-lepton category in each period and combined.

lated in each SR in each year and in combinations, including all the necessary systematics and the CRs for scaling the diboson contribution, as was introduced in Section 6.8.

The calculated limits per Run in each category are shown in Fig. 7.2. The dashed line indicates the expected limit, while the solid line indicates the observed one. The yellow band encapsulates the 68 % CL band of the expected limit, while the blue band shows the 95 % CL. The SR 4.1 provides a lower upper limit mostly due to the relatively lower background rates, and similarly Run 2 is more sensitive due to the higher integrated luminosity. Not shown in the figure, but the tightest limit is set using data from the luminosity richest period, the 2018 data-taking period. Altogether, **the combination of both categories at integarted luminosity of 200 fb^{-1} allows to set an observed (expected) 95 % CL upper limit of 142.3 (176.8) times the SM value of the HH cross section**. The observed limit is lower than expected, as on average less data have been observed in the SRs than expected. However, it is well within the one standard deviation of the expected value.

It is not possible to do a direct comparison with other or older results as this is a novel analysis. Moreover, not many analyses have combined data from the full Run 2 and early Run 3 (none at the time of writing this Thesis, but very soon, hopefully!). The closest comparison can be made with the full Run 2 multilepton analyses performed by the CMS collaboration [34]. More specifically, its four-lepton category, which targets $WWWW \rightarrow \nu l \nu l\ \nu l \nu l$. For integrated luminosity of 138 fb^{-1}, this channel has set an observed (expected) 95 % CL upper limit of 56.7 (76.8) times the SM value of the HH cross section. Alternatively, it can be compared to the CMS full Run 2 analysis of $bbZZ$ decay channel [157] which has set an observed (expected) 95 % CL upper limit of 32.4 (39.6) times the SM value of the HH cross section. Thus rendering the result achieved by the $HH \to WW^*ZZ^* \to 4l$ channel with a significantly smaller BR impressive. Clearly, it does not aim to become the leading HH decay channel; however, it is a reliable one for the combination.

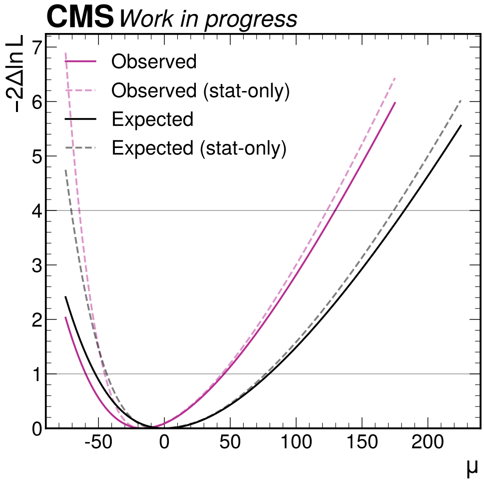

Figure 7.3. The expected and observed likelihood scan, comparing the full model and the model with excluded systematics, thus showing only the statistical contribution. four-lepton category combination.

Diving into the details of the results obtained by the statistical model, in Fig. 7.3 the expected and observed likelihood scan is shown for the full model and for a model that contains no systematics, thus it is referred to "stat-only", meaning containing only statistical effects. It can be seen that the likelihood is statistically limited. The observed best-fit value of the signal strength gives a negative value which is unphysical. However, as discussed in Section 6.8, it is not unusual when performing calculations near a physical boundary. Moreover, in this case, when scanning for the minimised likelihood, no additional a priori reason has been set to reject negative values of μ. The negative minimum of the likelihood scan is consistent with the observed data deficit. When examining the scan towards larger negative values, it is possible to notice that the full and statistics-only model diverges slightly. This can be explained with the rather low background yields in the SRs, and a rather high $S/\sqrt{B}$. When performing the fit and scaling the signal to large negative values, the full probability density function can become negative, which becomes problematic for the fit.

Following the evaluation of the likelihood scan, to assess the impact of systematic uncertainties on the sensitivity, expected and observed upper limits are computed with the "stat-only" model and compared with the full model. Table 7.2 summarises the limits calculated with the "stat-only" model and the full model ("stat and syst"). The comparison of these limits quantifies the degradation of sensitivity as a result of systematic effects, and it can be seen that the influence is less than a half percent.

Table 7.2

Comparison of the expected and observed 95 % CL limit on the μ set from the $HH \rightarrow WW^{*}ZZ^{*} \rightarrow 4l$ analysis, using full CMS Run 2 and early Run 3 dataset

Scenario	Expected limit	Observed limit
stat.-only	169.5	135.8
stat. and syst.	176.8	142.3

Although the measurement is statistically dominated, it is useful to understand which are the dominating systematics and how to mitigate them, such that when more statistics are available, systematics wil not be the bottleneck of this analysis. In Fig. 7.4, the observed impact of nuisances is shown for the fitted signal strength. Here, the greatest influence comes from the MC statistics, more specifically, the SR 4.1 in 2018, followed by the contribution of electron efficiency and the ZZ normalisation. It clearly outlines the insufficient MC statistics. Overall, post-fit values are not shifted far away from their priors, and within uncertainties overlap (filled points). Also, pulls are moderate and condensed around the central value.

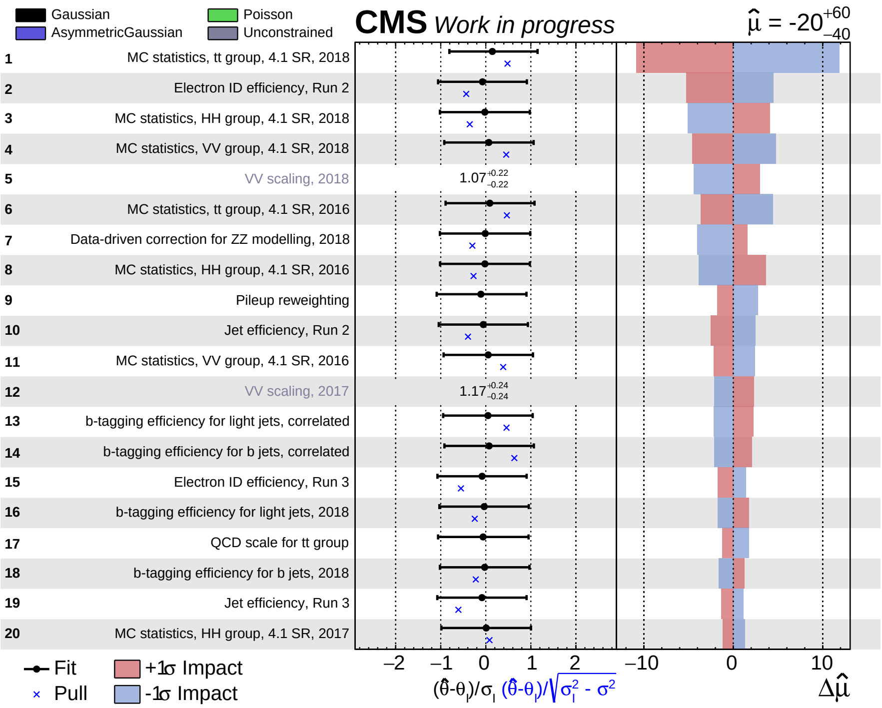

Figure 7.4. The observed ranking of the top 20 nuisance parameters by their impact on the signal strength modifier μ, for the 4l categories, combining full Run 2 and early Run 3 data.

7.1. Projection to HL-LHC and Combination with Other Channels

As the upcoming HL-LHC is expected to deliver an integrated luminosity up to 3 ab^{-1} at a centre-of-mass energy of at least 13.6 TeV, it is interesting to see how the calculated limit would be affected. It is well established that such a major increase in data will allow precision measurements of rare processes such as the HH production. In this section, projections are made to estimate the magnitude of the achievable sensitivity at the HL-LHC for the $HH \to WW^{*}ZZ^{*} \to 4l$ decay channel.

Table 7.3

Expected yields for 3 ab^{-1} in the signal and control regions considered for the extrapolation

Process	SR 4.1, events	SR 4.2, events	CRlow 4.1, events	CRlow 4.2, events
signal ($\times 100$)	34.05 ± 1.95	26.55 ± 1.65	7.96 ± 1.83	12.14 ± 2.63
background	68.1 ± 6.3	114.9 ± 6.3	122.4 ± 15.9	3298 ± 395

A simple extrapolation to 3 ab^{-1} is employed, scaling the signal and background yields with luminosity and assuming the current efficiencies and systematic uncertainties. This matches the most conservative extrapolation scenario, S1, as was introduced in Section 2.6. The total yields in both CRs and SRs are shown in Table 7.3, as they are used in the calculation. The extrapolation allows to set a median 95 % CL expected upper limit of 51.5 times the SM value of the HH production cross section. A per-category limit can be seen in Fig. 7.5. It is interesting to note that only with such an increase in integrated luminosity this channel's sensitivity would be of the same order as achieved by the CMS's full Run 2 analysis of $bbZZ$ as mentioned above. Yet, this only strengthens the idea that this channel could be included in the HH search combination.

Moreover, it had been intended from the very beginning that the four-lepton analysis will be combined with other $HH \to WW^{*}ZZ^{*}$ channels to improve the analysis sensitivity. As was mentioned in Chapter 6, the three-lepton category with a reduced dataset has been studied in parallel to this Thesis [126]. Therefore, it is further introduced in the following section, before providing a rough estimate of the combination of $WW^{*}ZZ^{*}$ channels.

The three-lepton category targets $WW \to l\nu qq$ and $ZZ \to llqq$. To target leptons decaying from the Z boson, the invariant mass of two OSSF leptons have to pass a loose invariant mass window of $m_{ll} \in (25, 100)$. To account for the semileptonic W boson decay, the missing energy has to satisfy $E_T > 20$ GeV. To account for the hadronic decay of the vector bosons, events must have at least three jets that are not b-tagged. The three-lepton category is subdivided into two subcategories – category 3.1 targets the on-shell Z boson and category 3.2 the off-shell. This analysis was considering the full Run 2 data only, therefore cannot be directly compared, however, it is possible to extrapolate the yields

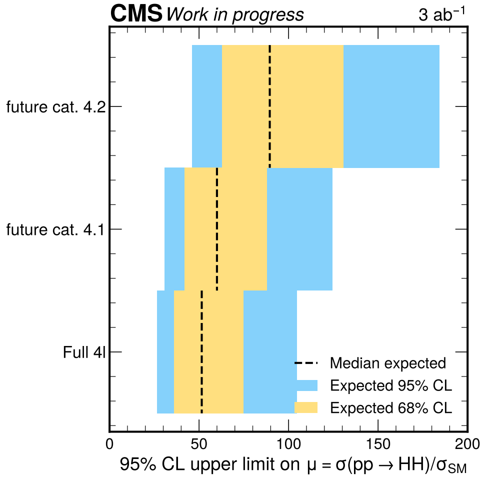

Figure 7.5. Expected upper limits on the signal strength modifier μ per 4l category and combined, when extrapolating to integrated luminosity of 3 ab^{-1}.

for a fair comparison. When extrapolating the event yields of these subcategories to the integrated luminosity covered in this Thesis, we get 0.044 for the signal and 1032 for the background in the category 3.1 and 0.028 for the signal and 257 for the background in category 3.2.

The main backgrounds after pre-selection are WZ, DY and $t\bar{t}$. The tighter requirement on jet multiplicity already allows to disfavour background. However, to combat DY contribution even more, the third lepton's transverse momentum requirement is raised to 15 GeV, same as for the sub-leading lepton. Two CRs are built to control the two main backgrounds. To target WZ the pre-selection is enhanced by adding $m_{ll} > 80$ GeV and $E_T > 50$ GeV. This allows to reach a 85 % pure CR. Overall, a good data to MC agreement is reached. However, similarly as for the ZZ modelling in the four-lepton categories, discrepancies were seen in the high jet multiplicity. Therefore, a data-driven correction was created based on the third, fourth and fifth jet's transverse momentum. After applying this correction, not only the shapes agreed well but the overall scaling was also much improved. To create a CR for DY, the pre-selection was slightly loosened requiring $m_{ll} < 80$ GeV, $E_T < 70$ GeV and at least two jets. This lead to around 50 % pure CR.

The three-lepton category uses a BDT to extract the signal. A BDT is built for each subcategory, and uses similar features – angular separation variables, Higgs boson pair related kinematic features, event kinematics. For both categories, the most impactful features are the angular distances between leptons and jets. In contrast to the four-lepton categories, the three-lepton category has three signal regions, selected based on the BDT score. The BDT score threshold is evaluated separately in each year. One SR comes from the on-shell subcategory and targets the most signal-like BDT score region, while in off-shell subcategory one SR targets the $WWZZ$ signal in the high-BDT score region, and one targets the full $VVVV$ contribution in the intermediate BDT score region.

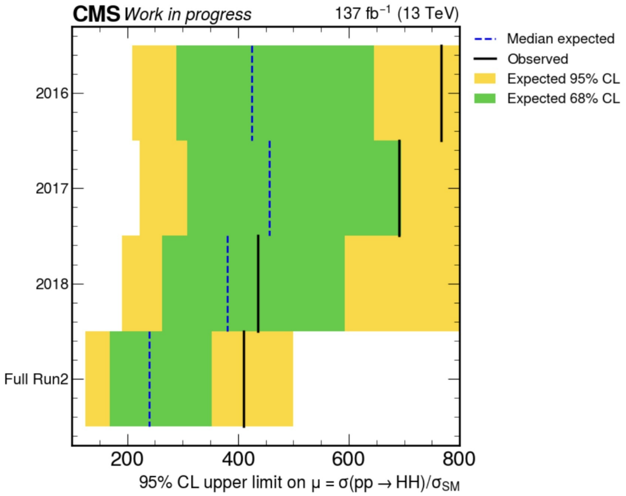

Figure 7.6. Expected and observed upper limits on the signal strength modifier μ per combined three-lepton category per year and across full Run 2 [126].

With full Run 2 data, the three-lepton category has been able to set an observed (expected) 95 % CL upper limit of 410 (240) times the SM value of the HH cross section [126]. A per-year evaluation is shown in Fig. 7.6. Similarly as in the four-lepton categories, the most impactful systematics come from MC statistics, lepton identification, as well as the WZ normalisation. Different to the four-lepton categories, the three-lepton categories observe a slight data surplus, however, it is compatible with the expectations within the uncertainties.

For the HL-LHC extrapolation, the results of only Run 2 will be considered for the three-lepton decay channel, however, work is ongoing to acquire improved results also with the early Run 3 dataset. Moreover, since both five- and six-lepton categories have not yet matured to output a result, their initial sensitivity will be used, as was shown in Table 6.1. As mentioned before, the extrapolation works with the assumption that the analysis strategy and systematic uncertainties remain unchanged. For the four-lepton categories, the previously quoted limit is used, while for the three-lepton channel the expected limit is extrapolated using Eq. (7.1):

$$\mu(\mathcal{L}_2) = \mu(\mathcal{L}_1)\sqrt{\frac{\mathcal{L}_1}{\mathcal{L}_2}}, \tag{7.1}$$

where $\mu(\mathcal{L}_2)$ is the signal strength at integrated luminosity $\mathcal{L}_2$, and $\mu(\mathcal{L}_1)$ is the signal strength at integrated luminosity $\mathcal{L}_1$. As a quick sanity check, if the signal strength of the four-lepton category was scaled using Eq. (7.1), a limit of 46.5 was reached. While using the full model and calculating the limit with `COMBINE` yielded an upper limit of 51.5. For other categories, the expected limit is estimated using Eq. (7.2):

$$\mu \propto \frac{S}{\sqrt{B}}, \tag{7.2}$$

When using Eq. (7.2) on the four-lepton categories, it was found out that a proportionality coefficient of 2.15 needs to be applied, thus, it is applied when calculating estimates for two-, five- and six-lepton categories. For the estimate on the expected combined sensitivity, an assumption is used that the sensitivities add in quadrature and that the sensitivity is inverse to the limit, thus, the combined signal strength, $\frac{1}{\mu^2_{\text{comb}}}$, is calculated using Eq. (7.3) by summing each individual signal strength, μ_i.

$$\frac{1}{\mu^2_{\text{comb}}} = \sum \frac{1}{\mu^2_i} \tag{7.3}$$

Following these assumptions, for 3 ab^{-1} the combination of all the mentioned WW^*ZZ^* categories, gives an estimate of the mean value of the 95 % CL upper limit of 34 times the SM value. The breakdown of the limit by category is shown in Table 7.4. This is in the magnitude of the result obtained for the $HH \to bbZZ$ channel, when analysing the full Run 2 data. Clearly, this approach ignores any correlated systematics, but is powerful enough to give a “back of the envelope” estimate that motivates future studies. Also, the sensitivities used for other $HH \to WW^*ZZ^*$ decays are slightly outdated, and significant improvement is expected. Moreover, a possible assimilation in the CMS multilepton analysis could allow for an even greater combined improvement and a complete reduction of the overlap.

Table 7.4

The estimate of the expected upper limit on the signal strength μ at 3 ab^{-1}

Category	Cat. 2	Cat. 3	Cat. 4	Cat. 5	Cat. 6	Combined
limit	3494	46.5	51.5	2038	2953	34.5

7.2. Summary

In this chapter, the $HH \to WW^*ZZ^* \to 4l$ analysis results were discussed, also outlining prospects for the future measurements in the HL-LHC era. The results obtained in this analysis represent an important step in the experimental exploration of the HH production. The following and the final chapter summarises the main conclusions of this Thesis and gives an outlook to the following HL-LHC eras, not only in the context of HH production studies, but also detector development.

8. CONCLUSIONS AND OUTLOOK

Within this Thesis, extensive work was carried out on the DCS and DSS for a MTD's test-stand, as well as a novel physics analysis was designed and performed in the four-lepton channels of the $HH \to WW^*ZZ^*$ decay channel. The set tasks for the Doctoral Thesis have been accomplished, theses defended, and the work outlined in this Thesis has allowed to form the following conclusions.

1. The review of literature summarised in Chapter 2 has shown that the analysis of HH production provides a direct probe of the Higgs potential and allows to experimentally constrain the Higgs boson self-coupling parameter.

2. In recent years the HH production has become an increasingly active area of research within the LHC program; it is especially highlighted by the HH production combination articles published by both the CMS and ATLAS collaboration.

3. A dedicated $HH \to WW^*ZZ^*$ decay channel analysis in the four-lepton decay channels as part of its categories is a strong and complementing contender for the HH analysis community, moreover, previously, this decay channel has not been explicitly targeted and optimised for.

4. As summarised in Chapter 3 and Chapter 4, the CERN accelerator complex with the LHC provides high-energy and high-luminosity pp collisions, and the multi-purpose CMS detector allows to reconstruct and identify many final states of these collisions, thus making it the perfect experimental setup for the $HH \to WW^*ZZ^* \to 4l$ decay channel analysis.

5. A novel $HH \to WW^*ZZ^* \to 4l$ decay channel analysis has been developed, and Chapter 6 encapsulates all the necessary building blocks of it. Several optimisation steps are shown for the designing of the framework, categories and object selection.

6. The performed analysis of $HH \to WW^*ZZ^* \to 4l$ decay channel has allowed to set an observed (expected) 95 % CL upper limit of 142.3 (176.8) times the SM value of the HH cross section. This is in agreement with the SM expectations, given the current experimental uncertainties.

7. The developed analysis framework is applicable for future $HH \to WW^*ZZ^* \to 4l$ and more generally, the $HH \to WW^*ZZ^*$ decay channel studies with increased amount of data, motivating such an analysis for the HL-LHC era studies.

8. Work detailed in Chapter 5 shows how a DCS has been built for the MTD test-stand. It has been built following the CMS production guidelines and has met all the set requirements. Moreover, it serves as a prototype for the final MTD DCS.

8.1. Outlook on the DCS Work

Now, as the LS3 is getting closer and closer, the work on the DCS becomes increasingly relevant. Section 5.5 already detailed three development scenarios for the built DCS prototype. The successful continuation of the project is crucial not only for the MTD test-stand, but also for the whole progression towards the final detector's DCS. It will need to continue to meet the needs of the experimental team, as well as follow the recommended production guidelines in order to shape into a self-sufficient, reliable, and robust system. Judging from previous experience, attaining such qualities is well within reach.

8.2. Outlook on the HH Analysis

The timing of this Thesis allowed to analyse the full Run 2 dataset and only a partial Run 3 dataset. Now, as the Run 3 is near its end, it is clear to see that when reanalysed, this analysis would be dominated by the Run 3 data. Moreover, the integrated luminosity would be more than doubled, ensuring a great playground for any HH production analysis. Section 7.1 already outlined the prospects of combining the $HH \to WW^*ZZ^* \to 4l$ analysis with other $HH \to WW^*ZZ^*$ decay channels, thus here the focus remains on the individual $HH \to WW^*ZZ^* \to 4l$ analysis.

Run 3 has brought many technical improvements in particle reconstruction and identification. An example are the powerful b-taggers that were not available in Run 2, such as the `ParticleNet` [128]. It is shown to have higher b-tagging efficiency and lower mis-tagging rates than the `DeepJet`, mainly because it considers jets as an unordered set of its constituent particles or a "particle cloud", rather than a set of ordered constituents. There is a high chance that by selecting a more performative tagger it would be possible to relax the jet transverse momentum requirements, thus recovering more signal while not sacrificing precision.

Similarly, attention would need to be given to the lepton identification. It is no surprise that with the increase in collected luminosity, the detector material has dealt with significant radiation damage. Thus, making precise measurements more challenging. Therefore, it would be interesting to investigate what could be improved, especially in the electron identification. As an example, a dedicated ID could be trained with a high signal efficiency, that is as effective also for the low-p_T electrons, on which the sensitivity of this analysis heavily depends on.

The increase in the analysed eras might allow to pivot from using a BDT discriminant in favour of a DNN one. This change would allow to use low-level variables for training the network. However, this could be done only if enough statistics are collected, which was not the case when analysing the dataset described in this Thesis. In such a case again the event categorisation and object selection requirements could be loosened to allow for more events to be used for the network.

Finally, it would be truly interesting to open two more aspects of the current analysis. The first would be the inclusion of a dedicated BSM study. In Section 6.5 the current BDT's response to several BSM scenarios was shown. However, it would be interesting to train a separate BDT (or DNN following the idea in the previous paragraph), to evaluate the upper limits on the HH production in these scenarios. Second, it would be interesting to explicitly target the second most popular HH production mode, the VBF.

Altogether, the foreseen data-taking periods ensure exciting years ahead for the HH production analyses and analysers. It will truly be a collaborative effort, as claiming the discovery of the HH production is in closer reach when working together, when combining as many decay channels and analysis as possible, thus showcasing what the high energy particle physics field is all about. Although the $HH \rightarrow WW^*ZZ^*$ decay channel will not play a central role in this search, it will be a significant contributor, pulling its own weight. I am excited to see what the next years will bring and will celebrate together with the community the discovery of HH production when the time comes.

ACKNOWLEDGEMENTS

I wish I could say that these formative years have been nothing but frolicking through meadows and greeting sunrises on mountain tops. If I had to do this again, I would change so many, many things (oh, hindsight, you silly thing), mainly being more present and cherishing the beautiful, beautiful souls around me throughout this journey. I hope you all know who to call when visiting the beautiful Latvia.

Enormous thanks go out to my supervisors. I thank you, **Kārli**, with all my heart for being our forever-light house, for your guidance and support, although at times I wished we had five of you. Thank you, **Toni**, for training me to be statistics a police, your enthusiasm and time, even when you were away on your World tour! Thank you, **Frank**, for your calm and encouraging presence, for being the most complete source of information on everything CERN and CMS!

A shout out to my closest teams. Dear Central DCS team, thank you for adopting me, I have learnt so much from each of you! **Cristina**, thank you for the trainings and being such a wonderful role model. **Wassef**, thank you for all the cycling talks, office's unlimited chocolate source, and being the absolute best office mate I've ever had, I wish I could be as kind and smart as you are! **Abdullah** and **Vaiva**, thank you for the normalcy! Dear HH-WWZZ team and especially the amazing dynamic duo of **Claude** and **Ana**, we achieved something truly amazing! This was such a pedagogically beautiful analysis, but oh, how often I wished it moved quicker. Ana, we did it!

I need to shine some spotlight on the catalysts in my life. Thank you, **CERN**, the most wonderful village, for bringing so many motivated and sparkling people together and into my life. Thank you, **CMS**, for showing what particle physics is about, and how it is to work in a big collaboration. Thank you, **LLR**, for the most physics discussions I've had in a two-week span. Thank you, **DTF**, for adopting the little IPPAT island. An honourable mention goes out to the **CJLST** and its Gods, the forever-changing **BTL** team, **Amrutha**, you're the best! As well as **Michael** and **Han** for the little STXS project we collaborated on. I'm so sad that our timing was off, as this truly was the best team work I have ever done.

My dear CMS **YSC** and **LHC EC Fora**, oh the ups and downs! This experience has been truly invaluable, from the daunting responsibility to the rewarding "we made this happen"! Thank you to the irreconcilable force that you are, **Kathryn**, I loved sharing afternoon crepes with you, and wished that our paths would have crossed more. My ALICE's bestie **Carolina**, thank you for holding the fort down for the LHC EC mentoring initiative. My dearest mentoring@CERN, thank you for forming my dream team and achieving the absolute highs. My LHCb bestie **Olaf**, thank you! **Simona**! Thank you for being the absolute icon and role model, for our Mentoring exchange outing! My only regret is that I got to hang out with you and the girls only in my final summer. Thank you, **WIT**, for introducing me to so many inspiring women, thank you, **Angelika**

Drees, for being my mentor exactly at the months when I arrived to CERN!

Oh, my comrades in the trenches, thank you for keeping up the morale! Dear **419**, thank you for the lunches! **Normund**, I'm happy we survived the electron task. I had my doubts. Thank you, **Lazar**, for trusting me with ice-skating, thank you, **Dace**, for saying yes to outings, although we did too little of them. **Marija**, thank you for your spark and trust in us all. Keep your momentum, gain new boosts, and I will be happy to see you reach your dreams. I'm sorry we sometimes were too cloudy. **Andri**, thank you for being at the right place at the right time. I (we) needed you so much. Will you ever recon your impact? Thank you for finding CERN's gems and introducing me to them.

My friends along the way, thank you for your laughter! **Niklas**, thank you for trusting me to blab about CMS to your smartest kids, and being so down to earth. **Tom**, thank you for letting me almost win in 7 Wonders, and dream about taking a gap year in New Zeeland. **Andrew**, thank you for saving my frisbee and showing me the source of Allondon. Thank you, **Rahul**, for picking the best office, it was lovely to see you grow. **Arkadiusz**, thank you for teaching me how to count my ping-pong goals in polish. **Afiq**, thank you for letting me pour out my heart about my favourite show of 2023. My LHCP family, especially **Yu-Wei Kao**, thank you for your hospitality in Taipei! My CSC sisters **Anna** and **Simran**, thank you for making it so memorable! **Jolanta**, my favourite French teacher of all time, thank you for enabling me to enjoy my time at France! **Katharine Leney**, thank you for creating my favourite plot of 2024, it single handedly raised the morale by 120 %. My HH bestie, **Torben**, it's a pity I met you only in my second half of the studies, I guess Baltics are too big. Thank you for making me wonder if Higgs boson is fun at parties, thank you for saying we are not broken, just PhD students. **Sven** and **Kristjan**, I am so glad I missed my DC tour and got to join yours. You've made all CBCs better. **Viktor**, thank you for the almost monthly check-ins and the grounding! Thank you my **Renaissance friends** for the hikes and sunburns, thank you, **Julian**, for noting that within my PhD I will learn more about myself than what I study.

Finally, my nearest and dearest, I couldn't have done it without you. **Ame**, thank you for being the most loyal friend I've ever had. I'm happy our paths keep crossing; however, I wish they'd be more in sync. My closest family, thank you for your unconditional love. **Ruta** and **Andris**, thank you for reminding me of afternoon cacao, and oh, how you read all your grandkids like open books, thank you! **Dad**, I'm so happy that you are proud of me, and I'm so proud of you slaying your PhD! **Brother**, it has always been so lovely to be on the same wavelength. Thank you for always understanding me! **Mārieši**, thank you for visiting me at CERN. **Vitaut** and **Inita**, thank you for asking about the LHC. **Adrian** and **Aiden**, thank you for all the puzzles and Legos, and the ones yet to come! Thanks to your parents for always warm invitations to visit! **Reini**, thank you for filling my heart with overflowing love, and taking the leap of faith and sampling the Francophone sphere with me. And above all, despite the always annoying, time-warying distances between us, thank you for wanting to go around Lac Leman with me.

References

[1] ATLAS Collaboration. "Observation of a new particle in the search for the Standard Model Higgs boson with the ATLAS detector at the LHC". In: *Physics Letters B* 716.1 (Sept. 2012), pp. 1–29. ISSN: 0370-2693. DOI: https://doi.org/10.1016/j.physletb.2012.08.020 (cit. on pp. 11, 17, 19, 45).

[2] CMS Collaboration. "Observation of a new boson at a mass of 125 GeV with the CMS experiment at the LHC". In: *Physics Letters B* 716.1 (2012), pp. 30–61. ISSN: 0370-2693. DOI: 10.1016/j.physletb.2012.08.021 (cit. on pp. 11, 17, 19, 45).

[3] CERN. *The High-Luminosity LHC Project. 298th Meeting of Scientific Policy Committee*. Tech. rep. CERN, 2016. URL: https://cds.cern.ch/record/2199189 (cit. on pp. 11, 47).

[4] CMS Collaboration. *A MIP Timing Detector for the CMS Phase-2 Upgrade*. Tech. rep. Geneva: CERN, 2019. URL: https://cds.cern.ch/record/2667167 (cit. on pp. 11, 64–66).

[5] F. Englert and R. Brout. "Broken Symmetry and the Mass of Gauge Vector Mesons". In: *Phys. Rev. Lett.* 13 (9 Aug. 1964), pp. 321–323. DOI: 10.1103/PhysRevLett.13.321 (cit. on pp. 17, 21).

[6] P. W. Higgs. "Broken Symmetries and the Masses of Gauge Bosons". In: *Phys. Rev. Lett.* 13 (16 Sept. 1964), pp. 508–509. DOI: 10.1103/PhysRevLett.13.508 (cit. on pp. 17, 21).

[7] D. Galbraith and C. Burgard. *Standard model of physics*. https://texample.net/model-physics/. Accessed: 2025-09-01 (cit. on p. 18).

[8] C. Giganti, S. Lavignac, and M. Zito. "Neutrino oscillations: The rise of the PMNS paradigm". In: *Progress in Particle and Nuclear Physics* 98 (2018), pp. 1–54. ISSN: 0146-6410. DOI: https://doi.org/10.1016/j.ppnp.2017.10.001 (cit. on p. 19).

[9] S. Mele. "The Measurement of the Number of Light Neutrino Species at LEP". In: *Adv. Ser. Dir. High Energy Phys.* 23 (2015), pp. 89–106. DOI: 10.1142/9789814644150_0004 (cit. on p. 19).

[10] S. Navas et al. "Review of Particle Physics". In: *Phys. Rev. D* 110 (3 Aug. 2024), p. 030001. DOI: 10.1103/PhysRevD.110.030001 (cit. on pp. 19, 26).

[11] M. Kobayashi and T. Maskawa. "CP-Violation in the Renormalizable Theory of Weak Interaction". In: *Progress of Theoretical Physics* 49.2 (Feb. 1973), pp. 652–657. ISSN: 0033-068X. DOI: 10.1143/PTP.49.652 (cit. on p. 20).

[12] G. S. Guralnik, C. R. Hagen, and T. W. B. Kibble. "Global Conservation Laws and Massless Particles". In: *Phys. Rev. Lett.* 13 (20 Nov. 1964), pp. 585–587. DOI: 10.1103/PhysRevLett.13.585 (cit. on p. 21).

[13] A. A. Migdal and A. M. Polyakov. “Spontaneous Breakdown of Strong Interaction Symmetry and the Absence of Massless Particles”. In: *Sov. Phys. JETP* 24 (1967), pp. 91–98 (cit. on p. 21).

[14] J. Riebesell. *The Higgs Potential.* https://tikz.net/higgs-potential/. Accessed: 2025-09-01 (cit. on p. 22).

[15] J. Goldstone. “Field theories with Superconductor solutions”. In: *Il Nuovo Cimento (1955-1965)* 19.1 (Jan. 1961), pp. 154–164. ISSN: 1827-6121. DOI: 10.1007/BF02812722 (cit. on p. 21).

[16] CMS Collaboration. *Combined measurements and interpretations of Higgs boson production and decay at sqrt(s)=13 TeV.* Tech. rep. Geneva: CERN, 2025. URL: https://cds.cern.ch/record/2929999 (cit. on p. 23).

[17] ATLAS Collaboration. *Combined measurements of Higgs boson production and decay at $\sqrt{s}$ = 13 TeV using up to 140 fb^{-1} of data collected by the ATLAS Experiment.* Tech. rep. Geneva: CERN, 2025. URL: https://cds.cern.ch/record/2937634 (cit. on p. 23).

[18] LHC Higgs Cross Section Working Group. *Handbook of LHC Higgs Cross Sections: 3. Higgs Properties: Report of the LHC Higgs Cross Section Working Group.* Ed. by S. Heinemeyer. CERN Yellow Reports: Monographs. CERN, 2013. DOI: 10.5170/CERN-2013-004 (cit. on p. 22).

[19] CMS Collaboration. “A portrait of the Higgs boson by the CMS experiment ten years after the discovery”. In: *Nature* 607 (July 2022), pp. 60–68. ISSN: 1476-4687. DOI: 10.1038/s41586-022-04892-x (cit. on p. 24).

[20] CMS Collaboration. “Precise determination of the mass of the Higgs boson and tests of compatibility of its couplings with the standard model predictions using proton collisions at 7 and 8 TeV”. In: *The European Physical Journal C* 75 (2015), p. 212. ISSN: 1434-6052. DOI: 10.1140/epjc/s10052-015-3351-7 (cit. on p. 24).

[21] J. C. Romao and J. P. Silva. “A resource for signs and Feynman diagrams of the Standard Model”. In: *Int. J. Mod. Phys. A* 27 (2012), p. 1230025. DOI: 10.1142/S0217751X12300256. eprint: 1209.6213 (cit. on p. 24).

[22] CMS Collaboration. “Constraints on the Higgs boson self-coupling from the combination of single and double Higgs boson production in proton-proton collisions at $\sqrt{s}$=13 TeV”. In: *Physics Letters B* 861 (2025), p. 139210. ISSN: 0370-2693. DOI: https://doi.org/10.1016/j.physletb.2024.139210 (cit. on p. 26).

[23] I. Neutelings. *Izaak Neutelings’ contribution to tikz.* https://tikz.net/author/izaak/. Accessed: 2025-06-19 (cit. on pp. 26, 49).

[24] LHC LHC Higgs Cross Section Working Group. *Handbook of LHC Higgs Cross Sections: 4. Deciphering the Nature of the Higgs Sector*. Tech. rep. Geneva: CERN, 2017. DOI: 10.23731/CYRM-2017-002. arXiv: 1610.07922. URL: https://cds.cern.ch/record/2227475 (cit. on pp. 26, 27, 31, 134).

[25] B. D. Micco et al. “Higgs boson potential at colliders: Status and perspectives”. In: *Reviews in Physics* 5 (2020), p. 100045. ISSN: 2405-4283. DOI: 10.1016/j.revip.2020.100045 (cit. on pp. 30, 31).

[26] R. Frederix et al. “Higgs pair production at the LHC with NLO and parton-shower effects”. In: *Physics Letters B* 732 (2014), pp. 142–149. ISSN: 0370-2693. DOI: 10.1016/j.physletb.2014.03.026 (cit. on p. 31).

[27] A. L. Read. “Presentation of search results: the CLs technique”. In: *Journal of Physics G: Nuclear and Particle Physics* 28.10 (Sept. 2002), p. 2693. DOI: 10.1088/0954-3899/28/10/313 (cit. on pp. 33, 136, 139).

[28] CMS Collaboration. “Search for Higgs Boson Pair Production in the Four b Quark Final State in Proton-Proton Collisions at $\sqrt{S}$=13 TeV”. In: *Physics Review Letters* 129 (2022), p. 081802. DOI: https://doi.org/10.1103/PhysRevLett.129.081802 (cit. on p. 33).

[29] CMS Collaboration. “Search for nonresonant Higgs boson pair production in final state with two bottom quarks and two tau leptons in proton-proton collisions at $\sqrt{S}$=13 TeV”. In: *Physics Letters B* 842 (2023), p. 137531. ISSN: 0370-2693. DOI: https://doi.org/10.1016/j.physletb.2022.137531 (cit. on p. 33).

[30] CMS Collaboration. “Search for nonresonant Higgs boson pair production in final states with two bottom quarks and two photons in proton-proton collisions at $\sqrt{S}$= 13 TeV”. In: *Journal of High Energy Physics* 2021.3 (Mar. 2021), p. 257. ISSN: 1029-8479. DOI: 10.1007/JHEP03(2021)257 (cit. on p. 33).

[31] ATLAS Collaboration. “Search for pair production of boosted Higgs bosons via vector-boson fusion in the bb¯bb¯ final state using pp collisions at s=13TeV with the ATLAS detector”. In: *Phys. Lett. B* 858 (2024), p. 139007. DOI: 10.1016/j.physletb.2024.139007 (cit. on p. 34).

[32] ATLAS Collaboration. “Search for the nonresonant production of Higgs boson pairs via gluon fusion and vector-boson fusion in the bb¯τ+τ- final state in proton-proton collisions at s=13 TeV with the ATLAS detector”. In: *Phys. Rev. D* 110.3 (2024), p. 032012. DOI: 10.1103/PhysRevD.110.032012 (cit. on p. 34).

[33] ATLAS collaboration. “Studies of new Higgs boson interactions through nonresonant HH production in the $b\bar{b}\gamma\gamma$ final state in pp collisions at $\sqrt{s} = 13$ TeV with the ATLAS detector”. In: *PoS* EPS-HEP2023 (2024), p. 422. DOI: 10.22323/1.449.0422 (cit. on p. 34).

[34] CMS Collaboration. “Search for Higgs boson pairs decaying to WW*WW*, WW*$\tau\tau$, and $\tau\tau\tau\tau$ in proton-proton collisions at $\sqrt{s}$= 13 TeV”. In: *Journal of High Energy Physics* 95 (2023), p. 101801. ISSN: 1029-8479. DOI: 10.1007/JHEP07(2023)095 (cit. on pp. 34, 39, 105, 113, 143).

[35] ATLAS Collaboration. “Search for non-resonant Higgs boson pair production in final states with leptons, taus, and photons in pp collisions at $\sqrt{s}$= 13 TeV with the ATLAS detector”. In: *Journal of High Energy Physics* 164 (2024). ISSN: 1029-8479. DOI: 10.1007/JHEP08(2024)164 (cit. on pp. 34, 39).

[36] ATLAS Collaboration. “Combination of Searches for Higgs Boson Pair Production in pp Collisions at $\sqrt{s}$= 13 TeV with the ATLAS Detector”. In: *Physics Review Letters* 133 (2024), p. 101801. DOI: https://doi.org/10.1103/PhysRevLett.133.101801 (cit. on pp. 34, 35).

[37] CMS Collaboration. *Combination of searches for nonresonant Higgs boson pair production in proton-proton collisions at $\sqrt{s}$= 13 TeV*. Tech. rep. Geneva: CERN, 2024. URL: https://cds.cern.ch/record/2917252 (cit. on pp. 34, 35).

[38] CMS and ATLAS collaborations. *Combination of ATLAS and CMS searches for Higgs boson pair production at 13 TeV*. Tech. rep. Geneva: CERN, 2025. URL: https://cds.cern.ch/record/2947521 (cit. on pp. 34, 36).

[39] CMS Collaboration. *Improved results on Higgs boson pair production in the 4b final state*. Tech. rep. Geneva: CERN, 2025. URL: https://cds.cern.ch/record/2947325 (cit. on p. 36).

[40] CMS Collaboration. *Search for HH production decaying into two b quarks and two photons in pp collisions at 13.6 TeV with a partial CMS Run 3 dataset*. Tech. rep. Geneva: CERN, 2025. URL: https://cds.cern.ch/record/2945062 (cit. on p. 36).

[41] ATLAS Collaboration. *Study of Higgs boson pair production in the $HH \to b\bar{b}\gamma\gamma$ final state with 308 fb^{-1} of data collected at $\sqrt{s}$ = 13 TeV and 13.6 TeV by the ATLAS experiment*. Tech. rep. CERN, July 2025. URL: https://cds.cern.ch/record/2937468 (cit. on p. 36).

[42] CMS Collaboration. *Novel strategy targeting HH and HHH production at High Level Trigger in Run 3*. Tech. rep. CERN, 2023. URL: https://cds.cern.ch/record/2868787 (cit. on p. 37).

[43] CMS Collaboration. *Efficiencies of New Low-pT Lepton+HT+b-tag Triggers for Run-3*. Tech. rep. CERN, 2025. URL: https://cds.cern.ch/record/2930808 (cit. on p. 37).

[44] ATLAS and CMS Collaborations. *Highlights of the HL-LHC physics projections by ATLAS and CMS*. Tech. rep. Geneva: CERN, 2025. URL: http://cds.cern.ch/record/2928907 (cit. on pp. 37, 38).

[45] S. Holmes, R. S. Moore, and V. Shiltsev. “Overview of the Tevatron collider complex: goals, operations and performance”. In: *Journal of Instrumentation* 6.08 (Aug. 2011), T08001. DOI: 10.1088/1748-0221/6/08/T08001 (cit. on p. 40).

[46] CDF Collaboration. “Observation of Top Quark Production in $\overline{p}p$ Collisions with the Collider Detector at Fermilab”. In: *Phys. Rev. Lett.* 74 (14 Apr. 1995), pp. 2626–2631. DOI: 10.1103/PhysRevLett.74.2626 (cit. on p. 40).

[47] D0 Collaboration. “Observation of the Top Quark”. In: *Phys. Rev. Lett.* 74 (14 Apr. 1995), pp. 2632–2637. DOI: 10.1103/PhysRevLett.74.2632 (cit. on p. 40).

[48] H. Hahn et al. “The RHIC design overview”. In: *Nuclear Instruments and Methods in Physics Research Section A: Accelerators, Spectrometers, Detectors and Associated Equipment* 499.2 (2003). The Relativistic Heavy Ion Collider Project: RHIC and its Detectors, pp. 245–263. ISSN: 0168-9002. DOI: https://doi.org/10.1016/S0168-9002(02)01938-1 (cit. on p. 40).

[49] K. Akai, K. Furukawa, and H. Koiso. “SuperKEKB collider”. In: *Nuclear Instruments and Methods in Physics Research Section A: Accelerators, Spectrometers, Detectors and Associated Equipment* 907 (2018). Advances in Instrumentation and Experimental Methods (Special Issue in Honour of Kai Siegbahn), pp. 188–199. ISSN: 0168-9002. DOI: https://doi.org/10.1016/j.nima.2018.08.017 (cit. on p. 40).

[50] Lopienska, Ewa. *The CERN accelerator complex, layout in 2022.* https://cds.cern.ch/images/CERN-GRAPHICS-2022-001-1. Accessed: 2025-01-14 (cit. on p. 41).

[51] M. Vretenar et al. *Linac4 design report.* Vol. 6. CERN Yellow Reports: Monographs. Geneva: CERN, 2020. DOI: 10.23731/CYRM-2020-006 (cit. on p. 41).

[52] R. Garoby and M. Vretenar. *Proposal for a 2 GeV LINAC injector for the CERN PS.* Tech. rep. Geneva: CERN, 1996. URL: https://cds.cern.ch/record/1599430 (cit. on p. 41).

[53] K. Schindl. *The PS Booster as Pre-Injector for LHC.* Tech. rep. Geneva: CERN, 1997. URL: https://cds.cern.ch/record/323757 (cit. on p. 42).

[54] J.-P. Burnet et al. *Fifty years of the CERN Proton Synchrotron: Volume 1.* CERN Yellow Reports: Monographs. Geneva: CERN, 2011. DOI: 10.5170/CERN-2011-004 (cit. on p. 42).

[55] N. Doble et al. “The Super Proton Synchrotron (SPS): A Tale of Two Lives”. In: *Technology Meets Research.* World Scientific, 2017. Chap. Chapter 5, pp. 135–177. DOI: 10.1142/9789814749145_0005 (cit. on p. 42).

[56] L. Evans and P. Bryant. “LHC Machine”. In: *Journal of Instrumentation* 3.08 (Aug. 2008), S08001. DOI: 10.1088/1748-0221/3/08/S08001 (cit. on p. 42).

[57] T. S. Pettersson and P. Lefèvre. *The Large Hadron Collider: conceptual design.* Tech. rep. CERN, 1995. DOI: 10.17181/CERN-AC-95-05-LHC (cit. on p. 43).

[58] ATLAS Collaboration. "The ATLAS Experiment at the CERN Large Hadron Collider". In: *Journal of Instrumentation* 3.08 (Aug. 2008), S08003. DOI: 10.1088/1748-0221/3/08/S08003 (cit. on p. 44).

[59] ALICE Collaboration. "The ALICE Experiment at the CERN Large Hadron Collider". In: *Journal of Instrumentation* 3.08 (Aug. 2008), S08002. DOI: 10.1088/1748-0221/3/08/S08002 (cit. on p. 44).

[60] CMS Collaboration. "The CMS experiment at the CERN LHC". In: *Journal of Instrumentation* 3.08 (Aug. 2008), S08004. DOI: 10.1088/1748-0221/3/08/S08004 (cit. on pp. 44, 48).

[61] LHCb Collaboration. "The LHCb Experiment at the CERN Large Hadron Collider". In: *Journal of Instrumentation* 3.08 (Aug. 2008), S08005. DOI: 10.1088/1748-0221/3/08/S08005 (cit. on p. 44).

[62] HL-LHC Collaboration. *The HL-LHC project*. https://hilumilhc.web.cern.ch/content/hl-lhc-project. Accessed: 2025-01-30 (cit. on p. 45).

[63] R. Alemany-Fernandez et al. *Operation and Configuration of the LHC in Run 1*. Tech. rep. 2013. URL: https://cds.cern.ch/record/1631030 (cit. on p. 45).

[64] J. Wenninger. *Operation and Configuration of the LHC in Run 2*. Tech. rep. 2019. URL: https://cds.cern.ch/record/2668326 (cit. on p. 46).

[65] D. J. et al. "The LHC run 2022". English. In: *Proc. IPAC'23* (Venice, Italy). IPAC'23 - 14th International Particle Accelerator Conference 14. JACoW Publishing, Geneva, Switzerland, May 2023, pp. 551–554. ISBN: 978-3-95450-231-8. DOI: 10.18429/JACoW-IPAC2023-MOPL020 (cit. on p. 46).

[66] A. C. et al. "Operation of the LHC during the 2023 proton run". English. In: *Proc. IPAC'24* (Nashville, TN). IPAC'24 - 15th International Particle Accelerator Conference 15. JACoW Publishing, Geneva, Switzerland, May 2024, pp. 87–90. ISBN: 978-3-95450-247-9. DOI: 10.18429/JACoW-IPAC2024-MOPC17 (cit. on p. 46).

[67] CMS Collaboration. *Public CMS Luminosity Information*. https://twiki.cern.ch/twiki/bin/view/CMSPublic/LumiPublicResults. Accessed: 2025-06-18 (cit. on p. 47).

[68] T. Sakuma and T. McCauley. "Detector and Event Visualization with SketchUp at the CMS Experiment". In: *Journal of Physics: Conference Series* 513.2 (June 2014), p. 022032. DOI: 10.1088/1742-6596/513/2/022032 (cit. on p. 48).

[69] C. Collaboration. "Precise mapping of the magnetic field in the CMS barrel yoke using cosmic rays". In: *Journal of Instrumentation* 5.03 (Mar. 2010), T03021. DOI: 10.1088/1748-0221/5/03/T03021 (cit. on pp. 50, 51).

[70] V. Karimäki et al. *The CMS tracker system project: Technical Design Report*. Technical design report. CMS. Geneva: CERN, 1997. URL: https://cds.cern.ch/record/368412 (cit. on pp. 52, 53).

[71] CMS Collaboration. "The CMS Phase-1 pixel detector upgrade". In: *Journal of Instrumentation* 16.02 (Feb. 2021), P02027. DOI: 10.1088/1748-0221/16/02/P02027 (cit. on pp. 52, 53).

[72] CMS Collaboration. "CMS tracking performance results from early LHC operation". In: *The European Physical Journal C* 70.4 (Dec. 2010), pp. 1165–1192. ISSN: 1434-6052. DOI: 10.1140/epjc/s10052-010-1491-3 (cit. on p. 52).

[73] CMS Collaboration. "Strategies and performance of the CMS silicon tracker alignment during LHC Run 2". In: *Nuclear Instruments and Methods in Physics Research Section A: Accelerators, Spectrometers, Detectors and Associated Equipment* 1037 (2022), p. 166795. ISSN: 0168-9002. DOI: https://doi.org/10.1016/j.nima.2022.166795 (cit. on p. 52).

[74] CMS Collaboration. *Track impact parameter resolution for the full pseudo rapidity coverage in the 2017 dataset with the CMS Phase-1 Pixel detector*. Tech. rep. CERN, 2020. URL: https://cds.cern.ch/record/2743740 (cit. on p. 53).

[75] CMS Collaboration Tracker Group. "CMS Phase-1 pixel detector refurbishment during LS2 and readiness towards the LHC Run 3". In: *Journal of Instrumentation* 17.09 (Sept. 2022), p. C09017. DOI: 10.1088/1748-0221/17/09/C09017 (cit. on p. 53).

[76] CMS Collaboration. *CMS Tracker Detector Performance Results*. https://twiki.cern.ch/twiki/bin/view/CMSPublic/DPGResultsTRK. Accessed: 2025-02-01 (cit. on p. 54).

[77] CMS Collaboration. *The CMS electromagnetic calorimeter project: Technical Design Report*. Technical design report. CMS. Geneva: CERN, 1997. URL: https://cds.cern.ch/record/349375 (cit. on pp. 54, 55).

[78] CMS Collaboration. "Performance of the CMS electromagnetic calorimeter in pp collisions at $\sqrt{s} = 13$ TeV". In: *Journal of Instrumentation* 19.09 (Sept. 2024), P09004. DOI: 10.1088/1748-0221/19/09/P09004 (cit. on p. 55).

[79] CMS Collaboration. *ECAL calibration performance in Run 3 with reprocessed data*. Tech. rep. CERN, 2024. URL: https://cds.cern.ch/record/2897806 (cit. on p. 55).

[80] CMS Collaboration. *The CMS hadron calorimeter project: Technical Design Report*. Technical design report. CMS. Geneva: CERN, 1997. URL: http://cds.cern.ch/record/357153 (cit. on p. 56).

[81] J. Mans et al. *CMS Technical Design Report for the Phase 1 Upgrade of the Hadron Calorimeter*. Tech. rep. CERN, 2012. URL: https://cds.cern.ch/record/1481837 (cit. on p. 56).

[82] CMS Collaboration. “Calibration of the CMS hadron calorimeters using proton-proton collision data at $\sqrt{S} = 13$ TeV”. In: *Journal of Instrumentation* 15.05 (May 2020), P05002. DOI: 10.1088/1748-0221/15/05/P05002 (cit. on p. 56).

[83] J. G. Layter. *The CMS muon project: Technical Design Report*. Technical design report. CMS. Geneva: CERN, 1997. URL: https://cds.cern.ch/record/343814 (cit. on p. 57).

[84] C. Collaboration. *Technical proposal for the upgrade of the CMS detector through 2020*. Tech. rep. CERN, 2011. URL: https://cds.cern.ch/record/1355706 (cit. on p. 57).

[85] A. Colaleo et al. *CMS Technical Design Report for the Muon Endcap GEM Upgrade*. Tech. rep. CERN, 2015. URL: https://cds.cern.ch/record/2021453 (cit. on pp. 57, 59).

[86] CMS Collaboration. “Development of the CMS detector for the CERN LHC Run 3”. In: *Journal of Instrumentation* 19.05 (May 2024), P05064. DOI: 10.1088/1748-0221/19/05/P05064 (cit. on pp. 58, 59).

[87] CMS Collaboration. “Calibration of the CMS drift tube chambers and measurement of the drift velocity with cosmic rays”. In: *Journal of Instrumentation* 5.03 (Mar. 2010), T03016. DOI: 10.1088/1748-0221/5/03/T03016 (cit. on p. 58).

[88] J. Hauser. “Cathode strip chambers for the CMS endcap muon system”. In: *Nuclear Instruments and Methods in Physics Research Section A: Accelerators, Spectrometers, Detectors and Associated Equipment* 384.1 (1996). BEAUTY ’96, pp. 207–210. ISSN: 0168-9002. DOI: https://doi.org/10.1016/S0168-9002(96)00905-9 (cit. on p. 58).

[89] J. Eysermans, M. I. P. Morales, and on behalf of the CMS Collaboration. “Operation and performance of the CMS Resistive Plate Chambers during LHC run II”. In: *Journal of Physics: Conference Series* 912.1 (Oct. 2017), p. 012015. DOI: 10.1088/1742-6596/912/1/012015 (cit. on p. 59).

[90] CMS Collaboration. “Performance of the CMS Level-1 trigger in proton-proton collisions at $\sqrt{S}$=13 TeV”. In: *Journal of Instrumentation* 15.10 (Oct. 2020), P10017. DOI: 10.1088/1748-0221/15/10/P10017 (cit. on pp. 60, 61, 98).

[91] CMS Collaboration. “Performance of the CMS high-level trigger during LHC Run 2”. In: *Journal of Instrumentation* 19.11 (Nov. 2024), P11021. DOI: 10.1088/1748-0221/19/11/P11021 (cit. on pp. 61, 62).

[92] ATLAS Collaboration. “Enriching the physics program of the CMS experiment via data scouting and data parking”. In: *Physics Reports* 1115 (2025). CMS physics results from the first decade of LHC data, pp. 678–772. ISSN: 0370-1573. DOI: https://doi.org/10.1016/j.physrep.2024.09.006 (cit. on p. 62).

[93] S. Cittolin, A. Rácz, and P. Sphicas. *CMS The TriDAS Project: Technical Design Report, Volume 2: Data Acquisition and High-Level Trigger. CMS trigger and data-acquisition project.* Technical design report. CMS. Geneva: CERN, 2002. URL: https://cds.cern.ch/record/578006 (cit. on p. 63).

[94] CMS Collaboration. *The Phase-2 Upgrade of the CMS Tracker.* Tech. rep. Geneva: CERN, 2017. DOI: 10.17181/CERN.QZ28.FLHW (cit. on p. 64).

[95] CMS Collaboration. *The Phase-2 Upgrade of the CMS Endcap Calorimeter.* Tech. rep. Geneva: CERN, 2017. DOI: 10.17181/CERN.IV8M.1JY2 (cit. on p. 65).

[96] CMS Collaboration. *The Phase-2 Upgrade of the CMS Barrel Calorimeters.* Tech. rep. Geneva: CERN, 2017. URL: https://cds.cern.ch/record/2283187 (cit. on p. 65).

[97] CMS Collaboration. *The Phase-2 Upgrade of the CMS Muon Detectors.* Tech. rep. Geneva: CERN, 2017. DOI: 10.17181/CERN.5T9S.VPMI (cit. on p. 65).

[98] CMS Collaboration. *The Phase-2 Upgrade of the CMS Level-1 Trigger.* Tech. rep. Geneva: CERN, 2020. URL: https://cds.cern.ch/record/2714892 (cit. on p. 65).

[99] F. Addesa et al. "Optimization of LYSO crystals and SiPM parameters for the CMS MIP timing detector". In: *Journal of Instrumentation* 19.12 (Dec. 2024), P12020. DOI: 10.1088/1748-0221/19/12/P12020 (cit. on p. 66).

[100] CMS Collaboration. "Particle-flow reconstruction and global event description with the CMS detector". In: *Journal of Instrumentation* 12.10 (Sept. 2017), P10003. DOI: 10.1088/1748-0221/12/10/P10003 (cit. on pp. 68, 69, 73).

[101] T. Speer et al. "Track reconstruction in the CMS tracker". In: *Nucl. Instrum. Meth. A* 559 (2006). Ed. by J. Blumlein et al., pp. 143–147. DOI: 10.1016/j.nima.2005.11.207 (cit. on p. 69).

[102] CMS Collaboration. "Performance of the CMS muon detector and muon reconstruction with proton-proton collisions at $\sqrt{s}$=13 TeV". In: *Journal of Instrumentation* 13.06 (June 2018), P06015. DOI: 10.1088/1748-0221/13/06/P06015 (cit. on pp. 70, 71).

[103] C. Collaboration. "Performance of CMS muon reconstruction in cosmic-ray events". In: *Journal of Instrumentation* 5.03 (Mar. 2010), T03022. DOI: 10.1088/1748-0221/5/03/T03022 (cit. on p. 70).

[104] CMS Collaboration. "Electron and photon reconstruction and identification with the CMS experiment at the CERN LHC". In: *Journal of Instrumentation* 16.05 (May 2021), P05014. DOI: 10.1088/1748-0221/16/05/P05014 (cit. on p. 71).

[105] W. Adam et al. "Reconstruction of electrons with the Gaussian-sum filter in the CMS tracker at the LHC". In: *Journal of Physics G: Nuclear and Particle Physics* 31.9 (July 2005), N9. DOI: 10.1088/0954-3899/31/9/N01 (cit. on p. 71).

[106] J. H. Friedman. "Greedy Function Approximation: A Gradient Boosting Machine". In: *The Annals of Statistics* 29.5 (2001), pp. 1189–1232. ISSN: 00905364, 21688966 (cit. on p. 71).

[107] M. Cacciari, G. P. Salam, and G. Soyez. "The anti-kt jet clustering algorithm". In: *Journal of High Energy Physics* 2008.04 (Apr. 2008), p. 063. DOI: 10.1088/1126-6708/2008/04/063 (cit. on p. 72).

[108] CMS Collaboration. "Pileup mitigation at CMS in 13 TeV data". In: *Journal of Instrumentation* 15.09 (Sept. 2020), P09018. DOI: 10.1088/1748-0221/15/09/P09018 (cit. on p. 73).

[109] D. Bertolini et al. "Pileup per particle identification". In: *Journal of High Energy Physics* 59.10 (Oct. 2014), pp. 1029–8479. DOI: 10.1007/JHEP10(2014)059 (cit. on p. 73).

[110] E. Bols et al. "Jet flavour classification using DeepJet". In: *Journal of Instrumentation* 15.12 (Dec. 2020), P12012. DOI: 10.1088/1748-0221/15/12/P12012 (cit. on pp. 73, 108).

[111] CMS Collaboration. *CMS Monte Carlo production overview*. https://opendata.cern.ch/docs/cms-mc-production-overview. Accessed: 2025-07-07 (cit. on p. 74).

[112] J. Alwall et al. "The automated computation of tree-level and next-to-leading order differential cross sections, and their matching to parton shower simulations". In: *Journal of High Energy Physics* 2014.7 (July 2014), p. 79. ISSN: 1029-8479. DOI: 10.1007/JHEP07(2014)079 (cit. on pp. 75, 95).

[113] T. Sjöstrand, S. Mrenna, and P. Skands. "PYTHIA 6.4 physics and manual". In: *Journal of High Energy Physics* 2006.05 (May 2006), p. 026. DOI: 10.1088/1126-6708/2006/05/026 (cit. on pp. 75, 95).

[114] P. Nason. "A new method for combining NLO QCD with shower Monte Carlo algorithms". In: *Journal of High Energy Physics* 2004.11 (Dec. 2004), p. 040. DOI: 10.1088/1126-6708/2004/11/040 (cit. on pp. 75, 95).

[115] G. Heinrich, J. Lang, and L. Scyboz. "Erratum to: SMEFT predictions for gg → hh at full NLO QCD and truncation uncertainties". In: *Journal of High Energy Physics* 2023.10 (Oct. 2023), p. 86. ISSN: 1029-8479. DOI: 10.1007/JHEP10(2023)086 (cit. on pp. 75, 95).

[116] J. Bellm et al. "Herwig 7.0/Herwig++ 3.0 release note". In: *Eur. Phys. J. C* 76.4 (2016), p. 196. DOI: 10.1140/epjc/s10052-016-4018-8 (cit. on p. 75).

[117] J. Allison et al. "Recent developments in Geant4". In: *Nuclear Instruments and Methods in Physics Research Section A: Accelerators, Spectrometers, Detectors and Associated Equipment* 835 (2016), pp. 186–225. ISSN: 0168-9002. DOI: https://doi.org/10.1016/j.nima.2016.06.125 (cit. on p. 76).

[118] M. Peruzzi et al. “The NanoAOD event data format in CMS”. In: *Journal of Physics: Conference Series* 1525.1 (Apr. 2020), p. 012038. DOI: 10.1088/1742-6596/1525/1/012038 (cit. on p. 76).

[119] J. Shiers. “The Worldwide LHC Computing Grid (worldwide LCG)”. In: *Computer Physics Communications* 177.1 (2007). Proceedings of the Conference on Computational Physics 2006, pp. 219–223. ISSN: 0010-4655. DOI: https://doi.org/10.1016/j.cpc.2007.02.021 (cit. on p. 77).

[120] M. Gonzalez-Berges. “The Joint COntrols Project Framework”. In: *arXiv: Instrumentation and Detectors* (2003). URL: https://api.semanticscholar.org/CorpusID:18412592 (cit. on p. 78).

[121] DELPHI Collaboration. “The DELPHI detector at LEP”. In: *Nuclear Instruments and Methods in Physics Research Section A: Accelerators, Spectrometers, Detectors and Associated Equipment* 303.2 (1991), pp. 233–276. ISSN: 0168-9002. DOI: https://doi.org/10.1016/0168-9002(91)90793-P (cit. on p. 79).

[122] B. Franek and C. Gaspar. “SMI++ object oriented framework used for automation and error recovery in the LHC experiments”. In: *Journal of Physics: Conference Series* 219.2 (Apr. 2010), p. 022031. DOI: 10.1088/1742-6596/219/2/022031 (cit. on p. 79).

[123] B. Copy et al. *Monitoring of CERN’s Data Interchange Protocol (DIP) system.* Tech. rep. CERN, 2018, THPHA162. DOI: 10.18429/JACoW-ICALEPCS2017-THPHA162 (cit. on p. 85).

[124] C. Gaspar, M. Dönszelmann, and P. Charpentier. “DIM, a portable, light weight package for information publishing, data transfer and inter-process communication”. In: *Computer Physics Communications* 140.1 (2001). CHEP2000, pp. 102–109. ISSN: 0010-4655. DOI: https://doi.org/10.1016/S0010-4655(01)00260-0 (cit. on p. 85).

[125] CMS Collabortion. *Results of the thermal tests performed using the BTL cooling setup at TIF*. Tech. rep. CERN, 2024. URL: https://cds.cern.ch/record/2901316 (cit. on p. 86).

[126] A. Sculac. “Measurement of electron identification efficiency and the search for Higgs boson pair production in the WWZZ decay channel using the CMS detector at the at the Large Hadron Collider”. Theses. Institut Polytechnique de Paris; PMF, University of Zagreb, Nov. 2025. URL: https://theses.hal.science/tel-05540175 (cit. on pp. 92, 146, 148).

[127] CMS Collaboration. “Operation and performance of the CMS silicon strip tracker with proton-proton collisions at the CERN LHC”. In: *JINST* 20.08 (2025), P08027. DOI: 10.1088/1748-0221/20/08/P08027. arXiv: 2506.17195 (cit. on p. 94).

[128] CMS Collaboration. *Run 3 commissioning results of heavy-flavor jet tagging at $\sqrt{s}$ =13.6 TeV with CMS data using a modern framework for data processing.* Tech. rep. CERN, 2024. URL: https://cds.cern.ch/record/2898463 (cit. on pp. 95, 151).

[129] S. Alioli et al. "NLO Higgs boson production via gluon fusion matched with shower in POWHEG". In: *JHEP* 04 (2009), p. 002. DOI: 10.1088/1126-6708/2009/04/002. arXiv: 0812.0578 `[hep-ph]` (cit. on p. 95).

[130] P. Nason and C. Oleari. "NLO Higgs boson production via vector-boson fusion matched with shower in POWHEG". In: *JHEP* 02 (2010), p. 037. DOI: 10.1007/JHEP02(2010)037. arXiv: 0911.5299 `[hep-ph]` (cit. on p. 95).

[131] T. Melia et al. "W+W-, WZ and ZZ production in the POWHEG BOX". In: *JHEP* 11 (2011), p. 078. DOI: 10.1007/JHEP11(2011)078. arXiv: 1107.5051 `[hep-ph]` (cit. on p. 95).

[132] R. Frederix and S. Frixione. "Merging meets matching in MC@NLO". In: *Journal of High Energy Physics* 2012.12 (Dec. 2012), p. 61. ISSN: 1029-8479. DOI: 10.1007/JHEP12(2012)061 (cit. on p. 97).

[133] P. Artoisenet et al. "Automatic spin-entangled decays of heavy resonances in Monte Carlo simulations". In: *Journal of High Energy Physics* 2013.3 (Mar. 2013), p. 15. ISSN: 1029-8479. DOI: 10.1007/JHEP03(2013)015 (cit. on p. 97).

[134] A. V. Gritsan et al. "New features in the JHU generator framework: constraining Higgs boson properties from on-shell and off-shell production". In: *Phys. Rev. D* 102.5 (2020), p. 056022. DOI: 10.1103/PhysRevD.102.056022. arXiv: 2002.09888 `[hep-ph]` (cit. on p. 97).

[135] K. Hamilton, P. Nason, and G. Zanderighi. "MINLO: multi-scale improved NLO". In: *Journal of High Energy Physics* 2012.10 (Sept. 2012), p. 155. ISSN: 1029-8479. DOI: 10.1007/JHEP10(2012)155 (cit. on p. 97).

[136] A. M. Sirunyan et al. "Extraction and validation of a new set of CMS PYTHIA8 tunes from underlying-event measurements". In: *Eur. Phys. J. C* 80 (2020), p. 4. DOI: 10.1140/epjc/s10052-019-7499-4. arXiv: 1903.12179 `[hep-ex]` (cit. on p. 97).

[137] R. D. Ball et al. "Parton distributions from high-precision collider data". In: *The European Physical Journal C* 77.10 (Oct. 2017), p. 663. ISSN: 1434-6052. DOI: 10.1140/epjc/s10052-017-5199-5 (cit. on p. 97).

[138] CMS GEN XSEC TASK FORCE. *Cross Section DB Tool.* https://xsecdb-xsdb-official.app.cern.ch/xsdb/. Accessed: 2025-02-18 (cit. on pp. 97, 134).

[139] J. Baglio et al. "$gg \to HH$: Combined Uncertainties". In: *Phys. Rev. D* 103 (2021), p. 056002. DOI: 10.1103/PhysRevD.103.056002. arXiv: 2008.11626 (cit. on pp. 97, 134).

[140] B. Mellado Garcia et al. “CERN Report 4: Part I Standard Model Predictions”. In: (2016). URL: https://cds.cern.ch/record/2150771 (cit. on pp. 97, 134).

[141] Common ATLAS-CMS effort. *NNLO+NNLL top-quark-pair cross sections*. https://twiki.cern.ch/twiki/bin/view/LHCPhysics/TtbarNNLO. Accessed: 2025-02-17 (cit. on pp. 97, 134).

[142] CMS Collaboration. “Measurement of the inclusive W and Z production cross sections in pp collisions at $\sqrt{S} = 7$ TeV with the CMS experiment”. In: *Journal of High Energy Physics* 2011.10 (Oct. 2011), p. 132. ISSN: 1029-8479. DOI: 10.1007/JHEP10(2011)132 (cit. on p. 98).

[143] CMS Collaboration. *Low-p_T Electron ID scale factors from CMS in proton-proton collisions at $\sqrt{s}$ =13 TeV using J/ψ events*. Tech. rep. CERN, 2023. URL: https://cds.cern.ch/record/2879279 (cit. on p. 98).

[144] CMS Collaboration. “Measurement of the Higgs boson production rate in association with top quarks in final states with electrons, muons, and hadronically decaying tau leptons at $\sqrt{S}$=13 TeV”. In: *The European Physical Journal C* 81.4 (Apr. 2021), p. 378. ISSN: 1434-6052. DOI: 10.1140/epjc/s10052-021-09014-x (cit. on p. 104).

[145] A. Hocker et al. *TMVA - Toolkit for Multivariate Data Analysis with ROOT*. Tech. rep. Geneva: CERN, 2007 (cit. on p. 104).

[146] T. Chen and C. Guestrin. “XGBoost: A Scalable Tree Boosting System”. In: *Proceedings of the 22nd ACM SIGKDD International Conference on Knowledge Discovery and Data Mining*. KDD ’16. San Francisco, California, USA: Association for Computing Machinery, 2016, pp. 785–794. ISBN: 9781450342322. DOI: 10.1145/2939672.2939785 (cit. on pp. 106, 114).

[147] S. M. Lundberg and S.-I. Lee. “A unified approach to interpreting model predictions”. In: *Proceedings of the 31st International Conference on Neural Information Processing Systems*. NIPS’17. Long Beach, California, USA: Curran Associates Inc., 2017, pp. 4768–4777. ISBN: 9781510860964 (cit. on p. 118).

[148] A. Karlberg et al. *Ad interim recommendations for the Higgs boson production cross sections at $\sqrt{s} = 13.6$ TeV*. Tech. rep. 13 pages, 9 tables. Official report of the LHC Higgs Working Group. Geneva: CERN, 2024. arXiv: 2402.09955. URL: https://cds.cern.ch/record/2886099 (cit. on p. 134).

[149] CMS Collaboration. “Precision luminosity measurement in proton-proton collisions at $\sqrt{s} = 13$ TeV in 2015 and 2016 at CMS”. In: *Eur. Phys. J. C* 81 (2021), p. 800. DOI: 10.1140/epjc/s10052-021-09538-2. arXiv: `2104.01927 [hep-ex]` (cit. on p. 134).

[150] CMS Collaboration. *CMS Luminosity Measurements for the 2016 Data Taking Period*. Tech. rep. Geneva: CERN, 2017. URL: https://cds.cern.ch/record/2257069 (cit. on p. 134).

[151] CMS Collaboration. *CMS luminosity measurement for the 2017 data-taking period at $\sqrt{s}$ = 13 TeV*. Tech. rep. Geneva: CERN, 2018. URL: https://cds.cern.ch/record/2621960 (cit. on p. 134).

[152] CMS Collaboration. *CMS luminosity measurement for the 2018 data-taking period at $\sqrt{s}$ = 13 TeV*. Tech. rep. Geneva: CERN, 2019. URL: https://cds.cern.ch/record/2676164 (cit. on p. 134).

[153] CMS Collaboration. *Luminosity measurement in proton-proton collisions at* 13.6 TeV *in 2022 at CMS*. Tech. rep. Geneva: CERN, 2024. URL: http://cds.cern.ch/record/2890833 (cit. on p. 134).

[154] CMS Collaboration. "Measurement of the offline integrated luminosity for the CMS proton-proton collision dataset recorded in 2023". In: (2024). URL: https://cds.cern.ch/record/2904808 (cit. on p. 134).

[155] CMS Collaboration. "The CMS Statistical Analysis and Combination Tool: Combine". In: *Computing and Software for Big Science* 8.1 (Nov. 2024), p. 19. ISSN: 2510-2044. DOI: 10.1007/s41781-024-00121-4 (cit. on p. 137).

[156] G. Cowan et al. "Asymptotic formulae for likelihood-based tests of new physics". In: *The European Physical Journal C* 71.2 (Feb. 2011), p. 1554. ISSN: 1434-6052. DOI: 10.1140/epjc/s10052-011-1554-0 (cit. on p. 138).

[157] CMS Collaboration. "Search for nonresonant Higgs boson pair production in the four leptons plus two b jets final state in proton-proton collisions at $\sqrt{s} = 13$ TeV". In: *Journal of High Energy Physics* 2023.6 (June 2023), p. 130. ISSN: 1029-8479. DOI: 10.1007/JHEP06(2023)130 (cit. on p. 143).

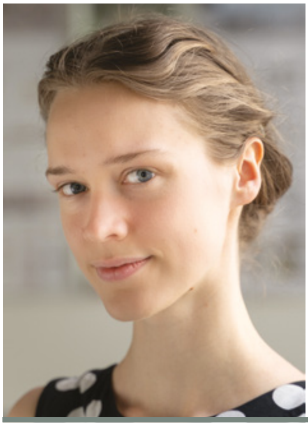

Antra Gaile was born in 1997. She obtained a Bachelor's degree (2019) and a Master's degree (2021) in Physics from the University of Latvia. She has worked at the MHD Technology Laboratory at the Institute of Physics of the University of Latvia and then at the Institute of Particle Physics and Accelerator Technologies of Riga Technical University. She developed an interest in particle physics during the CERN summer student programme in 2019 and during her two PhD years at CERN.